Real space analysis of *operando* X-ray spectroscopy and scattering studies of Cobalt Fischer-Tropsch Synthesis catalysts

Jennifer J. Herbert

A thesis presented for the Degree of

Doctor of Engineering

Department of Chemistry

University College London

March 2019

Supervised by

Professor Andrew M. Beale

I, Jennifer Herbert confirm that the work presented in this thesis is my own. Where information has been derived from other sources, I confirm that this has been indicated in the thesis.

Abstract

Size effects on Co-based Fischer Tropsch synthesis (FTS) catalysts are well known, however their evolution over time is less well interrogated. Three key issues related to particle size remain: the behaviour of small Co^0 nanoparticles during FTS and their potential re-oxidation, the evolution and influence of the Co^0 nanostructure (fcc/hcp/intermixed Co^0), and the formation of metal-support interactions during FTS.

Two synthesis methods were used to produce Co/SiO_2 catalysts. The first experimental chapter concerns the application of an inverse micelle synthesis (IMS) method for preparing powder-supported FTS catalysts. The aim was to create a catalyst with tight particle size control in order to better study particle size effects, however this was limited by the difficulty in removing the surfactant.

While the final two experimental chapters focus on *operando* characterization using synchrotron-based X-ray techniques for two different sized catalysts synthesized using a standard Schlenk technique; 3 and 11 nm which fall below and above the stable size range respectively.

Novel Debye simulations using a unic model were applied to synchrotron-based X-Ray diffraction (XRD) data acquired from a working FTS catalyst. While the 11 nm particle size catalyst is stable, this analysis shows a small variation in the hcp/fcc/intermixed ratio over the first 12 h of FTS, possible related to a known drop in activity during the initial stages of FTS. The hcp fraction decreases by -5.03 %, fcc increase by 1.24 %, and the mixed block increase by 3.7 %. About 20 % of the initial sample is unreduced CoO which reduces very slightly under FTS conditions.

The majority of the Co^0 content in the 3 nm sample oxidizes in the first hour of exposure to FTS conditions, although some of the larger Co^0 particles remain active - as observed by XRD. Additionally, no support phases are observed initially or being formed during FTS on either of the different average particle sized catalysts.

Impact Statement

Fischer-Tropsch synthesis (FTS) has experienced a renaissance over the last decade and a half due to drastic increases in oil price between 2002 and 2014, traditional long-term fuel supply concerns and environmental factors. Additionally, the process has attracted significant investment due to advances in the extraction of natural gas, recent legislation, and the increasing interest in the use of syngas derived from partial combustion or pyrolysis of biomass.

Synchrotron-based X-ray o*perando* techniques use X-ray radiation from the high spatial and time resolution source of synchrotrons to probe catalysts as they function, while monitoring gas output. Such experiments can monitor, analyse, and interpret the behaviour and evolution of a catalyst while on stream. The information gathered improves our understanding of the system and can be used to improve industrial catalysts.

In this thesis synchrotron-based *operando* X-ray diffraction (XRD) and X-ray absorption spectroscopy (XAS) were applied to a Co/MCF-17 (silica) catalyst of two sizes. One in the stable size range (11 nm) and one in the smaller unstable size range (3 nm). The findings from this work provide insight into the reoxidation of small Co^0 nanoparticles under FTS condition, only observed in the smaller nanoparticle sample. While the larger Co^0 nanoparticle catalyst (11 nm) remains very stable during FTS. Showing only a minimal variation in XRD patterns and XAS spectra in the first 12 h of FTS, attributed to a slight increase in particles size or the fcc/hcp/intermixed Co0 ratio as determined by novel Debye simulations of the XRD data (a decrease of -5.03 % in the hcp fraction).

The formation of metal support interactions in these samples were also ruled out during pre-treatment and FTS.

These findings could aid in the development of a greater understanding of small Co^0 deactivation and the influence of the Co^0 polymorphs during the initial stages of FTS. They may also improve the understanding of the system in order to design experiments to better target key issues relating to FTS catalysts.

Acknowledgements

Firstly, I would like to express my appreciation and thanks to my supervisor Andrew Beale. Your guidance, encouragement, support, and advice has been invaluable. I would also like to thank Alessandro Longo for his support, encouragement, and friendship while I was based in France and to all the staff at DUBBLE.

Special thanks go to those who worked with me, especially on beamtimes. To Daniela Farmer, Miren Agote, Yaroslav Odarchenko, Donato Decarolis, and Peixi Cong. Last but not least, I thank my family and closest friends for their support throughout my EngD.

Contents

1. Introduction

Our society is heavily dependent on the use of catalysts. Approximately 85-90 % of all products from the chemical industry are made using catalytic processes[1] and it is estimated that approximately 30 % of the gross domestic product of European economies is dependent on their use.[2] More vitally still, catalysts are significantly embedded in the processes which produce the fundamental factors of our survival: food, fuel and water.[2] As such, there is a great societal and economic imperative to study and improve catalysts across the board.

Catalysts increase the rate of chemical reactions or lower the reaction temperature by lowering the activation energy – the minimum amount of energy required to perform the reaction. Catalysts are grouped into three categories: heterogeneous, homogeneous and biocatalysts.[1] Heterogeneous catalysts are solids which catalyse reactions of molecules in gas or solutions, and are by far the most common type of industrial catalyst. Homogeneous catalysts, on the other hand, are in the same phase as the reactants (liquids), and biocatalysts are enzymes.[1]

In Figure 1.1, a generalised example of a heterogeneous catalytic bimolecular reaction is shown, as well as the corresponding reaction coordinate diagram. A and B are the reactants, which react to form the product P. In the uncatalyzed reaction A and B would need to collide with enough energy to overcome the activation energy, the maximum of the orange curve (Figure 1.1). However, a catalyst allows for an alternative route. There are two popular mechanisms for bimolecular reactions: the Langmuir-Hinshelwood mechanism (a reaction between two adsorbed molecules) and Eley-Rideal mechanism (a reaction between an adsorbed molecule and a gas molecule).

A generalised example of the Langmuir-Hinshelwood mechanism is shown below in Figure 1.1. The process starts with the adsorption of the reactants onto the catalyst surface, on the surface they react to form P, after which P desorbes from the surface. This alternative route, although more complex, lowers the activation energy.[1] It is worth noting however, that there is no change in the

free energy (ΔE) of the overall reaction, and so the equilibrium constant also remains unchanged. Therefore, unfavourable reactions will remain unfavourable.[3]

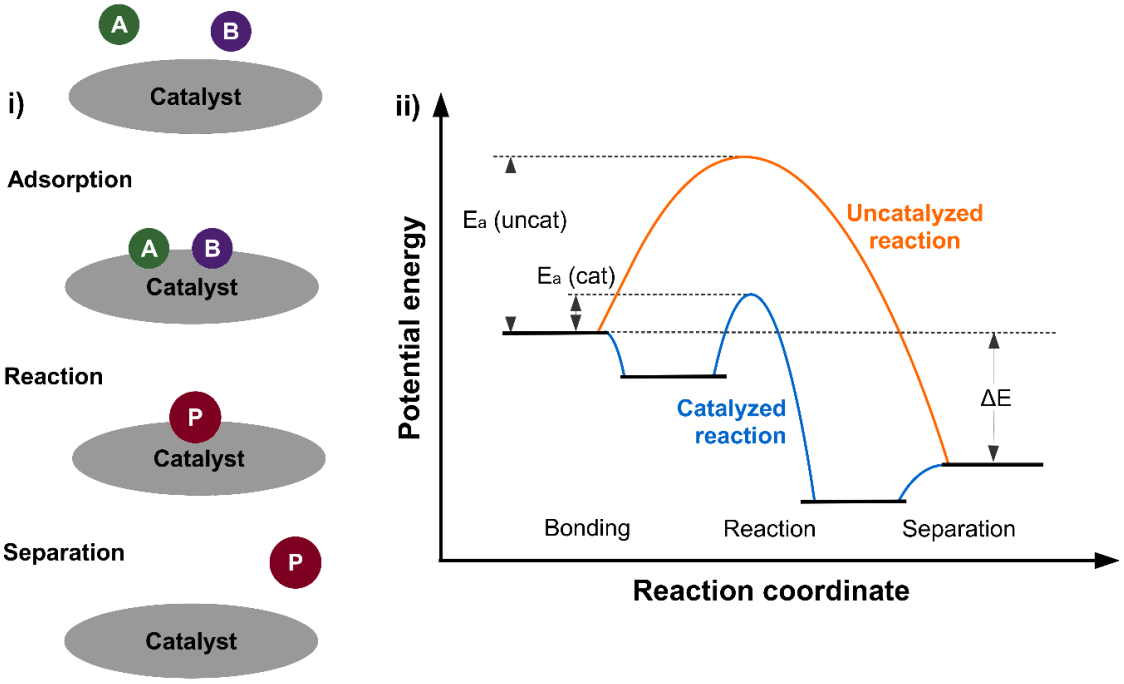

Figure 1.1: i) Diagram representing catalytic processes of a generalized homogeneous catalyst, and ii) the corresponding reaction coordinate diagram showing both the uncatalysed and catalysed reactions. Adapted from reference [1].

Reactions occur on the catalyst surface at active sites. For heterogeneous catalysts, active sites are defined as the ensemble of atoms that directly catalyse a reaction.[4] Such catalysts are commonly comprised of nanoparticles distributed over a support,[1] high surface area solids to which the catalyst particles are deposited or otherwise affixed.[5] As such, heterogenous catalysts are typically polycrystalline materials. Different crystal facets possess different atomic surface structures, as well as edges and corners defined by the nanoparticles size and shape,[6] all of which influence available active sites.

The three key qualities of any catalyst are activity, selectivity, and lifetime.[3] Activity is the ability of a catalyst to convert a feedstock to products, selectivity is the ability of a catalyst to produce the desired product, and lifetime is the time for which a catalyst keeps a sufficiently high level of activity and selectivity.[3] Activity

and selectivity are both influenced by the type and number of active sites available on the catalyst surface.

FTS catalysts were first developed in 1923 by Franz Fischer and Hans Tropsch.[7] Interest in FTS has historically been deeply intertwined with oil prices and access to oil reserves. The world's first FT plant was built in 1936 in Oberhausen, Germany, in an attempt to convert Germany's large coal reserves into liquid hydrocarbons for the German war effort.[8] Later in 1955, SASOL implemented the first large-scale FTS plant, again for conversion of coal to liquid hydrocarbons, this time in a bid for South African energy independence.[8]

FTS has experienced a renaissance due to traditional long-term fuel supply concerns, environmental factors, and drastic increases in oil price between 2002 and 2014 (appendix 1). It has attracted significant investment due to advances in the extraction of natural gas, and the increasing interest in the use of syngas derived from partial combustion or pyrolysis of biomass.[9] Although oil prices dropped suddenly in 2014 and have fluctuated with a slight increase since then, interest remains in FTS as a process due to the long-term instability of oil prices.

Figure 1.2: Flow diagram highlighting the main stages of FTS.

FTS plays a significant role in XTL conversion (X To Liquid; where X=natural gas, coal or biomass).[10] The FTS-based XTL process begins with syngas generation from the chosen feedstock via gasification, reforming or partial oxidation. This is followed by FTS for the conversion of syngas to syncrude, which is finally upgraded or refined into the final products: fuels and petrochemicals - as shown in Figure 1.2.

Although syngas can be obtained from practically any carbon source, natural gas and coal are the most commonly used, and the processes in which they are used are by far the most technologically mature.[11] Additionally, biomass to liquid (BTL) conversion is an attractive process potentially providing a

renewable source of fuels.[12] However the energy density of biomass is significantly less than that of coal which increases the cost of production and requires additional processing steps for the production of the biomass feedstock.[9]

Ideally, the composition of the syngas is tuned to the requirements of the specific form of FTS used but is primarily dependent on the feedstock, the specific conversion method, and the conditions of conversion. Commercial FTS plants use one of three types of synthesis conditions: Fe-based high temperature FTS (Fe-HTFT), Fe-based low temperature FTS (Fe-LTFT) or Co-based low temperature FTS (Co-LTFT). Each of which produce syncrude of differing compositions.[13] These syntheses use either Co or Fe catalysts as they are the only variety that have both the required high activity and appropriate selectivity to be commercially viable for FTS. Ru has a higher activity than that of the Co and Fe based catalysts, however Ru has such a low abundance in nature that it is prohibitively expensive on the scale required for commercial use. Fe-based catalysts are best suited for coal to liquid (CTL) conversion, but also have potential for BTL due to the typically low H_2 to CO ratio of the syngas produced from coal and biomass.[14,15] The Fe catalysts exhibit activity in the water-gas shift (WGS) reaction (equation 1.1) which is used alongside FTS in the reactor to compensate for the less than ideal CO rich syngas.[16]

$$\mathrm{CO} + \mathrm{H_2O} \leftrightarrow \mathrm{CO_2} + \mathrm{H_2} \qquad (1.1)$$

Whereas, the Co-based catalysts are typically used in the synthesis of Gas to Liquid (GTL) wax from natural gas, the syngas produced from which is H_2 rich and does not require the WGS reaction to run in parallel. Despite the high financial cost of cobalt compared to iron, the Co-based catalysts are still industrially attractive as they are more resistant to deactivation than their iron counterparts due to lower susceptibility to attrition, resulting in higher stability under FTS conditions.[17,18]

Fuels from syncrude produced by FTS are often described as ultra-clean, due to the absence of sulphur, nitrogen or aromatic poisons. Therefore, they could substitute for gasoline or diesel fuel produced in refineries. Theoretically representing one possible way to replace dwindling oil resources, especially as a drop-in replacement for transport fuels. Also, FTS presents an alternative source

of petrochemicals regardless of future issues with oil supplies and a method for the retrieval of isolated gas reserves.

During FTS, syngas is passed over the metal which catalyses the formation of longer length hydrocarbon chains by polymerization[19] (a more detailed description of FTS mechanisms in the Co-based catalyst is given below). The chain growth probability (α) can be described using the Anderson-Schultz-Flory (ASF) distribution (equation 1.2).[19]

$$\frac{W_n}{n} = (1-\alpha)^2\alpha^{n-1} \qquad (1.2)$$

Where n is the number of carbon atoms in a chain, and W_n is the weight fraction corresponding to n. It is worth noting that the ASF distribution is based on an ideal polymerisation which FTS polymerisation deviates from.[19] However, this is only a broad discussion of factors effecting chain growth, therefore the ASF distribution is an appropriate approximation.

Figure 1.3 is a product distribution based on the ASF model in terms of α. In FTS, the chain growth probability is dependent on temperature, syngas composition, the partial pressure of H_2 and CO, the catalyst, and the promotor.[20] α increases with CO partial pressure, as this increases the available surface C resulting in a greater likelihood of chain growth. Whereas, α decreases with H_2 partial pressure, as more surface H increases the likelihood of chain termination.[20]

It has been observed that α decreases at higher temperatures – with FTS catalysts displaying a higher selectivity to CH_4.[20] This is thought to be due to an increase in hydrogenation at higher temperatures, reducing surface CH_2, therefore favouring the production of shorter chain length hydrocarbons.[20] Due to this behaviour, and as FTS is highly exothermic, FT reactors are built to remove excess heat from the system.

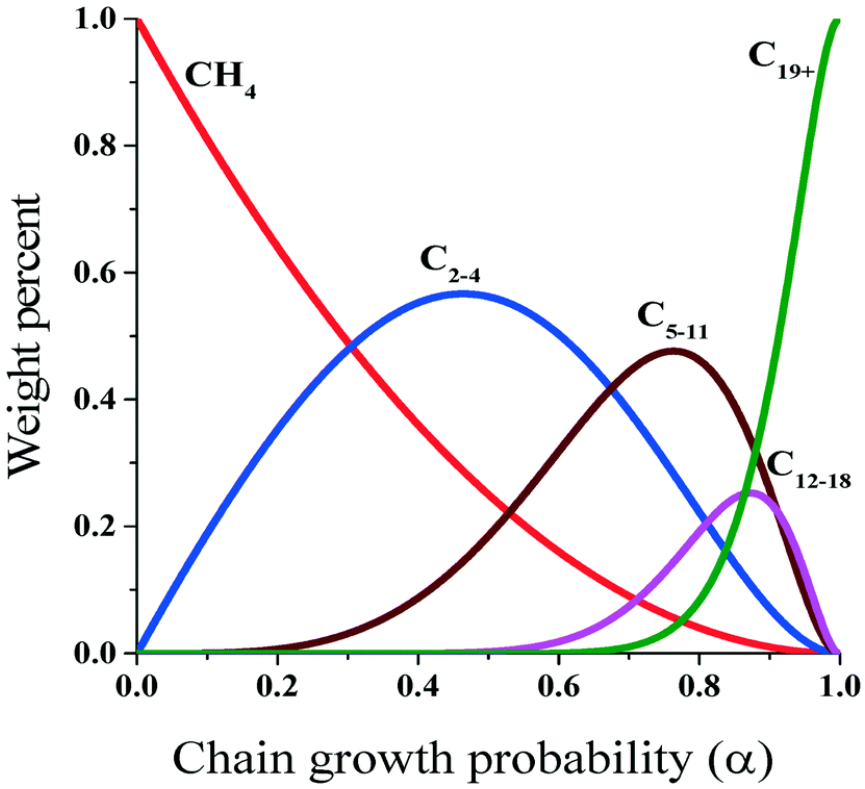

Figure 1.3: Product distribution according to the Anderson Schultz Flory (ASF) model. Figure taken from reference [21].

FTS is a surface polymerisation reaction which converts the simple reactants H_2 and CO into a wide range of linear and branched hydrocarbon and oxygenated products, from C_1 to C_{40}.[22] Equations 1.3 – 1.6 are general forms of reaction equations summarising the reactions which occur during FTS.

Alkanes: $$nCO + (2n+1)H_2 \rightarrow C_nH_{2n+2} + nH_2O \quad (1.3)$$

Alkenes: $$nCO + 2nH_2 \rightarrow (CH_2)_n + nH_2O \quad (1.4)$$

Alcohol: $$nCO + 2nH_2 \rightarrow H(CH_2)_nOH + (n-1)H_2O \quad (1.5)$$

Carbonyls: $$nCO + (2n-1)H_2 \rightarrow (CH_2)_nO + (n-1)H_2O \quad (1.6)$$

The polymerisation involves a stepwise incorporation of monomer units[22] and as such linear alkanes and α-alkenes (equations 1.3 and 1.4) are the most common products.[22] However, FTS also produces other products including alcohols (equation 1.5) and carbonyls (equation 1.6).[22] The precise composition

of the resultant syncrude depends on the reaction kinetics and therefore the FTS conditions used.

Currently, there is no consensus on the dominate FTS reaction mechanism.[23,24] This is due to both the complexity of the products formed and the significant challenge of differentiating between reaction pathways in real world experiments.[24] The FT reaction can be broken down into six general steps common to the reaction mechanisms discussed here:[22]

1) Reactant adsorption
2) Chain initiation (monomer formation)
3) Chain growth
4) Chain termination
5) Product desorption
6) Re-adsorption and further reactions

Three key FTS reaction mechanisms are discussed in the literature: the carbide mechanism, CO insertion, and the oxygenate (enol) mechanism.[25,26] Although, the carbide and CO insertion methods tend to be discussed more. Diagrams summarising generalisations of these three mechanisms are shown in Figure 1.4.

Fischer was the first to suggest a version of the carbide mechanism for Fe-based FTS in 1926.[27] In this variant syngas was thought to react with the metal forming bulk carbide that would then hydrogenate to form methylene groups, which in turn would polymerise to form hydrocarbon chains that eventually terminate.[28] However, this bulk carbide form was shown to be inconsistent with the thermodynamics of the system.[26] The conceptualisation of the carbide mechanism has changed over time, particularly after the introduction of surface science techniques. In current carbide mechanisms the carbide takes the form of surface species rather than bulk. A detailed description of the evolution of theorised FTS mechanisms over time is give in reference [26]. There is still some debate over the exact chemistry of these mechanisms, but discussion of more detailed differences is outside of the scope of this introduction. A general version of the modern version of the carbide mechanism is shown in Figure 1.4i.

Figure 1.4i shows the chain initiation and chain propagation stages of the carbide mechanism. CO is adsorbed onto the catalyst surface, where it dissociates. C then reacts with H_2 forming monomer units (M-CH_x), while the oxygen is removed from the surface through the formation of steam (H_2O). During chain propagation, two monomer units bond together with a H starting the hydrocarbon chain. Another monomer bonds with the units creating a longer chain, which continues until the chain terminates. The termination step produces alkanes by the insertion of a H or CH_3 unit to the chain, or alkenes by the removal of H. A diagram of various termination steps is shown in Figure 1.5.

The CO insertion mechanism differs from that of the carbide mechanism in that the monomer unit still contains a C-O bond which is broken and removed from the growing hydrocarbon chain after insertion.

In CO insertion there are two stages which both involve CO molecules. One during monomer formation and another during each chain propagation step, which is shown in the schematic in Figure 1.4ii. First there is dissociation of CO molecules which react with surface H, which then react with more H forming steam. Chain growth then occurs by the insertion of adsorbed CO into the hydrocarbon chain, after which the C-O bond is cleaved, and the O is removed from the molecule via the formation of steam.[24]

CO in the enol mechanism (Figure 1.4iii) is adsorbed without dissociation, unlike the other two mechanisms discussed here. Once adsorbed, CO reacts with surface H atoms to create M-CHOH. Chain growth occurs by the by condensation of the hydroxyl groups of adjacent M-CHOH species.[25]

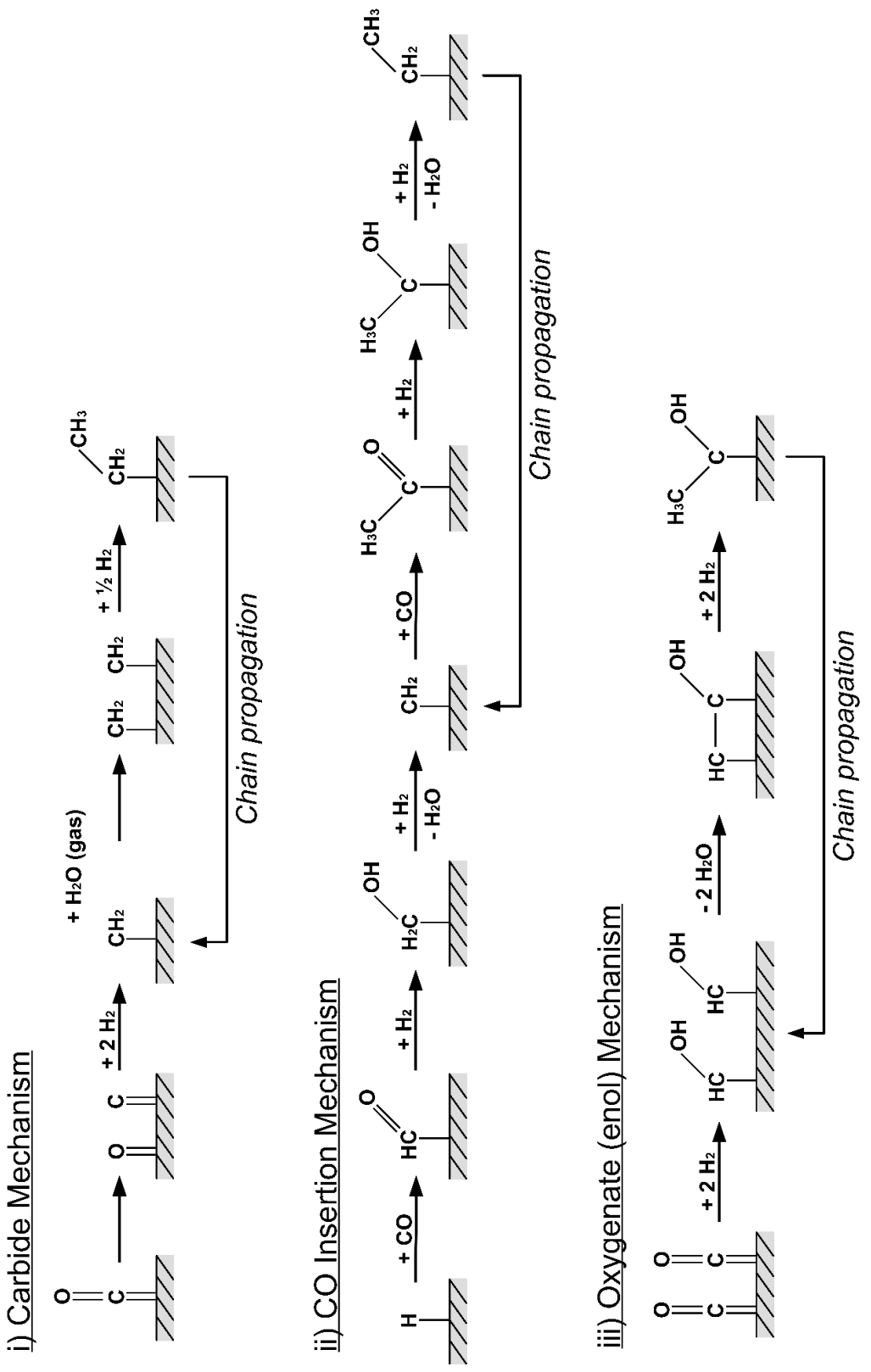

Figure 1.4: Common proposed reaction mechanism for FTS (showing initiation and chain growth stages only). [25,26]

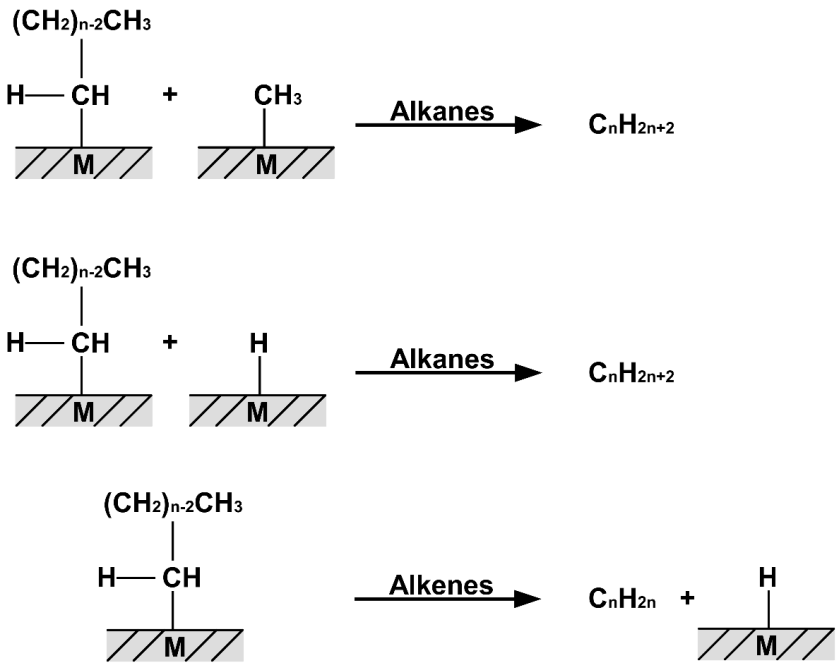

Figure 1.5: A schematic showing various potential termination steps.

FTS cobalt catalysts take the form of metallic cobalt nanoparticles typically dispersed on a metallic oxide support such as Al_2O_3, SiO_2 or TiO_2.[29] Metallic Co has long been identified as the active phase of the Co FTS catalysts due to its presence before, during and after reactions.[18] Co^0 in both the face centred cubic (fcc) and hexagonal close packed (hcp) crystal structures are observed in FTS catalysts. Diagrams of these structures are shown in Figure 1.6.

The reaction mechanisms are influenced by the topology of the metallic cobalt nanoparticles.[30] The influence on CO adsorption, a key initial step in FTS, has been well summarised in Shetty *et al.*[30] Overall, active sites on stepped surfaces are more active than those of flat surfaces for the Co-based catalysts.[30,31] Additionally, on flat surfaces the C-O bond cleavage of the HCO intermediate seen in the CO insertion mechanism (see Figure 1.4), has a lower energy barrier than that of direct CO dissociation seen in the carbide mechanism.[30,32]

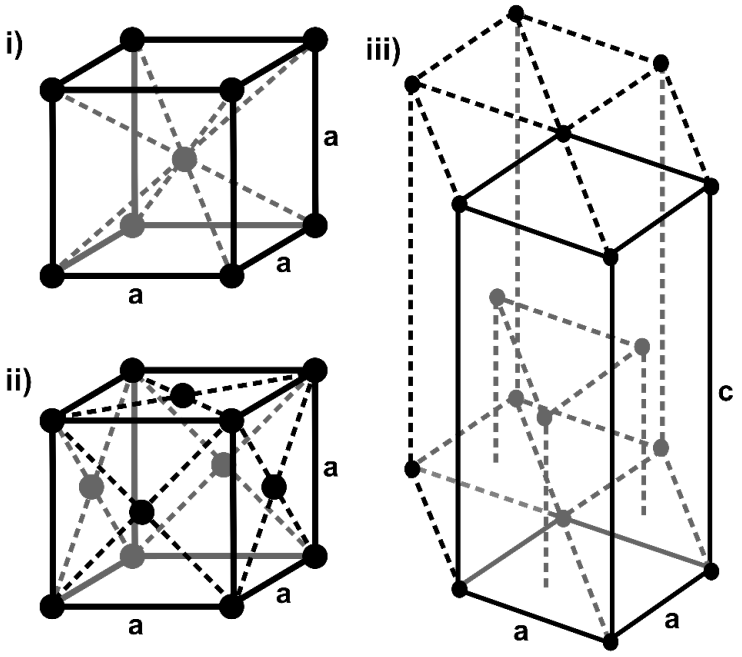

Figure 1.6: Diagrams of the crystal structures of: i) body centred cubic (bcc), ii) face centred cubic (fcc), and iii) hexagonal close packed (hcp).

While metallic cobalt is the active phase, it is cobalt oxide nanoparticles that are typically synthesised. These are then reduced in the reactor, as metallic Co is very air sensitive and difficult to transfer without accidental oxidation.[33] The reduction pathway is: $Co_3O_4 \rightarrow CoO \rightarrow Co^0$. It is possible, and common, for both oxides to remain in the system after (partial) reduction. Co_3O_4 has a normal spinel crystal structure.[34] Co^{2+} and Co^{3+} ions are present in the tetrahedral (T_d) and octahedral (O_h) interstices, respectively. Whereas, the crystal structure of CoO is the rocksalt structure (Figure 1.6), and all cobalt is in the 2+ oxidation state.

Under hydrogen deficient conditions the formation of cobalt carbide (Co_2C) is possible in Co-based FTS catalysts.[35,36] Co_2C has a hcp crystal structure (Figure 1.6iii) with C incorporated at interstitial sites.[36]

The structures discussed above may be present in FTS systems and so a good understanding of their respective crystal structures is vital to this work. Table 1.1 lists these common phases present in Co-based FTS catalysts, alongside relevant information on the crystallographic structure.

Table 1.1: Common crystallographic phases observed in cobalt-based FT catalysts.[34,37–40]

Cobalt Compound	Form	Crystallographic Structure							
		Space Groups	Lattice Parameters						Units per cell
			a(Å)	*b(Å)*	*c(Å)*	*α(°)*	*β(°)*	*γ(°)*	
Co^0	**hcp**	P63/mmc (194)	2.505	2.505	4.089	90	90	120	2
	fcc	Fm-3m (225)	3.544	3.544	3.544	90	90	90	4
CoO	**Rocksalt Structure**	Fm-3m (225)	4.263	4.263	4.263	90	90	90	4
Co_3O_4	**Normal Spinel**	Fd-3mS (227)	8.065	8.065	8.065	90	90	90	8
Co_2C	**Hexagonal structure**	Pmnn (58)	2.896	4.446	4.370	90	90	90	2
$CoAl_2O_4$	**Normal Spinel**	Fd-3mS (227)	8.095	8.095	8.095	90	90	90	8

The particle size of the Co^0 nanoparticles is a crucial factor in obtaining optimal activity. The highest activity is typically observed in particles of sizes 6-10 nm (synthesis and support dependant), although commercial catalysts tend to be larger in size (~16 nm).[41] The underlying cause of the particle size effect remains unclear, potentially caused by either size dependant reducibility issues or the size dependent formation of different crystal phases.

Both the fcc-Co and hcp-Co metallic phases are stable and active during FTS.[42] Fcc-Co and hcp-Co share the same coordination number and atom density in any given volume, yet they have different surface structures which in turn affects the catalytic reactivity and electronic properties, affecting the absorption and desorption of the reactants and products.[43] Computational studies have suggested that the hcp Co^0 structure may allow for the direct catalytic route, whereas fcc Co^0 only allows for the slower hydrogen assisted route.[44] This may account of the origin of the particle size effect, as Co^0 nanoparticles less than 10 nm tend to form in the less active fcc structure.[42] However this remains far from conclusive. The size effect is also commonly attributed to the lower reducibility of smaller cobalt nanoparticles.[45] It is therefore difficult to conclusively determine whether the most active polymorph is the hcp, fcc or a mixed hcp/fcc Co^0 phase.

The oxidation of cobalt as a deactivation mechanism has been frequently studied in the literature. It is thought that oxidation is a mechanism for deactivation by reducing the number of available metallic active sites.[46] Some studies have shown that under FTS conditions only small Co crystallites under ~4.5 nm are able to from oxides,[47,48] while other more recent studies have suggested this particle size may even be as large as 6.5 nm.[49] A more detailed discussion of the oxidation of Co-based FTS catalysts and the relationship with water in the system is included in the literature review (chapter 2).

Loss of activity through metal support interaction (MSI) is also a significant issue for the Co-based catalysts.[50] More generally, MSI refers to interactions between metal nanoparticles and support materials, which can be strong (SMSI) or weak (WMSI). SMSI is known to strongly influence the intrinsic actively and selectivity of catalyst nanoparticles,[51] either by enhancing or lessening these properties.

Both electronic and geometric factors contribute to MSI.[52] Electronic factors are due to the behaviour at reactive interfaces, where chemical bonds are broken and formed causing electron transfer,[51] which perturbs the electronic structure of the metal catalyst influencing its catalytic properties.[52] Geometric factors arise from a thin layer of reduced oxide support covering the metal nanoparticle (either partially which is described as decoration, or entirely which is described as encapsulation), which acts to block available active sites.[52]

In Co-based FTS, of the most commonly used metal oxide supports Al_2O_3 has the strongest MSI followed by TiO_2 and then SiO_2.[53] In the alumina supported Co-based catalyst the MSI takes the form of $CoAl_2O_4$ which is a spinel structure. Whereas, in the silica supported catalysts the MSI is $CoSi_2O_4$ in the olivine structure (the spinel is a high-pressure polymorph only).

Carbon-based supports show potential in minimising MSI, as they have been shown not to react strongly with the Co^0 particles.[54,55] However, such novel supports are far more expensive to produce than the commonly used metal oxide supports making them less attractive commercially. The most practical method of reducing MSI remains the addition of small quantities of noble metal promotors, which reduce at far lower temperatures than cobalt. The noble metal is thought

to more readily dissociate H at low temperatures which is readily reactive and reduces the cobalt oxide.[10]

At the temperatures required for FTS the surface of the metallic cobalt can undergo restructuring – reverting to a more thermodynamically favourable atomic arrangement.[46] This is due to the fact that for Co^0 particles in the size range 5-22 nm, the Hüttig temperature (the temperature at which surface atoms become significantly mobile) corresponds to that of the temperatures required for FTS (200-250 °C).[56] This also accounts for instability of smaller nanoparticles (>5 nm), as the smaller the nanoparticle, the closer the corresponding Tammann temperature (the temperature at which atoms/molecules in the bulk of a solid become mobile) moves to FTS conditions. Surface reconstruction is known to affect the initial activity of FTS catalysts and potentially contributes to deactivation in the longer term.[57] However, such surface variation is difficult to detect experimentally. Bulk techniques are not well suited to the detection of such subtle changes. While surface science techniques, which would lend themselves to the detection, are challenging to perform under realistic FTS conditions as the surface signal is often obscured by the heavy gas atmosphere above the catalyst surface. As such it is difficult at this time to evaluate the true effect of surface reconstruction on catalytic activity. Computational studies suggest that of all potential adsorbates only atomic carbon can cause surface restructuring meaning the carbon source can only be from CO dissociation onto the catalyst.[58]

Although cobalt FTS catalysts have been well researched there is still much about their nature and function that is not fully understood. Due to the high cost of cobalt, optimized dispersion of the nanoparticles is required to facilitate lower catalyst loadings.[18] In order to achieve this, methods of synthesis have been developed to tightly control the size of the metallic cobalt nanoparticles. For example, the addition of promotors or additional chemicals to the impregnating solution containing the precursor of $Co(NO_3)_2$ has been shown to enhance the catalyst performance either by improved control of the metal support interaction, or improved control of the size of metallic cobalt nanoparticles formed after activation.[17,59] Studies using a variety of both incipient wetness[60] and model catalyst systems or size controlled nanoparticles have generally indicated large nanoparticles above ~ 6 nm to be optimal.[12,60,61] This particle size dependence

has been attributed to a higher quantity of low-coordinated Co surface sites on particles of less than 6 nm as larger CH_x residence times and lower CH_x surface coverage have been observed by Steady-State Isotopic Transient Kinetic Analysis (SSITKA).[59]

Currently, the major impediment which prevents the widespread use of the cobalt-based FTS catalytic process is the financial cost involved compared to the price of alternatives such as petroleum products. It has been estimated that FTS will become viable once the price of oil consistently exceeds 60 USD per barrel. This prediction is based on the equivalent cost per barrel produced using FTS at a Coal to Liquid (CTL) demonstration project run by Shenhua (2011).[62] Oil prices tend to fluctuate significantly over time, however for comparison, in the last five months (as of March 2019) the barrel price of Brent Crude has dropped from 86.3 to 65.1 USD/barrel.[63] Much of the expense associated with FTS is due to the short lifetimes of the catalyst arising from relatively fast deactivation and less than optimal selectivity.[35] The deactivation of FTS catalysts is of foremost concern particularly in light of the expense of cobalt and the high metal loadings required (in the order of 20 wt%). Since deactivation is a key issue concerning these catalysts the understanding of the role of deactivation mechanisms is crucial in the effort to increase the commercial potential of FTS. Once these issues are better understood the design of catalysts and reactors can be improved accordingly. Key deactivation mechanisms observed in Co FTS catalysts include metal support interaction, sintering of the active Co^0, surface reconstruction and carbon deposition.[46]

Diverse X-ray scattering and spectroscopic methods have been employed to understand the stages involved in the creation and application of active cobalt-based FTS catalysts, the origins of activity, and possible mechanisms of deactivation. Due to the energy dependant interaction of electromagnetic radiation with common matter, X-rays can be used to investigate bulk/surface properties, the degree of crystallinity, element specific features, or all these properties combined in certain coupled systems. Notably, X-ray scattering techniques find their main utility in studies of the cobalt catalyst itself, which make such techniques highly complementary to a variety of both optical techniques

(Raman and infrared spectroscopy) and adsorption-desorption techniques (notably SSITKA[59]), used for the study of the reactive adsorbates.

Most X-ray techniques are best performed using synchrotron radiation (SR), due to the very high flux which allows for measurements with high time resolution that can be performed *in situ/operando*. *In situ* experiments are those in which measurements are taken of a sample undergoing some change (either during a reaction or pre-treatments), in real time to follow the evolution of the system. Whereas *operando* measurements are defined as measurements performed under reaction conditions while simultaneously measuring catalytic activity – typically using either mass spectrometry (MS), or gas chromatography (GC). The exact sense of "reaction conditions", and how close to industrial reaction conditions counts as *operando* is debatable as some compromise is necessary to acquire good quality, analysable data.

References

1 I. Chorkendorff; and J. W. Niemantsverdriet, Eds., *Wiley: Concepts of Modern Catalysis and Kinetics, 2nd, Revised and Enlarged Edition* -, Wiley, 2nd edn., 2006.
2 R. Catlow, M. Davidson, C. Hardacre and G. J. Hutchings, *Philos. Trans. R. Soc. A Math. Phys. Eng. Sci.*, 2016, **374**, 20150089.
3 M. V. Twigg, *Catalyst handbook*, Manson Pub, London, 2nd ed., 1997.
4 J. P. Greeley, *Science (80-.).*, 2012, **336**, 810–811.
5 Y. Sakata, Y. Tamaura, H. Imamura and M. Watanabe, *Stud. Surf. Sci. Catal.*, 2006, **162**, 331–338.
6 W. Huang and W.-X. Li, *Phys. Chem. Chem. Phys.*, 2019, **21**, 523–536.
7 F. Fischer and H. Tropsch, *Brennstoff-Chem, 1923*.
8 B. H. Davis and M. L. Occelli, *Fischer-Tropsch synthesis, catalysts and catalysis*, Elsevier, 2007.
9 F. Trippe, M. Fröhling, F. Schultmann, R. Stahl and E. Henrich, *Fuel Process. Technol.*, 2011, **92**, 2169–2184.
10 F. Diehl and A. Y. Khodakov, *Oil Gas Sci. Technol. - Rev. l'IFP*, 2008, **64**, 11–24.
11 A. de Klerk, *Fischer-Tropsch Refining*, John Wiley & Sons, 2012.
12 G. Prieto, A. Martínez, P. Concepción and R. Moreno-Tost, *J. Catal.*, 2009, **266**, 129–144.
13 A. de Klerk, *Energy & Fuels*, 2009, **23**, 4593–4604.
14 E. de Smit and B. M. Weckhuysen, *Chem. Soc. Rev.*, 2008, **37**, 2758–81.
15 E. de Smit, A. M. Beale, S. Nikitenko and B. M. Weckhuysen, *J. Catal.*, 2009, **262**, 244–256.
16 M. E. Dry, *Catal. Today*, 2002, **71**, 227–241.
17 A. Martinez and G. Prieto, *J. Catal.*, 2007, **245**, 470–476.
18 A. Y. Khodakov, W. Chu and P. Fongarland, *Chem. Rev.*, 2007, **107**, 1692–744.
19 I. Puskas and R. S. Hurlbut, in *Catalysis Today*, Elsevier, 2003, vol. 84, pp. 99–109.

20 M. E. Dry, *Appl. Catal. A Gen.*, 1996, **138**, 319–344.
21 H. Yang, C. Zhang, P. Gao, H. Wang, X. Li, L. Zhong, W. Wei and Y. Sun, *Catal. Sci. Technol.*, 2017, **7**, 4580–4598.
22 G. P. Van Der Laan and A. A. C. M. Beenackers, *Catal. Rev. - Sci. Eng.*, 1999, **41**, 255–318.
23 E. Rytter, N. E. Tsakoumis and A. Holmen, *Catal. Today*, 2016, **261**, 3–16.
24 R. A. Van Santen, A. J. Markvoort, I. A. W. Filot, M. M. Ghouri and E. J. M. Hensen, *Phys. Chem. Chem. Phys.*, 2013, **15**, 17038–17063.
25 W. Shafer, M. Gnanamani, U. Graham, J. Yang, C. Masuku, G. Jacobs and B. Davis, *Catalysts*, 2019, **9**, 259.
26 B. H. Davis, *Catal. Today*, 2009, **141**, 25–33.
27 H. Fischer, F., Tropsch, *Int. Conf. Bitum. Coal*, 1926, **7**, 97–104.
28 J. A. Schaidle and L. T. Thompson, *J. Catal.*, 2015, **329**, 325–334.
29 E. Iglesia, *J. Catal.*, 1992, **137**, 212–224.
30 S. Shetty and R. A. Van Santen, in *Catalysis Today*, Elsevier, 2011, vol. 171, pp. 168–173.
31 Q. Ge and M. Neurock, *J. Phys. Chem. B*, 2006, **110**, 15368–15380.
32 R. L. Toomes and D. A. King, *Surf. Sci.*, 1996, **349**, 1–18.
33 J. J. Herbert, P. Senecal, D. J. Martin, W. Bras, S. K. Beaumont and A. M. Beale, *Catal. Sci. Technol.*, 2016, **6**, 5773–5791.
34 W. L. Roth, *J. Phys. Chem. Solids*, 1964, **25**, 1–10.
35 N. E. Tsakoumis, M. Rønning, Ø. Borg, E. Rytter and A. Holmen, *Catal. Today*, 2010, **154**, 162–182.
36 J. C. Mohandas, M. K. Gnanamani, G. Jacobs, W. Ma, Y. Ji, S. Khalid and B. H. Davis, *ACS Catal.*, 2011, **1**, 1581–1588.
37 E. A. Owen and D. M. Jones, *Proc. Phys. Soc. Sect. B*, 1954, **67**, 456–466.
38 S. Sasaki, K. Fujino and Y. Takéuchi, *Proc. Japan Acad. Ser. B Phys. Biol. Sci.*, 1979, **55**, 43–48.
39 J. Clarke and K. H. Jack, *Chem. Ind.*, 1951, **46**, 1004–1005.
40 K. Toriumi, M. Ozima, M. Akaogi and Y. Saito, *Acta Crystallogr. Sect. B Struct. Crystallogr. Cryst. Chem.*, 1978, **34**, 1093–1096.
41 T. M. Eggenhuisen, J. P. Den Breejen, D. Verdoes, P. E. De Jongh and K. P. De Jong, *J. Am. Chem. Soc.*, 2010, **132**, 18318–18325.
42 Y. Qi, J. Yang, D. Chen and A. Holmen, *Catal. Letters*, 2014, **145**, 145–161.
43 S. Liu, Y. Li and W. Shen, *Chinese J. Catal.*, 2015, **36**, 1409–1418.
44 J.-X. Liu, H.-Y. Su, D.-P. Sun, B.-Y. Zhang and W.-X. Li, *J. Am. Chem. Soc.*, 2013, **135**, 16284–7.
45 A. Y. Khodakov, A. Griboval-Constant, R. Bechara and V. L. Zholobenko, *J. Catal.*, 2002, **206**, 230–241.
46 A. M. Saib, D. J. Moodley, I. M. Ciobîcă, M. M. Hauman, B. H. Sigwebela, C. J. Weststrate, J. W. Niemantsverdriet and J. van de Loosdrecht, *Catal. Today*, 2010, **154**, 271–282.
47 E. van Steen, M. Claeys, M. E. Dry, J. van de Loosdrecht, E. L. Viljoen and J. L. Visagie, *J. Phys. Chem. B*, 2005, **109**, 3575–7.
48 P. J. van Berge, J. van de Loosdrecht, S. Barradas and A. M. van der Kraan, *Catal. Today*, 2000, **58**, 321–334.
49 P. Senecal, S. D. M. Jacques, M. Di Michiel, S. A. J. Kimber, A. Vamvakeros, Y. Odarchenko, I. Lezcano-Gonzalez, J. Paterson, E. Ferguson and A. M. Beale, *ACS Catal.*, 2017, **7**, 2284–2293.
50 H. Karaca, O. V. Safonova, S. Chambrey, P. Fongarland, P. Roussel, A. Griboval-Constant, M. Lacroix and A. Y. Khodakov, *J. Catal.*, 2011, **277**, 14–26.
51 C.-J. Pan, M.-C. Tsai, W.-N. Su, J. Rick, N. G. Akalework, A. K. Agegnehu, S.-Y. Cheng and B.-J. Hwang, *J. Taiwan Inst. Chem. Eng.*, 2017, **74**, 154–186.
52 Q. Fu and T. Wagner, *Surf. Sci. Rep.*, 2007, **62**, 431–498.
53 G. Jacobs, T. K. Das, Y. Zhang, J. Li, G. Racoillet and B. H. Davis, *Appl. Catal. A*

Gen., 2002, **233**, 263–281.
54 G. L. Bezemer, J. H. Bitter, H. Kuipers, H. Oosterbeek, J. E. Holewijn, X. Xu, F. Kapteijn, A. J. van Dillen, K. P. de Jong, A. J. Van Diilen and K. P. de Jong, *J. Am. Chem. Soc.*, 2006, **128**, 3956–3964.
55 A. Tavasoli, R. M. M. Abbaslou, M. Trepanier and A. K. Dalai, *Appl. Catal. A Gen.*, 2008, **345**, 134–142.
56 M. Wolf, H. Kotzé, N. Fischer and M. Claeys, *Faraday Discuss.*, 2017, **197**, 243–268.
57 K. Høydalsvik, J. B. Fløystad, A. Voronov, G. J. B. Voss, M. Esmaeili, J. Kehres, H. Granlund, U. Vainio, J. W. Andreasen, M. Rønning and D. W. Breiby, *J. Phys. Chem. C*, 2014, **118**, 2399–2407.
58 I. M. Ciobîcă, R. A. van Santen, P. J. van Berge and J. van de Loosdrecht, *Surf. Sci.*, 2008, **602**, 17–27.
59 J. P. den Breejen, P. B. Radstake, G. L. Bezemer, J. H. Bitter, V. Frøseth, A. Holmen and K. P. de Jong, *J. Am. Chem. Soc.*, 2009, **131**, 7197–203.
60 R. Reuel, *J. Catal.*, 1984, **85**, 63–77.
61 Z. Wang, S. Skiles, F. Yang, Z. Yan and D. W. Goodman, *Catal. Today*, 2012, **181**, 75–81.
62 China Shenhua coal-to-liquids project profitable -exec | Reuters, http://www.reuters.com/article/2011/09/08/shenhua-oil-coal-idUSL3E7K732020110908, (accessed 13 June 2015).
63 Oil Price: Latest Price & Chart for Crude Oil - NASDAQ.com, http://www.nasdaq.com/markets/crude-oil.aspx?timeframe=6m, (accessed 13 June 2015).

2. Literature Review

This literature review includes four sections relating specifically to Co-based FTS catalysts: 1) reoxidation under FTS conditions, 2) characterisation by X-ray scattering techniques, 3) characterisation by X-ray absorption techniques, and 4) catalyst synthesis.

A version of the X-ray scattering and absorption sections have been published in the following: J. J. Herbert *et al.* Catalysis Science & Technology 6 (15), 5773-5791, 2016.[1]

2.1 Reoxidation of Co-based FTS catalysts

Reoxidation is one potential deactivation mechanism of Co-based FTS catalysts.[2] Other mechanisms include: the formation of coke deposits on the catalyst surface (or other carbon species), sintering, formation of metal support species, and sulphur/nitrogen poisoning.[2] There has been significant debate in the literature over the true impact of reoxidation on Co-based FTS catalysts. Some studies observe it, while others do not. Detailed discussions of these conflicting studies can be found in the referenced reviews.[3–6] The discrepancies may be due to a few factors.

First, characterisation. Many experiments use characterisation techniques which do not directly observe oxidation states, or bulk characterisation that would be insensitive to surface oxidation. Such studies may miss the subtle changes associated with surface oxidation or oxidation of only the smaller nanoparticles. Secondly, it is challenging to unambiguously differentiate between three deactivation mechanisms: reoxidation, sintering, and variations in the quantity of the metal support oxide phases.[1]

Some rule out variation in metal support phases as a deactivation mechanism as, in the case of Co/Al_2O_3 catalysts the oxidation of Co^0 to the $CoAl_2O_4$ spinel has been calculated to require a far higher temperature than that used for FTS.[3,7] Also, for Co/SiO_2 catalysts, while the formation of metal support species is thermodynamically favourable it has been theorised to be kinetically

inhibited.[8] However, metal support phases have been observed to form during FTS experiments[8–12] and is not so easy to discount.

Additionally, there is some variance in the reaction conditions used from study to study, so direct comparison can be difficult. This may influence reoxidation as the presence of H_2O (and therefore the conversion rate), is known to strongly influence reoxidation.[4] Also, different catalyst syntheses will result in catalysts with different physical properties which may influence the degree of reoxidation. For example, the oxide support used is known to influence the reoxidation behaviour.

Is reoxidation possible under realistic FTS conditions? Bulk oxidisation of metallic cobalt has been shown to be thermodynamically unfavourable under realistic conditions.[13,14] However, it is possible for smaller Co^0 nanoparticles under some FTS conditions to reoxidize.[15]

Van Steen *et al.* performed a thermodynamic analysis of a simplified cobalt catalyst. Figure 2.1i is a stability diagram for bulk Co^0, CoO and Co_3O_4, as a function of the ratio of the partial pressure of H_2O to H_2 (P_{H_2O}/P_{H_2}), and temperature. The grey region corresponds to industrially relevant FTS conditions and sits comfortably within the hcp Co^0 region. For bulk Co^0 to oxidise to form CoO a partial pressure ratio of more than 128 would be required, far exceeding those expected during FTS. For comparison, van Berge *et al.* estimated the partial pressure ratio to fall between 0.5 and 1.2 for a gradientless slurry phase reactor running between 170-240 °C and at 20 bar pressure.[13] In this study van Steen *et al.* use the estimate of $P_{H_2O}/P_{H_2}<1.5$ for FTS conditions.[16]

The ratio of the H_2O to H_2 partial pressures strongly influences the stability range, but so does nanoparticle size. As nanoparticle size decreases, the surface energy has a greater influence on the stability of the nanoparticles.[3] In their thermodynamic analysis van Steen *et al.* investigated this relation and estimated surface energies for spherical fcc Co^0 and CoO nanoparticles of various diameters. Figure 2.1ii is the stability diagram for fcc Co^0 and CoO in terms of P_{H_2O}/P_{H_2} and crystallite diameter at 493 K. This includes a 15 % window of tolerance indicated by the dashed line. As the nanoparticle size decreases the

H_2O to H_2 partial pressure ratio needed to oxidise also decreases resulting in less stable nanoparticles.

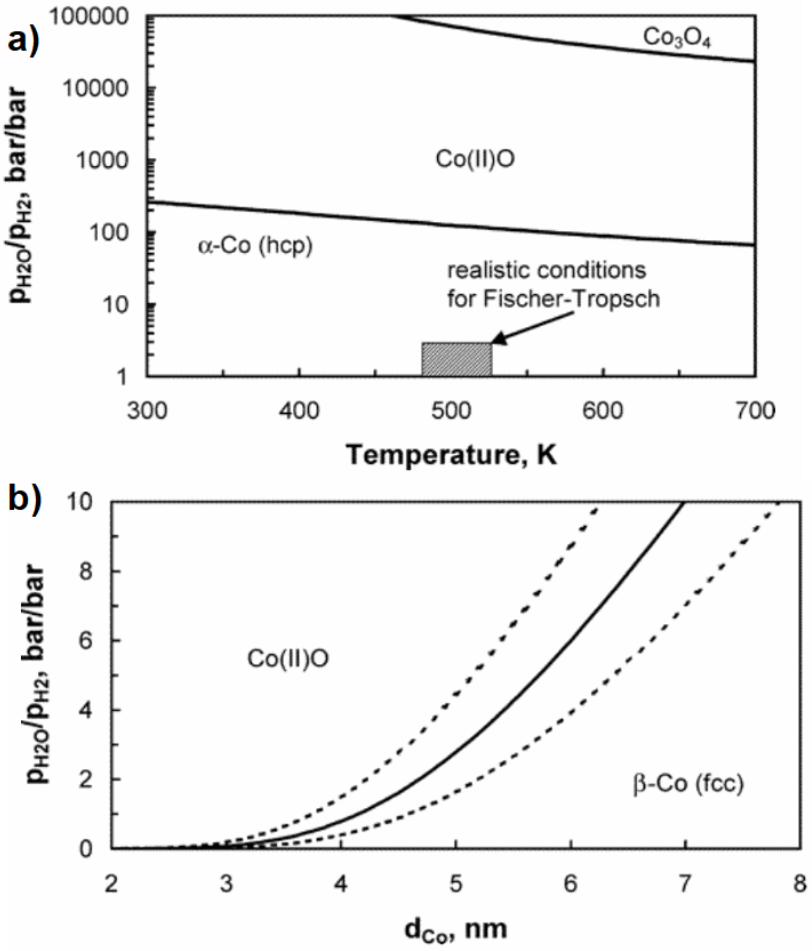

Figure 2.1: Stability diagrams i) of bulk Co^0, CoO and Co_3O_4, with the grey section representing FTS conditions with respect to PH2O/PH2 and temperature, and ii) of CoO and fcc Co0 with respect to PH_2O/PH_2 and nanoparticle diameter. Taken from reference [16].

It is also worth commenting on, as the authors do, that the calculations used in van Steen *et al.* assumed a simplified model of the cobalt catalyst. It was assumed that the nanoparticles were spherical, unsupported, unpromoted, and entirely in the fcc form. For some of the larger nanoparticle diameters in this range it would be likely that hcp Co^0 or stacking faults would also be present to some degree.[17] However, a more realistic model in terms of Co^0 polymorphs would drastically complicate such calculations. Additionally, the presence of an oxide support and a promotor would stabilise the system preventing attrition resistance[18] and therefore would shift the boundary between CoO and fcc Co^0 seen in Figure 2.1ii. However, while a realistic system would differ somewhat from

the absolute values, the general behaviour of the simplified system is applicable to a realistic system.

Co^0 reoxidation is also temperature dependent. Sintering of nanoparticles is often discussed in terms of the temperature dependent mobility of surface atoms.[19,20] Wolf *et al.* also describe reoxidation in this manner.[11] The relative thermal stability of a material can be described by two temperatures: the Hüttig and Tammann temperatures.

The Hüttig temperature is the temperature at which surface atoms start to become mobile.[20] These are typically atoms that are less strongly bound to the surface at defect sites.[19] Whereas, the Tammann temperature is the temperature at which bulk atoms become mobile.[19] The Hüttig and Tammann temperatures are proportional to the absolute melting point (T_m) by $0.3T_m$ and $0.5T_m$ respectively.[19] For bulk cobalt the Hüttig temperature is 526 °C and the Tammann temperature is 877 °C.[11] Some studies have ruled out thermal sintering in Co-based FTS catalysts as these temperatures are higher than those used during FTS. However, the Hüttig and Tammann temperatures are proportional to the absolute melting point, which is itself particle size dependant.[21] Therefore the Hüttig and Tammann temperatures must also be particle size dependent.

Wolf *et al.* used the Gibbs-Thomson equation to calculate the size dependence of the melting point for Co^0 nanoparticles under 100 nm, and the corresponding Hüttig and Tammann temperatures, shown in Figure 2.2.[11]

In their calculations Wolf *et al.* identified that Co^0 nanoparticles below 8.5 nm had a Tammann temperature below 220 °C, a realistic temperature for FTS. Therefore, nanoparticles of 8.5 nm would have mobile bulk and surface atoms, allowing for potential reoxidation and sintering.

But what causes reoxidation? Water is a significant product of FTS, is a strongly oxidising agent, and there is a strong relationship between the presence of water and an increase in reoxidation of Co^0 nanoparticles during FTS.[3–6] However, questions remain over the exact mechanism of reoxidation and under what conditions each mechanism occurs.

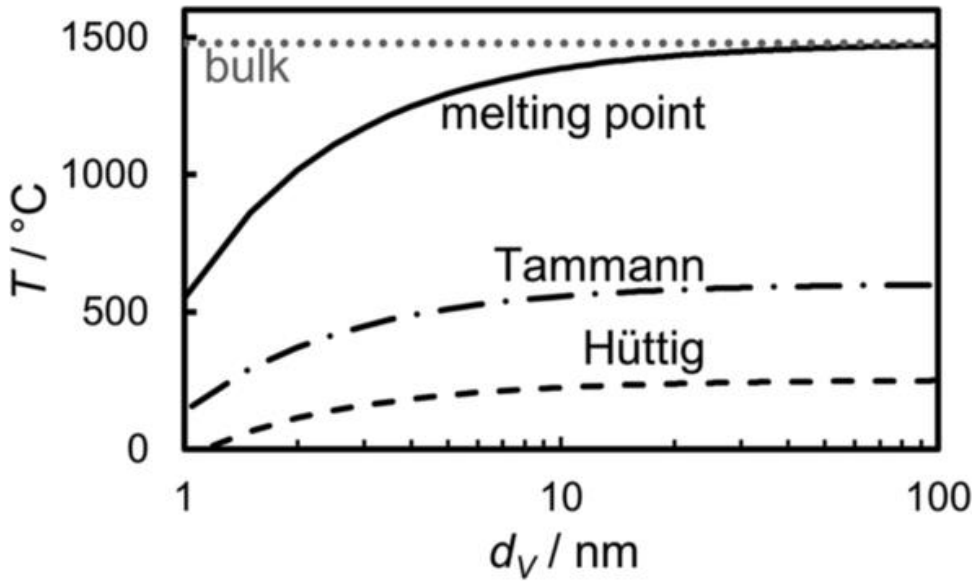

Figure 2.2: Graph of the variation in melting point, Tammann, and Hüttig temperatures with respect to temperature and crystallite size for metallic cobalt. [Taken from reference [11]].

There are two possible routes for reoxidation, the first is through direct water induced oxidation. The second is via an indirect CO oxygen-derived route.[22] Surface Co atoms have an oxidation/reduction cycle as O is adsorbed onto the catalyst surface then removed as steam – regenerating the active site.[10] If the P_{H_2O}/P_{H_2} ratio rises above a certain point the presence of a large amount of H_2O will hinder the removal of O from the catalyst surface resulting in some degree of surface oxidation proportional to the P_{H_2O}/P_{H_2} ratio.[10,22]

The influence of water on the catalyst is complex. Not only does water in the gas feed influence oxidation, it also influences both catalyst selectivity and activity.[6] The influence on selectivity is particularly marked. Water has been shown to universally enhance C_{5+} selectivity.[4,23] It has been suggested that H_2O interacts with the adsorbed CO species lowering the energy required for CO activation.[4]

The influence of water on activity is dependent on both support type and support pore diameter.[4] It is mostly negative on alumina, but mostly positive on silica and can range in effect on titania from little to no impact.[4] In alumina supported catalysts the difference between medium and large pore diameter has a strong effect.[4] Activity reduces in catalysts with smaller diameter pores, theorised to be a consequence of condensation in smaller pores.[4,6]

Claeys and co-workers developed an *in situ* magnetometer[24] to study catalysts with magnetic properties, which they have used to study Co-based FTS catalysts on a number of occasions.[9–11,22,25–30]

The magnetometer measures the magnetisation (M_{sat}) of the material held in a stainless steel fixed bed reactor when placed in an external magnetic field of 2 T, which is directly proportional to the amount of metallic cobalt present in the system and can be used to observe changes in the degree of reduction of the catalyst.[27]

Metallic cobalt is ferromagnetic above a certain domain size. Ferromagnetic materials – below the Curie temperature for that material – are magnetised when placed in a magnetic field and, once removed, have a remnant magnetisation.[11] Whereas, cobalt oxides are antiferromagnetic and possess the same behaviour, but when below the Néel temperature.[11] Under FTS conditions only the cobalt metal shows significant magnetisation susceptibility.[11] This is complicated by the superparamagnetic behaviour of metallic cobalt for domain sizes below approximately 15-20 nm at room temperature.[11,27] When the metal loading of the catalyst is known, the degree of reduction can be calculated after calibration of the magnetometer using defined amounts of metallic cobalt.[27] Therefore, an increase in the mass fraction of ferromagnetic material semi-quantitatively describes either in increase in the average cobalt crystallite size or a decrease in the overall fraction of smaller cobalt crystallites in the metallic phase.[27]

The two most pertinent studies using the *in situ* magnetometer to reoxidation are Wolf *et al.* (2017)[11] and *Wolf et al.* (2018)[22]. Both study the reoxidation of Co-based FTS catalysts and the influence of CO. This was achieved by exposing the reduced catalysts to a stepwise increase in P_{H_2O}/P_{H_2} in the absence and then presence of CO. First in a gas mixture of $H_2O/H_2/Ar$, then in $CO/H_2O/H_2/Ar$. For P_{H_2O}/P_{H_2} ratios of 0.15, 1.5, 5, 10, 20, 30, 40, ∞, and 0. The syngas ratio for runs which include CO was approximately $H_2/CO = 2.1$.

Wolf *et al.* (2017) examined Co/SiO_2 catalysts of three nanoparticle sizes (2.8, 5.5, and 7.1 nm as determined by Rietveld refinement), with a cobalt loading of 0.5 wt%.[11] However, on the Co/SiO_2 catalyst there was evidence that metal

support phases were formed during exposure to the CO gas mixture. *Wolf et al.* (2018) follows on from these experiments, the same *in situ* magnetometer was used and so was the same gas procedure but using a Co/C model catalyst of 5 wt% cobalt of one particle size (6.2 nm as determined by Rietveld).[22] The cobalt catalyst supported on inert carbon does not form metal support species.[22,31] Both catalysts are supported on spheres, presumably to avoid the complexity of support pore diameter on the influence of water.

Initial changes in magnetization were observed at P_{H_2O}/P_{H_2} of 0.15 and 1.5 and attributed to the adsorption of surface species for all experiments and all catalysts.

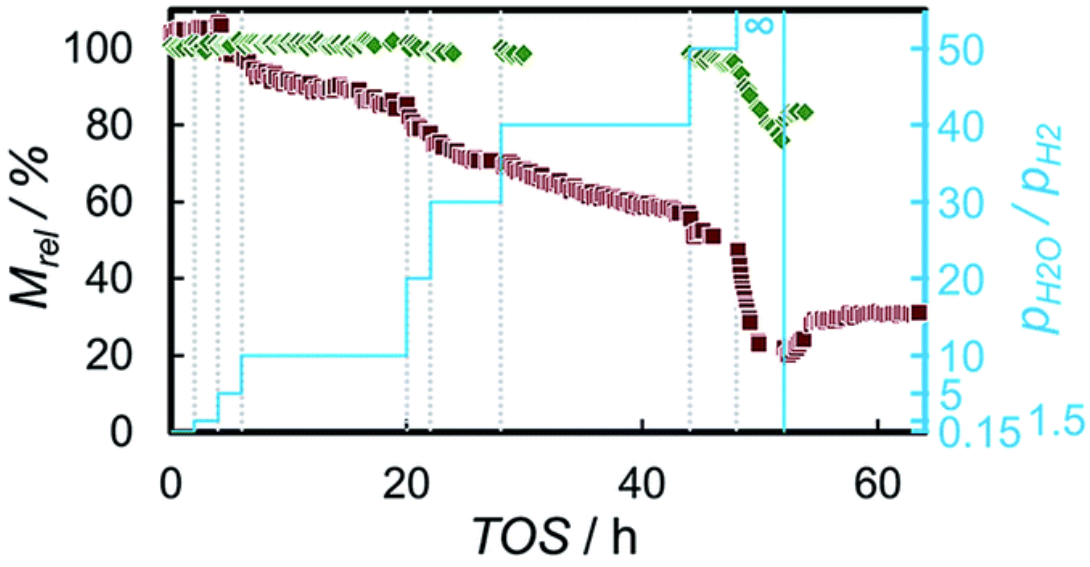

Figure 2.3: Graph of the magnetization at maximal field strength relative to the magnetization after reduction for CAT A (2.8 nm) (red squares) and CAT C (7.1 nm) (green diamonds) with respect to time on stream (TOS). Also showing relative partial pressures (PH_2O/PH_2) in light blue and on right axis.[11]

Some reoxidation (as indicated by a reduction in magnetisation) was observed in the experiments in the absence of CO. However, this was minimal compared to the total reoxidation observed when exposed to only H_2O.[22] Even a small quantity of H_2 in the gas mixture significantly hinders reoxidation by H_2O.[22] In the runs with CO a more rapid oxidation was observed to a greater degree in both studies. This suggests that while some reoxidation occurs via direct oxidation by H_2O at low P_{H_2O}/P_{H_2}, meaningful reoxidation occurs via indirect CO oxygen-derived oxidation at high P_{H_2O}/P_{H_2}, corresponding to high conversion rates.

The degree of oxidation and P_{H_2O}/P_{H_2} ratio at which oxidation started was also shown to be size dependent. At P_{H_2O}/P_{H_2}=50, 50 wt% of the smallest sized Co/SiO_2 catalyst (2.8 nm) had oxidised, whereas only 4 wt% of the largest (7.1 nm).[11] The 2.8 nm in size catalyst started to display a reduction in magnetisation consistent with surface reoxidation at P_{H_2O}/P_{H_2}=5, whereas this occurred at P_{H_2O}/P_{H_2}=50 for the larger nanoparticle size catalyst – see Figure 2.3.[11]

So far, the catalysts have only been discussed in the form of a powder. However, if such powder was used in a rising bed reactor or fluidized bed reactor the catalyst would be blown out, and in a large fixed bed reactor there would be a very significant pressure drop over the length of the reactor.[32] Therefore catalysts are typically shaped into larger bodies such as pellets, rings, or multichannel pellets. Which raises the question, does Co^0 nanoparticle reoxidation occur in pellets and, if so, is it homogenous throughout the structure?

In Senecal *et al.* a pellet (3 mm in diameter) of $Co/\gamma\text{-}Al_2O_3$ of 10 wt% cobalt, synthesised by pore volume impregnation was studied during reduction and FTS.[33] XRD-CT and PDF-CT (micro X-ray diffraction and pair distribution function computed tomography – see sections below), were used to characterise the catalyst pellet and recorded at ID15A at the ESRF. Both techniques provide image slices across the pellet diameter where each pixel (out of 66 x 66 pixels per processed image) has a corresponding XRD/PDF pattern. From this the cobalt species distribution can be determined as well as the average crystallite size of each phase. The FTS experiments were performed at atmospheric pressure, 250 °C, using a syngas ratio (H_2/CO) of 2:1 and with a gas hourly space velocity (GHSV) of 23000 h^{-1}.[33]

Both XRD-CT and PDF-CT showed a gradient of nanoparticles size over the diameter of the pellet, for both CoO and fcc Co^0 nanoparticles, where smaller nanoparticles tended to be found at the periphery of the pellet. The XRD-CT showed smaller nanoparticles (of 7 - 9.5 nm) present in the outer 1 mm of the pellet, and larger nanoparticles (of 10 - 12 nm) in the central 2 mm. This distribution was attributed to the process of impregnation and drying.[33]

Senecal *et al.* also observed a significant oxidation of the fcc Co^0 present in the periphery of the pellet (~ 90%), which they attributed to the greater

presence of water in that region due to diffusion effects of CO through the pellet.[33] The reoxidation may also be affected by the particles size gradient through the pellet. Smaller Co^0 nanoparticles are more prone to oxidation under FTS conditions and so, as those size nanoparticles are more present in the periphery, the nanoparticles in that region reoxidize more easily.

While this study is interesting, there are some limitations. As is the case in most imaging studies which observe individual or small numbers of pellets/catalyst particles, the statistical reliability is open to question. FTS was also performed at atmospheric pressures lower than those used in realistic reactors. Presumably, this was done to prevent the build-up of hydrocarbon wax which can block the small reactors used in synchrotron experiments ruining hours of work and expensive beamtime.

While reoxidation is both theoretically possible and observed experimentally, its relevance as a deactivation mechanism for realistic systems is still in question. Small particles are the most prone to reoxidation (approx. <7.5 nm)[11,33] which is smaller than the average nanoparticle size for the industrial catalyst,[34] and the P_{H_2O}/P_{H_2} ratio needed for significant indirect reoxidation corresponds to conversion rates higher than those reported in industrial FTS reactors.[4] For more detailed discussions of laboratory and commercial reactors and their corresponding CO conversion rates and other properties, see references [4,23,35].

However, it may not be so clear cut that these conditions (and therefore reoxidation) are not possible in a realistic reactor. As the water gas shift (WGS) activity is low in cobalt catalysed FTS the quantity of water will increase with time on stream.[6] Also, as shown in Senecal *et al.* the reoxidation behaviour of nanoparticles varies with position in the catalyst pellet.[33]

Even if CO oxygen-derived reoxidation was conclusively ruled out in the industrial system, an understanding of the mechanisms of reoxidation would still be worthwhile. Reoxidation has been observed in many experimental studies and a full understanding of the mechanisms would help to contextualise the relevance of reoxidation, the relation between reoxidation and other deactivation mechanisms, and improve the design of experiments.

2.2. X-Ray scattering techniques as applied to Co-based Fischer-Tropsch catalysts

Scattering methods provide vital insight into the structure of Co-based Fischer-Tropsch Synthesis (FTS) catalysts and the structural changes that occur over the course of catalyst formation and FTS. A variety of X-ray scattering techniques are available which can probe a wide range of length scales. This ranges from the long range (XRD for crystalline phase information), intermediate range (SAXS for morphology change), and short range (PDF for determining the presence of diffraction silent material such as amorphous Co or carbon deposition).

2.2.1. Powder X-Ray Diffraction (PXRD)

Powder X-Ray diffraction (PXRD) examines X-rays scattered from the ordered material present in a powder sample at angles characteristic of the crystal lattices present caused by constructive X-ray interference between the atomic planes. A more detailed description of the theory is given in chapter 3 section 3.1.3 X-Ray Diffraction.[36] The XRD data can be analysed to obtain information on the phases present and crystallite sizes (most commonly by Rietveld refinement).[37] PXRD is particularly relevant for the characterisation of FT catalysts due to the relatively large metal loadings leading to sufficient ordering of nanoparticles to render them readily identifiable (particularly in terms of phase composition and 'critical' particle size).

Operando and *in situ* measurements are frequently performed using synchrotron radiation (SR) due to the high spatial and time resolution available. Other advantages of using synchrotron-based PXRD include measurements that can be obtained in combination with other techniques (such as XAS) or used for multi-dimensional imaging. The majority of laboratory-based XRD measurements are typically performed *ex situ*, however *operando* measurements are achievable using such set-ups and can allow for the study of catalysts with considerably more time on stream, albeit at the expense of time and spatial resolution.[38] *Ex situ* measurements are straightforward to acquire as time on lab sources is more abundant than beamtime at synchrotrons. They do provide useful information

albeit with some limitations. Simple *ex situ* lab-based PXRD is widely used to compare the evolution of crystallite size and the cobalt phases (Co_3O_4, CoO, and both hcp/fcc Co^0) with variations in factors thought to affect FT catalysts. For example, hydrocarbon selectivity of cobalt on various supports (γ-Al_2O_3, θ-Al_2O_3, δ-Al_2O_3 and α-Al_2O_3),[39] the syngas ratio (H_2:CO; 1:1, 2:1, and 3:1),[40] and various deactivation mechanisms such as; sulphur poisoning, catalyst sintering and silicate and/or carbide formation.[41]

However, it is important to note that Co fluorescence and the more intense background it causes is often a major issue in lab-based XRD. Many lab-based diffractometers use Cu targets often without a secondary monochromator, triggering Co fluorescence which can obscure impurity phases in the measured data and makes detailed sample analysis difficult on data from such sources.

In contrast, SR-based PXRD facilities typically possess a combination of high photon source brightness, energy tunabilitiy and are equipped with superior detectors. This enables the collection of high quality data with superior temporal and, in some cases, high spatial resolution under both *in situ* and *operando* conditions.[42,43] Such *in situ* methods can also be combined with spectroscopic techniques such as XAS and in some instances with optical methods such as UV-Vis spectroscopy or Raman scattering.[44]

SR-PXRD measurements can be acquired with a time resolution ranging from milliseconds to minutes, thereby allowing for the acquisition of a series of PXRD patterns as time progresses throughout activation or a FTS reaction, or even tomographical measurements.[45,46] This allows for the tracking of crystalline phase changes with time, and importantly, variation in crystallite size – yielding valuable information on the system and its evolution with time under a controlled atmosphere. Characterization of Co FTS catalysts using *in situ* PXRD (and *in situ* XAS or combined studies) is best performed using glass or quartz capillaries, which can be considered as plug-flow micro-reactors. In contrast, pelletised wafers produce higher quality data and are easier to interrogate with analytical methods, but have less realistic reaction kinetics and impede the diffusion of reactants and products.[36] The mass of the loaded sample and gas flow are chosen to result in realistic weight hourly space velocities (WHSV) and gas hourly

space velocities (GHSV).[47] Sample mass loadings of a few mg allow for delivery flows in the order of ml/min. For example, 50 ml/min (STP) mass flow, in a reactor with 50 mg of catalyst would equal a WHSV of 26 h^{-1}, and yield products such as propene at 1 bar pressure. Ideally, *in situ* experiments use similar reaction conditions for FTS to those used industrially (T ≈ 473-523 K, P ≈ 20 bar, syngas ratio of $H_2/CO \approx 2$),[48–50] comparable to conditions in fixed bed reactors.[51] Sample environments as described above have been commissioned at the ESRF on both the Swiss-Norwegian Beamline (SNBL) and the Dutch-Belgian Beamline (DUBBLE).[52,53]

Common pre-treatment methods involve the reduction of Co_3O_4 particles (produced by the chosen preparation method), to the active species of metallic cobalt in a flow of H_2. The reduction path from Co_3O_4 to metallic Co has been shown to proceed via CoO.[54] Typically, both fcc and hcp Co^0 are present in Co-based catalysts (to varying degrees) depending on the synthesis method and the particle size (fcc being more dominant in Co particles <10 nm).

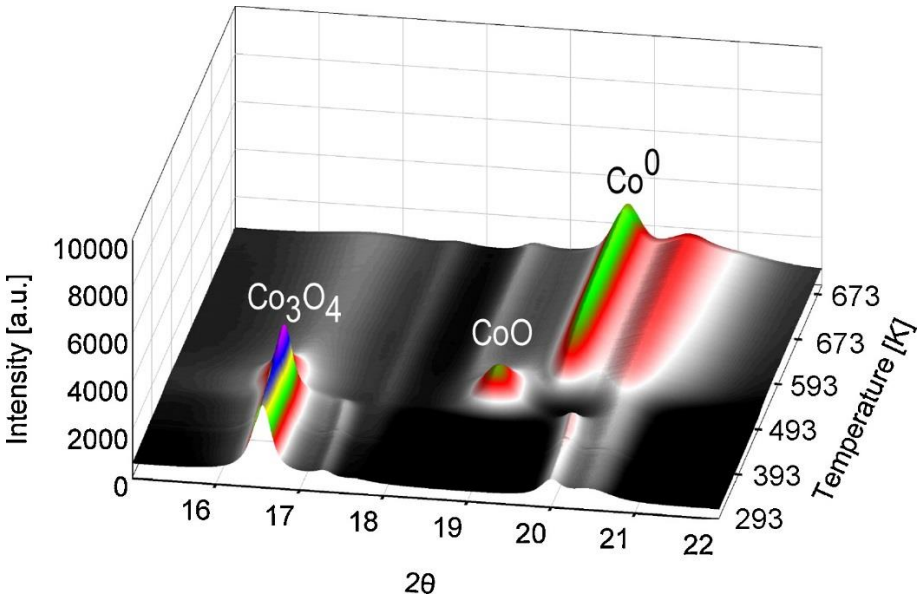

Figure 2.4: In situ PXRD patterns from reduction study of Re promoted Co/γ-Al_2O_3, recorded using a wavelength of 0.704 Å. The samples were heated from 293 K to 673 K at 3 K/min. Shows reflections of Co3O4 (311) at 16.54° 2θ, CoO (111) at 18.93° 2θ, and Co0 (111).

Figure 2.4 is taken from a typical reduction study, in which the evolution of the PXRD patterns during the reduction of a Re promoted Co/γ-Al_2O_3 catalyst (20 wt%) is examined. The catalysts were reduced in a flow of H_2 at a pressure

of 10 bar gas pressure.[51] It can be seen in Figure 2.4 that initially a Co_3O_4 reflection (311) was detected at 16.54° 2θ, which then disappears at 483 K, accompanied by the emergence of a CoO peak at 18.93° 2θ. The CoO peak then in turn disappears and a Co^0 peak at 20.44° 2θ is then detected.[51] The diffraction patterns in this study contain diffraction peaks which correspond to both fcc and hcp Co^0. Naturally it is difficult to ascertain the location and quantity of the two metallic phases without further analysis, as the diffraction peaks for both hcp and fcc phases overlap and can often be difficult to separate in nanoparticulate systems where peak broadening occurs. However, the two reflections around 20° 2θ suggest a majority of fcc content in the sample.

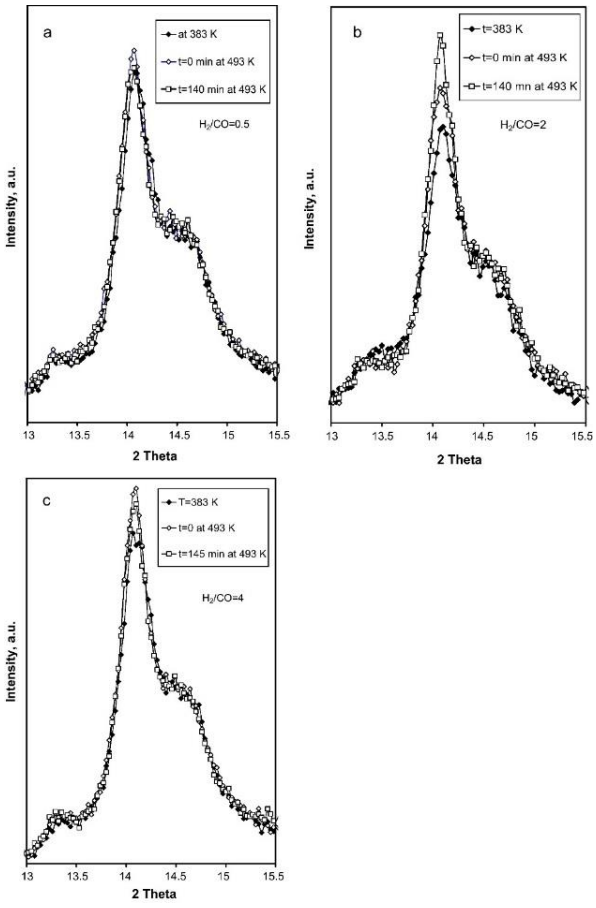

Figure 2.5: XRPD diffraction patterns of $CoPt/Al_2O_3$ catalysts under syngas at a pressure of 20 bar. All three frames display diffraction patterns before the temperature ramp to FTS conditions, at the beginning of FTS and after ~140 min. Of various syngas ratios a) $H_2/CO = 0.5$ b) $H_2/CO = 2$ and c) $H_2/CO = 4$.[48]

Although activation studies show the greatest variation in structure and are therefore easier to investigate, *operando* studies of FTS itself provide insight into

and the most relevant information on the actual process. For example, *operando* PXRD measurements were performed by Sadeqzadeh *et al.* in combination with XAS measurements.[55] Full profile matching was used to determine the size of the Co^0 crystallites and the behaviour of the variation in size throughout FTS was studied for various syngas ratios. Sadeqzadeh *et al.* observed an increase in crystallite size over the first 140 min of the reaction in all their samples, which they attributed to sintering of the Co^0 particles during the initial phase of FTS. However, this could also be due to the continued reduction of a partially reduced catalyst under FTS conditions. This effect is most pronounced in the sample treated with higher syngas ratios although most noticeable in the sample treated in $H_2/CO = 2$. Similar Co^0 crystallite behaviour was observed in the Rønning *et al.* study described above and Karaca *et al*.[48,51]

During *operando* experiments performed at industrially relevant pressures (in the order of 20 bar pressure), FT waxes are typically produced. The production of waxes during *operando* PXRD studies is often problematic as capillaries with small diameters (~ 0.5 – 2 mm), are required to give good quality diffraction data, which are easily blocked by wax resulting in short times on stream (< 4 h). The build-up of wax can been observed in *operando* diffraction patterns as an amorphous peak at low angles (~ 6 – 8 °2θ).[51,55]

The bulk Co_2C phase is also detectable by PXRD, the formation of which is believed to be a mechanism of deactivation of FT catalysts. A notable example of this was reported by Karaca *et al*. Co_2C was detected in platinum promoted Co/Al_2O_3 samples (5 wt%) studied under FTS conditions of T = 493 K, P = 20 bar and $H_2/CO = 2$ after a time on stream of > 8 h.[56] Small diffraction peaks that were attributable to a Co_2C phase emerged after 8 – 10 h and were accompanied by a decrease in the intensity of metallic cobalt peaks.[56] Cobalt sintering was also detected within the first 3 – 5 h of FTS, demonstrated by an increase in the mean size of the fcc Co crystallites from 6 to 10 nm for samples calcined at 573 K and 5.3 to 6.5 nm in those calcined at 773 K.[56]

In situ and *ex situ* studies both involve some degree of compromise. Most *in situ* FTS studies last only a few hours per sample, covering primarily the initial stages of FTS and are therefore are unable to examine any longer-term

deactivation. Whereas *ex situ* measurements of spent FTS catalyst from a reactor risk exposing the air sensitive sample to air. In this manner, it is possible to characterise a catalyst that has been online significantly longer and in a more realistic reactor, allowing longer term deactivation to occur. For example, Tsakoumis *et al*. studied spent catalysts that had been on stream in the reactor for 100 hours.[50] The study performs a comparison of crystallite particle size of the fcc Co^0 determined by PXRD for a Re promoted Co/Al_2O_3 catalyst after *in situ* PXRD of FTS (30 h on stream) in a micro plug flow reactor, pseudo *in situ* treatment in a fixed bed reactor (FBR), and 100 h in an FBR. The average crystallite size of the fcc Co^0 of the sample run for 100 h (6.9 nm) in the FBR is smaller than that of those tested in the *in situ* cell (8.6 nm), which they attribute to the passivation (superficial reduction) of the wax embedded spent catalyst. The latter closely mirrors the size of the initially reduced sample (8.5 nm). The difference in behaviour between the *in situ* and pseudo *in situ* (prone to the same vulnerabilities as *ex situ* measurements), highlights the need to test catalysts under realistic conditions.

Operando experiments are not only limited to synchrotrons. A notable example being Cats *et al.* (2016), in which longer-term (200 h) experiments were performed using a Mo source lab diffractometer, in combination with Raman spectroscopy, and monitored using GC.[38] The study measured Co/TiO_2 samples, Co^0 NP approximately 20 nm in size, and of 15 wt% during reduction and FTS at 250 °C and were performed at 0 bar (relative to atmospheric pressure) and 10 bar. The study shows an interesting difference between the presence of carbon at different pressures, with the 10 bar FTS experiment displaying some conversion of metallic cobalt into the carbide, not observed in the ambient pressure experiments. Although such lab-based studies allow for longer FTS experiments and mean that longer-term deactivation of catalysts can be studied, there are major limitations to non-SR operando studies. For example, laboratory X-ray sources, do not have high enough energy to observe smaller nanoparticles using XRD – meaning that catalysts with sizes close to the most active range ~6-10 nm are difficult to observe. The poor spatial resolution of lab-based XRD also reduces the accuracy of fcc vs hcp differentiation.

Although Co^0 is presumed to be the active site for FTS, it has been observed that there are notable differences between the catalytic performances of the fcc and hcp structures of Co, with some studies suggesting that the hcp form is more active.[55] Metallic cobalt can be challenging to interrogate thoroughly with XRD as there is a heavy overlap between the strongest reflections of fcc and hcp, and both polymorphs have a strong proclivity to form stacking faults. Stacking faults affect diffraction patterns by slightly shifting the position of the reflections (as the average value of d is slightly distorted) and altering the ratio between the reflection intensities. This results in problems for more conventional XRD analysis methods, such as Rietveld refinement, where studies will often resort to using unphysical preferred orientation models to compensate for the effect of stacking faults.

Most notably, the issue of stacking faults in FTS catalysts was explored by Ducreaux *et al.* in 2008.[57] In this study, the catalyst was modified after synthesis to produce hcp or fcc dominate Co^0, while maintaining the consistency of the other catalyst parameters. Hcp structures were achieved by carbonization of Co^0 under CO at 230 °C followed by a decomposition to Co^0 under H_2 at 230 °C. XRD patterns of these catalysts were recorded and modelled computationally to confirm that the fcc and hcp Co^0 (both clearly present in the material from the diffraction patterns), are stacked within the particles as a complex succession of stacking faults (opposed to individual hcp and fcc particles). Then catalytic testing was carried out on the hcp and fcc dominate catalysts, which found that although both produced products of similar selectivity, the hcp catalyst had a 50% higher conversion rate.[57] It has been suggested that this is due to either the differing reducibility of fcc and hcp cobalt or the structural stacking exhibited within fcc Co, which is surface defect deficient. Surface defect sites such as kinks and steps can be shown via DFT calculations to allow carbon monoxide (CO) and other gas molecules to bind to the site more easily.[58] The high binding energy possibly encourages CO dissociation and consequently increases the FTS turnover rate.[59]

Many SR-based studies have had difficulties evaluating the effect of fcc vs hcp Co^0 in FT catalysts diffraction patterns. It is worth noting, however, that techniques such as spin-echo NMR could be used for hcp vs fcc quantification purposes and which would be very powerful if used in conjunction with *in situ*

XRD. In one study, NMR on ^{59}Co nuclei in Co/UPTFE (ultra-dispersed poly(tetrafluoroethene)) samples has been reported. Co^0 in hcp and fcc structures have different environments and so appear in spin-echo NMR as two Gaussian curves at different signal frequencies.[60] The ratio was determined by comparing the areas of the Gaussian fits of the two peaks corresponding to hcp and fcc Co^0 respectively. The percentage values were fcc 16 ± 3 % and hcp 84 ± 3 %, however these samples are supported on a UPTFE support with distinctly different behaviour to the metal oxides commonly used for FT catalysts and the error values are relatively large.

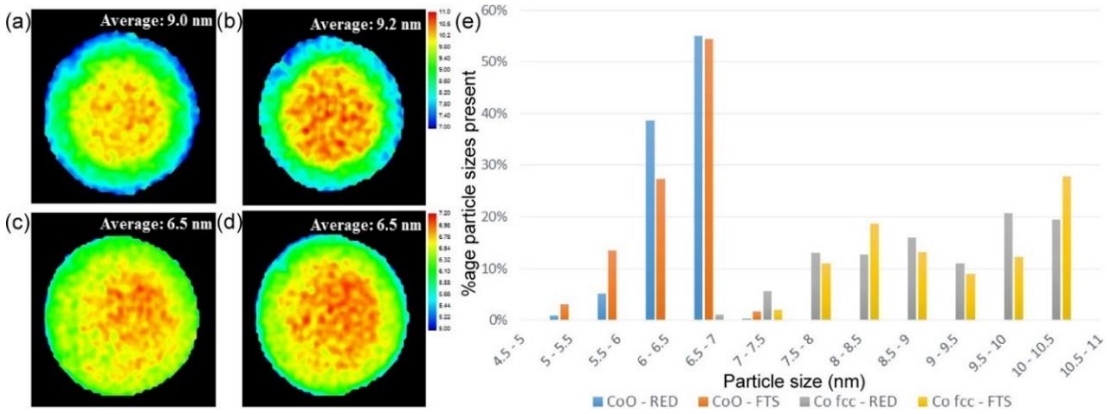

Figure 2.6: Reconstructed slices mapping nanocrystallite size of cobalt for fcc Co (a and b) and CoO (c and d) after reduction and during FTS. And (e) a histogram of fractional percentage of each size range given.

New frontiers of XRD for catalysis have recently opened by developments in XRD-CT (X-Ray Diffraction – Computer Tomography). XRD-CT measurements produce diffraction maps over 2D slices (or volumes built of slices) and thus are able to chemically image samples in real time. One of the limitations of bulk XRD is that it is not sensitive to local inhomogeneity, this is overcome by XRD-CT. μXRD-CT scans are recorded using an X-ray beam of small beam size (in the order of 10s of microns - which defines the resolution of the CT images), which is scanned across the width of a sample (in these cases a capillary reactor), and repeated for each position of rotation. The multiple diffraction patterns generated then undergo data reduction to produce sinograms, which are then in turn reconstructed into image slices of the catalyst bed. In XRD-CT each pixel in the reconstructed images has its own corresponding XRD pattern, which can be analysed as with bulk XRD while also providing information on inhomogeneity

over a cross section of the sample. Recently time resolutions have been pushed to fast enough speeds for XRD-CT to be performed *in situ/operando*.

XRD-CT can also be used to map particle sizes determined by XRD analysis across a sample. A notable example of this was performed by Senecal *et al.* (2017), in which XRD-CT measurements of a pellet during FTS (performed at 250 °C at ambient pressure).[33] Under FTS conditions the smaller fcc Co^0 NPs (<7.5 nm) were observed to disappear and the average NP size increased, which was attributed to the oxidation of the smaller NP by water produced by FTS (see Figure 2.6). Bulk XRD studies that observe similar increases in average particle size often attribute this to the continued reduction of CoO or sintering of the metallic particles.[48]

2.2.2 Total Scattering or Pair Distribution Function Analysis (PDF)

Total scattering presents the opportunity to examine FTS catalysts over many length scales simultaneously, independent of ordering. This is achieved by analysing the total scattering, which includes both the Bragg peaks, and diffuse scattering. Thereby detecting all the cobalt content as well as the support contribution regardless of crystallinity or particle size.

Briefly, total scattering data is analysed through the reduced structure factor, F(Q)-=-Q[S(Q)-1], extracted from the scattering pattern, where S(Q) is the total scattering function.[61] The pair distribution function (PDF) is obtained by performing a Fourier transform on F(Q). Numerically the PDF equation is obtained using equation (2.1), where Q is the momentum transfer vector.[62]

$$G(r) = \frac{2}{\pi}\int_0^\infty Q[S(Q) - 1]\sin(Qr)\,dQ, \qquad (2.1)$$

The PDF is the probability of finding two atoms separated by a distance in real space *r*. Unlike the other scattering techniques discussed, PDF data is analysed in real space rather than in reciprocal space. Structural information on the system can be extracted from the PDF by structural modelling or even by simple analysis of the peak positions.[63] Total scattering requires similar beam and detector properties to other scattering techniques, however for detailed

analysis a particularly high Q-range of approximately >20 $Å^{-1}$ is required which favours the use of higher energy X-rays.

Although neutron PDF has been in use for a long time X-ray PDF is a relatively new technique and as such there are currently few reports that have used PDF to analyse FTS catalysts. In work by du Plessis *et al.* PDF was used to follow the reduction of a Co/Al_2O_3 catalyst *in situ*, the PDF can be seen in Figure 2.7. In particular, a refinement of the data was performed to determine all cobalt phases present in the catalyst.

The first five peaks that correspond to the short-range order are indicated in Figure 2.7 by red arrows and are observed to increase or decrease during the course of the reduction reaction. Table 2.1 shows the possible combinations of atomic pairs/interatomic distances that could give rise to these contributions in Figure 2.7. The key observation in this study is that 32 % of the cobalt in the sample is undetectable by XRD but which is observable using PDF. The relative abundances of different phases present in the catalyst calculated using both Rietveld refinement and PDF are compared in Table 2.2.

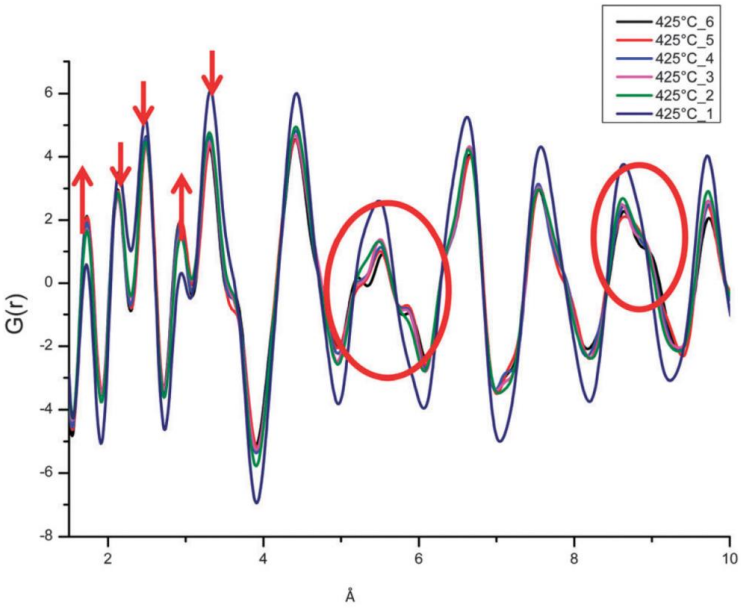

Figure 2.7: PDFs acquired during the reduction of Co/Al_2O_3. The temperature was held at 425 °C for 2 h. The numbers 1-6 in the figure legend correspond to consecutive 20 min diffractograms over the 2 h reduction period.[64]

Table 2.1: Summary of interatomic distances assigned, information extracted from reference [64].

Inter-Atomic Distance (Å)	Scattering pairs assigned to distances
1.7	Al-Al(γ-Al_2O_3), O-Al($Co_xAl_yO_2$), O-Co ($Co_xAl_yO_2$)
2.2	Al-O(γ-Al_2O_3)
2.5	Co-Co(Co_{fcc} and Co_{hcp})
3.1	Al-Al(γ-Al_2O_3), Al-Al(θ-Al_2O_3), Al-O(θ-Al_2O_3)
~3.5	Not assigned

More specifically, the results show that PDF analysis determined a relative abundance of 22 wt% (confirmed by ICP-OES, 21 wt%).[64] However, the Rietveld refinement finds only 15 wt% (68 % of the cobalt present in the sample). Considering the fact that not only the particle size, but the nature of the cobalt species is key to the activity of an FTS reaction. PDF enables the detection of species which are difficult to observe with conventional PXRD approaches – as the material is either not in crystalline form or the particles are too small to detect with XRD. The observation of such material is essential if the FTS is to be better understood and therefore this initial result highlights the potential of total scattering to the study of FTS.

Table 2.2: Relative abundances of material determined by PXRD and PDF. Information extracted from du Plessis *et al.*[64] *Inductively Coupled Plasma Optical Emission Spectroscopy (ICP-OES) wet chemical analysis.

	Relative Abundance (wt%)		
	Rietveld	**PDF**	**ICP-OES***
Si	9	9	-
$Co_xAl_yO_4$	2	2	-
θ-Al_2O_3	19	24	-
γ-Al_2O_3	52	44	-
CoO	11	6	-
Co(fcc)	4	12	-
Co(hcp)	<1	3	-
Amorphous	3	-	-
Total wt% Co	***15***	***22***	***21***

One of the challenges in the interpretation of PDF data is that, due to the presence of scattering pairs from all components in the sample (i.e. Co and Al-containing phases in this study), it is difficult to unambiguously assign a specific contribution to one specific component/phase. Thus, for example, the contribution at 1.7 Å could be assigned to tetrahedral Al^{3+}-O contributions typical of the support or else possibly, although unlikely, tetrahedral Co^{3+}-O species typical of an inverse spinel structure.[65] Notably however the lack of a significant positive component in the G(r) at ~ 1.9 Å suggests the absence of the normal tetrahedral Co^{2+} containing spinel $CoAl_2O_4$.[66] As with XRD, PDF-CT measurements can be performed *in situ/operando* (even in combination with XRD-CT), providing for a more complete characterisation of Co nano-crystallite behaviour under reaction conditions.[33]

2.2.3. Small Angle X-Ray Scattering (SAXS)

SAXS is the detection of elastically scattered X-rays at very low angles, which are caused by long range inhomogeneities in the electron density of a sample, consequently the features probed by this technique are in the range of 1-100 nm.[67] This length scale results in the study of comparatively large scattering entities within the samples; structures such as the cobalt particles and pores within the supports. However, when characterising catalytic particles on porous supports, it is non-trivial to differentiate particles from pores using SAXS.[68] SAXS is a very powerful technique for the examination of colloidal solutions, especially for systems that show high monodispersion.

SAXS is mainly used to determine the morphology of particles/pores, this includes average size, size distribution, specific surface area and the shape of these structures, as well as the average distance between such features.[69,70] Synchrotron-based SAXS offers the opportunity to study such variations *in situ*, with extremely short collection times that facilitate real-time monitoring of catalysts under reaction conditions. SAXS is frequently performed simultaneously with conventional XRD (referred to as Wide Angle X-ray Scattering (WAXS) when combined with SAXS) as the scattering radiation cone produced from scattering experiments (XRD/SAXS) contains both information and the different size ranges

probed are complimentary.[71] SAXS measurements are independent of the crystallinity of the sample and so can be used to determine particle size, whereas, WAXS is able to determine crystallite size and the degree of crystallinity or phase purity.

Although SAXS generally provides morphological information, structural information concerning the surface of the cobalt particles can be obtained from this data providing insight into variations in the surface structure under reaction conditions.[67] In a recent novel SAXS study, Høydalsvik *et al.* used synchrotron-based SAXS to study Co-based FTS catalysts, providing an insight into the changes in the surface morphology of Co particles at the beginning of FTS, as well as a good description of relevant SAXS analysis for such catalysts.[67] The catalysts examined in the study were two Re promoted Co/γ-alumina catalyst (sample A and sample B), and SAXS measurements were taken during reduction and FTS, in a flow of H_2 and syngas respectively. WAXS was performed simultaneously to study the reduction of the cobalt oxide, the results of which were consistent with previous studies.

ASAXS (Anomalous Small Angle X-ray Scattering), a technique in which the X-ray energy is deliberately tuned near to a absorption edge to provide some element specificity in the features being probed, was performed independently on one sample to distinguish between Co particles and pores in the γ-alumina, resulting in a more meaningful discussion of the SAXS data.[67]

The authors also used model *independent* analysis of the SAXS data and compared observations on the calculated values of the Porod exponent (α) and the scattering invariant (G*) (both explained in the following text) from the SAXS data in order to try and identify changes in morphology or shape of the Co particles during FTS and identify the most probable cause. The Porod exponent yields information concerning the surface of the particles. Whereas, the scattering invariant is dependent on the mean square fluctuation of electron density, a change in which would indicate a variation in density or mass of the particles.[67]

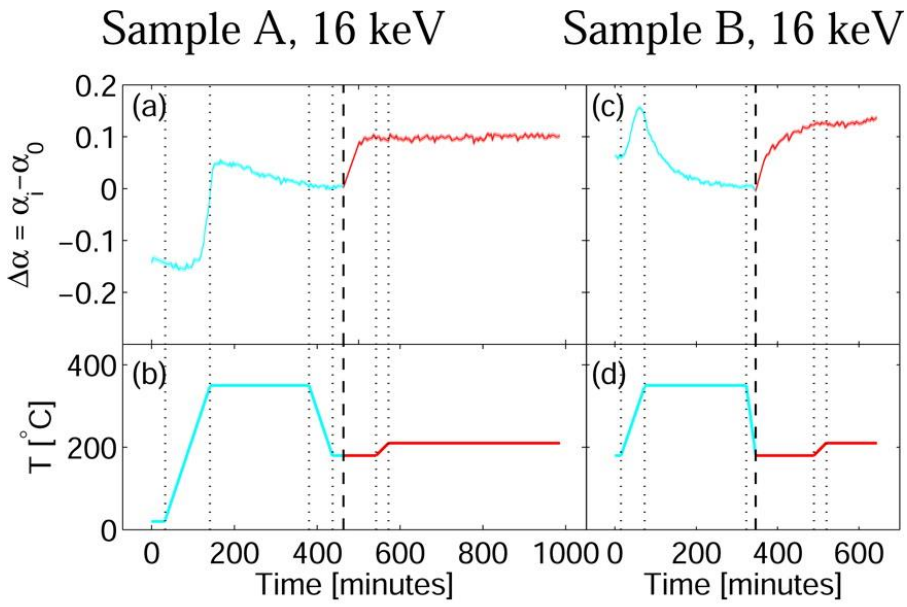

Figure 2.8: Variation in the Porod exponent and temperature over reduction and FTS.[67]

The value for the Porod slope (α_0) is approximately 4 during reduction and increases to a value > 4 after the syngas is introduced, indicative of the change from a smooth 3D object to one with a continuous interface transition.[67] It is assumed that only the Co contributes to α_0, as the γ-alumina should be thermally stable at the temperatures used. It is therefore concluded that a change in cobalt shape or particle morphology occurs at the start of an FTS reaction. The key results from this paper are shown in Figure 2.8 and Figure 2.10, where the cyan regions represent the reduction process, and the red regions FTS.

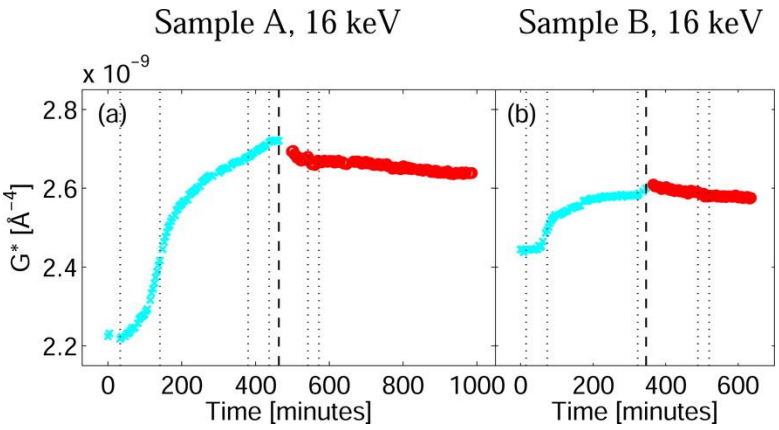

Figure 2.9: Variation in the scattering invariant (G) over reduction and FTS.*[67]

During reduction the scattering invariant increased significantly, this corresponds to reduction towards a cobalt metallic species, as Co^0 has a higher scattering density than Co_3O_4. As the syngas is introduced at the start of FTS there is a large increase in the Porod exponent for both samples, whereas, the invariant only reduces slightly with time on stream. Possible causes for the observed changes were proposed as follows (Figure 2.10): i) shape change/faceting, ii) surface reconstruction and relaxation, iii) formation of a subsurface carbon layer, iv) surface reoxidation, v) adsorbed monolayer of CO/layer of hydrocarbons, or vi) diffusion or interactions with the alumina support.

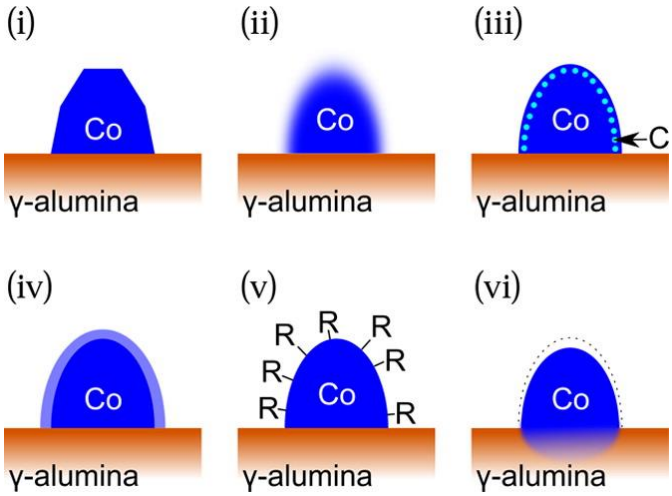

Figure 2.10: Schematic representations of the possible cobalt particle changes during FTS which could explain the observed data changes in the SAXS data: (i) faceting, (ii) surface reconstruction and relaxation, (iii) formation of a subsurface carbon layer, (iv) surface reoxidation, (v) adsorbed monolayer of CO or a layer of hydrocarbons, and (vi) diffusion/interaction with the alumina support.[67]

It was concluded that the most likely interpretation of the SAXS data is the migration of Co surface atoms caused by absorption of CO resulting in less well-defined particles.

2.3. Spectroscopic Techniques as applied to Co-based FTS catalysts

As cobalt-based catalysts possess a variety of coordination and oxidation states, spectroscopic techniques are well suited for their characterisation. XAS and X-ray photoelectron spectroscopy (XPS) techniques work particularly well for this purpose as they are element specific and directly interrogate the local geometry, coordination environment and oxidation state of cobalt.

Cobalt has the electron configuration [Ar] $3d^7$ $4s^2$ and the most commonly found oxidation states are 0, +2, +3 and +4. Co^{2+} (d^7) is cobalt's most common valence state, which can adopt high-spin octahedral[72] and tetrahedral ($CoAl_2O_4$) coordination environments.[54] Co^{3+} (d^6) is also present in octahedral coordination ($LaCoO_3$)[73] but on rare occasions is also found in the tetrahedral coordination.[74] Co^{4+} (d^5) is less stable and only observed as an intermediate during catalysis, particularly in electrocatalytic water splitting.[75] Cobalt can also exist in a mixed valence state within the same compound; for example, the tetrahedrally coordinated +2 and octahedrally coordinated +3 oxidation states of cobalt are both present in Co_3O_4.[76]

2.3.1. X-ray Photoelectron Spectroscopy

X-ray Photoelectron Spectroscopy (XPS) is a surface science technique by which elemental composition, chemical composition, and the electronic state of elements within a sample can be determined. On average, up to a depth of 5 nm from the surface of a sample.[77] The surface of a sample is excited by exposure to X-rays, and the energy of the emitted photoelectrons are measured. Photoelectron peaks are observed in XPS spectra and the binding energy and intensity of said peaks is used to determine elements present, their chemical state, and quantity.

XPS is most often used to detect the oxidative evolution of cobalt species following reduction and FTS reactions. The 2p transitions of Co are measured in order to carry out this characterization and the assignment of cobalt oxidation states is most readily accomplished by examination of the satellite structure of

the $2p_{3/2}$ level and also by consideration of the spin-orbital splitting of the 2p levels. Co_3O_4 consists of octahedrally coordinated Co^{3+} and tetrahedrally coordinated Co^{2+}. A peak around 778 eV is characteristic of metallic Co.[78] On ionization, the 2p levels are split into $2p_{3/2}$ and $2p_{1/2}$ as a result of spin-orbit coupling. A $2p_{3/2}$ XPS peak found around 782 eV "with an intense shoulder at about 787-788 eV" denotes the presence of Co^{2+}.[78] However, for Co^{3+} species, the $2p_{3/2}$ peak shifts to lower energy and the shoulder becomes less intense. The $2_{p1/2}$ is around 15 eV greater than that of the $2p_{3/2}$ peak in both cases with the characteristic 1:2 intensity ratio relative to the $2_{p3/2}$. During calcination of Co^{2+} species, the intensity of the $2p_{3/2}$ decreases and shifts to a lower energy, marking the conversion of Co^{2+} to Co^{3+}.[78]

Another interesting feature of XPS is the possibility to determine particle sizes assuming both uniform distribution of particles in catalyst grains and high specific surface area (>100 m^2/g) of the support. For example, Khodakov *et al.* applied this method to cobalt Co_3O_4 particles on a SiO_2 support.[79] A simplified Kerkhof–Moulijn formula[80] can be applied to calculate the sizes of Co_3O_4 particles:

$$\left(\frac{I_{\mathrm{Co}}}{I_{\mathrm{Si}}}\right)_{\mathrm{exp}} = \left(\frac{I_{\mathrm{Co}}}{I_{\mathrm{Si}}}\right)_{\mathrm{monolayer}} \frac{1-\exp\left(-\frac{d}{\lambda_{pp}}\right)}{\frac{d}{\lambda_{pp}}} \qquad (2.2)$$

Where $(I_{Co}/I_{Si})_{exp}$ is the experimental electron intensity ratio for Co 2p and the support (here Si 2p) peaks, d is the Co_3O_4 particle size, λ_{pp} is the inelastic mean free path (IMFP) of the Co 2p photoelectron passing through Co_3O_4 supported phase calculated using Seah and Dench's formula,[81] $(I_{Co}/I_{Si})_{monolayer}$ is the predicted electron intensity ratio for Co 2p and Si 2p bands assuming monolayer coverage of silica by Co_3O_4 phase. $(I_{Co}/I_{Si})_{monolayer}$ is obtained according to equation 2.2 and photoelectron cross section values (σ_{Si}, σ_{Co}) from Scofield.[82]

$$\left(\frac{I_{\mathrm{Co}}}{I_{\mathrm{Si}}}\right)_{\mathrm{monolayer}} = \left(\frac{n_{\mathrm{Co}}}{n_{\mathrm{Si}}}\right)_{\mathrm{bulk}} \frac{\sigma_{\mathrm{Co}}}{\sigma_{\mathrm{Si}}} \left(\frac{E_k^{\mathrm{Co}}}{E_k^{\mathrm{Si}}}\right)^{-0.23} \qquad (2.3)$$

Where $(n_{Co}/n_{Si})_{bulk}$ is the ratio of bulk atomic concentrations of Co and Si atoms, E_k^{Co} and E_k^{Si} are the kinetic energies of Co $2p_{3/2}$ and Si 2p electrons,

respectively. Equation 2.3 shows that for a given $(n_{Co}/n_{Si})_{bulk}$, $(I_{Co}/I_{Si})_{exp}$ ratio increases with decreasing particle sizes, $(I_{Co}/I_{Si})_{exp}$ ratio close to $(I_{Co}/I_{Si})_{monolayer}$ indicates monolayer coverage of the support by cobalt atoms. However, Khodakov *et al.* observed particle sizes considerably smaller than the one calculated from XRD using the Scherrer equation. This difference has already been reported[83] and seems to be related to the limitations of XPS and XRD methods. The assumption of a uniform distribution of the supported phase between the bulk and outer surface of catalyst grains may be different from the reality of a calcined catalyst and the Kerkhof and Moulijn model might not always be suited for this method.

Recently XPS has become a common technique in the field of catalysis but, despite its popularity, some limitations apply. Because XPS is a surface technique, there is a limited amount of bulk information XPS can provide, which may either be an advantage in understand surface processes or an impediment in studies of 3D porous materials. Also, size determination is reliant or the assumption that the catalyst grains are uniform, which is not the case in realistic catalysts. Additionally, although surface science is a mature field, there remain three main “gaps” between what surface science techniques can measure and realistic catalysis experiments. These being the materials, pressure and complexity gap.[84] Much work has been done to bridge these gaps in the last two decades, with experiments continuing to move towards realistic conditions and more complex samples, however they still lag well behind bulk techniques in this regard.[84]

More recently Near Ambient Pressure (NAP-) XPS has been developed significantly, due in large part to the higher flux and advantages of being able to tune the incident photon energy (and therefore limit the kinetic energy and consequent escape depth of electrons from within the sample), permitting depth profiling. The general development of synchrotron NAP-XPS is well described elsewhere,[85] however the key point is it enables the acquisition of XP spectra in the 0.1 – 10 torr range; as noted previously the significance of this to catalysis is it provides ~ 10^6 collisions of gas molecules per second per surface atom of the sample and so makes mass transfer of adsorbates in the gas phase cease to be rate limiting in most cases.[86] In 2011 NAP-XPS was applied to study the redox

behaviour of two Co nanoparticle systems pertinent to FTS (both in conjunction with XANES (X-ray Absorption Near-Edge Structure) measurements as discussed below). Use of the BESSY synchrotron allowed a detailed study of small (3.5 nm) cobalt nanoparticles as compared to Co(0001) single crystals in which the very different oxidation and reduction behaviour could be seen using the Co 2p edge, in particular the satellite structure in small pressures of oxygen is indicative of Co^{2+} in the nanoparticles, which is different to the bulk mixed oxide Co_3O_4 formed on the singly crystal.[87] The implications for the preparation and reduction of FTS catalysts are discussed.

In the same year, studies of Pt-Co bimetallic nanoparticles using NAP-XPS were used to better understand possible promotional effects of precious metals (in this case Pt) in FTS. The Pt 4f signal was monitored for bimetallic 1:1 Pt:Co size controlled nanoparticles in a reducing atmosphere (0.1 mbar H_2), which allowed depth profiling of the elemental composition of the bimetallic nanoparticles, indicating surface segregation of a Pt shell around the surface (an observation confirmed by *in situ* TEM of a single particle under 0.1 mbar H_2).[88] This is important in the context of FTS, where Pt is known to act as a promotor, as it argued that the "bimetallic metal particle" is the wrong model for understanding promotion as the Pt is seen to have a deleterious effect on reactivity in the analogous CO_2/H_2 reaction.

2.3.2. X-ray Absorption Spectroscopy

X-ray Absorption Spectroscopy (XAS) or X-ray Absorption Fine Structure (XAS/XAFS) comprises both XANES (X-ray Absorption Near Edge Structure), also known as Near Edge XAFS (NEXAFS), and Extended X-ray Absorption Fine Structure (EXAFS) spectroscopies.[89] Traditionally XANES has been used as a fingerprint technique providing information about both the electronic state and local geometry of cobalt, while EXAFS allows the determination of bond lengths and the coordination numbers of cobalt species under standard and *in situ* conditions to be obtained, without the need of long range ordering.[90]

A key advantage of XAS techniques is found in studies of oxidation state, in that it is element specific – especially for complex catalysts which contain a

number of components. This affords a substantive advantage in tracking the oxidation state of one part of the sample against techniques in which the oxidation or reduction must be inferred from the adsorption of desorption of gas molecules to/from the sample as a whole (e.g. temperature programmed reduction).[91]

In FTS catalysts, typically cobalt oxide in the form of the spinel Co_3O_4 is found in calcined catalysts immediately before activation in a reducing gas stream in preparation for FTS.[92] In this step Co_3O_4 is reduced to CoO and then to metallic fcc Co. Thus, it proceeds by this "two-step reduction": $[Co^{2+}][Co^{3+}] \rightarrow Co^{2+} \rightarrow Co^0$. As such the reduction can be monitored using XANES, an example of which is displayed in Figure 2.11.

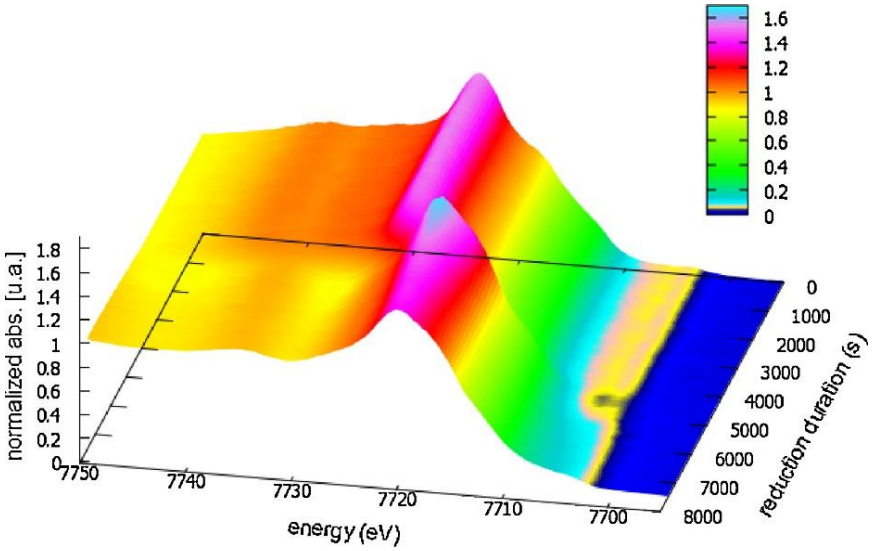

Figure 2.11: Time-resolved XANES spectra corresponding to the reduction of a Co/Al_2O_3 catalyst (7 wt%) in a flow of H_2 heated from RT to 400 °C with a ramp rate of 5 °C/min.[92]

Figure 2.11 is a continuum of XANES spectra recorded over the course of a typical *in situ* reduction. The catalyst was heated from RT to 400 °C, at a rate of 5 °C/min in a flow of H_2 of 20 ml/min.[92] As the reduction time increases a distinct edge shift is observed from approximately 7725 to 7722 eV as well as an increase in the intensity of the white line, followed by a reduction in intensity consistent with a reduction to CoO then Co^0. Such characteristic changes in XANES features are often used to monitor *in situ* reductions of such catalysts.

Another situation in which it is useful to monitor oxidation state is the study of water formation during the reaction to determine if it is a source of deactivation. Here, albeit at low pressure (0.4 mbar), studies of a Co/SiO_2/Si(100) model

catalyst using Co K-edge XAS showed that, even with H_2O:H_2 ratios of 1:1, the catalyst once reduced showed no evidence for oxidation occurring from 150 – 450 °C.[93]

Furthermore, Co K-edge data has also been used to improve understanding of the impact of precious metal promotors on maintaining cobalt in a reduced state during the reaction. Precious metals, such as Pt, are currently added to industrial catalysts, but the role of the precious metal has been an ongoing source of debate. To help understand this effect (which increasingly appears to be attributable to the improved reduction of Co in the present of precious metals), a study contrasting Pt promoted and unpromoted Co catalysts used Co k-edge data to follow the oxidation state of the cobalt component as a function of various reduction procedures, showing the more facile reduction of cobalt in the promoted case.[77]

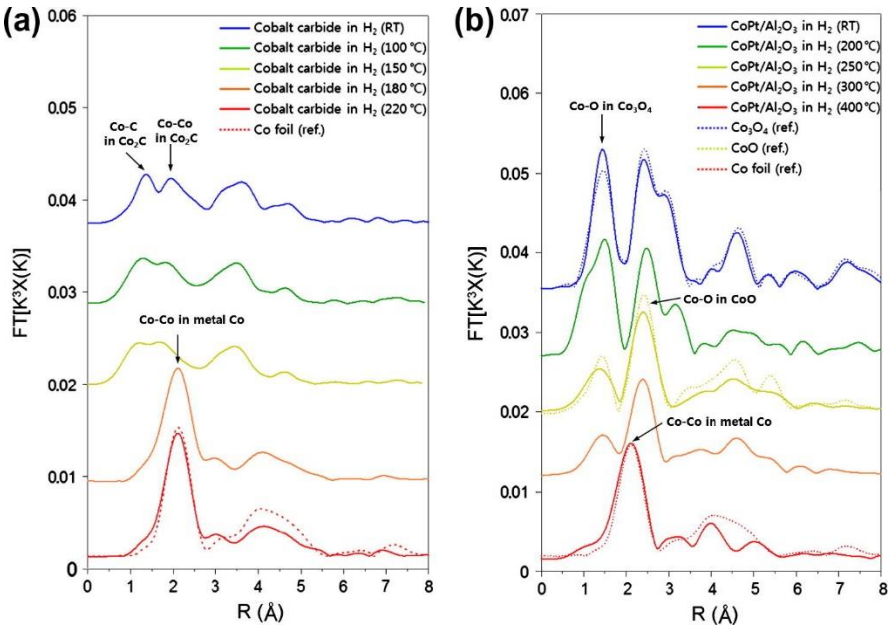

Figure 2.12: k^3-weighted Fourier-Transform magnitudes of Co K-Edge EXAFS spectra of the reduction in H_2 of a) Co_2C and b) $CoPt/Al_2O_3$. [94]

The ability to differentiate between fcc and hcp Co using XAS is limited as the Co-Co interatomic distances and coordination numbers are identical for each form. However, other features in EXAFS spectra can be indicative of the structure. For instance, in the Kwak *et al.* study, an *in situ* XAS study of the reduction of Co_2C and $CoPt/Al_2O_3$ catalysts, the 3rd and 4th peaks in the Fourier

transformed EXAFS spectra (Figure 2.12) were used to indicate the structure.[94] The transformed EXAFS spectra of the Co^0 reduced from Co_2C (Figure 2.12a) possess a low amplitude 3rd peak and no 4th peak corresponding to the 4th coordination shell suggesting the Co^0 is hcp.[95] Although this method of differentiating fcc from hcp Co is limited if a sample is a mixture of significant quantities of both polymorphs.

Carbon formed in FTS under hydrogen deficient conditions by the Boudouard reaction (equation 2.4) or via CO dissociation may interact with the cobalt-based catalyst,[5] affecting CO conversion and selectivity by forming cobalt carbide (Co_2C).[96] Although Co is thought to be in the +2 oxidation state in Co_2C, the carbide exhibits strong metallic properties (similar to most transition metal carbides) and therefore can be considered to be an hcp lattice with C incorporated at interstitial sites.[96] Co_2C can also be formed by the carburization of Co_3O_4 as shown in equation 2.5.

Boudouard reaction:[54] (2.4)

$$2CO \rightarrow CO_2 + C$$

Carburization of Co_3O_4:[96] (2.5)

$$Co_3O_4 + CO \rightarrow 3CoO + CO_2$$
$$2CoO + 4CO \rightarrow Co_2C + 3CO_2$$

An example of the use of EXAFS to identify Co_2C in cobalt based catalysts is a study by Mohandas *et al.*, which investigated the role of Co_2C in the hydrogenation of CO.[96] Unsupported Co_2C catalysts were synthesised by the carburisation of Co_3O_4. The presence of Co_2C was verified by XRD. *Ex situ* XAS measurements were taken after carburisation and once the catalyst was spent (tested in a slurry phase reactor at P = 20 bar, H_2:CO = 2:1 and T = 493-523 K). The corresponding EXAFS are displayed in Figure 2.13 and the Fourier transform spectra for the carburized catalysts (with and without passivation) show Co-C (at 1.924 Å and 1.862 Å) and Co-Co (2.505 Å and 2.441 Å) in the first and second nearest neighbour shells, thus detecting the carbide present in the sample.

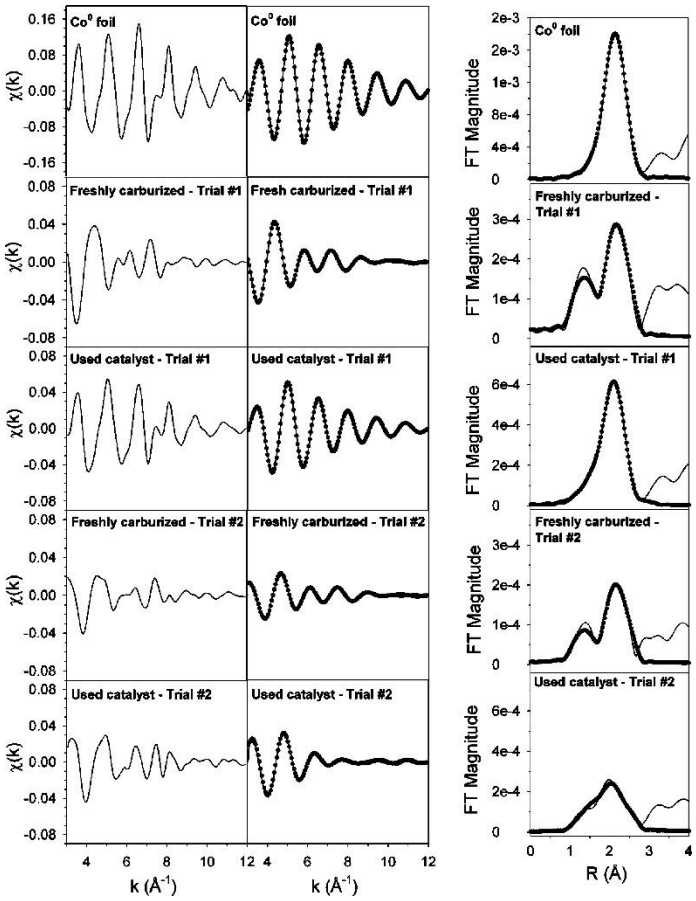

Figure 2.13: EXAFS and Fourier Transform magnitude spectra of a Co^0 reference, Co_2C catalyst once prepared and once spent, recorded at the Co K-edge.[96].

Cobalt aluminate ($CoAl_2O_4$) species are formed from the solid-state reaction between the alumina and the cobalt at the metal-support interface and are thought to mainly form under reducing conditions.[3,54] When investigating oxidation as a deactivation process, for Co/Al_2O_3 catalysts of 15 and 25 wt%, studied pseudo *in situ* after high H_2O/CO ratios (up to 25% H_2O) removed at various stages from a slurry FTS reactor, an increased tetrahedral environment of Co^{2+} clusters can be seen in the XANES spectra. This indicates the formation of $CoAl_2O_4$ over Co_3O_4, which is likely as this transformation is thermodynamically favourable[97] (see Figure 2.14).

By observing the XANES derivative spectra of the cobalt species found during FTS (Figure 2.14), the change in oxidation state of cobalt species can be portrayed by observing the shift of the peaks (with the aid of the line drawn through the centre of the tallest peak in spectrum g).[98] The Co K-edge peak of the Co_3O_4 and $CoAl_2O_4$, which is located around 7717 eV, is characteristic of

Co^{2+}.[5] This increasing intensity of the Co^{2+} pre-edge peak in the spectra indicates the absence of a centrosymmetrical structure.[99] Thus, the Co^{2+} is in a tetrahedral environment as opposed to an octahedral environment, which has a centre of inversion. Conversely, the reduced peak that is shifted to a higher energy (around 7722 eV) conveys the presence of Co^{3+} in an octahedral coordination.

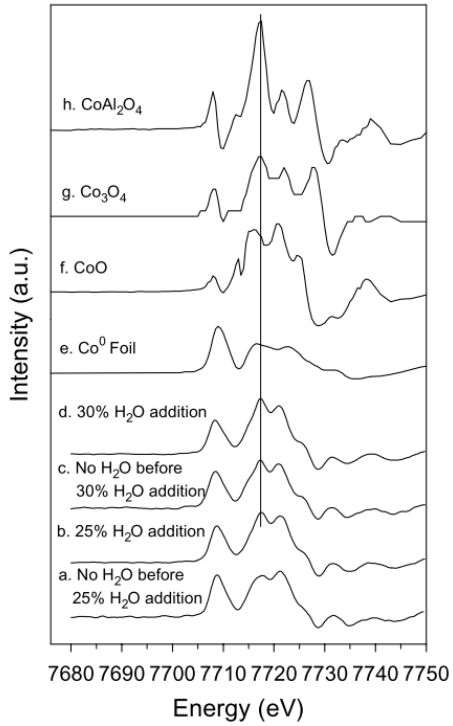

Figure 2.14: XANES first derivative spectra of cobalt species present during FTS synthesis a) after stabilisation of FTS, b) after the addition of 25 % H_2O, c) after a period of recovery, d) after addition of 30 % H_2O, e-h) reference foils/compounds. For a Co/Al_2O_3 25 wt% catalyst.[98]

However, it must be noted that the identification of small quantities of species using XANES must be performed carefully. This is particularly true for alumina supported Co-based FTS samples as both the $CoAl_2O_4$ and Co_3O_4 XANES spectra bear a great resemblance to one another and are near indistinguishable in small quantities.[1] In the study Tsakoumis *et al.*, a CoRe/Al_2O_3 (20 wt% Co, 0.5 wt% Re), prepared by incipient wetness impregnation (IWI) was studied using XANES. The authors identified Co^0 NPs under 5.3 nm (as determined by TEM) oxidised to a Co^{2+} species, which they identify as some form of cobalt aluminate ($Co_xAl_yO_z$). It is more probable that the Co^{2+} species observed is from Co_3O_4. This explanation would also result in a simpler oxidation mechanism than the one suggested in Tsakoumis *et al.* The difference in lowest

stable NP size between the studies could be due to either the techniques used to determine particles size (XRD favouring larger particles within a system), or the effect of the Re promotor in the study.

2.3.3. Soft XAS

XAS can also be performed using soft X-rays from a synchrotron source (X-rays of energies less than 5 keV). Although significantly less penetrating than hard X-rays, soft X-ray energies in the range of 200 – 4000 eV allow for the examination of the K-edges of 'ligand elements' such as C, O, S and Cl. Which are able to act as 'reporter' elements for metal sites determining the electronic state of the ligand and its metal complex,[100] or in the case of FTS may themselves be present in adsorbed species on the catalyst (C or O K-edges fall in this region). Additionally, soft X-rays allow for the probing of Co L-edges, which are typically more sensitive to Co oxidation and coordination state.

Co/TiO_2 and Co/Mn/TiO_2 FTS catalysts were studied using a differential pumping method similar to that described above for NAP-XPS. The extent of Co reduction was identified as an important parameter as a result of monitoring the evolution of Co oxidation state based upon it L-edge spectra.[101]

As soft X-rays are readily absorbed by most gases over relatively short length scales (mm), *in situ* measurements have relied upon probing samples placed close to an X-ray transparent window, which is able to hold pressure on one side with vacuum on the other, an example of which is given in Figure 2.15. For this purpose silicon nitride membrane windows have been employed and Co L-edge spectra have been reported up to several atmospheres using this technique.[102] Spectra are then acquired using the total electron yield method in which a drain current is measured between electrical ground and the sample (resulting from ejected electrons, and secondary electron emission from the sample).

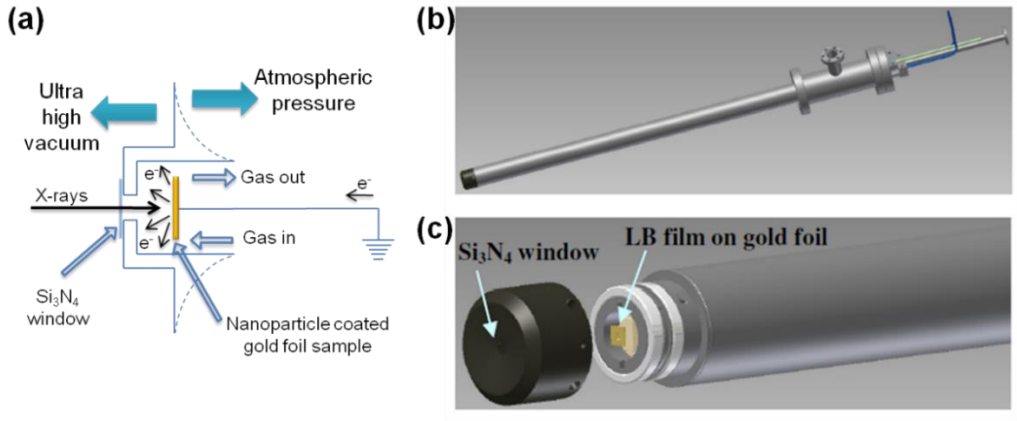

Figure 2.15: a) Schematic of in situ soft XAS cell showing gas flow and b, c) 3D visualisation of the cell and sample holder.[103]

This method was adopted for studying model Co FTS catalysts at higher pressures by Salmeron *et al.* in 2009.[104] They were able to follow the reduction in hydrogen flow at 1 bar of 3 and 10 nm (average sized) nanoparticles using the Co L-edge by this technique, starting in both cases with octahedrally co-ordinated CoO, and observing the formation of metallic cobalt. Notably they identify in addition to the more realistic pressure, the choice of using nanoparticle models of improved size control allows them to address questions about particle size effects, not addressed in previous studies using incipient wetness catalysts. The same group more recently studied CO dissociation on similar cobalt nanoparticle based FTS catalysts.[105] XAS measurements were taken at both the O K-edge at 543.1 eV and the Co L_2-edge and L_3-edge at 793.2 eV and 778.1 eV respectively during various stages of the experiment. The samples were in the form of cobalt nanoparticles (of sizes of 4, 10 and 15 nm) deposited on gold foil, which was held within a cell with a nitride window approximately 100 nm thick. The samples were heated using an IR laser and the reactive gas was passed though the cell at a flow rate of 40 ml/min.

The XAS measurements of 4, 10, and 15 nm cobalt nano-particles were taken after 5 min in a flow of CO/He (1:1) at 250 °C or room temperature are shown in Figure 2.16. The O K-edge spectra show an intense π* peak at 534.2 eV and a weak σ* peak at 550 eV, consistent with the absorption of CO on cobalt.

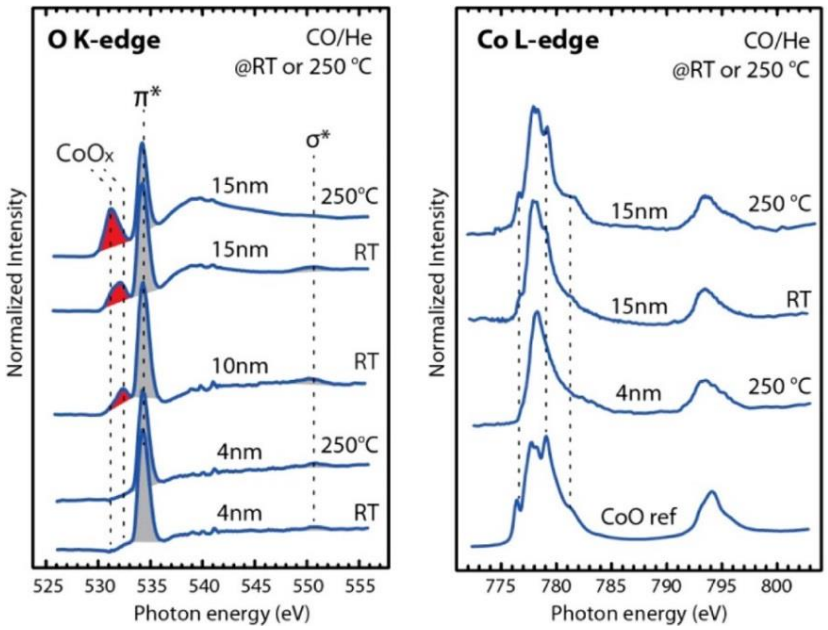

Figure 2.16: XAS spectra of O K-edge and Co L-edge of various Co^0 particle sizes and reaction temperatures.[105]

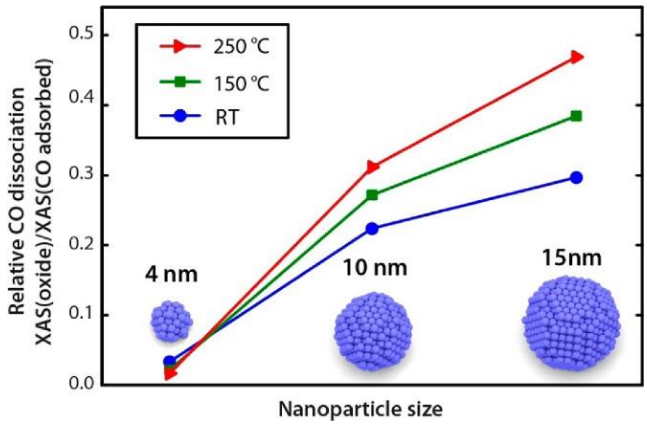

Figure 2 17: Calculated variations in relative CO dissociation for particle sizes of 4, 10 and 15 nm, at temperatures of RT, 150°C and 250°C.[105]

Another peak at ~531 eV which was attributed to CoO_x was observed in some of the spectra, the breadth of the peak indicates the potential presence of mixed cobalt oxides. Subsequently, this is also supported by the detection of CoO peaks in the corresponding Co L-edge spectra (Figure 2.16). The CoO_x peak in the O K-edge spectra was attributed to the emergence of surface oxides on the nanoparticles indicating a sizeable proportion of CO molecules had (directly or indirectly) undergone dissociative absorption. The peak is barely detectable in the 4 nm sample, clearly observed in the 10 nm, and most prominent in the 15 nm

sample. This indicated a size dependence of CO dissociation as well as a temperature dependence.

The size dependence is illustrated more clearly when the sizes of nano-particles are plotted against the ratio between the integrals of the CoO_x peaks and the π* peaks, providing an approximate measure of the tendency of CO to dissociate. Some caution must be exercised in the wider implications for FTS, however, as the results obtained use gold as a support (rather than a more conventional oxide) and the nanoparticles used are reported to be prepared via a synthetic route employing triphenylphosphine oxide,[106] a potential FTS poison.[107] Nevertheless, it represents an interesting demonstration of the use of soft X-ray XAS to probe cobalt nanoparticles reacting with the FTS reactant CO. Additionally it shows the capacity of soft X-rays to monitor low atomic number elements, typical of those originating from the adsorbate, such as oxygen in CO, or dissociated onto the cobalt surface.

Tuxen *et al.* also performed measurements on the 4 nm nanoparticles during a repeated run of the treatment described above, in a flow of CO/He then pure He, however that was then followed by a pure H_2 step. All steps were also performed at temperatures of: 20°C, 150°C and 250°C. For the initial repeated stages, the results are consistent with earlier experiments on the 4 nm particles, with an absence of a CoO_x peak and low CO absorption. However, once the H_2 was added a clearly observable CoO_x peak emerged in the O K-edge spectra (Figure 2.18a), the evolution of the intensities of these peaks can be seen in Figure 2.18c. These results indicate a size dependence of the nanoparticles for CO dissociation, and that that CO dissociation occurs more rapidly in the presence of H_2. However, the apparent activation energy for the process resulting in the loss of the π* peak shown in Figure 2.16 is given as 24 kJ $mol^{-1.}$ This is not only much less than typical apparent activation energies for FTS in general (~100 kJ mol^{-1}),[108] but significantly less than even the lowest calculated energy barriers for H-assisted pathways on corrugated surfaces (~ 43 kJ mol^{-1}).[109] In combination with the cautions raised above this suggests further work is needed to understand the relevance of these results to practical FTS catalysts.

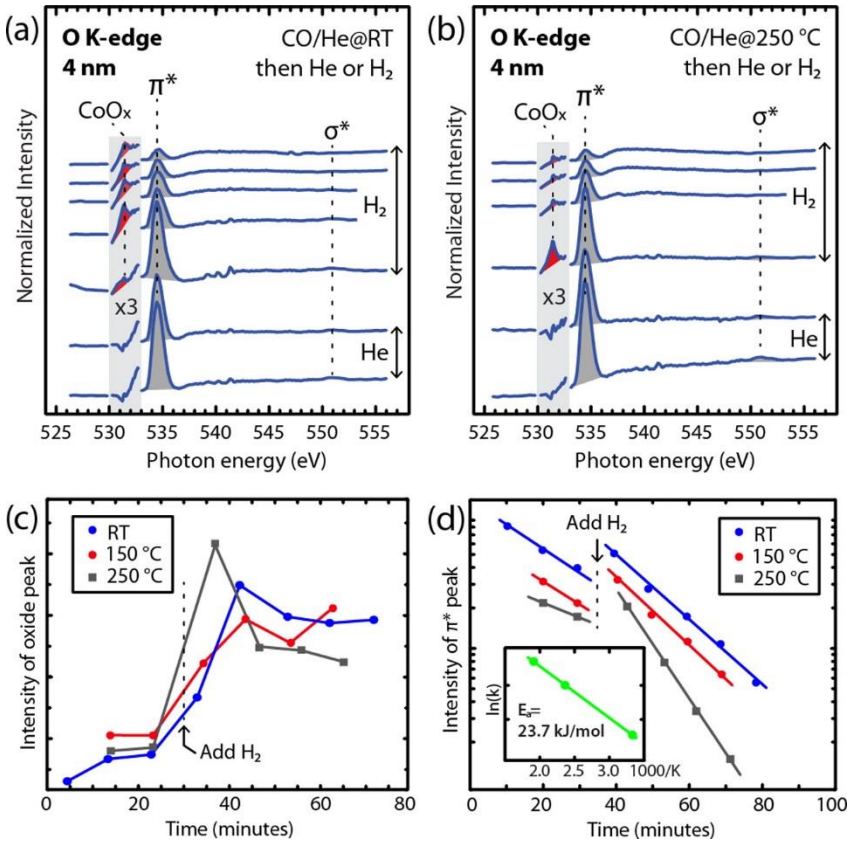

Figure 2.18: XAS spectra of O k-edge and Co L-edge of 4 mm Co^0 particle sizes at a) room temperature and b) 250 °C and graphs displaying how the intensity of the c) CoOx and d) π peaks vary with treatment time run at various temperatures (note logarithmic y-axis in d; the inset in d shows the apparent E_a for the process changing the π* peak intensity in the region after H_2 addition.*[105]

Soft X-ray XAS has also been used to investigate the possible promotional effects of Pt (discussed above as important for the mechanism of FT and possible reducibility of cobalt oxide). Co and CoPt nanoparticles were first studied in oxidising environments – the Pt being shown to enhance both reducibility and oxidation.[110] The Co L-edge spectra were analysed using a least square fit to a linear combination of reference spectra for cobalt in different oxidation states and environments (e.g. tetrahedral vs octahedral). Although it can be shown that CoPt bimetallic nanoparticles achieve improved reducibility of the Co (as demonstrated by soft X-ray XANES,[88,110] the NAP-XPS results discussed above showed this to be a poor model for an actual catalyst as a result of Pt surface segregation. The same group therefore also employed Co-L edge spectroscopy to study the effect of H_2 spillover between Pt and Co nanoparticles prepared separately and co-deposited onto a silicon wafer. During *in situ* reduction experiments, in all case the Pt nanoparticles were found to significantly increase the extent of reduction

of the adjacent cobalt nanoparticles – suggesting H_2 migration is implicated in the mechanism by which platinum promotes the activity of cobalt in these catalyst.[111]

More recently, Co-based FT catalysts using TiO_2 as a support have been compared to SiO_2 supported catalysts, again using soft X-ray Co L-edge spectroscopy to monitor oxidation state. An interesting redox behaviour has been observed in which for Co/TiO_2, partially oxidised Co appears more active. This remains to be fully understood, but is thought to be due in part to the interfacial CoO/TiO_2 sites present in the materials and to the TiO_2 decorating (and blocking reactant access to) some of the Co surface area in the fully reduced material obtained only at higher temperatures where oxide migration also occurs.[112] Again, the ability to follow the oxidation state of a specific component of the material is invaluable. Interestingly in this same work the speciation of carbon on the surface was also monitored during CO_2 hydrogenation and provides evidence mostly of carbon bonded to hydrogen or oxygen on the surface, with no evidence for any carbide formation.

2.3.4. Transmission X-Ray Microscopy

Transmission X-ray Microscopy (TXM) using synchrotron radiation was originally performed on Co catalysts by Cats *et al.*[113] The catalysts studied were Co/TiO_2 of 10 wt% and 15 wt% cobalt, examined during reduction in a flow of H_2 and FTS under conditions of T = 523K, P = 10 bar and $H_2/CO = 2$. TXM was used to obtain 2D chemical maps, XANES spectra were collected for each pixel by varying the beam energy, and the 3D elemental distribution of an individual particle was collected using acquisition tomography above and below an absorption edge.[113]

TXM and XANES were used to examine the change in chemical composition for the sample in terms of Co^0, CoO and $CoTiO_3$ on the local and long-range length scales respectively. Both the 2D chemical maps produced by TXM and the composition obtained from analysis of the XANES spectra agree that before reduction the cobalt is in the form of Co_3O_4. After reduction the composition changes to mostly Co^0 with a statistically insignificant quantity of CoO and $CoTiO_3$.[113]

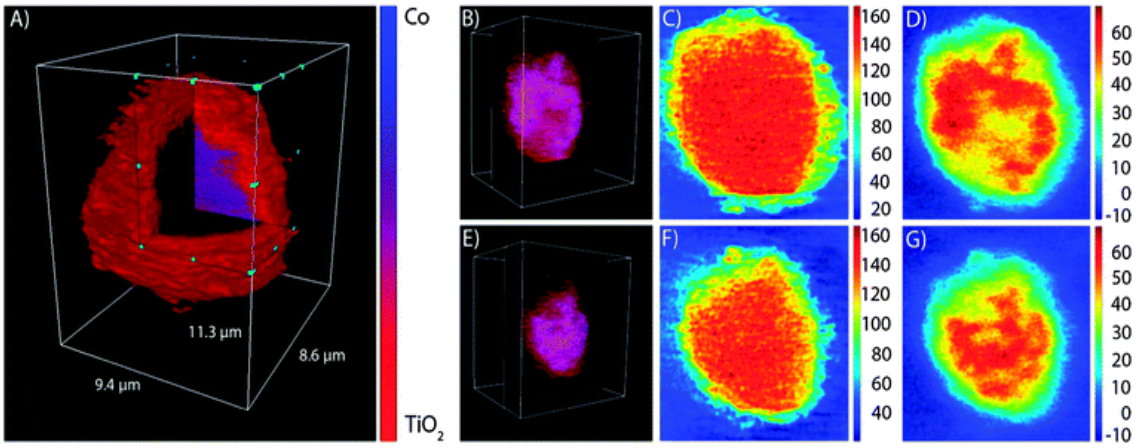

Figure 2.19: TXM images. A) 3D representation of an unreduced Co/TiO_2 particle measured at the Co K-edge. Red represents contributions from TiO_2 and blue represents contributions from cobalt. Images B-D and E-G show two slices though the particle.[113]

The 3D tomographic image of a catalyst particle of the unreduced 15 wt% Co/TiO_2 at the Co K-edge is seen in Figure 2.19, as well as 2D slices of the image.[113] It can be seen that the cobalt in the sample is concentrated at the centre of the catalyst particle, and under standard FTS conditions, there is no re-oxidation of cobalt or a metal-support intermediate compound formation. However, considering the size of the nanoparticle (18 nm average as determined by XRD Scherrer analysis) and the spatial resolution of the beam (30 nm), the truly active nanoparticles – either metallic or mixed oxides – might not be observed. Previous studies have also shown that small Co_xO_y nanoparticles are extremely difficult to reduce, retaining their oxidic nature.[114–117] Since this study cannot include these small particles in the analysis, it would not be sensitive to their role in the FTS reaction.

An additional study by Cats *et al.* published recently used multiple microscopy techniques over several length scales (hard and soft X-ray TXM, as well as STEM-EELS) to study Co/TiO_2 catalysts.[118] Here it was observed that during FTS Co became redistributed on the microscale forming a layer around the TiO_2 particles in the presence of carbon. This result is notable as it appears contrary to the previously reported behaviour of Co on TiO_2 samples where Co was observed to become encapsulated by TiO_2, leading to FTS catalysts with lower activity. However, both studies suggest that Co exhibits a strong metal support interaction (SMSI) with TiO_2.[119,120]

2.3.5. Challenges of in situ studies

This literature survey has focused mainly on the study of Co-based FTS catalysts using SR radiation, and testifies to the wealth of information attainable with these techniques. However, to perform the experiments, there is often a necessary trade-off between the properties of the catalyst, its reactor, or the reaction conditions, and the requirements of the characterisation technique. For example, experimental geometry can limit the size of the reactor, as is the case with PDF and some XRD set-ups, where the sample-detector distance is relatively small. As can absorption due to sample thickness (for example in XAS).[121]

Combined techniques can add additional complications. This is especially true in the case of combined XAS/XRD or XAS/SAXS. The beam size in scattering techniques is ideally as small as possible to prevent spatial smearing of the patterns. However, in XAS experiments a larger beam size is often used to probe a larger quantity of sample and therefore improve data quality. In practise, both are tuned to optimise data quality.

In Co-based FTS *operando/in situ* experiments pressure becomes an issue as at the most industrially relevant pressures (~ 20 bar) waxes form.[51] A commonly used *in situ* cell is a borosilicate/quartz capillary, mounted into a holder, and placed in a gas rig – heated at and around the measurement point. Outside of these heated zones are cold regions where the wax can solidify and block gas flow, prematurely ending the experiment and preventing long term deactivation studies at that pressure.[67] To avoid this, experiments can be run at lower pressures, however this results in the production of mainly lower weight hydrocarbons (FTS pressure is one of the properties that effects the hydrocarbon chain growth probability).[122] In the experimental chapters later in this work, a pressure of 2 bar was chosen for the *in situ* experiments, to be more realistic than ambient pressure, while still reducing wax production.

2.4. Catalyst Preparation

Cobalt FTS catalysts are synthesised using a variety of preparation techniques. More conventional methods include impregnation and co-precipitation,[123–125] while less common methods such as colloidal methods and the use of microemulsions (of which inverse micelle synthesis (IMS) is included) are also used, principally to produce model catalysts.

2.4.1. Common Synthesis Methods - Impregnations and Co-precipitations

The most common methods used to prepare catalysts are impregnation and co-precipitation. Impregnation involves the following stages. First a metal salt is dissolved in a solvent (most commonly water), a volume of the resultant solution is added to a quantity of support. Then the solvent is removed by drying, frequently the drying stage is performed by heating the sample to a gentle heat, ~70 °C, to reduce sintering of the cobalt oxide particles. The catalysts are then calcined in order to decompose the metal salt and chemically bond the oxide to the support. The temperature used for calcination varies from 170 °C to 450 °C,[126,127] however higher temperatures tend to result in more sintering and therefore larger particles.[127] Calcinations are often performed in a flow of air,[39,128] but can be performed under a range of gasses, including NO.[126] Finally the catalyst is reduced in H_2 to produce the active metallic phase.

In incipient wetness impregnation (IWI) the volume of solution added to the support is equal to the total pore volume, whereby the cobalt is impregnated into the support by capillary action within the pores.[129] If the volume of the solution is greater than that of the pores then the cobalt diffuses into the support – a far slower process.[130] Conventionally, cobalt nitrate hexahydrate ($Co(NO_3)_2.6H_2O$) is used as the cobalt precursor for IWI due to its high solubility in water. This allows for the synthesis of samples of higher loadings without resorting to sequential impregnations, a more time-consuming process. Particularly useful for the metal loadings required for FTS catalysts, which are typically 10–20%. Alternatively, cobalt carbonyl ($Co_2(CO)_8$) has also been used as a cobalt precursor.[131]

Impregnations using $Co_2(CO)_8$ produce catalysts with greater dispersion and higher selectivity than those produced using a cobalt nitrate precursor, however this is at the expense of FTS reaction rates.[54] Another disadvantage of using the $Co_2(CO)_8$ precursor is that impregnations must be performed in a controlled environment, either under vacuum or inert gas, complicating the procedure,[132] as well as the strong toxicity of the compound.[133]

Impregnations can produce catalysts relatively quickly, at low cost, with repeatable metal loadings and are simple to perform from a practical perspective. However, there are major limitations to this method. Impregnations often produce samples with non-uniform dispersion and with large cobalt particle size distributions, which therefore have a less than optimal activity. For example cobalt particles of 6.9 nm with a size distribution of ±2.6 nm on carbon nano-fibre supports were achieved by IWI by den Breejen *et al*.[126] Other limitations include the presence of counter ions from the salt in the samples with can react uncontrollably changing the composition of the samples.[129] The drying stage is also prone to cause sintering of the particles in impregnations as the particles are not yet chemically bonded to the support.

Co-precipitations differ fundamentally from impregnations in that precursors are used for both the support and the cobalt content.[134] The precursors react with each other mixing at an intimate level, causing the cobalt to disperse not only on the surface, but also throughout the bulk of the support. This method allows control of both the metal evolution while simultaneously controlling the support formation process. The presence of the cobalt within the bulk will affect the pore structure of the support (the structure of which is known to affect FTS). Similarly, to impregnations, it is difficult to control particle size distribution using co-precipitations which most often create inhomogeneous samples.

2.4.2. Inverse Micellular Synthesis (IMS)

Inverse micelle synthesis falls under the umbrella term of colloidal methods. These are attractive methods for the synthesis of model catalysts due to the controllability of a range of particle properties. They produce particles of well-defined size and with well-defined surfaces, as the surfactants involved

direct particle growth, limit the maximum size of nanoparticles and prevent agglomeration or precipitation of particles within the solution.[135]

Colloidal methods typically involve the use of a metal precursor (commonly ionic metal salts), a surfactant, a solvent, and a reducing agent. Surfactants are materials which lower the interfacial surface tension between two phases (either two liquid phases or a solid and liquid phase) and are formed of a hydrophilic head and hydrophobic tail. When dissolved in a solvent above a critical aggregation constant (CAC), surfactants self-assemble to form a range of possible shaped structures. Although it is more typical for catalysis applications to use spherical micelles. Metal salts are encapsulated within the micelle and deposited on the support.

The structure of the micelle limits both the size of the nanoparticles and their packing once deposited onto the support. The chain length of the PVP units that comprise the micelle core limit nanoparticle size, and that of the PS chains in the micelle corona limit the proximity of the nanoparticles to one another during deposition.[135] In the case of two-dimensional supports, it is even possible to synthesize nanoparticles in ordered hexagonal arrays, useful for characterisation using grazing incidence scattering techniques (GISAXS/GIWAXS).[136]

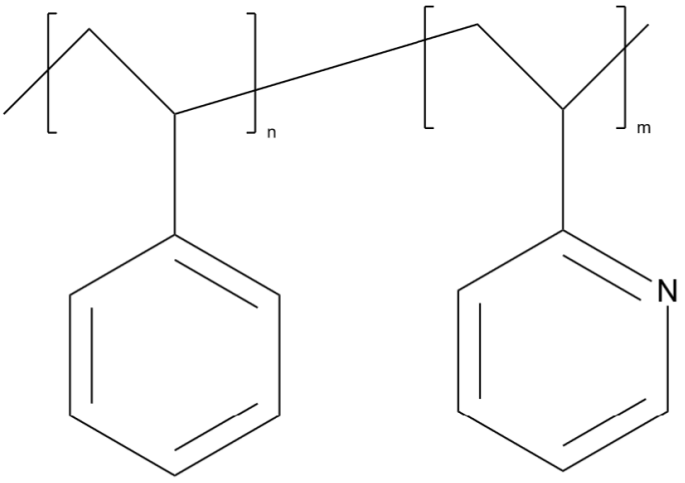

Figure 2.20: Chemical structure of poly(styrene-b-2-vinyl pyridine) - PS-P2VP.

The inverse micelle synthesis discussed in this work used di-block copolymers as the surfactant. A di-block copolymer is formed of multiple

repeating units arranged in two covalently bound blocks. A block copolymer is amphiphillic when the two blocks have widely different affinities for water allowing phase separation to occur. However, as the blocks are covalently bound together full macroscopic phase separation is not possible, only microphase separation, allowing for the formation of complex structures such as micelles. [137] These amphiphillic molecules are typically formed of a hydrophilic group and a hydrophobic group. Poly(styrene-b-2-vinylpyridine) (PS-P2VP) in an example of such a di-block copolymer, the structure of which can be seen in Figure 2.20.

When in aqueous solution and above the critical aggregate concentration (CAC), amphiphillic molecules self-assemble forming complex structures.[137] The structure that is formed is dependent on a range of factors, however the main one determining structure formation when the polymer and its properties used remains constant, is the CAC. The aggregates formed with increasing polymer concentrations are:

$$\text{spherical micelles} \rightarrow \text{cylindrical micelles} \rightarrow \text{bilayers} \rightarrow \text{vesicles}$$

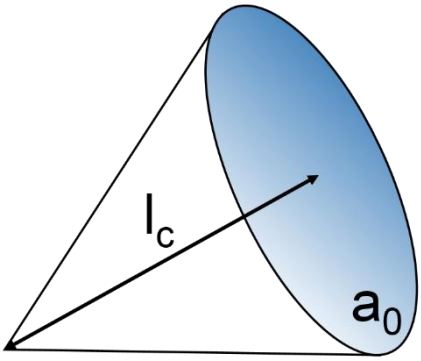

Figure 2.21: Diagram of the shape features exhibited by aggregates in spherical micelles. The shape is defined by the packing parameter N_s.

The type of aggregate formed can be identified by the packing parameter (N_s), which is related to the critical chain length (l_c) and volume (v) of the hydrophobic tail, as well as the optimum area per molecule at the liquid interface (a_0) by equation 2.6.[138] The parameter a_0 is influenced by a range of factors including the size and charge of the hydrophilic group, and the hydration of the same group. In non-polar solvents such as toluene the structures formed are inversed (see Figure 2.22), where the hydrophilic blocks form the core and the

non-polar, hydrophobic blocks the corona. Aggregates form the spherical micelle shape when $N_s \leq 1/3$, the cylindrical micelle shape when $1/3 < N_s \leq 1/2$, bilayers when $1/2 < Ns < 1$, and inverse micelles when $N_s > 1$.[138] In the specialised case of micelles the concentration of assembly is denoted at the critical micelle concentration (CMC).

$$N_s = \frac{v}{l_c a_0} \tag{2.6}$$

A metal precursor can be added to the micelle solution and the metal will be encapsulated within the micelle – in the case of cobalt and PS-PVP, forming ligands between the Co and the VP units.

Once reduced the metal forms nanoparticles effectively capped by the copolymer. When this synthesis is performed using gold the metal can be chemically reduced,[139,140] however performing the synthesis with cobalt requires heating the solution, even with the addition of a reducing agent, which can cause the micelles to distort significantly.[137]

Micellular-based syntheses have been successfully used to produce cobalt FTS catalysts,[141] however block copolymers have rarely been used. Block copolymers form micelles at lower concentrations than other surfactants allowing the formation of smaller nanoparticles at lower loadings. For comparison, the CMC of PS-P2VP is 0.1 mg/mL compared to 94 mg/mL for TTABr.[142] Block copolymer micelles are also more stable and therefore do not require the addition of a stabiliser, as well as being capable of encapsulating a wider range of metals.[143]

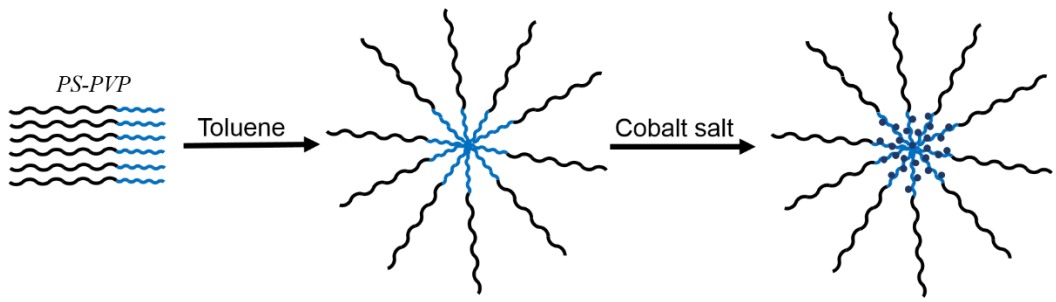

Figure 2.22: Representation of block copolymer micelle showing PVP core and PS shell before the addition of a cobalt salt and after encapsulation of the Co^{2+} ions within the micelle core.

Although occasionally used for the production of cobalt nanoparticles, block co-polymer inverse micelle synthesis (IMS) has mainly been used to produce dispersions of nanoparticles on flat substrates, most commonly using noble metals.[139,140,144] There has been some interest in cobalt nanoparticles produced using block co-polymers, although produced for magnetic applications.[145,146] Most notably Boyen *et al.* in which a two-dimensional array of Co^0 nanoparticles was synthesised.[147] In this study, anhydrous $CoCl_2$ was added to solutions of PS[1700]-P2VP[450] in toluene or mesitylene at a ratio of Co^{2+}/2VP = 0.5, then dip coated onto Si(001) wafers. The samples were then plasma treated in O_2 for 5-15 min at a pressure of 0.005 mbar and power of 50 W removing the polymer matrix, removing the Cl_2 and oxidising the cobalt cores. The samples were then reduced by H_2 plasma treatment. This method was capable of producing cobalt nanoparticles of 3.6 nm with a particle size distribution of 0.8 nm (determined by AFM).

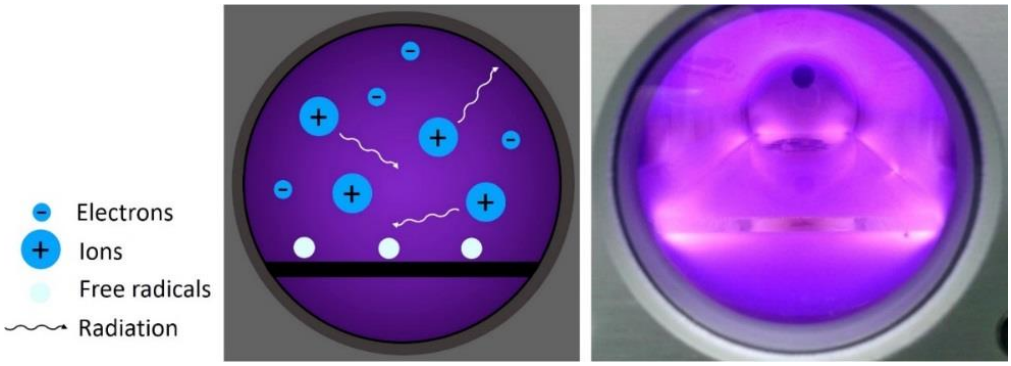

Figure 2.23: *Schematic and photograph of glow discharge plasma.*

The final step in the synthesis involves the removal of the polymer from the sample, which can be achieved by plasma treatment or by more conventional thermal treatment.[140,148,149] Plasma treatment was used to decompose the cobalt salt and remove the residual polymer.[140]

Plasma is a state of matter comprised of atoms, molecules, ions, photons, electrons, free radicals and metastables, and as such has a high internal energy which is transferred to the surface of the sample as it is bombarded by the plasma (Figure 2.23). Glow discharge plasmas are generated by applying a RF field across a low-pressure gas, which also generates UV and visible EM radiation.

The polymer is removed from the samples mostly by UV degradation, and interactions with radicals and ions. The cobalt salt is decomposed by the electron bombardment and then oxidised by the oxygen present in the plasma. The treatment is achieved at low temperatures (>70 °C) therefore sintering of the nanoparticles is minimal.

2.5. Summary

The theme that runs through all chapters within this work is the importance of Co^0 particle size, both its effect on FTS under reaction conditions and its control using novel preparation methods.

Within this thesis two methods are used to synthesize Co/SiO_2 catalysts: an inverse micelle synthesis (IMS), and a standard Schlenk technique performed under an argon atmosphere and provided by S.K. Beaumont (Durham University). Both attempting to tightly control the particles size of the catalyst for further investigation of size effects.

Although particle size effects have been well studied, there still remains quite significant gaps in the understanding of how these effects evolve with time on stream under reaction conditions as the catalyst particles are not wholly stable, displaying some phase evolution with time on stream. *In situ* studies using SR-based characterisation techniques are well suited to observing these properties.

2.6. References

1 J. J. Herbert, P. Senecal, D. J. Martin, W. Bras, S. K. Beaumont and A. M. Beale, *Catal. Sci. Technol.*, 2016, **6**, 5773–5791.
2 M. D. Argyle, T. S. Frost and C. H. Bartholomew, *Top. Catal.*, 2014, **57**, 415–429.
3 J. van de Loosdrecht, B. Balzhinimaev, J.-A. Dalmon, J. W. Niemantsverdriet, S. V. Tsybulya, A. M. Saib, P. J. van Berge and J. L. Visagie, *Catal. Today*, 2007, **123**, 293–302.
4 E. Rytter and A. Holmen, *ACS Catal.*, 2017, **7**, 5321–5328.
5 N. E. Tsakoumis, M. Rønning, Ø. Borg, E. Rytter and A. Holmen, *Catal. Today*, 2010, **154**, 162–182.
6 A. K. Dalai and B. H. Davis, *Appl. Catal. A Gen.*, 2008, **348**, 1–15.
7 P. Bolt, University of Utrecht, 1994.
8 G. Jacobs, T. K. Das, P. M. Patterson, J. Li, L. Sanchez and B. H. Davis, *Appl. Catal. A Gen.*, 2003, **247**, 335–343.
9 M. Wolf, E. K. Gibson, E. J. Olivier, J. H. Neethling, C. R. A. Catlow, N. Fischer

and M. Claeys, *Catal. Today*, 2020, **342**, 71–78.
10 M. Wolf, E. K. Gibson, E. J. Olivier, J. H. Neethling, C. R. A. Catlow, N. Fischer and M. Claeys, *ACS Catal.*, 2019, **9**, 4902–4918.
11 M. Wolf, H. Kotzé, N. Fischer and M. Claeys, *Faraday Discuss.*, 2017, **197**, 243–268.
12 A. M. Hilmen, D. Schanke, K. F. Hanssen and A. Holmen, *Appl. Catal. A Gen.*, 1999, **186**, 169–188.
13 P. J. van Berge, J. van de Loosdrecht, S. Barradas and A. M. van der Kraan, *Catal. Today*, 2000, **58**, 321–334.
14 M. W. J. Crajé, A. M. Van der Kraan, J. Van de Loosdrecht and P. J. Van Berge, *Catal. Today*, 2002, **71**, 369–379.
15 C. Hou, G. Xia, X. Sun, Y. Wu, C. Jin, Z. Yan, M. Li, Z. Hu, H. Nie and D. Li, *Catal. Today*, 2016, **264**, 91–97.
16 E. van Steen, M. Claeys, M. E. Dry, J. van de Loosdrecht, E. L. Viljoen and J. L. Visagie, *J. Phys. Chem. B*, 2005, **109**, 3575–7.
17 A. Longo, L. Sciortino, F. Giannici and A. Martorana, *J. Appl. Crystallogr.*, 2014, **47**, 1562–1568.
18 G. Jacobs, T. K. Das, Y. Zhang, J. Li, G. Racoillet and B. H. Davis, *Appl. Catal. A Gen.*, 2002, **233**, 263–281.
19 M. Argyle and C. Bartholomew, *Catalysts*, 2015, **5**, 145–269.
20 J. A. Moulijn, A. E. Van Diepen and F. Kapteijn, *Appl. Catal. A Gen.*, 2001, **212**, 3–16.
21 P. R. Couchman and W. A. Jesser, *Nature*, 1977, **269**, 481–483.
22 M. Wolf, B. K. Mutuma, N. J. Coville, N. Fischer and M. Claeys, *ACS Catal.*, 2018, **8**, 3985–3989.
23 E. Rytter, N. E. Tsakoumis and A. Holmen, *Catal. Today*, 2016, **261**, 3–16.
24 US Patent, US8773118B2, 2014.
25 N. Fischer, B. Clapham, T. Feltes, E. van Steen and M. Claeys, *Angew. Chemie Int. Ed.*, 2014, **53**, 1342–1345.
26 M. Claeys, M. E. Dry, E. Van Steen, P. J. Van Berge, S. Booyens, R. Crous, P. Van Helden, J. Labuschagne, D. J. Moodley and A. M. Saib, *ACS Catal.*, 2015, **5**, 841–852.
27 M. Wolf, N. Fischer and M. Claeys, *Catal. Today*, 2016, **275**, 135–140.
28 L. Fratalocchi, C. G. Visconti, L. Lietti, N. Fischer and M. Claeys, *Appl. Catal. A Gen.*, 2018, **556**, 92–103.
29 P. van Helden, F. Prinsloo, J. A. van den Berg, B. Xaba, W. Erasmus, M. Claeys and J. van de Loosdrecht, *Catal. Today*, 2020, **342**, 88–98.
30 M. Wolf, N. Fischer and M. Claeys, *J. Catal.*, 2019, **374**, 199–207.
31 G. L. Bezemer, J. H. Bitter, H. Kuipers, H. Oosterbeek, J. E. Holewijn, X. Xu, F. Kapteijn, A. J. van Dillen, K. P. de Jong, A. J. Van Diilen and K. P. de Jong, *J. Am. Chem. Soc.*, 2006, **128**, 3956–3964.
32 I. Chorkendorff; and J. W. Niemantsverdriet, Eds., *Wiley: Concepts of Modern Catalysis and Kinetics, 2nd, Revised and Enlarged Edition* -, Wiley, 2nd edn., 2006.
33 P. Senecal, S. D. M. Jacques, M. Di Michiel, S. A. J. Kimber, A. Vamvakeros, Y. Odarchenko, I. Lezcano-Gonzalez, J. Paterson, E. Ferguson and A. M. Beale, *ACS Catal.*, 2017, **7**, 2284–2293.
34 T. M. Eggenhuisen, J. P. Den Breejen, D. Verdoes, P. E. De Jongh and K. P. De Jong, *J. Am. Chem. Soc.*, 2010, **132**, 18318–18325.
35 E. Rytter and A. Holmen, *Catalysts*, 2015, **5**, 478–499.
36 S. D. M. Jacques, O. Leynaud, D. Strusevich, P. Stukas, P. Barnes, G. Sankar, M. Sheehy, M. G. O'Brien, A. Iglesias-Juez and A. M. Beale, *Catal. Today*, 2009, **145**, 204–212.
37 M. Behrens and R. Schlögl, in *Characterization of Solid Materials and Heterogeneous Catalysts*, Wiley-VCH Verlag GmbH & Co. KGaA, 2012, pp. 609–

653.
38 K. H. Cats and B. M. Weckhuysen, *ChemCatChem*, 2016, **8**, 1531–1542.
39 S. Rane, Ø. Borg, E. Rytter and A. Holmen, *Appl. Catal. A Gen.*, 2012, **437**–**438**, 10–17.
40 W. Zhou, J.-G. Chen, K.-G. Fang and Y.-H. Sun, *Fuel Process. Technol.*, 2006, **87**, 609–616.
41 A. M. Saib, D. J. Moodley, I. M. Ciobîcă, M. M. Hauman, B. H. Sigwebela, C. J. Weststrate, J. W. Niemantsverdriet and J. van de Loosdrecht, *Catal. Today*, 2010, **154**, 271–282.
42 A. M. Beale, S. D. M. Jacques and B. M. Weckhuysen, *Chem. Soc. Rev.*, 2010, **39**, 4656–72.
43 J. D. Grunwaldt and C. G. Schroer, *Chem. Soc. Rev.*, 2010, **39**, 4741–53.
44 D. Grandjean, A. M. Beale, A. V Petukhov and B. M. Weckhuysen, *J. Am. Chem. Soc.*, 2005, **127**, 14454–65.
45 S. W. T. Price, D. J. Martin, A. D. Parsons, W. A. Sławiński, A. Vamvakeros, S. J. Keylock, A. M. Beale and J. F. W. Mosselmans, *Sci. Adv.*, 2017, **3**, e1602838.
46 A. Vamvakeros, S. D. M. Jacques, V. Middelkoop, M. Di Michiel, C. K. Egan, I. Z. Ismagilov, G. B. M. Vaughan, F. Gallucci, M. van Sint Annaland, P. R. Shearing, R. J. Cernik and A. M. Beale, *Chem. Commun.*, 2015, **51**, 12752–12755.
47 Ø. Borg, N. Hammer, S. Eri, O. A. Lindvåg, R. Myrstad, E. a. Blekkan, M. Rønning, E. Rytter and A. Holmen, *Catal. Today*, 2009, **142**, 70–77.
48 H. Karaca, O. V. Safonova, S. Chambrey, P. Fongarland, P. Roussel, A. Griboval-Constant, M. Lacroix and A. Y. Khodakov, *J. Catal.*, 2011, **277**, 14–26.
49 W. Chu, P. Chernavskii, L. Gengembre, G. Pankina, P. Fongarland and A. Khodakov, *J. Catal.*, 2007, **252**, 215–230.
50 N. E. Tsakoumis, A. Voronov, M. Rønning, W. Van Beek, Ø. Borg, E. Rytter and A. Holmen, *J. Catal.*, 2012, **291**, 138–148.
51 M. Rønning, N. E. Tsakoumis, A. Voronov, R. E. Johnsen, P. Norby, W. van Beek, Ø. Borg, E. Rytter and A. Holmen, *Catal. Today*, 2010, **155**, 289–295.
52 W. van Beek, O. V. Safonova, G. Wiker and H. Emerich, *Phase Transitions*, 2011, **84**, 726–732.
53 S. Nikitenko, A. M. Beale, A. M. J. van der Eerden, S. D. M. Jacques, O. Leynaud, M. G. O'Brien, D. Detollenaere, R. Kaptein, B. M. Weckhuysen and W. Bras, *J. Synchrotron Radiat.*, 2008, **15**, 632–640.
54 A. Y. Khodakov, W. Chu and P. Fongarland, *Chem. Rev.*, 2007, **107**, 1692–744.
55 M. Sadeqzadeh, H. Karaca, O. V. Safonova, P. Fongarland, S. Chambrey, P. Roussel, a. Griboval-Constant, M. Lacroix, D. Curulla-Ferré, F. Luck and a. Y. Khodakov, *Catal. Today*, 2011, **164**, 62–67.
56 H. Karaca, J. Hong, P. Fongarland, P. Roussel, A. Griboval-Constant, M. Lacroix, K. Hortmann, O. V Safonova and A. Y. Khodakov, *Chem. Commun. (Camb).*, 2010, **46**, 788–90.
57 O. Ducreux, B. Rebours, J. Lynch, M. Roy-Auberger and D. Bazin, *Oil Gas Sci. Technol. - Rev. l'IFP*, 2008, **64**, 49–62.
58 Z.-P. Liu and P. Hu, *J. Am. Chem. Soc.*, 2003, **125**, 1958–67.
59 M. K. Gnanamani, G. Jacobs, W. D. Shafer and B. H. Davis, *Catal. Today*, 2013, **215**, 13–17.
60 V. V. Matveev, D. A. Baranov, G. Y. Yurkov, N. G. Akatiev, I. P. Dotsenko and S. P. Gubin, *Chem. Phys. Lett.*, 2006, **422**, 402–405.
61 S. Alayoglu, P. Zavalij, B. Eichhorn, Q. Wang, A. I. Frenkel and P. Chupas, *ACS Nano*, 2009, **3**, 3127–37.
62 S. J. L. Billinge, *J. Solid State Chem.*, 2008, **181**, 1695–1700.
63 C. L. Farrow, P. Juhas, J. W. Liu, D. Bryndin, E. S. Božin, J. Bloch, T. Proffen and S. J. L. Billinge, *J. Phys. Condens. Matter*, 2007, **19**, 335219.
64 H. E. du Plessis, R. P. Forbes, W. Barnard, W. J. Erasmus and A. Steuwer, *Phys. Chem. Chem. Phys.*, 2013, **15**, 11640–5.

65 A. M. Beale and G. Sankar, *Chem. Mater.*, 2006, **18**, 263–272.
66 J. M. Thomas, G. N. Greaves, G. Sankar, P. A. Wright, J. Chen, A. J. Dent and L. Marchese, *Angew. Chemie Int. Ed. English*, 1994, **33**, 1871–1873.
67 K. Høydalsvik, J. B. Fløystad, A. Voronov, G. J. B. Voss, M. Esmaeili, J. Kehres, H. Granlund, U. Vainio, J. W. Andreasen, M. Rønning and D. W. Breiby, *J. Phys. Chem. C*, 2014, **118**, 2399–2407.
68 G. Bergeret and P. Gallezot, in *Handbook of Heterogeneous Catalysis*, Wiley-VCH Verlag GmbH & Co. KGaA, 2008.
69 Z. Sun, B. Sun, M. Qiao, J. Wei, Q. Yue, C. Wang, Y. Deng, S. Kaliaguine and D. Zhao, *J. Am. Chem. Soc.*, 2012, **134**, 17653–60.
70 H. Borchert, E. V. Shevchenko, A. Robert, I. Mekis, A. Kornowski, G. Grübel and H. Weller, *Langmuir*, 2005, **21**, 1931–6.
71 W. Bras, I. P. Dolbnya, D. Detollenaere, R. van Tol, M. Malfois, G. N. Greaves, A. J. Ryan and E. Heeley, *J. Appl. Crystallogr.*, 2003, **36**, 791–794.
72 H. Guan, X. Wang, H. Li, C. Zhi, T. Zhai, Y. Bando and D. Golberg, *Chem. Commun.*, 2012, **48**, 4878.
73 P. H. T. Ngamou and N. Bahlawane, *Chem. Mater.*, 2010, **22**, 4158–4165.
74 L. E. Iton, I. Choi, J. A. Desjardins and V. A. Maroni, 1989, **9**, 535–538.
75 A. Singh and L. Spiccia, *Coord. Chem. Rev.*, 2013, **257**, 2607–2622.
76 N. Osakoo, R. Henkel, S. Loiha, F. Roessner and J. Wittayakun, *Appl. Catal. A Gen.*, 2013, **464**–**465**, 269–280.
77 G. Jacobs, J. A. Chaney, P. M. Patterson, T. K. Das, J. C. Maillot and B. H. Davis, *J. Synchrotron Radiat.*, 2004, **11**, 414–22.
78 A. A. Verberckmoes, B. M. Weckhuysen and R. A. Schoonheydt, *Microporous Mesoporous Mater.*, 1998, **22**, 165–178.
79 A. Y. Khodakov, A. Griboval-Constant, R. Bechara and V. L. Zholobenko, *J. Catal.*, 2002, **206**, 230–241.
80 F. P. J. M. Kerkhof and J. A. Moulijn, *J. Phys. Chem.*, 1979, **83**, 1612–1619.
81 M. P. Seah and W. A. Dench, *Surf. Interface Anal.*, 1979, **1**, 2–11.
82 J. H. Scofield, *J. Electron Spectros. Relat. Phenomena*, 1976, **8**, 129–137.
83 D. G. Castner, P. R. Watson and I. Y. Chan, *J. Phys. Chem.*, 1989, **93**, 3188–3194.
84 H.-J. Freund, H. Kuhlenbeck, J. Libuda, G. Rupprechter, M. Bäumer and H. Hamann, *Top. Catal.*, 2001, **15**, 201–209.
85 D. F. Ogletree, H. Bluhm, G. Lebedev, C. S. Fadley, Z. Hussain and M. Salmeron, *Rev. Sci. Instrum.*, 2002, **73**, 3872.
86 S. K. Beaumont, S. Alayoglu, V. V. Pushkarev, Z. Liu, N. Kruse and G. A. Somorjai, *Faraday Discuss.*, 2013, **162**, 31.
87 V. Papaefthimiou, T. Dintzer, V. Dupuis, A. Tamion, F. Tournus, A. Hillion, D. Teschner, M. Hävecker, A. Knop-Gericke, R. Schlögl and S. Zafeiratos, *ACS Nano*, 2011, **5**, 2182–90.
88 S. Alayoglu, S. K. Beaumont, F. Zheng, V. V. Pushkarev, H. Zheng, V. Iablokov, Z. Liu, J. Guo, N. Kruse and G. A. Somorjai, *Top. Catal.*, 2011, **54**, 778–785.
89 F. De Groot, *Chem. Rev.*, 2001, 101, 1779–1808.
90 M. Fernández-García, *Catal. Rev.*, 2002, **44**, 59–121.
91 G. Jacobs, W. Ma, P. Gao, B. Todic, T. Bhatelia, D. B. Bukur and B. H. Davis, *Catal. Today*, 2013, **214**, 100–139.
92 A. Rochet, V. Moizan, C. Pichon, F. Diehl, A. Berliet and V. Briois, *Catal. Today*, 2011, **171**, 186–191.
93 A. M. Saib, A. Borgna, J. van de Loosdrecht, P. J. van Berge and J. W. Niemantsverdriet, *J. Phys. Chem. B*, 2006, **110**, 8657–64.
94 G. Kwak, M. H. Woo, S. C. Kang, H. G. Park, Y. J. Lee, K. W. Jun and K. S. Ha, *J. Catal.*, 2013, **307**, 27–36.
95 A. M. Beale and B. M. Weckhuysen, *Phys. Chem. Chem. Phys.*, 2010, **12**, 5562–74.

96 J. C. Mohandas, M. K. Gnanamani, G. Jacobs, W. Ma, Y. Ji, S. Khalid and B. H. Davis, *ACS Catal.*, 2011, **1**, 1581–1588.
97 D. J. Moodley, A. M. Saib, J. van de Loosdrecht, C. A. Welker-Nieuwoudt, B. H. Sigwebela and J. W. Niemantsverdriet, *Catal. Today*, 2011, **171**, 192–200.
98 G. Jacobs, P. M. Patterson, T. K. Das, M. Luo and B. H. Davis, *Appl. Catal. A Gen.*, 2004, **270**, 65–76.
99 M. Benfatto, C. R. Natoli, A. Bianconi, J. Garcia, A. Marcelli, M. Fanfoni and I. Davoli, *Phys. Rev. B*, 1986, **34**, 5774–5781.
100 D. C. Edwards and S. C. B. Myneni, *J. Phys. Chem. A*, 2005, **109**, 10249–56.
101 F. Morales, F. M. F. de Groot, P. Glatzel, E. Kleimenov, H. Bluhm, M. Hävecker, A. Knop-Gericke and B. M. Weckhuysen, *J. Phys. Chem. B*, 2004, **108**, 16201–16207.
102 S. Alayoglu, S. K. Beaumont, G. Melaet, A. E. Lindeman, N. Musselwhite, C. J. Brooks, M. A. Marcus, J. Guo, Z. Liu, N. Kruse and G. A. Somorjai, *J. Phys. Chem. C*, 2013, **117**, 21803–21809.
103 G. A. Somorjai, S. K. Beaumont and S. Alayoglu, *Angew. Chem. Int. Ed. Engl.*, 2011, **50**, 10116–29.
104 T. Herranz, X. Deng, A. Cabot, J. Guo and M. Salmeron, *J. Phys. Chem. B*, 2009, **113**, 10721–7.
105 A. Tuxen, S. Carenco, M. Chintapalli, C.-H. Chuang, C. Escudero, E. Pach, P. Jiang, F. Borondics, B. Beberwyck, A. P. Alivisatos, G. Thornton, W.-F. Pong, J. Guo, R. Perez, F. Besenbacher and M. Salmeron, *J. Am. Chem. Soc.*, 2013, **135**, 2273–8.
106 V. F. Puntes, K. M. Krishnan and A. P. Alivisatos, *Science*, 2001, **291**, 2115–7.
107 V. Iablokov, S. K. Beaumont, S. Alayoglu, V. V. Pushkarev, C. Specht, J. Gao, A. P. Alivisatos, N. Kruse and G. A. Somorjai, *Nano Lett.*, 2012, **12**, 3091–3096.
108 Z. Yan, Z. Wang, D. B. Bukur and D. W. Goodman, *J. Catal.*, 2009, **268**, 196–200.
109 O. R. Inderwildi, S. J. Jenkins and D. A. King, *J. Phys. Chem. C*, 2008, **112**, 1305–1307.
110 F. Zheng, S. Alayoglu, J. Guo, V. Pushkarev, Y. Li, P.-A. Glans, J. Chen and G. Somorjai, *Nano Lett.*, 2011, **11**, 847–53.
111 S. K. Beaumont, S. Alayoglu, C. Specht, W. D. Michalak, V. V Pushkarev, J. Guo, N. Kruse and G. A. Somorjai, *J. Am. Chem. Soc.*, 2014, **136**, 9898–901.
112 G. Melaet, W. T. Ralston, C.-S. Li, S. Alayoglu, K. An, N. Musselwhite, B. Kalkan and G. A. Somorjai, *J. Am. Chem. Soc.*, 2014, **136**, 2260–3.
113 K. H. Cats, I. D. Gonzalez-Jimenez, Y. Liu, J. Nelson, D. van Campen, F. Meirer, A. M. J. van der Eerden, F. M. F. de Groot, J. C. Andrews and B. M. Weckhuysen, *Chem. Commun. (Camb).*, 2013, **49**, 4622–4.
114 B. Ernst, A. Bensaddik, L. Hilaire, P. Chaumette and A. Kiennemann, *Catal. Today*, 1998, **39**, 329–341.
115 A. Y. Khodakov, J. Lynch, D. Bazin, B. Rebours, N. Zanier, B. Moisson and P. Chaumette, *J. Catal.*, 1997, **168**, 16–25.
116 D. G. Castner, P. R. Watson and I. Y. Chan, *J. Phys. Chem.*, 1990, **94**, 3188–3194.
117 R. Bechara, D. Balloy, J.-Y. Dauphin and J. Grimblot, *Chem. Mater.*, 1999, **11**, 1703–1711.
118 K. H. Cats, J. C. Andrews, O. Stéphan, K. March, C. Karunakaran, F. Meirer, F. M. F. de Groot and B. M. Weckhuysen, *Catal. Sci. Technol.*, 2016, **6**, 4438–4449.
119 V. A. de la P. O'Shea, M. C. Á. Galván, A. E. P. Prats, J. M. Campos-Martin and J. L. G. Fierro, *Chem. Commun. (Camb).*, 2011, **47**, 7131–3.
120 R. P. Galhenage, H. Yan, S. A. Tenney, N. Park, G. Henkelman, P. Albrecht, D. R. Mullins and D. A. Chen, *J. Phys. Chem. C*, 2013, **117**, 7191–7201.
121 A. I. Frenkel, J. A. Rodriguez and J. G. Chen, *ACS Catal.*, 2012, **2**, 2269–2280.
122 L. J. France, P. P. Edwards, V. L. Kuznetsov and H. Almegren, *Carbon Dioxide Util.*, 2015, 161–182.

123 H. MING and B. BAKER, *Appl. Catal. A Gen.*, 1995, **123**, 23–36.
124 J. Girardon, E. Quinet, A. Gribovalconstant, P. Chernavskii, L. Gengembre and A. Khodakov, *J. Catal.*, 2007, **248**, 143–157.
125 A. A. Khassin, T. M. Yurieva, V. V. Kaichev, V. I. Bukhtiyarov, A. A. Budneva, E. A. Paukshtis and V. N. Parmon, *J. Mol. Catal. A Chem.*, 2001, **175**, 189–204.
126 J. P. den Breejen, J. R. A. Sietsma, H. Friedrich, J. H. Bitter and K. P. de Jong, *J. Catal.*, 2010, **270**, 146–152.
127 J.-S. Girardon, A. Constant-Griboval, L. Gengembre, P. A. Chernavskii and A. Y. Khodakov, *Catal. Today*, 2005, **106**, 161–165.
128 G. Jacobs, P. M. Patterson, Y. Zhang, T. Das, J. Li and B. H. Davis, *Appl. Catal. A Gen.*, 2002, **233**, 215–226.
129 K. P. de Jong, Ed., *Synthesis of Solid Catalysts*, Wiley-VCH Verlag GmbH & Co. KGaA, Weinheim, Germany, 2009.
130 P. Serp and E. Castillejos, *ChemCatChem*, 2010, **2**, 41–47.
131 D. C. Bailey and S. H. Langer, *Chem. Rev.*, 1981, **81**, 109–148.
132 H. P. Withers, K. F. Eliezer and J. W. Mitchell, *Ind. Eng. Chem. Res.*, 1990, **29**, 1807–1814.
133 Fisher Scientific, 2018, CAS-No: 10210-68-1.
134 D. Carta, G. Mountjoy, G. Navarra, M. F. Casula, D. Loche, S. Marras and A. Corrias, *J. Phys. Chem. C*, 2007, **111**, 6308–6317.
135 D. James Martin, D. Decarolis, Y. I. Odarchenko, J. J. Herbert, T. Arnold, J. Rawle, C. Nicklin, H. G. Boyen and A. M. Beale, *Chem. Commun.*, 2017, **53**, 5159–5162.
136 D. J. Martin, D. Decarolis, R. Tucoulou, G. Martínez-Criado and A. M. Beale, *Catal. Struct. React.*, 2017, **3**, 63–70.
137 R. A. L. Jones, *Soft Condensed Matter*, Oxford University Press, 2002.
138 M. J. Rosen, in *Surfactants and Interfacial Phenomena*, John Wiley & Sons, Inc., 2004, pp. 105–177.
139 J. P. Spatz, S. Mößmer and M. Möller, *Chem. - A Eur. J.*, 1996, **2**, 1552–1555.
140 J. P. Spatz, S. Mo, C. Hartmann, M. Mo, D.- Ulm, T. Herzog, M. Krieger, H. Boyen, P. Ziemann and F. Ju, *Langmuir*, 2000, **16 (2)**, 407–415.
141 J. P. Chen, K. M. Lee, C. M. Sorensen, K. J. Klabunde and G. C. Hadjipanayis, *J. Appl. Phys.*, 1994, **75**, 5876.
142 A. Dominguez, A. Fernandez, N. Gonzalez, E. Iglesias and L. Montenegro, *J. Chem. Educ.*, 1997, **74**, 1227.
143 G. Kästle, H.-G. Boyen, F. Weigl, G. Lengl, T. Herzog, P. Ziemann, S. Riethmüller, O. Mayer, C. Hartmann, J. P. Spatz, M. Möller, M. Ozawa, F. Banhart, M. G. Garnier and P. Oelhafen, *Adv. Funct. Mater.*, 2003, **13**, 853–861.
144 S. Mossmer, J. P. Spatz, M. Moller, T. Aberle, J. Schmidt and W. Burchard, *Macromol. Rapid Commun.*, 2000, **33**, 4791–4798.
145 O. A. Platonova, L. M. Bronstein, S. P. Solodovnikov, I. M. Yanovskaya, E. S. Obolonkova, P. M. Valetsky, E. Wenz and M. Antonietti, *Colloid Polym. Sci.*, 1997, **275**, 426–431.
146 G. Liu, X. Yan, Z. Lu, S. A. Curda and J. Lal, *Chem. Mater.*, 2005, **17**, 4985–4991.
147 H.-G. Boyen, G. Kästle, K. Zürn, T. Herzog, F. Weigl, P. Ziemann, O. Mayer, C. Jerome, M. Möller, J. P. Spatz, M. G. Garnier and P. Oelhafen, *Adv. Funct. Mater.*, 2003, **13**, 359–364.
148 T. Pietsch, P. Müller-Buschbaum, B. Mahltig and A. Fahmi, *ACS Appl. Mater. Interfaces*, 2015, **7**, 12440–12449.
149 B. P. Bastakoti, Y. Li, T. Kimura and Y. Yamauchi, *Small*, 2015, **11**, 1992–2002.

3. Methodology

3.1. X-Ray Characterisation Techniques

3.1.1. X-Ray Sources

X-ray characterisation is fundamental to this work. All experimental chapters contain at least some form of X-ray technique; either laboratory or synchrotron-based. Synchrotron radiation (SR) sources are large central facilities such as the European Synchrotron Facility (ESRF), Grenoble, France (Figure 3.1). The key properties of X-ray radiation from SR sources are a very high photon flux, radiation that is highly collimated, polarised, and energy tuneable.[1] This often results in superior time and spatial resolution than can be achieved using lab-based sources. However, diffractometers or spectrometers that use laboratory sources are more freely available than beamtime at central synchrotron facilities, and certainly have their place in characterisation.

Figure 3.1: Photograph of the ESRF (European Synchrotron Radiation Facility), Grenoble, France.[2]

X-ray tubes are the typical source of choice for lab-based techniques. X-rays are generated via cathode ray tubes by the acceleration of electrons - emitted from a filament (cathode) - across a vacuum between the cathode and anode.[3] The electrons then collide with the material of the anode and, at high

enough energies, dislodge inner shell electrons generating X-ray spectra characteristic of the anode material. The spectra consist of Kα (both $K_{\alpha 1}$ and $K_{\alpha 2}$), K_β radiation and significantly less intense bremsstrahlung (breaking) radiation.[3]

XRD is by far the most common laboratory-based X-ray technique, although lab-SAXS and lab-XAS (X-ray Absorption Spectroscopy) are also achievable.[4] In X-Ray diffraction (XRD) and Small Angle X-ray Scattering (SAXS) diffractometers, filters and monochromators are then used to remove the K_β and bremsstrahlung radiation. The remaining X-ray beam is then collimated and focused onto the sample.[3] The potential q-range and resolution of lab-SAXS is limited by both the available wavelengths of laboratory X-ray sources and the small sample-detector distance in lab-diffractometers.[5] XAS measurements, however, require a continuum of wavelengths, which is achieved in lab-based experiments using the bremsstrahlung radiation produced by conventional laboratory sources.[4] However, the energy range is limited and spectra produced by such sources have poorer energy resolution and significantly poorer X-ray flux than that of SR experiments.[6]

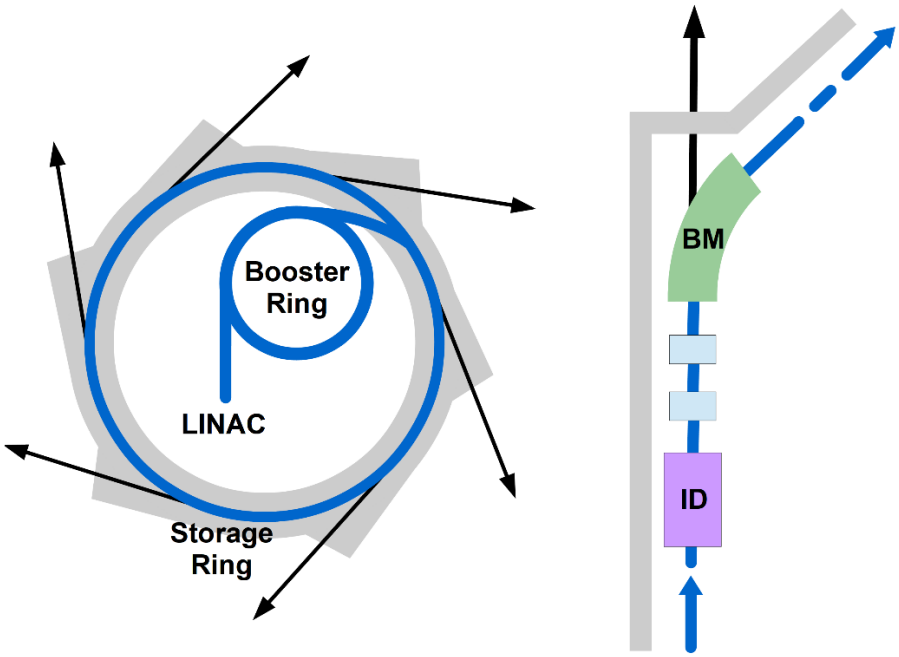

Figure 3.2: Left) Simplified diagram of a synchrotron radiation facility: linear accelerator (LINAC), booster and storage ring. The blue lines indicate the path of the electrons, and the black arrows the path of the X-rays generated by bending magnets (BM) or insertion devices (ID). Right) Diagram of ID in the storage ring, including quadrupole and sextuples (light blue rectangles).

Synchrotron sources, however, are particle accelerators which generate X-rays via varying the trajectory of a charged particle (typically electrons) travelling at relativistic velocities using strong magnetic fields. At synchrotrons, electrons are first produced by an electron gun, which functions in a similar manner to the X-ray tubes described above. Then the electrons are passed into a linear accelerator (LINAC) to be pre-accelerated and the stream of electrons is cut into bunches. From here the electron bunches are then injected into the booster ring for further acceleration, at which point the electron bunches are accelerated using dipole magnets and forced into a finer beam by quadrupole magnets. The beam is then in turn injected into the storage ring. Although described as a ring, the storage ring is in fact a series of straight sections linked by bending magnets that correspond to different beamlines around the ring (as well as straight sections dedicated to electron injection and RF-generators which compensate for energy lost from the electron beam when passing though bending magnets and insertion devices).[7]

Before each beamline is an X-ray source, either a bending magnet (BM) or insertion device (ID) — either an undulator or a wiggler. Figure 3.2b shows an ID line source, bending magnets are necessary even on ID lines to maintain the pseudo-circular orbit of the electrons and to separate the X-ray beams. A BM line would have a similar set-up to Figure 3.2b but excluding the insertion device. Bending magnets are large electro-magnets which exert a uniform magnetic field on the electron bunches, causing them to bend while generating a wide fan of X-rays covering a broad spectrum.

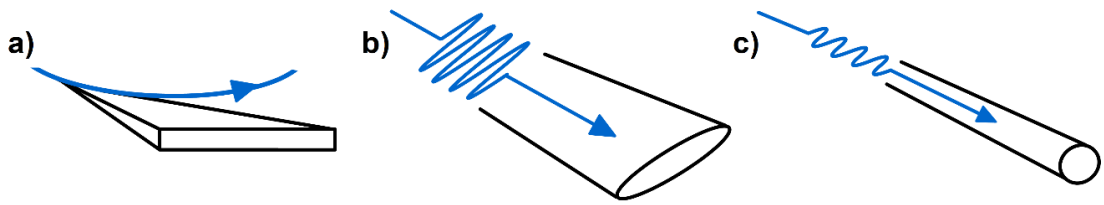

Figure 3.3: Simplified diagram of the electron trajectory through and X-ray profile generated by a) bending magnets, b) a wiggler, and c) an undulator.

Insertion devices use the same principle to generate X-rays, however, take the form of a periodic structure of small bending magnets of identical length. In a

wiggler the electron trajectory at each wiggle has a tighter curvature than bending magnets (see Figure 3.3), resulting in a greater radial acceleration and therefore producing harder x-rays, but with a similar spectrum to that produced by bending magnets.

Undulators, on the other hand, use magnets of weaker fields, each pole of which has an individual radiation emission which constructively and destructively interfere to create a narrower spectrum than wigglers, but of greater spectral brightness. The greater number of magnets increase the intensity of the radiation and the smaller bending radius shift the critical energy as well as increasing the spectral brightness.[7]

Table 3.1: Brief list of synchrotrons – comparison of energy and circumference.[8]

Synchrotron Facility	Location	Energy (GeV)	Circumference (m)
European Synchrotron Radiation Facility (ESRF)	France	6	844
Diamond Light Source	UK	3	562
SOLEIL	France	3	354
Australian Synchrotron	Australia	3	216
Spring-8	Japan	8	1436
National Synchrotron Light Source (NSLS-II)	USA	3	792

A brief list of some third-generation synchrotrons from around the world are presented in Table 3.1. All the experiments performed in this work were carried out at the ESRF, primarily on the Dutch-Belgian beamline.

3.1.2. DUBBLE BEAMLINE

The Dutch-Belgium beamline (DUBBLE/BM26) is a collaborative research group (CRG) beamline at the ESRF, jointly funded by the Dutch and Belgium research councils (NWO and FWO).[9] CRG beamlines run independently of the ESRF but compensate the ESRF for the provision of photons by dedicating 30% of their beamtime to the ESRF public user program.

DUBBLE is sourced by a bending magnet and is a branch line consisting of a SAXS/WAXS (BM26B) and an XAS (BM26A) line. The radiation fan from the

bending magnet is separated for these two branches using a splitter. The harder X-rays closer to the curvature of the ring are used for the SAXS/WAXS branch and the softer X-rays are given to the XAS branch. All XAS data presented in this work were obtained during experiments performed on the DUBBLE XAS line (BM26A).

A diagram of BM26A specific optics is shown in Figure 3 4 – the bending magnet and splitter are not included. First is a set of slits, which controls the divergence of the X-ray beam in the vertical and horizontal directions, (other slits in the system clean up and shape the beam after each optical component). After the first set of slits comes a collimating mirror with silicon and platinum strips, which parallelises the beam reducing divergence, and consequently also reduces the bandwidth transmitted by the monochromator that follows. The two coatings allow for the prevention of higher harmonics associated with one coating in the beam without having to change mirror angles, only by translating the mirror laterally to the other coating. The operating energies for the Si coating is 5-12 keV, and that of the Pt coating is 12-30 keV.

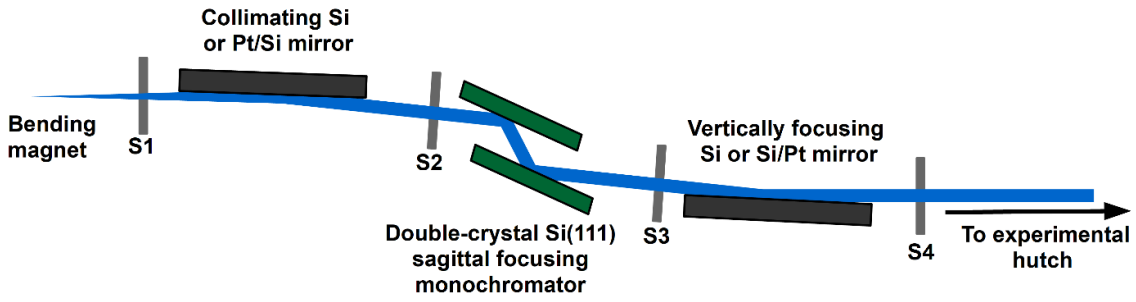

Figure 3 4: Diagram of the optics of BM26A. The dark grey blocks represent mirrors, the green blocks the double-crystal monochromator, the blue line the X-ray beam, and the light grey blocks slits S1-4.

The X-ray beam is then monochromated using a double-crystal monochromator, which takes the form of two silicon crystals in parallel. The beam is diffracted off both crystals, which results in a monochromatic beam, the energy of which is dependent on the angle of the monochromator. The double crystal reflects the beam back into the direction of the beamline, parallel to the incoming beam. As this line is dedicated to XAS, the majority of experiments involve moving the monochromator to scan though a range of X-ray energies. For most

experiments, the Si 111 monochromator is used, however for higher energies ~>30 keV BM26A is also capable of using a Si 311 monochromator. Finally, the beam is fed through to the experimental hutch.

The experiments described in this work are consistent with the typical *operando/in situ* catalytic experiments run on BM26A. In the typical DUBBLE set-up catalysts are sieved into appropriately sized sieve fractions, packed into borosilicate or quartz capillaries (the size of which is dependent on the X-ray absorption of the sample), and mounted into the capillary holder. The DUBBLE capillary holder is described elsewhere[10] and can be seen in Figure 3.5. BM26A has a permanent built-in gas rig complete with mass flow controllers, pressure controllers, a dedicated mass spectrometer, and gas cupboards positioned outside the experimental hutch. The temperature of the cell is controlled using a heat gun – also visible in Figure 3.5. Although this is the conventional set-up, users can swap in other cells, heating systems or other equipment when necessary for the demands of the experiment.

In this work, XAS measurements were recorded at the Co k-edge (7.712 keV) and catalyst samples were packed into 1 mm diameter borosilicate capillaries. The catalyst was calcined in a two-step process, first from room temperature to 350 °C at a ramp rate of 5 °C/min in a flow of He, then from 350 °C to 550 °C at a ramp rate of 10 °C/min in a flow of O_2/He. The catalyst was then reduced under a flow H_2 from 150 °C to 550 °C at a rate of 2 °C/min. FTS was performed at 250 °C at a pressure of 2 bar with a H_2:CO ratio of 2:1. The pressure was chosen to limit the formation of waxes which risk blocking the capillary cell and limiting the time on stream to a couple of hours. Total gas flow was 10 ml/min corresponding to a gas hourly space velocity (GHSV) of approximately 10000 h^{-1}.

Although a dedicated XAS beamline, BM26A is also capable of running combined XAS/XRD/SAXS experiments – photographs of example set-ups are in Figure 3.5. Figure 3.5a is a photograph of an XRD/SAXS experiment performed on BM26A, while Figure 3.5b and c are a side and top view respectively of a combined SAXS/XAS experiment. Both samples are mounted in the u-bend sample holder.

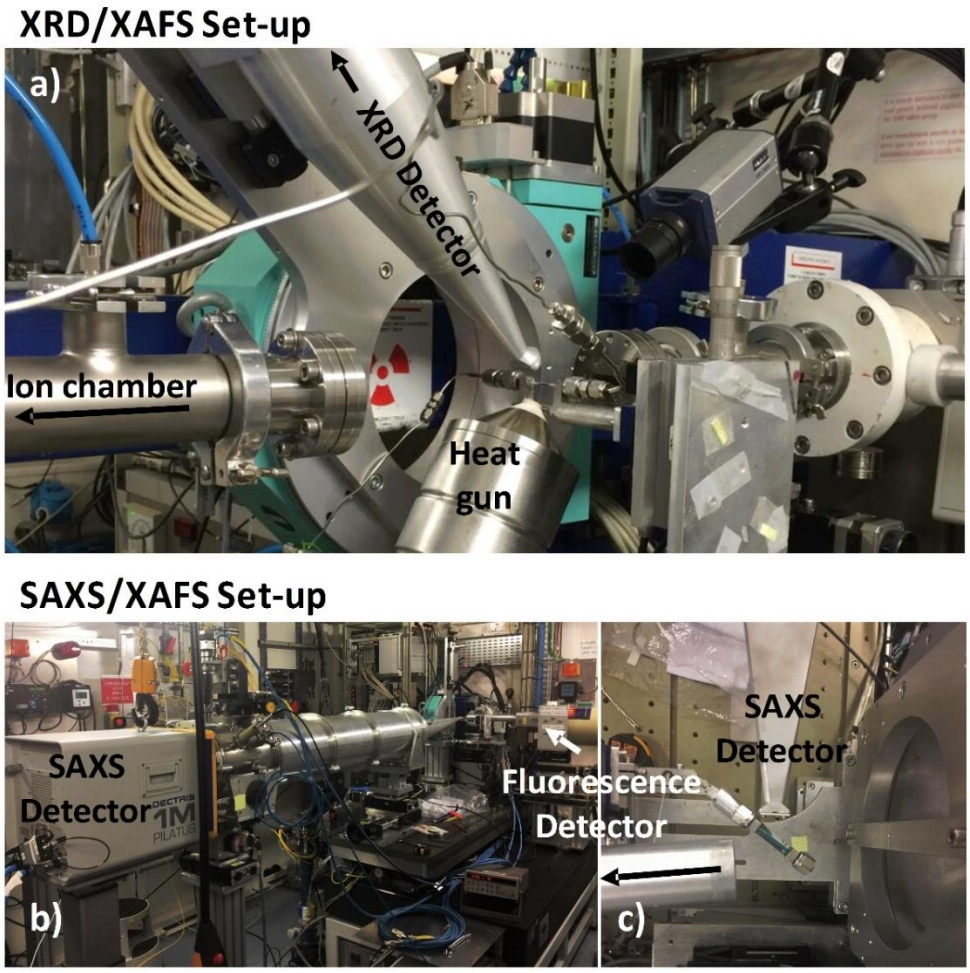

Figure 3.5: Photographs of a) an XAS/XRD set-up on BM26A, and b-c) XAS/SAXS set-up taken from b) the side and c) the top.

The combined XRD/XAS set-up consists of a line detector for XRD measurements approximately 50 cm from the sample and two ion chambers for XAS measurements before and after the sample. This specific experiment was performed under *operando* conditions and so the cell is connected into the gas system and a heat gun is positioned just below the sample. In the combined SAXS/XAS set-up a 2D detector is used for measuring SAXS, but it is not possible to use the ion chambers for XAS as they would block X-rays from the SAXS detector. In this case, XAS measurements are recorded using a photodiode placed on the SAXS beamstop. The photodiode collects substantially poorer data than that of the ion chambers, constituting a large compromise on the XAS data to collect combined SAXS. It is possible to measure both SAXS and XAS simultaneously if the XAS is measured in fluorescence mode (Figure 3.5). However, as SAXS is best performed with as small a beam size as possible,

and in XAS data collection the beam is often widened to improve the data quality, there is also a sacrifice in one or both techniques. Most combined experiments involve some degree of compromise, as different experiments require different properties of the X-ray beam, the sample, or the experimental geometry.

Complementary XRD experiments were also performed on ID15 at the ESRF. For consistency and to ensure better comparison between the experiments, the same cell was mounted on both beamlines, and the same gas and temperature procedure was used.

3.1.3 X-Ray Diffraction

Powder XRD is a frequently used tool in materials science, which can be used to chemically fingerprint crystalline material, as well as providing more detailed information on crystallite size, strain, site occupancy, variation in lattice parameters, etc.

At a fundamental level when X-rays interact with matter they interact with the electrons. Upon interaction, several phenomena occur including absorption and scattering of the X-rays.[11] The diffracted X-rays are those that are elastically scattered (only those interactions are discussed in this section). Elastic scattering occurs when an X-ray beam interacts with an electron causing it to become excited to periodic vibrations by the changing magnetic field.[12] Consequently, the electron itself becomes a source of X-rays of the same frequency and wavelength as the original beam emitted from the electron with a spherical wavefront. The wavefront from each electron within an individual atom's electron cloud combine. Superposition of X-rays occurs when elastic X-ray scattering from a series of atoms within a crystal lattice structure interfere with one another. The constructive interference results in a diffracted X-ray beam, the scattering angle of which is characteristic of the interplanar distance, via Braggs law (equation 3.1).[11]

$$n\lambda = 2dsin\theta \qquad (3.1)$$

Where λ is the wavelength, d is the distance between each lattice place, θ is the Bragg angle, and n is the order of reflection (a positive integer). Bragg conditions are met when λ is comparable to the interatomic spacing, and if there

are a large quantity of lattice planes in the crystal. This behaviour is analogous to reflection off the lattice planes and the diffracted beams are often referred to as reflections for historic reasons. As such Braggs law can also be derived geometrically.

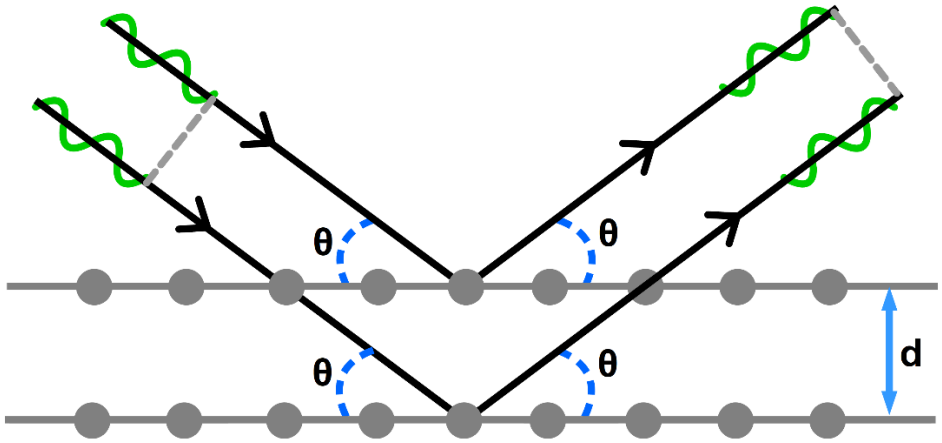

Figure 3.6: Diagram showing Bragg conditions. The black lines are X-ray's, the grey lines and circles are lattice planes and the atoms that form them, the green wave indicates the phase (in that the diffracted X-rays are in phase, as they can constructively interfere with one another), and the dotted grey line represents the wavefront.

Diffraction from a single crystal takes the form of a series of diffracted beams, observable on a 2D detector as distinct points. However, powder samples are comprised of a vast number of randomly orientated crystallites. Consequently, the diffraction points from each individual crystal combine to form diffraction cones of a fixed angle $2\theta_{hkl}$ – characteristic of each d_{hkl} spacing in the crystal.

A wealth of physical information is contained within a powder diffraction pattern (a summary of which is shown in Figure 3.7) and can be extracted by a range of analysis methods. Although it should be noted that the diffuse scattering present in the background is not analysable using XRD analysis, only with PDF analysis.

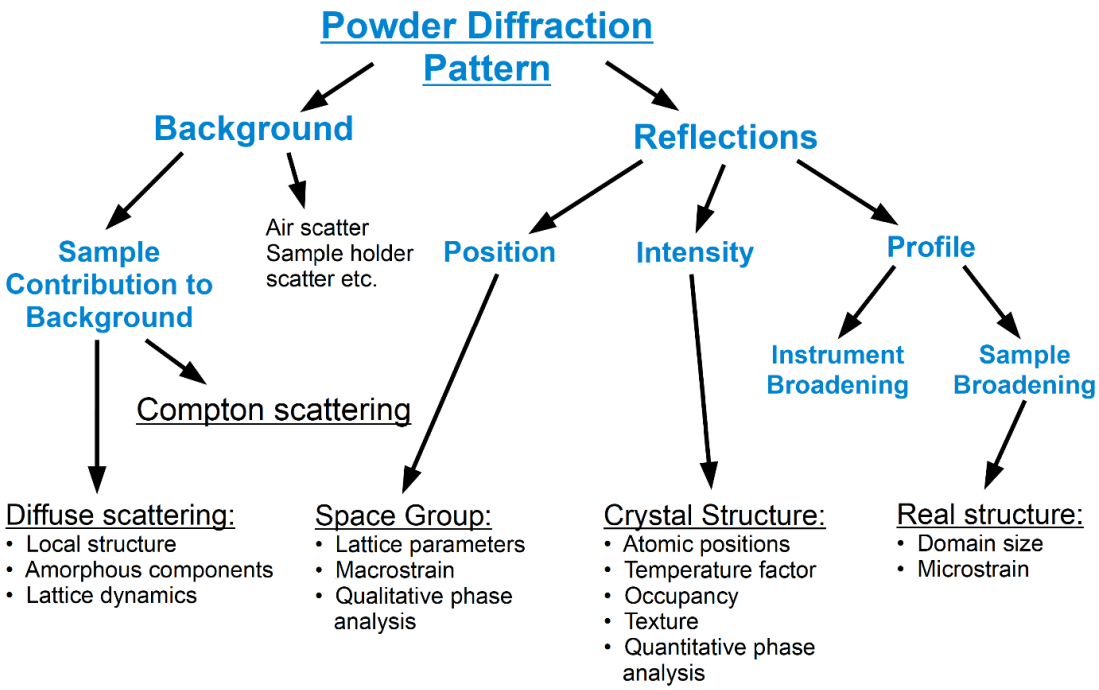

Figure 3.7: A summary of the physical information contained within the various features of powder diffraction patterns. [Adapted from reference [13]].

The most basic form of analysis of PXRD patterns is a simple phase identification (ID) based on reflection positions and, to some degree, the relative intensities. The reflections in an experimental diffraction pattern are matched to known patterns from structural databases (e.g. PDF2/POW_COD) either using software (such as QualX2[14] or Highscore Plus[15]), or manually. This can be performed in isolation to merely identify the component phases of a sample, or as an initial step before other more advanced analyses, such as Rietveld refinement.

Beyond this, the most basic size analysis is performed using the Scherer equation (equation 3.2), which estimates crystallite size from the peak width of a reflection.[16]

$$D_{hkl} = \frac{K\lambda}{B_{hkl}cos\theta} \qquad (3.2)$$

Where, D_{hkl} is the crystallite size in the direction perpendicular to the lattice plane defined by hkl, K is the crystallite shape factor, B_{hkl} is the width (FWHM or integrated width) and θ is the Bragg angle. This version of the equation does not account for instrument broadening and so would predict a larger crystallite size

than reality. If the instrumentational contribution to broadening is known, then that can be deconvoluted from the total broadening. However, even instrument corrected Scherrer analysis ignores many factors that can affect reflection width, including sample displacement, strain and disorder.[17] If micro-strain and size are both large contributors to broadening, then Williamson-Hall analysis is considered a more appropriate method,[17] but is only accurate when performed on at least five reflections from the same family and so typically requires a large q-range.

Alternatively, Rietveld refinement is a full profile fitting method first developed in 1967 that has revolutionized the way powder patterns are treated.[13] In this method a least square fitting procedure is used to minimise the difference between an experimental and calculated pattern using parameters of a known crystal structure as well as global parameters (described in more detail below). The intensity of the calculated pattern is described by:

$$y_{ci} = S \sum_{hkl} L_{hkl} |F_{hkl}|^2 \varphi(2\theta_i - 2\theta_{hkl}) P_{hkl} A + y_{bi} \qquad (3.3)$$

Where y_{ci} is the calculated intensity at point i, S is a scaling factor, L_{hkl} contains correction factors, $|F_{hkl}|$ is the structure factor, φ is the profile factor accounting for diffractometer effects, P_{hkl} is any preferred orientation, A is absorption and y_{bi} is the background at point i.

The refinement minimises the squared differences between the observed and calculated intensities at each point i, weighted by w_i.

$$\Phi = \sum_i w_i (y_{Oi} - y_{Ci})^2 \qquad (3.4)$$

Where w_i is:

$$w_i = 1/\sigma^2[y_{Oi}] \qquad (3.5)$$

Although the “chemical reasonableness” of a model determined using the refinement is the most important criterion for judging the quality of the refinement, the criterion χ^2 and the R factors provide a statistical method of assessing the appropriateness of the fit.[18] The two R-factors are the weighted profile R-factor (R_{wp}) and the expected R-value (R_{exp}), where R_{wp} is defined by:

$$R_{wp}^2 = \sum_i w_i (y_{Oi} - y_{Ci})^2 / \sum_i w_i (y_{Oi})^2 \quad (3.6)$$

R_{exp} can be considered as the best possible R_{wp} value.[18]

$$R_{exp}^2 = N / \sum_i w_i (y_{Oi})^2 \quad (3.7)$$

Where n is the number of data points minus the number varied parameters in the refinement. The value χ^2 is related to these R-factors. χ^2 is sometimes described as the goodness of fit and is always larger than 1. When the model is ideal and with correct standard uncertainty values for the data, R_{exp} would be 1. χ^2 is then be the average of these values:

$$\chi^2 = \left(\frac{1}{\mathrm{N}}\right) \sum_i \frac{(y_{Ci} - y_{Oi})^2}{\sigma^2 [y_{Oi}]} \quad (3.8)$$

$$\chi^2 = (R_{wp}/R_{exp})^2 \quad (3.9)$$

Full profile analyses', such as Rietveld, model data using empirical peak-shape functions. Rietveld has proven itself a robust method for the analysis of powder diffraction.[13] However, there is a limit to the applicability of Rietveld refinements on samples that strongly deviate from ideal crystal structures with long-range translational symmetry, either by the presences of faults, layered materials, or small sized nanoparticles.[19] This is a particular issue for Co-based FT catalysts as metallic cobalt is well known for forming stacking faults in both fcc and hcp polymorphs.[20] If the effect of stacking faults is minimal, it can be accounted for using an unphysical preferred orientation, or size/shape. However, this approach is problematic at best.

Alternatively, in the Debye approach, powder XRD patterns are simulated using the Debye equation (equation 3.10), which considers the diffraction or interference contributions for each pair of atoms within the scattering domain.[19] Equation 3.10 is broken up into two parts. The first sum combines the scattering power of all individual atoms in the scattering domain, and the second set of sums combines the sinusoidal components of the scattering power of each pair of atoms in the domain.

$$I(\theta) = \sum_n f_n^2(\theta) + \sum_i \sum_{j,i \neq j} f_i(\theta) f_j(\theta) \left(\frac{\sin(4\pi r_{ij} sin\theta/\lambda)}{4\pi r_{ij} sin\theta/\lambda} \right) \quad (3.10)$$

Where f_n is the atomic form-factor of the nth atom in the array, f_i and f_j are the form factors of each atom in the pair, λ is the X-ray wavelength, θ is half the scattering angle, and r_{ij} is the distance between each pair of atoms. As Debye simulations consider each pair of atoms in a domain, they are significantly more computationally expensive than Rietveld refinements, which becomes a major issue for large domains.

In this work, XRD Debye simulations using the unic model are performed. The unic model is based on the probability of various concatenations of four-layer blocks of metallic cobalt occurring within a scattering domain for a defined particle size. When fitted to experimental data, this model provides values for the relative percentages of fcc, hcp, and mixed regions (either stacking faults or intergrown phases).

These Debye simulations using the unic model as applied to model cobalt systems were first used in Longo *et al.* (2014),[21] and the simulations were written in Fortran77. Improvements have since been made to the model to tailor it to more realistic data for FT catalysts. It is common for FT catalysts to contain unreduced oxidic components, either unreduced CoO, Co_3O_4, or metal support interaction. These oxidic components are fitted using a very basic Rietveld refinement outlined in X-Ray Diffraction Procedure[12] – where the peak widths are defined solely by the Caglioti parameters: U, V and W defined by the Caglioti formula:

$$H = (U \tan 2\theta + V \, tan \, \theta + W)^{\frac{1}{2}} \qquad (3.11)$$

Where H is the peak breadth, measured as either the full width at half maximum (FWHM) or the integral breadth.

This is an unsophisticated analysis of the oxidic components. It is only used because the aim is not to fully refine the oxide structure – which can be done more effectively with pre-existing analysis software – but to quantify fractional percentages in relation to the metallic blocks and prevent unaccounted oxidic components influencing the metal cluster simulations. In addition a background diffraction pattern of the support can be input and any variation in that is defined by a polynomial linear spline.[22]

The parameters are minimised using MINUIT.[23] The MINUIT package acts on a multiparameter user defined function (FCN), and is typically used to minimise a value calculated using the function. The original version, and that which is used in this work, was written in Fortran 77, although it is now also available in C++.[23] The user function in used in this code calculates the χ^2 value between the simulated unic model and the observed diffraction data. MINUIT then minimises χ^2 with respect to a range of model parameters described below. The MINUIT commands can be input either in the command line or as data cards for batch processing, an example Minuit data card detailing all the variables and commands is shown in appendix 2. All parameters were either fixed or variable with limits to ensure a physically meaningful fit. MINUIT offers multiple minimisation algorithm options. The key algorithms being MIGRAD, SIMPLEX, and MINIMISE.

The MIGRAD algorithm is a local function minimisation using a gradient provided by the user or calculated using a subroutine, based on Fletchers switching algorithm.[24] First starting parameter values X(I), the first derivatives GS(I) and the covariance matrix V(i,j). Secondly a “Newton step” is taken so that X’=X-V*GS, which would be the maximum if the function is quadratic and V(i,j) were the true covariance matrix, but this is often not the case so a linear search is performed for the maximum in that dimension. The new updated point and gradient at that point are X’(I) and GS’(I). V(i,j) is updated to V’=V+f(V,X,X’,GS,GS’) where f is wither Davidsons formula of Fletcher’s switching criterion, which repeats until convergence.

In the SIMPLEX algorithm an initial point is defined by the initial parameters of number n. A simplex (the simplest object of n-dimensions that will fill the space) is constructed near that initial point, with each corner set as the nearest local minima in each dimension. The function is evaluated at each corner of the simplex. The worst point is then excluded from the shape and reflected in the centre of the shape, creating a new simplex. MINAMIZE performs a MIGRAD minimisation, but if that fails to convert SIMPLEX is called instead. Then when that is complete, switches back to MIGRAD.

Table 3.2: Table of the 24 elementary blocks and their corresponding type (e.g. cc, ch, hc or hh).

cubic-cubic (cc)	ABCA	ACBA	BCAB	BACB	CABC	CBAC
cubic-hexagonal (ch)	ABCB	ACBC	BCAC	BACA	CABA	CBAB
hexagonal-cubic (hc)	ABAC	ACAB	BCBA	BABC	CACB	CBCA
hexagonal-hexagonal (hh)	ABAB	ACAC	BCBC	BABA	CACA	CBCB

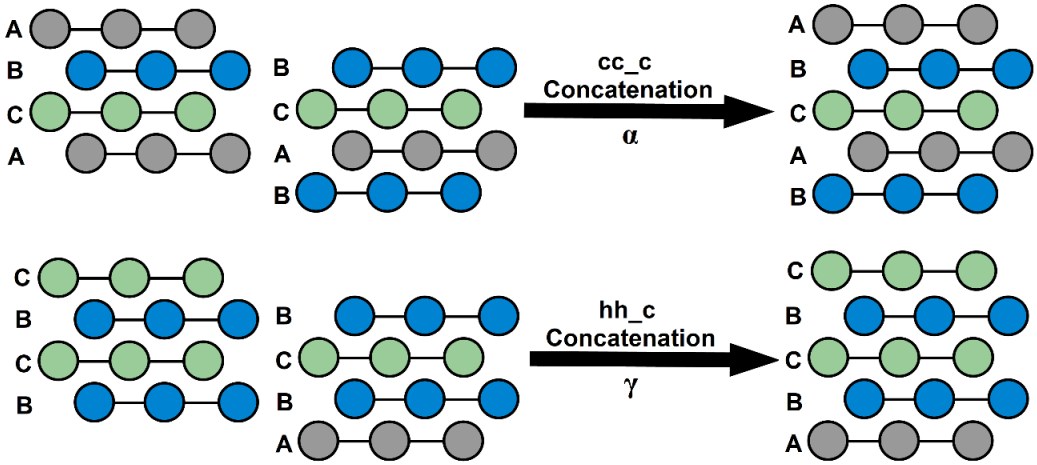

Figure 3.8: Schematic showing two example concatenations of elemental units into five-layer blocks defined by the probability factors α and γ.

The structural model is based on the concatenation of elemental blocks of atomic layers in the (001) direction of the hcp phase (using ABC notation). To model the occurrence of hexagonal-hexagonal (hh), cubic-cubic (cc), hexagonal-cubic (hc), and cubic-hexagonal (ch) concatenations - and so the frequency of fcc, hcp and intergrown structures in the NPs – it is necessary to use a "Reichweite" factor of s=4, which defines the number of atomic layers in the elemental blocks and therefore the number of layers that influence the statistical occurrence of the next layer. In this case, there are 24 distinct elementary blocks ($S=3.2^{s-1}$), of which four types of major blocks are distinguishable from one another (cc, ch, hc and hh) – given in Table 3.2.

The model depends on the independent probability factors: α, β, γ, and δ, which define the probability of concatenations of two of the four types of major blocks, forming a five-layer combined block (two examples are visualised in Figure 3.8). α, β, γ, and δ correspond to cc_c, hc_c, hh_c and ch_c concatenations respectively. From the probability of the various concatenations it is possible to determine the frequency of the five-layer building blocks via equations 3.12-3.15. As such these simulations are capable of accurately determining the relative ratio of fcc, hcp and mixed cobalt within the clusters.

$$f_{cc} = \frac{\beta\gamma}{\Delta} \quad (3.12), \quad f_{ch} = f_{hc} = \frac{(1-\alpha)\gamma}{\Delta} \quad (3.13),$$

$$f_{hh} = \frac{(1-\alpha)(1-\delta)}{\Delta} \ (3.14),$$

$$\Delta = 6[(1-\alpha)(1-\delta) + 2(1-\alpha)\gamma + \beta\gamma] \qquad (3.15)$$

The statistical treatment used is taken from Warren (2nd edition 1990).[11] The model is also able to account for the size, size distribution, and shape of the scattering domains, horizontal and vertical strain (in the plane defined by abc notation), and temperature via the Debye-Waller factor.

The advantage of using the unic model with a S value of 4 is that all possible variations of stacking faults and intergrown structures of metallic cobalt can be modelled. Whereas other probabilistic methods involve tailoring the model for the system (e.g. fcc with stacking faults, fcc and intergrown structure, hcp with stacking faults and fcc with stacking faults).[25] The same type of simulations and model can be used on more simple systems by reducing the S number to three.

3.1.4. X-ray Absorption Spectroscopy (XAS)

Theory

X-Ray Absorption Spectroscopy (XAS), a.k.a. X-ray Absorption Fine Structure (XAFS) is a spectroscopic X-ray technique which probes the energy range around core level binding energies. As the binding energies are characteristic of, not only the shell, but also the element being probed, the

technique is element specific. XAS also probes the average local structure around the targeted element, it can be performed on samples irrespective of order or crystallinity. XAS is best performed using SR due to the high flux and energy tunability. An XAS spectra shows the intensity of μ (the absorption coefficient) as a function of energy around an absorption edge, and consists of two regions, XANES (X-ray absorption near edge spectroscopy), and EXAFS (Extended X-ray Absorption Fine Structure) - Figure 3.9.

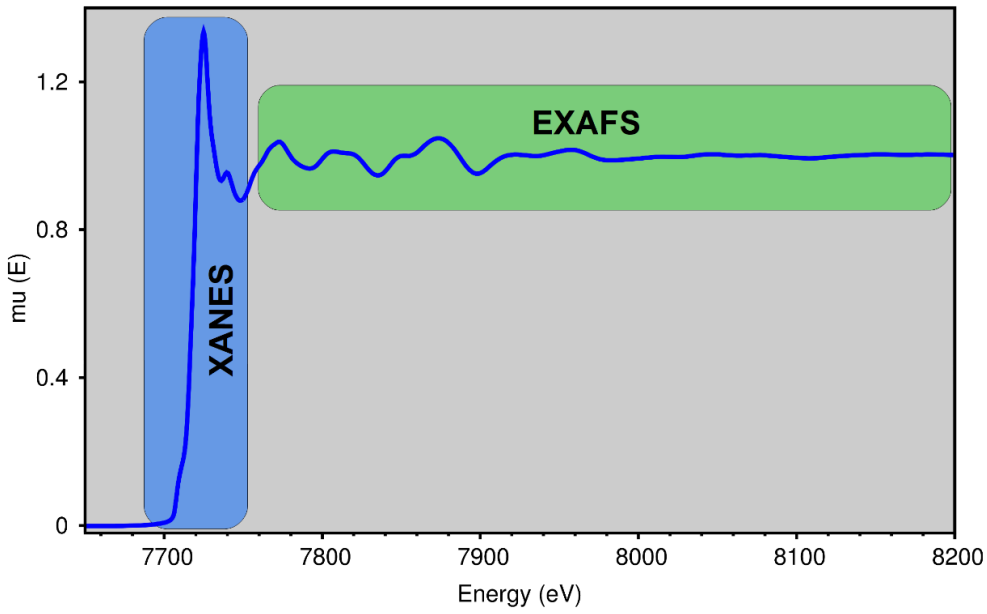

Figure 3.9: Example normalised XAS spectra of Co_3O_4/MCF-17 at the Co k-edge giving the approximate XANES and EXAFS regions within the XAS spectra.

The underlying physical phenomenon behind XAS is the photoelectric effect, in which an X-ray photon is absorbed by a core electron within an atom, and the electron is ejected from the core. This leaves a core-hole which decays, either by fluorescence (where a higher energy electron drops down to fill the hole producing an X-ray photon of characteristic energy), or by the Auger Effect (where an electron drops down from a higher energy level, and another electron is emitted into the continuum).

In XAS experiments we are chiefly interested in μ (the absorption coefficient), which is defined (for transition mode) using Beer's Law:[26]

$$In\frac{I_0}{I_t} = \mu(E)x \qquad (3.16)$$

Where I_0 and I_t are the initial and transmitted X-ray intensity, μ is the absorption coefficient in terms of E, and x is the sample thickness. The most used XAS measurement modes are transmission and fluorescence, both of which are used in this work. At high enough atomic concentrations of the element being probed, and at appropriate sample thicknesses, it is possible to measure in transmission mode. Where I_0 and I_t can be directly measured using ion chamber detectors. Under ideal conditions the thickness of the sample is adjusted so that μt ≈ 2.5 above the absorption edge, and so that the edge step is approximately 1.[26] However, some compromise on these values is often needed for *in situ/operando* measurements, when using combined techniques, or for challenging samples. Fluorescence measurements are preferred for dilute samples, which use multi-element semiconductor detectors that can target and detect X-rays of specific energies, here being the fluorescence emission.

$$\mu(E) \approx \frac{I_t}{I_0} \tag{3.17}$$

EXAFS describes the region of the XAS spectra which starts from about 50 eV above the edge and contains the oscillations observable in Figure 3.9. The oscillations are due to the interaction of the photoelectrons ejected from core electron shells, and the neighbouring atoms. In the simplest example, a path between an absorber atom and its nearest neighbour, the photoelectron is ejected from the core of the absorber atom. Due to particle-wave duality the photoelectron has a wavefront which then interacts with the neighbouring atom to be absorbed and emitted. The original and re-emitted photoelectron waves are in superposition (experience constructive and destructive interference). Photoelectrons like these from a range of types of paths, from all absorbing atoms average together producing the oscillations observed in the EXAFS. This behaviour is described by the EXAFS equation.

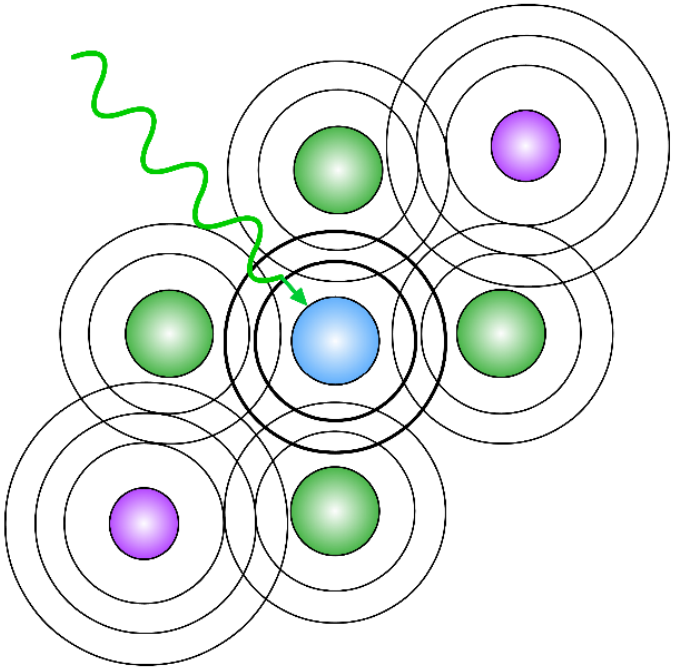

Figure 3.10: Diagram illustrating the constructive and destructive interference observed during XAS measurements from the perspective of the probed species (blue).

$$\chi(k) = S_0^2 \sum_j \frac{N_j}{kR_j^2} \left| f\left(k, R_j\right) \right| \sin\left(2kR_j + 2\delta(k) + \psi\left(k, R_j\right)\right) \exp\left(-A_j k^2\right) \exp\left(\frac{-2R_j}{\lambda(k)}\right) \quad (3.18)$$

Where A is the Debye-Waller factor ($A=2\sigma^2$, σ is standard deviation in R), analogous to the Debye-Waller factor used in XRD. R_j is the distance between absorbing and scattering atom, N_j is the number of neighbouring atoms, S_0^2 is the amplitude reduction factor, $f_i(k)$ is the scattering amplitude at atom j, δ is the phase shift undergone by the photoelectron at the central atoms and, ψ is the phase shift undergone by the scattered photoelectron. The parameters that are used for fitting EXAFS are coloured blue in equation 3.18.

XANES is defined as the region that begins ~30 eV before the edge and ends ~50 eV after. Although it is increasingly common to perform simulations of XANES spectra, fingerprinting techniques such as Linear Combination Analysis (LCA) and Principle Component Analysis (PCA) remain commonly used. XANES directly probes the angular momentum of unoccupied electronic states, where the allowed transitions are predominantly determined by the dipole selection rule: $\Delta l=\pm 1$, with additional contributions from quadrupole transitions.

The key features in XANES spectra are pre-edge peaks, the edge itself, the rising edge (more commonly referred to as the white line), and near edge intensities. These features are best discussed here in context with the most common cobalt phases observed in this work: Co_3O_4, CoO and Co^0 (Figure 3.11).

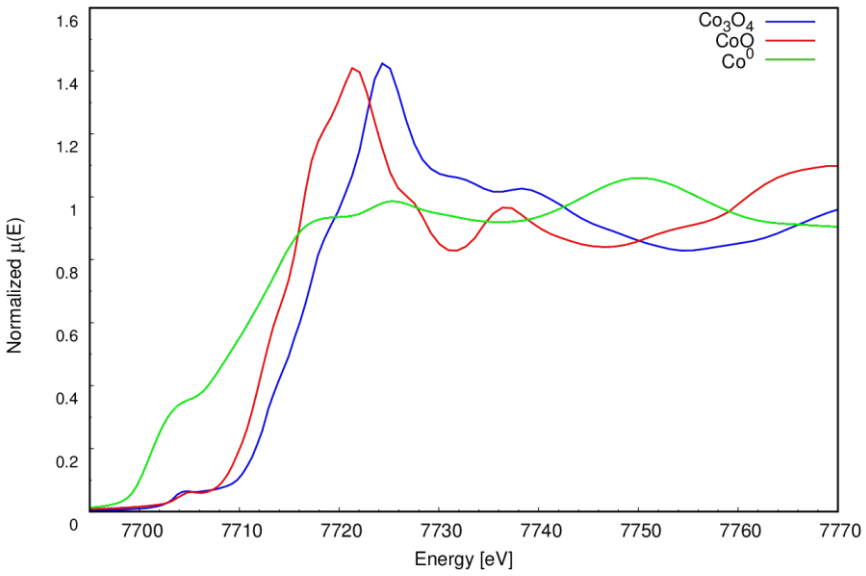

Figure 3.11: Normalised XANES spectra for Co^0 foil, CoO and Co_3O_4 reference samples. (CoO and Co_3O_4 data taken from IXAS XAS database[27]).

Like all 3d transition metals, cobalt systems that are tetrahedrally coordinated have a more intense pre-edge peak than those of octahedral coordination.[28] This is because in octahedral systems only the weaker 1s to 3d electric quadrupole transition contributes to the pre-edge peak.[28] Whereas, in the tetrahedral geometry the transition to the p component in d-p hybridisation is allowed,[28] as well as the 1s to 3d transition.[29] Additionally, in tetrahedral systems the pre-edge peak intensity varies as a function of the number of d electrons, as the fewer the number of d-electrons the higher the probability of the transition.[28]

In the key cobalt species shown in Figure 3.11 all show some type of pre-edge feature. Both oxides have a distinct pre-edge peak, with that of Co_3O_4 at a marginally lower energy. Whereas the pre-edge feature of the Co^0 is closer to the edge creating a shoulder.

Oxidation state sensitive edge energy shifts are conceptualised as either due to bond length differences or explained using an electrostatic model. In the

first, the shorter absorber-scatterer distance observed in oxides result in the photoelectron experiencing a higher energy, which translates into edge energy shift in XANES spectra to higher energies. In terms of the cobalt system the absorber-scatterer distance in bulk for first shells of Co_3O_4 (Co-O), CoO (Co-O), and Co^0 (Co-Co) respectively are approximately: 1.9 Å, 2.1 Å, and 2.5 Å. Secondly, in the electrostatic model, atoms of a higher oxidation state require more energetic X-rays to excite core electrons as the nucleus is less shielded with a higher effective charge. In the case of the example cobalt species, the oxidation states of metallic cobalt, CoO and Co_3O_4 respectively are 0, +2, and mixed +3 and +2. Therefore, over the course of reduction the average cobalt nucleus is less shielded, resulting in the edge energy shifting to a lower value.

Data Analysis

Although the underlying theory behind XANES is arguably more complex than that of EXAFS, many of the analyses of XANES are simplistic, often considered to be fingerprint analysis. For example, in LCA (linear combination analysis) reference or simulated spectra of known/guessed phases within the sample are fitted as a linear combination of the spectra, scaled to their percentages within the sample. The normalisations must be consistent between reference and experimental data.[26]

A common issue with this type of analysis in Co-based FT catalysts samples is that the XANES spectra of Co_3O_4 and $CoAl_2O_4$, as well as CoO and $CoSiO_2$ are similar enough to one another to be misinterpreted at the low percentages they are observed in the catalysts. PCA (principle component analysis) analyses a series of related spectra to determine if they can be represented as a linear combination of a small number of reference spectra.[26] Additionally, the smaller a nanoparticle is the less the XANES spectra resembles a bulk reference, which is an additional limitation on LCA as a technique.

EXAFS analysis first involves some pre-treatment where the pre-edge line is subtracted and the normalisation of μ(E) to make an edge jump of 1. Leaving three key plots: normalised XAS spectra in terms of μ(E), the EXAFS χ(k) and the Fourier transform in R-space. Then follows curve fitting of the k-space

contribution of paths, although the Demeter package is by far the most popular. In this work both Demeter[30] (Artemis and Athena), as well as Viper[31] are used. Demeter has the advantage of being continuously updated and improved with an active and vocal user community,[32] the ability to fit multiple patterns simultaneously, as well as easy correlation of parameters. Artemis also provides a front end for FEFF – a feature Viper lacks. However, Viper has better visualisation, and a substantially better background removal (allowing for more realistic fitting of samples with short absorber-scatterer distance in R such as CoO and Co_3O_4) than that of Demeter.

Scattering paths are generated using FEFF (either FEFF6.0 integrated into Dementor or FEFF9.0 separately for VIPER) based on theoretical standards (computed from either .cif files or by the creation of a tailored list of atomic positions). The model is then fitted to the experimental curve, typically in R and/or k-space using parameters of these paths from the EXAFS equation (equation 3.18). The parameters are N, S_0^2, E_0 ΔR, and σ^2 from the theoretical standard in Artemis, and N, E_0, R and σ^2 in Viper. EXAFS fitting is performed using a least square fitting procedure, much like Rietveld refinement. Goodness of fit and the appropriateness of the model are assessed, and properties of the system as well as their variation over time can be deduced. The maximum number of fitting parameters is defined by the Nyquist criterion: $N \approx 2\Delta r \Delta k/\pi$. Where N is the maximum number of fitting parameters, Δr is the range I r-space, and Δk is the range of Fourier transform. Although this is the upper bound, the number of parameters should be kept as low as possible.

Important factors to consider in the appropriateness of the fit are the errors associated with each fitted parameter. Parameters which effect intensity in R-space EXAFS plots (N, S_0^2, and σ^2), have larger errors compared to R. For example, n values will often have an approximate error of ±1.

3.2. Other Characterisation Techniques

3.2.1. Surface Area Determination: BET

Surface area and porosity of materials are measured using nitrogen physisorption. The most common analysis of this data is BET (Brunauer–

Emmett–Teller), named after the equation used to calculate surface area determined from adsorption-desorption isotherms.[33] However, other analyses of isotherms are available including total pore volume, BJH (mesopore volume area and distribution), micropore distribution, and modelling using DFT.[33] In this work both BET and BJH analyses were used.

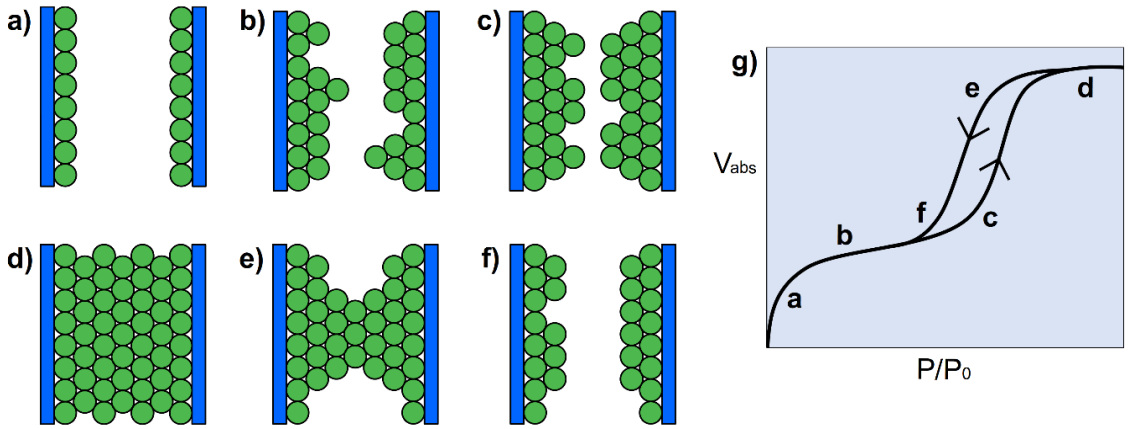

Figure 3.12: a-f Images representing various stages of nitrogen (green circles) adsorption/desorption on microporous material and which stages they correspond to on the type IV isotherm (g). a) monolayer formation, b) multilayer adsorption, c) critical thickness, d) capillary condensation, e) evaporation form pores, and f) breakdown to multilayer film. [Adapted from reference [34]].

Adsorption-desorption isotherms are measured which plot relative pressure vs N_2 volume absorbed. There are currently (as of 2015)[33] eight observed types of isotherms. Type IV(a) (formerly type IV) isotherms which include a hysteresis loop, caused by capillary condensation that occurs in mesoporous (pores of width 2 - 50 nm) material. The sections before the hysteresis loop include the mono- and multi-layer adsorption, complete adsorption is observed at the point at the beginning of the near linear region – shown in Figure 3.12.

BET analysis consists of two steps, transformation of the adsorption-desorption isotherm into a "BET plot", and from that derived the BET monolayer capacity (n_m).[33] Where the "BET plot" consists of $(p/p_0)/n_a(1-p/p_0)$ by p/p_0 in the approximate range ~0.05-0.03 where the plot is approximately linear (see section around (b) in Figure 3.12). The BET equation is given as:

$$\frac{p}{n_a(p_0-p)} S_{total} = \frac{1}{n_m C} + \frac{(C-1)}{n_m C} \cdot \frac{p}{p_0} \qquad (3.19)$$

Where n_a is the amount of absorbed gas at a relative pressure p/p_0, C is the BET constant and n_m is the monolayer capacity. When the BET plot is linear (in type II and IV(a) isotherms) then the values for C and n_m can determined from the gradient and intercept of the line.

$$s_{total} = \frac{n_m N_S}{V} \tag{3.20}$$

Where s_{total} is the total surface area, and V is the volume of nitrogen adsorbed.

In this work nitrogen absorption-desorption isotherms were collected at 77 K using a Quadrsorb evo (Quantachrome Instruments). All samples measured were degassed at 190 °C for 3 h in a FLOVAC degasser. The surface areas of the silicas were determined using multi-point BET (Brunauer–Emmett–Teller), and the pore volumes and pore radii were calculated using BJH (Barrett–Joyner–Halenda), both of which were calculated from the full isotherms. All surface area data analysis was performed using the ASiQWin software.[35]

3.2.2. Transmission Electron Microscopy (TEM)

TEM, as its name indicates, is a microscopy technique which probes thin samples using an electron beam in a transmission mode. Commonly used in catalysis for particle size and shape determination. An electron beam is generated by an electron gun (described in the above x-ray sources section), the beam is then focused on to a sample using a lens. The transmitted electron beam is then passed through a series of lenses which magnify and focus the generated image onto the image recording device (e.g. a fluorescent screen, photographic film, or a CCD in modern microscopes).

Typical sample preparation of powdered catalysts for TEM measurements involve the dispersion via sonification of the catalyst powder in a solvent, which is then pipetted onto a TEM grid or support. Supports typically take the form of an amorphous carbon film on top of a metal mesh. The solvent evaporates off the TEM support leaving the sample distributed across the carbon film. The most common method of TEM image analysis is determination of average particle size and size distribution, either using image processing algorithms for the most

straightforward samples (nanoparticles only, or well contrasted particles) or by hand.

TEM images recorded throughout this work were captured using a Jeol-2100 (200 keV accelerating voltage) at the Research Complex at Harwell. Images were captured by and the particle sizes in the images were obtained using Gatan DigitalMicrograph[36] and ImageJ.[37] There was some variation in the number of particles counted per sample as some samples were more challenging to image. However, the minimum number of particles was 100 and the typical measurement was between 200-300 particles to produce a statistically reliable average.

Major limitations to the technique include the statistical reliability of microscopy measurements in general, potential user bias during measurement and analysis, and the limit of resolution (as TEM is effectively blind to small nanoparticles). Additionally, Co/Silica catalysts have a specific issue regarding low contrast. In many Co/SiO_2 samples, particularly those with supports formed of spherical pores/particles, it is challenging to differentiate nanoparticles and support with any clarity. This is due to a combination of the greater thickness of the support, as well as the relatively low scattering potential of the Co compared to other metals. Nevertheless, TEM remains a useful technique in catalysis especially when used alongside other complimentary techniques.

3.2.3. Thermo-Gravimetric Analysis (TGA)

TGA is a thermal analytic technique which can determine physio-chemical changes by measuring the variation in sample mass as a function of temperature. Typically, small quantities of sample (2 – 50 mg) are subject to one or a series of temperature ramps in a flow of gas. Loss of mass from catalyst samples can be attributed to a range of causes including, but not limited to, loss of water, decomposition of the metal salt, and residual carbon burn-off. In this work TGA was used primarily to quantify residual organic carbon content from the synthesis.

TGA measurements were obtained with a TGA Q50 (TA Instruments) and the data was collected and analysed using the QSeries software.[38] Samples in this project that were analysed using TGA were heated from room temperature

to 550 °C with a temperature ramp rate of 5 °C/min, in steps of 0.1 °C and in a flow of air.

3.2.4. UV-Vis Spectroscopy

UV-Vis is a spectroscopic technique which uses UV and visible light — covering the wavelength range 200 nm to 800 nm (50,000-12,000 cm^{-1} in wavenumber). It is typically used in catalysis to probe electronic transitions in transition metals.[39] The energy range probed is consistent with that needed to excite electrons in d-orbitals in transition metals discussed in XANES section - 3.1.4. X-ray Absorption Spectroscopy (XAS). Reflectance spectrometers do not directly measure absorption, but reflectance. It is necessary to convert reflection spectra to absorption spectra for comparison with other data sets. Absorption spectra are approximated from reflectance spectra by the Kubelka–Munk function (equation 3.21).[40]

$$F(R) = \frac{(1-R)^2}{2R} \qquad (3.21)$$

Where R is the reflectance, and F is the approximate absorption.

UV-Vis spectra were collected for both powders and micellular solutions. UV-Vis spectra for powder samples were collected using an UV-2600 UV-Vis spectrometer (Shimadzu), and UV-Vis spectra of micellular solutions were collected using a UV-1800 UV-Vis Spectrophotometer (Shimadzu). Most measurements were taken between 450 nm and 800 nm while others were taken between 200 nm and 1400 nm, all in steps of 0.5 nm. Solutions were held in plastic cuvettes and measurements were recorded between 300 nm and 1100 nm in steps of 0.5 nm. The data was collected and analysed by both spectrometers using the software UVProbe 2.43.[41]

3.3. Catalyst Synthesis

3.3.1. Block Copolymer Micelle Synthesis

The synthesis procedure was developed primarily from the methods used in Spatz *et al*.[42] and Boygen *et al*.[43] The initial step involved first creating a 5 wt%

solution of PS-P2VP (PS[16000Mn]-P2VP[3500Mn], Polymer Source Inc.) in toluene (Fluka, reagent ≥99.7 %). Followed by the addition of the cobalt salt. The salts used were cobalt chloride hexahydrate, $CoCl_2.6H_2O$ (Sigma-Aldrich, 98 %) and cobalt acetate $Co(C_2H_3O_2)_2(H_2O)_4$ (Sigma-Aldrich). The quantity of salt varied depending on the desired micellular loading (the ratio of Co^{2+}/2VP units). The solutions were left stirring in a sealed volumetric flask to allow the cobalt to fully encapsulate. The time given for full encapsulation of noble metals is approximately 24 h,[44] however, during these syntheses the encapsulation time for the cobalt is substantially longer at approximately 10-14 days. Initially this was improved by heating the solution to 40 °C during encapsulation. However, theoretically, increasing the micelle temperature will distort the micelle shape even at such low temperatures, and is less than ideal. All samples discussed here were not heated. Instead the $CoCl_2.6H_2O$ was ground by mortar and pestle to significantly decrease encapsulation time to 48 h. The amount of cobalt salt required was defined by equation 3.22.

$$m_{salt} = \frac{m_{PS-PVP}.MM_{PVP}.MM_{salt}.L}{MM_{PS-PVP}.MM_{VP}} \quad (3.22)$$

Where L is the micelle loading (in the range of 0-1), and m_{salt} and $m_{PS\text{-}PVP}$ are the mass of the cobalt salt and total polymer respectively, and, $MM_{PS\text{-}PVP}$, MM_{PVP} and MM_{VP} are the molecular masses of the total polymer, the PVP blocks and a single VP unit respectively.

The solutions were then transferred to a Teflon beaker along with the silica support. The amount of which was varied according to required metal loadings (wt%) (see Table 3.3 for a list of the silicas used), and left for 24 h to allow the toluene to evaporate. Teflon beakers were used because the dried samples were difficult to remove from glassware – resulting in an unacceptably large amount of sample loss. Finally, the catalysts were either calcined in a furnace or plasma treated. The plasma treatments were performed using a Femto Plasma System from Diener Electronics, in a flow of compressed air (20.9 % O_2), of 10 ml/min at a potency of 100 %. The majority of samples were plasma treated for 90 min. Calcinations were performed using a furnace in air at a range of temperatures, times and ramp rates.

Table 3.3: Reference table of silica supports used in synthesis.

	Name	Supplier	Purity (%)	Particle Size (μm)	Surface Area (m^2/g)
SiO_2(a)	Silicon Dioxide	Sigma Aldrich	~99	0.5-10	4.60
SiO_2(b)	CAB-O-SIL M5	Acros Organics	99.8	0.2-0.3	120.36
SiO_2(c)	Silica, nanopowder	Aldrich Chemistry	99.80	0.012 (primary particle)	108.56
SiO_2(d)	Fumed Silica	Sigma Life Sciences	≥ 99.8	0.2-0.3	107.84

3.3.2. Durham sample synthesis

The samples used in both chapters 5 and 6 were provided by Simon K. Beaumont at Durham university, and were synthesised using a colloidal method.[45] Oleic acid was evacuated for 10 min, then anhydrous o-dicholorobenzene was added under Ar.[46] The samples were stirred and heated until stabilised at the required temperature. At which point cobalt carbonyl was dissolved in o-dicholorobenzene under Ar, and injected into the solution.[46] Colloidal particle formation is indicated by a change in colour from brown to black.[46,47]

The nanoparticles were then deposited onto mesoporous silica, MCF-17 (synthesised using the method given in S. Alayoglu *et al.*)[45]. to give a metal loading of 5 wt%, which were dispersed in chloroform along with a nanoparticle solution.[47] The solutions were sonicated for 40 min, then centrifuged at 3000 rpm and washed with ethanol and acetone seven times, then finally oven dried at 100 °C.[47]

3.4. References

1 J. Cockcroft, P. Barnes, S. D. M. Jacques and M. Vickers, Course Material Master Index, http://pd.chem.ucl.ac.uk/pdnn/pdindex.htm#inst2, (accessed 5 March 2018).

2 ESRF Photograph, http://www.esrf.fr/Apache_files/press/image5.jpg, (accessed 20 October 2017).

3 P. Luger, *Modern X-Ray Analysis on Single Crystals, A Practical Guide*, De Gruyter, Berlin, Boston, 2014.

4 D. R. Mortensen, G. T. Seidler, A. S. Ditter and P. Glatzel, *J. Phys. Conf. Ser.*, 2016, **712**, 012036.

5 Small angle X-ray scattering (SAXS) measurements of nanomaterials | Rigaku,

https://www.rigaku.com/en/products/xrd/ultima/app035, (accessed 27 September 2017).
6 G. T. Seidler, D. R. Mortensen, A. S. Ditter, N. A. Ball and A. J. Remesnik, *J. Phys. Conf. Ser.*, 2016, **712**, 012015.
7 Storage Ring, http://www.esrf.eu/machine/accelerators/storagering.html, (accessed 2 November 2017).
8 Light Source Facility Information | Lightsources, http://www.lightsources.org/light-source-facility-information, (accessed 29 November 2017).
9 About DUBBLE, http://www.esrf.eu/UsersAndScience/Experiments/CRG/BM26/Dubble, (accessed 12 December 2017).
10 S. Nikitenko, A. M. Beale, A. M. J. van der Eerden, S. D. M. Jacques, O. Leynaud, M. G. O'Brien, D. Detollenaere, R. Kaptein, B. M. Weckhuysen and W. Bras, *J. Synchrotron Radiat.*, 2008, **15**, 632–640.
11 B. E. Warren, *X-ray diffraction*, Dover Publications, 1990.
12 H. P. (Harold P. Klug and L. E. (Leroy E. Alexander, *X-ray diffraction procedures for polycrystalline and amorphous materials*, John Wiley & Sons, 1974.
13 R. Dinnebier and M. Müller, in *Modern Diffraction Methods*, Wiley-VCH Verlag GmbH & Co. KGaA, Weinheim, Germany, 2013, pp. 27–60.
14 A. Altomare, N. Corriero, C. Cuocci, A. Falcicchio, A. Moliterni and R. Rizzi, *J. Appl. Crystallogr.*, 2015, **48**, 598–603.
15 T. Degen, M. Sadki, E. Bron, U. König and G. Nénert, *Powder Diffr.*, 2014, **29**, S13–S18.
16 U. Holzwarth and N. Gibson, *Nat. Nanotechnol.*, 2011, **6**, 534–534.
17 J. S. J. Hargreaves, *Catal. Struct. React.*, 2016, **2**, 33–37.
18 B. H. Toby, *Powder Diffr.*, 2006, **21**, 67–70.
19 Y. G. Andreev, in *Uniting Electron Crystallography and Powder Diffraction*, ed. W. I. . D. Ute Kolb, Kenneth Shankland, Louisa Meshi, Anatoly Avilov, Springer Netherlands, 2012, pp. 195–205.
20 O. S. Edwards and H. Lipson, *Proc. R. Soc. A Math. Phys. Eng. Sci.*, 1942, **180**, 268–277.
21 A. Longo, L. Sciortino, F. Giannici and A. Martorana, *J. Appl. Crystallogr.*, 2014, **47**, 1562–1568.
22 W. H. Press, *Numerical recipes in FORTRAN : the art of scientific computing*, Cambridge University Press, 1992.
23 F. James, *Unpublished*, 1994, 50.
24 F. James and M. Roos, *Comput. Phys. Commun.*, 1975, **10**, 343–367.
25 S. W. T. Price, D. J. Martin, A. D. Parsons, W. A. Sławiński, A. Vamvakeros, S. J. Keylock, A. M. Beale and J. F. W. Mosselmans, *Sci. Adv.*, 2017, **3**, e1602838.
26 S. Calvin, *XAFS for Everyone*, CRC Press, 2018.
27 XAFS database, http://ixs.iit.edu/database/, (accessed 8 March 2018).
28 T. Yamamoto, *X-Ray Spectrom.*, 2008, **37**, 572–584.
29 F. De Groot, G. Vankó and P. Glatzel, *J. Phys. Condens. Matter*, 2009, **21**, 104207.
30 B. Ravel and M. Newville, in *Journal of Synchrotron Radiation*, 2005, vol. 12, pp. 537–541.
31 K. V. Klementev, *Nucl. Instruments Methods Phys. Res. Sect. A Accel. Spectrometers, Detect. Assoc. Equip.*, 2000, **448**, 299–301.
32 The Ifeffit Archives, http://millenia.cars.aps.anl.gov/pipermail/ifeffit/, (accessed 20 October 2017).
33 *Pure Appl. Chem.*, 2015, **87**, 1051.
34 M. Thommes, *Ser. Chem. Eng.*, 2004, **4**, 317–364.
35 Quantachrome Instruments, Autosorb(TM): automated gas sorption analyzer, http://www.uni-export.com.pl/files/Qchrome/autosorb_iQ.pdf, (accessed 12 March 2018).

36 Gatan, GMS 3 Software Registration | Gatan, Inc., http://www.gatan.com/datasheets/gms-3-software-registration, (accessed 12 March 2018).
37 ImageJ User Guide - IJ 1.46r, https://imagej.nih.gov/ij/docs/guide/index.html, (accessed 12 March 2018).
38 TA Instruments, TGA Q Series Getting Started Guide, https://engineering.tamu.edu/media/4133232/tga-q500.pdf, (accessed 12 March 2018).
39 R. A. Schoonheydt, *Chem. Soc. Rev.*, 2010, 39, 5051–5066.
40 J. H. Nobbs, *Rev. Prog. Color. Relat. Top.*, 1985, **15**, 66–75.
41 SHIMADZU, UVProbe Multifunctional UV Control Software|Top : SHIMADZU (Shimadzu Corporation), https://www.shimadzu.com/an/molecular_spectro/uv/uvprobe/probe.html, (accessed 12 March 2018).
42 J. P. Spatz, S. Mo, C. Hartmann, M. Mo, D.- Ulm, T. Herzog, M. Krieger, H. Boyen, P. Ziemann and F. Ju, *Langmuir*, 2000, **16 (2)**, 407–415.
43 H.-G. Boyen, G. Kästle, K. Zürn, T. Herzog, F. Weigl, P. Ziemann, O. Mayer, C. Jerome, M. Möller, J. P. Spatz, M. G. Garnier and P. Oelhafen, *Adv. Funct. Mater.*, 2003, **13**, 359–364.
44 J. P. Spatz, S. Mößmer and M. Möller, *Chem. - A Eur. J.*, 1996, **2**, 1552–1555.
45 S. Alayoglu, S. K. Beaumont, G. Melaet, A. E. Lindeman, N. Musselwhite, C. J. Brooks, M. A. Marcus, J. Guo, Z. Liu, N. Kruse and G. A. Somorjai, *J. Phys. Chem. C*, 2013, **117**, 21803–21809.
46 V. Iablokov, S. K. Beaumont, S. Alayoglu, V. V. Pushkarev, C. Specht, J. Gao, A. P. Alivisatos, N. Kruse and G. A. Somorjai, *Nano Lett.*, 2012, **12**, 3091–3096.
47 S. K. Beaumont, S. Alayoglu, C. Specht, N. Kruse and G. A. Somorjai, *Nano Lett.*, 2014, **14**, 4792–4796.

4. Inverse Micellular Synthesis of Co-based FT Catalysts

4.1. Introduction

The broad focus of this thesis is the examination of particle size effects in cobalt-based Fischer Tropsch Synthesis (FTS) catalysts. The following experimental chapters have examined the behaviour of two Co/MCF-17(silica) catalysts of two different sizes, synthesised using a standard Schlenk technique developed by S.K. Beaumont (Durham University), by *operando* X-ray techniques. This chapter deals primarily with the synthesis and characterisation of a Co/SiO_2 FTS catalyst prepared via an inverse micellular synthesis (IMS) technique – an approach successfully applied to nanoparticle samples supported on flat substrates – to powdered support.

Industrial FTS catalysts typically have a larger average particle size and size distribution than what is thought to be optimum – mostly due to practical and economic restraints.[1] However, when studying such a catalyst with a broad particle size distribution it is difficult to determine what size range is responsible for any given behaviour.[2] In practice it is often assumed that the average particle size is responsible for any behavioural responses, however it is possible that particles of sizes less abundant in the sample have a disproportionate effect. The study of model catalysts with a narrow particle size distribution can determine the true effect of particle size.

Microemulsion methods are well suited to the synthesis of model catalysts as they ensure a maximum NP size limit, maintain the desired NP shape, and limit particle aggregation.[2] These methods typically involve the encapsulation of a metal precursor, within a micelle formed of a surfactant dissolved in a solvent. Surfactants lower interfacial surface tension between two phases (either two liquid phases or a solid and liquid phase) and are formed of a hydrophilic head and hydrophobic tail. Above a critical concentration the surfactant self-assembles to form a micelle (although other shaped structures are possible at higher concentrations). Metal salts can then be encapsulated within the micelles and the resulting structures deposited onto a support. Key limitations of microemulsion

techniques are their low production yields, the need for large volumes of solvent (in this case toluene), and the difficulty fully removing the residual polymer/capping agent.[3]

The microemulsion method used in this work is IMS using a block co-polymer surfactant. The theory of micelle formation is discussed more fully in chapter 3. IMS using block copolymers has been widely applied to the synthesis of gold nanoparticles,[4–9] however has been applied less frequently to cobalt systems.[10,11]

Block copolymers form micelles at lower concentrations than other surfactants allowing the formation of smaller nanoparticles at lower loadings (the CMC of PS-P2VP is 0.1 mg/mL compared to 94 mg/mL for TTABr[12]). They are also more stable in comparison to other common surfactants and therefore do not require the addition of a stabiliser, as well as being capable of encapsulating a wider range of metals.[9] While there are advantages to using block copolymer surfactants they are very expensive,[13] which is often prohibitive.

IMS using block-copolymers has been widely used to produce gold nanoparticles on 2D supports,[4–7] and have been used to synthesize gold and palladium nanoparticles on powder oxide supports.[14] In the gold system a gold salt (typically $HAuCl_4$), is added to a micelle solution of the block copolymer in toluene.[4–7] The salt is encapsulated in the micelle cores, forming $AuCl_4^-$ counterions[4] bonded to the PV units in the micelle core.[7] The metal encapsulated micelles are deposited onto 2D supports by dip coating,[6,7] or on 3D supports by drying of the solution once the support has been added.[14] Some studies use hydrazine to reduce the gold while still in the micelle core,[4,15] while others rely on the later plasma treatment to reduce the gold.[6,7]

The chemical composition of cobalt encapsulated micelles using this method is less well interrogated than that of gold systems. Cobalt salts take longer to encapsulate than noble metals, taking approximately two weeks.[10] Therefore, the greater stability over a longer period provided by using the polymer surfactant is necessary for this system.

The final step in the synthesis involves the removal of the polymer from the sample, so that the catalyst surface can be accessible to the reactants.[16]

However, this must also be done by a technique that conserves the tight particle size control and separation of nanoparticles on the support. In the literature this is achieve by O_2 plasma treatment,[4–7] which has been shown to fully remove the polymer on 2D supports by XPS studies.[4,6,7] This could also be achieved by conventional thermal treatments, but with the risk of particle migration over the support surface and sintering of the nanoparticles.[6]

The species present after plasma treatment is dependent on the metal used. In the case of gold, plasma treatment results in the presence of both metallic and oxidic gold, with the Au^{3+} was observed in several studies to be in the form of an oxide shell.[6,16] However less noble metals, such as cobalt and iron, form only oxides when exposed to plasma treatment alone.[4,5]

4.2. Methodology

First a 0.5 wt% solution of PS-P2VP (PS[16000Mn]-P2VP[3500Mn], Polymer Source Inc.) in toluene (Fluka, reagent ≥99.7%) was prepared. Cobalt chloride hexahydrate, $CoCl_2.6H_2O$ (Sigma-Aldrich, 98%) was ground using a mortar and pestle and added to the solution. The $CoCl_2.6H_2O$ mass depended on the desired micelle loading – the ratio of Co^{2+}/2VP units. Solutions were left stirring in a sealed volumetric flask to allow the cobalt to fully encapsulate.

$$m_{salt} = \frac{m_{PS-PVP}.MM_{PVP}.MM_{salt}.L}{MM_{PS-PVP}.MM_{VP}} \quad (4.1)$$

The $CoCl_2.6H_2O$ mass was defined by equation 4.1, where L is the fractional micelle loading (in the range of 0-1), m_{salt} and $m_{PS\text{-}PVP}$ are the mass of the cobalt salt and total polymer respectively, and $MM_{PS\text{-}PVP}$, MM_{PVP} and MM_{VP} are the molecular masses of the total polymer, the PVP blocks and a single VP unit respectively.

Once the cobalt was fully encapsulated, the solutions were then transferred with the silica support to Teflon beakers and left for approximately 24 h to allow the toluene to evaporate.

Finally, the catalysts underwent a treatment intended to remove the polymer from the samples - plasma treatment or calcination. The plasma treatments were performed using a Femto Plasma System from Diener Electronics, in a flow of compressed air (20.9 % O_2), of 10 ml/min at a potency of 100 %. Calcinations were performed using a furnace in air at a range of temperatures, times, and ramp rates. Both *Operando* and *ex situ* XAS measurements were collected on BM26A (DUBBLE) at the European Synchrotron Radiation Facility (ESRF) and recorded at the Co k-edge (7.712 keV). During *ex situ* XAS measurements the catalysts were pressed into spectroscopic pellets, the mass of which was calculated (using XAFSmass[18]). Small quantities of glucose were added to bulk out the most concentrated sample (15 wt %) as the sample was too thin and fragile to attach to the sample holder.

Additional *ex situ* XAS measurements were recorded of the Co micelle solutions on BM26A. These were recorded in Florescence mode due to the low concentration of cobalt in the solutions, using a 9-element monolithic Ge detector (Ortec).

Operando XAS measurements were performed using the same procedure as the other experimental chapters. Samples were packed into 1 mm diameter capillaries, which were mounted in the BM26A sample environment cell, and secured in place using high temperature epoxy resin. The catalyst was pre-treated; first a treatment in He then oxygen to clean the surface of the Co_3O_4 nanoparticles using a temperature ramp of room temperature to 350 °C at a ramp rate of 5 °C/min in a flow of He, then from 350 °C to 550 °C at a ramp rate of 10 °C/min in a flow of O_2/He. Secondly the catalyst was then reduced under a flow H_2 from 150 °C to 550 °C at a rate of 2 °C/min. Total gas flow was 10 ml/min corresponding to a gas hourly space velocity (GHSV) of 10000 h^{-1} and the temperature was controlled using a heat gun. XAS data was normalised and analysed in Artemis.[19]

Powder XRD measurements were performed using a Rigaku MiniFlex diffractometer and a Rigaku Smartlab diffractometer in the Materials Characterisation Laboratory at ISIS. Both diffractometers are equipped with a Cu K_α source (λ=0.15418 nm). The MiniFlex desktop diffractometer uses flat plate

sample holders and these measurements were taken at room temperature between a range of 5–85° 2θ, with a 2θ step of 0.01° and a sample spin speed of 1.2-1.4 °/min.

Temperature dependant (pseudo *in situ*) measurements were recorded using the Smartlab diffractometer set up with an Anton Paar HTK hot stage (performed in air), measured between 2-55° 2θ, at a 2θ step of 0.01° and at a sample spin speed of 0.4 °/min. Measurements were recorded at room temperature, and held for 2 h at 240, 550 and 800 °C with a temperature ramp rate of 5 °C/min. Rigaku PDXL X-ray powder diffraction software was used for sample measurement and instrument control, phase identification and data processing was performed using QualX2.[20]

Silica surface areas were determined using nitrogen absorption-desorption isotherms. Samples were degassed at 190 °C for 3 h in a FLOVAC degasser, then isotherms were collected at 77 K using a Quadrasorb evo (Quantachrome Instruments). The surface areas of the silicas were determined using multi-point BET (Brunauer–Emmett–Teller), and the pore volumes and pore radii were calculated using BJH (Barrett–Joyner–Halenda). All surface area data analysis was performed using the ASiQWin software.[21]

Transmission electron microscopy (TEM) images were captured using a Jeol-2100 (200 keV accelerating voltage) at the Research Complex at Harwell. Images were captured by Gatan DigitalMicrograph[22] and the particle sizes were obtained using ImageJ.[23]

Thermogravimetric analysis (TGA) measurements were obtained with a TGA Q50 (TA Instruments) and the data was collected and analysed using the QSeries software.[24] The samples were heated from room temperature to 550 °C with a temperature ramp rate of 5 °C/min, in steps of 0.1 °C and in a flow of air.

UV-Vis spectra were collected for both powders and micellular solutions. UV-Vis spectra for powder samples were collected using an UV-2600 UV-Vis spectrometer (Shimadzu). Most measurements were taken between 450 nm and 800 nm while others were taken between 200 nm and 1400 nm, all in steps of 0.5 nm. UV-Vis spectra of the micellular solutions were collected using a UV-1800 UV-Vis Spectrophotometer (Shimadzu). The solutions were held in plastic

cuvettes and measurements were recorded between 300 nm and 1100 nm in steps of 0.5 nm. The data was collected and analysed by both spectrometers using the software UVProbe 2.43.

4.3. Results

4.3.1. Cobalt encapsulated micelle solutions

The first stage of IMS is the encapsulation of cobalt into the micelle cores. The focus of this sub-section is on characterising the Co micelle solution using UV-Vis spectrometry and XAS in order to identify the cobalt species present, to better understand the evolving local Co state in the IMS system.

UV-Vis spectrometry was performed on a powder sample, a Co encapsulated micelle solution, a micelle solution alone, and a solution of $CoCl_2.6H_2O$ in distilled water (Figure 4.1). The powder sample is 5 wt% Co/SiO_2 L=1 which was not calcined, or plasma treated. Although intensity varies between the powder samples, the wavelength of shoulders is similar in the UV-Vis spectra of all powder samples measured.

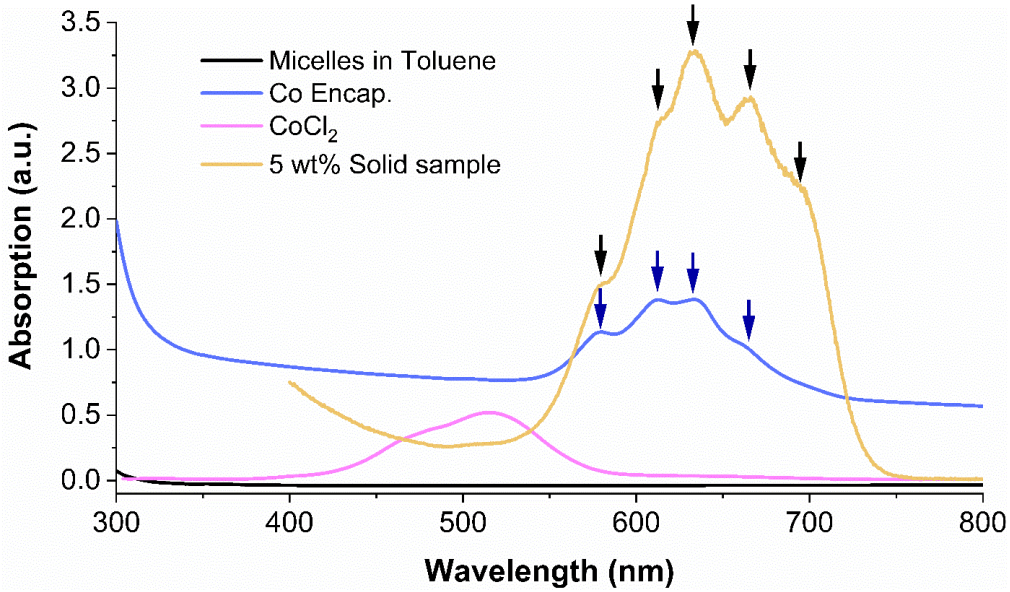

Figure 4.1: UV-Vis spectra of a 5 wt% Co/SiO_2 L=1 solid sample, a micelle only solution, an encapsulated cobalt solution, and *a solution of $CoCl_2$ in distilled water. Arrows indicate the position of the bands in the cobalt-based samples. Dark blue arrows for the Co micelle solution: bands at 580, 613, 634 and 661 nm. Black arrows for the powdered sample: the same bands plus one at 695 nm.*

The Co encapsulated solution, and the Co/SiO_2 powder sample UV-Vis spectra strongly resemble one another suggesting the Co micelles and the deposited Co-species have similar coordination environments. Neither the spectra of the Co micelle solution or the Co/SiO_2 sample resemble the $CoCl_2$ solution, as the $CoCl_2$ absorption feature is shifted approximately 150 nm lower in wavelength than in both the Co samples. As the structures are different and no strong $CoCl_2.6H_2O$ features are present in the sample it is most probable that the vast majority of the Co-species have been encapsulated within the micelle core, forming a different structure.

The Co/SiO_2 sample in Figure 4.1 is typical of all the dried and plasma treated samples. They possess the common feature of a broad peak between 540 and 750 nm with five shoulders at 580, 613, 634, 661 and 695 nm corresponding to overlapping bands. The bands with peak maximums at 634, 613 and 580 nm correspond to the $\upsilon_3[^4A_2(F) \rightarrow {}^4T_1(P)]$ transition of Co^{2+} in a tetrahedral ligand field accounting for the blue colour of the samples.[25] It is possible that the other features in the spectra are due to some interaction between the Co and O within the micelle core, which would result in both tetrahedral and octahedral Co being present in the system.[33] However, it may also be possible that either of these two extra bands are part of a split band caused by the Jahn-Teller effect in tetrahedral or octahedral Co^{3+} species.[26]

Similar spectral features are observed in the UV-Vis spectra of the encapsulated cobalt solution (Figure 4.1) at 580, 613, 634 and 661 nm and in the dried, uncalcined catalyst. It is notable however, that the transition which appears at 695 nm in the UV-Vis of the solid sample is not present in that of the encapsulated solution, suggesting some coordination change on drying or deposition. It is not possible to determine more information with UV-Vis alone, so additional XAS measurements were recorded.

Figure 4.2a and b are the XANES and EXAFS spectra of a 0.5 wt. % solution of cobalt encapsulated in inverse PS-PVP micelles compared to a series of reference compounds. The cobalt species present in the micelle cores is challenging to identify as the spectra has features that do not match the most common cobalt species. Aside from the cobalt in the system, the other available

atomic species the cobalt could be interacting within the micelle cores are nitrogen from the PVP units of the polymer, chlorine that was also introduced into the system in the $CoCl_2.6H_2O$, and oxygen from the H_2O present in both the salt and some impurities in the toluene.

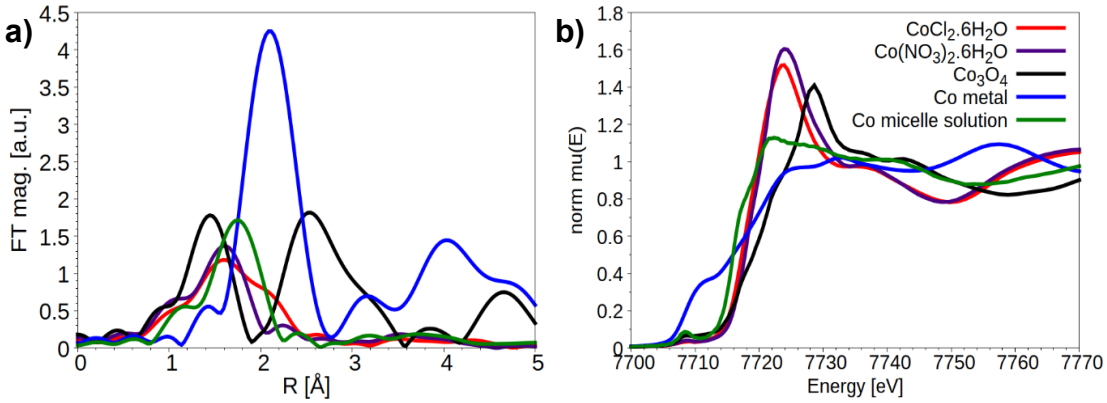

Figure 4.2: Comparison of powder samples of $CoCl_2.6H_20$, $Co(NO_3)_2.6H_2O$, a Co_3O_4 reference, and an example Co micelle solution (0.05 wt%). a) Fourier Transform of EXAFS and b) XANES.

The Co micelle solution has a comparatively large pre-edge peak in the XANES (Figure 4.2b), characteristic of tetrahedral coordination around the cobalt.[27] This is in agreement with the UV-Vis interpretation and rules out CoO and Co^0. The edge energy is shifted lower than in Co_3O_4 samples, which leave N and Cl as potential nearest neighbours.

Table 4.1: Table of bond lengths corresponding to possible 1st shells of the reference EXAFS spectra in Figure 4.2a. Bond length information taken from ISCD except where otherwise indicated.

Species	Bond	Bond length (Å)
Co^0	Co-Co	2.505
CoO	Co-O	2.132
Co_3O_4	Co-O	1.943
$Co(NO_3)_2.6H_2O$	Co-N	1.947
Co_2N	Co-N	1.940
$CoCl_2.6H_2O$	Co-O	2.036
$[CoCl_4]^{2-}$	Co-Cl	2.230[28]

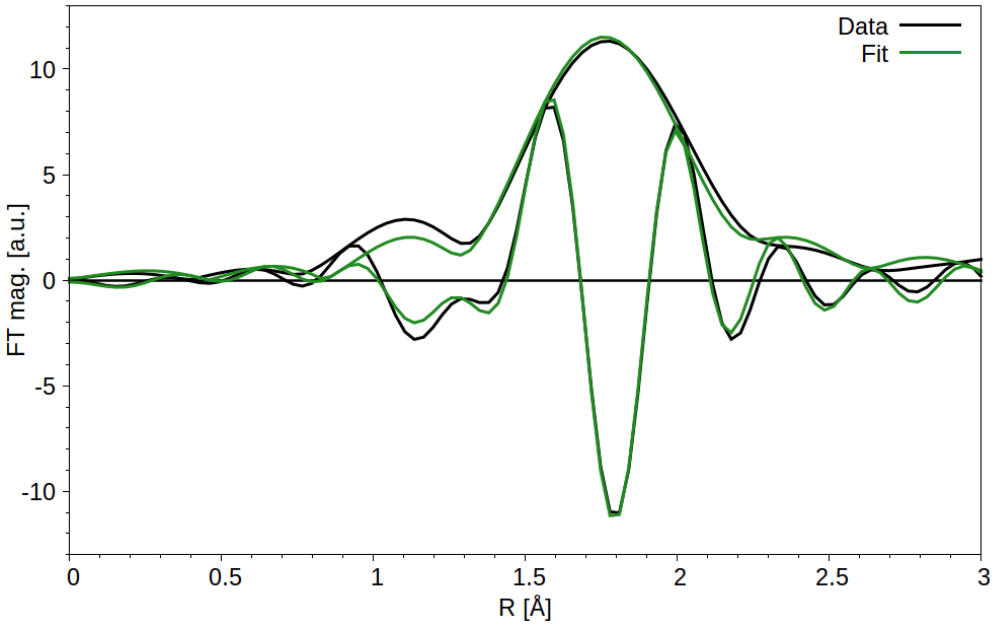

Figure 4.3: Fit of EXAFS spectra of a Co micelle solution 0.05 wt% concentration.

A Co-N first shell EXAFS fit of the Co micelle solution was poor. However, that of a Co-Cl first shell fitted well (Figure 4.3), albeit with a higher bond length (2.215 Å) than that of the $CoCl_2.6H_2O$ reference (Table 4.1 and Figure 4.2), suggestive of a different coordination environment. Additionally, the XANES and the UV-Vis of $CoCl_2.6H_2O$ do not correspond to those of the Co micelle solution. Therefore, most of the Co-Cl shells are from a different system, not residual salt.

Table 4.2: Parameters from first shell fitting of Co-Cl shell in solution and solid sample.

	N	**σ^2**	**e0 (eV)**	**R (Å)**
Co micelle solution	3.5	0.003	-9.19	2.215
Co/SiO2 5wt% L=0.8	3.9	0.007	-1.93	2.149

$[CoCl_4]^{2-}$ ionic solution and some similar complexes have EXAFS and XANES spectra closely resembling that of the Co micelle solution.[28,29] They also possess a similar Co-Cl distance (Table 4.1) and share the characteristic blue colouration. This would also be in line with the behaviour of the gold system. When $HAuCl_4$ is encapsulated in the same type of block copolymer $[AuCl_4]^-$ ions have been shown to be present in the micelle cores.[6] However, both the XANES and EXAFS suggest a change in coordination number and symmetry between

the solution and solid samples. It is possible that on drying and deposition on the SiO_2 the Co expands its coordination to include oxygen from the support.

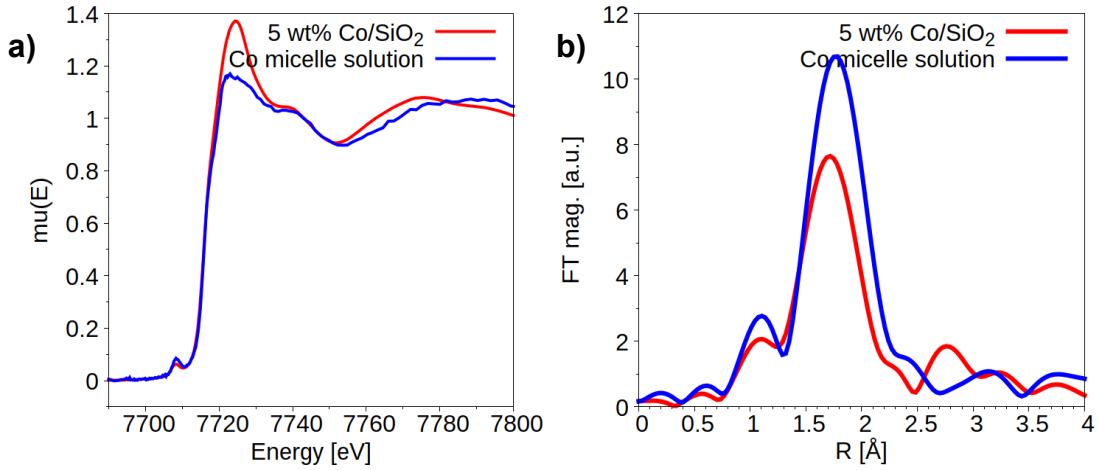

Figure 4.4: XAS spectra of a Co micelle solution of 1 wt % L=0.8 and a Co/SiO_2 solid sample 5 wt% L=0.8.

The deposited and dried solid samples (pre-calcination) and Co micelle solution have similar features in the XAS spectra (Figure 4.4). However, in the XANES, the white line is more intense, and the pre-edge peak is less intense in the solution measurements. The EXAFS first shell fitting of the Co-Cl shell shows a decrease in the coordination number (Table 4.2). Unfortunately, this is not a direct comparison of micelle size as the Co micelle solution was prepared using a larger [30KPS-8.5KPVP] polymer. As a consequence, the micelle cores are larger as can be seen in the EXAFS spectra. However, it is reasonable to say, based on fitting of the EXAFS data (Figure 4.3 and Table 4.2), that the major feature in the spectra is a Co-Cl 1st shell with a bond distance consistent with $[CoCl4]^{2-}$, and that there is some change in coordination between the sample in solution and the Co/SiO_2 sample. Although, the energy shift (e0) for the latter fit is quite high at -9.46 eV.

Due to the differences in XAS between the micelle solution and dried sample discussed above, and the presence of octahedrally coordinated Co in the UV-Vis spectra of the dried sample but not in the micelle solution. It is most likely that in the micelle solution the Co environment is T_d^{2+} and bound to 4 Cl and is 5-6 coordinate Co^{2+} (4 Cl + ½ O) when deposited on SiO_2.

4.3.2. Effect of Metal and Micelle Loading

Once fully encapsulated the SiO_2 supports were added to the solutions. The toluene was then allowed to evaporate from the samples, depositing the micelles onto the supports. This sub-section analyses the characterisation of the dried samples after deposition and examines two key parameters — the micelle and metal loading.

Micelle loading refers to the ratio between cobalt atoms and VP units of the polymer within the micelle core. The higher the micelle loading (L) the larger the quantity of cobalt within each core. Metal loading, on the other hand, refers to the quantity of metal in the catalyst as a percentage of the total mass of the samples.

Co/SiO_2 samples were synthesised with various metal loadings (5, 7, 10, and 12 wt%), on the CAB-O-SIL M5 support with a constant micelle loading of 1. Corresponding XRD patterns are given in Figure 4.5a. The two samples with the lowest loading have low intensity, broad reflections characteristic of the support (reflections at ~21 °2θ, ~23 °2θ, ~39.5 °2θ and ~68.5 °2θ are assigned to the CAB-O-SIL support). The highest percentage weight loaded sample (12 wt%), had visibly more crystalline material than that of the other samples. A phase ID of the XRD pattern (Figure 4.5b), indicates the presence of $CoCl_2.6H_2O$ even after plasma treatment. The 10 wt% sample also shows a small number of these $CoCl_2.6H_2O$ reflections.

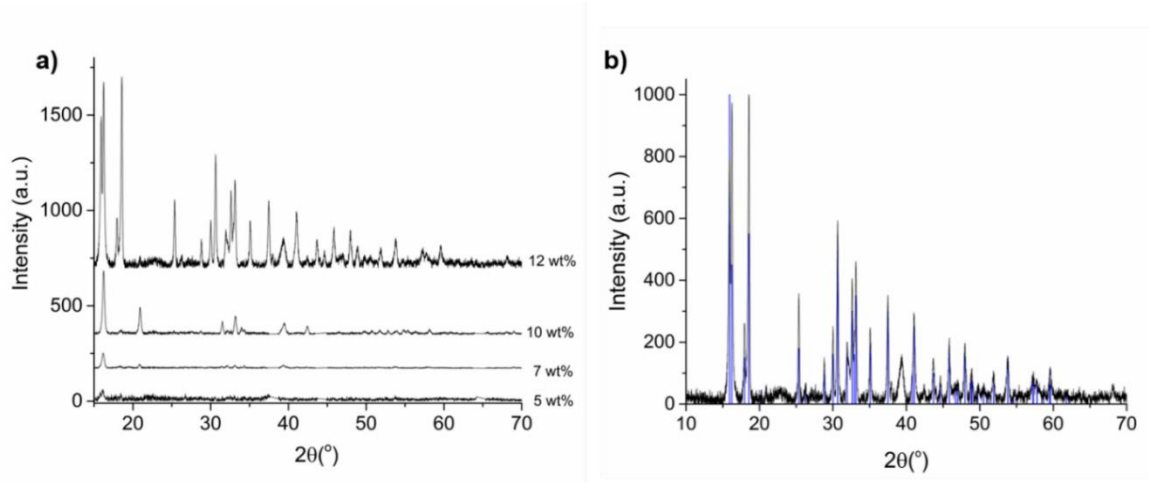

Figure 4.5: a) XRD diffraction *patterns of Co/(CAB-O-SIL M5) L=1 of various metal loadings b) phase ID of 12 wt% CAB-O-SIL M5 samples including $CoCl_2.6H_2O$ reference pattern from PDF2 database.*

Three diffraction peaks have been removed from some diffraction patterns at 38.1, 44.2 and 64.4 °2θ. The peaks have been attributed to the steel sample holder. All diffraction patterns before background subtraction and any removal of peaks attributed to the sample holder are given in appendix 3.

It could be physically possible for the $CoCl_2.6H_2O$ detected by XRD to have been encapsulated within the micelle core, perhaps in the form of a solution in the trace amounts of water present in the toluene. However, both XAS and UV-Vis spectrometry do not observe any $CoCl_2.6H_2O$, as discussed above. This would suggest that the $CoCl_2.6H_2O$ comprises only a small percentage of the overall cobalt content but is present in large enough particles to be detected by XRD. The most likely source of such large particles would be unencapsulated $CoCl_2.6H_2O$. To address this in future samples the $CoCl_2.6H_2O$ could be ground up more thoroughly, even more time could be left for encapsulation, or the solutions could be filtered before deposition.

To evaluate the effect of micelle loading Co/(CAB-O-SIL M5) samples were synthesised by IMS with micelle loadings ranging from 0.5–1.0 with a constant metal loading of 5 wt%. Figure 4.6 shows the corresponding XRD patterns.

It was not possible to phase ID the diffraction patterns shown in Figure 4.6 or the three lower metal loaded samples in Figure 4.5. They all share many of the same features: reflections at 16.2, 18.3, 31.4, 32.0, 39.5, and 53.1 ° 2θ. However, there are some reflections only present in individual patterns (significant reflections at 21.0, 38.0, 42.1 ° 2θ) suggesting there is more than one unidentified phase present. The reflections do not resemble anhydrous $CoCl_2$, Co_2N, or any of the common Co-based phases, and a search of the peak positions through PDF-2 and POW_COD databases using QualX2 generated no results. The intense low angle peak suggests a layered structure. The only component of the system that could realistically form such a structure is the PS-P2VP, however it was not possible to find XRD patterns of the specific polymer and the reflections do not correspond to PS or PVP alone.

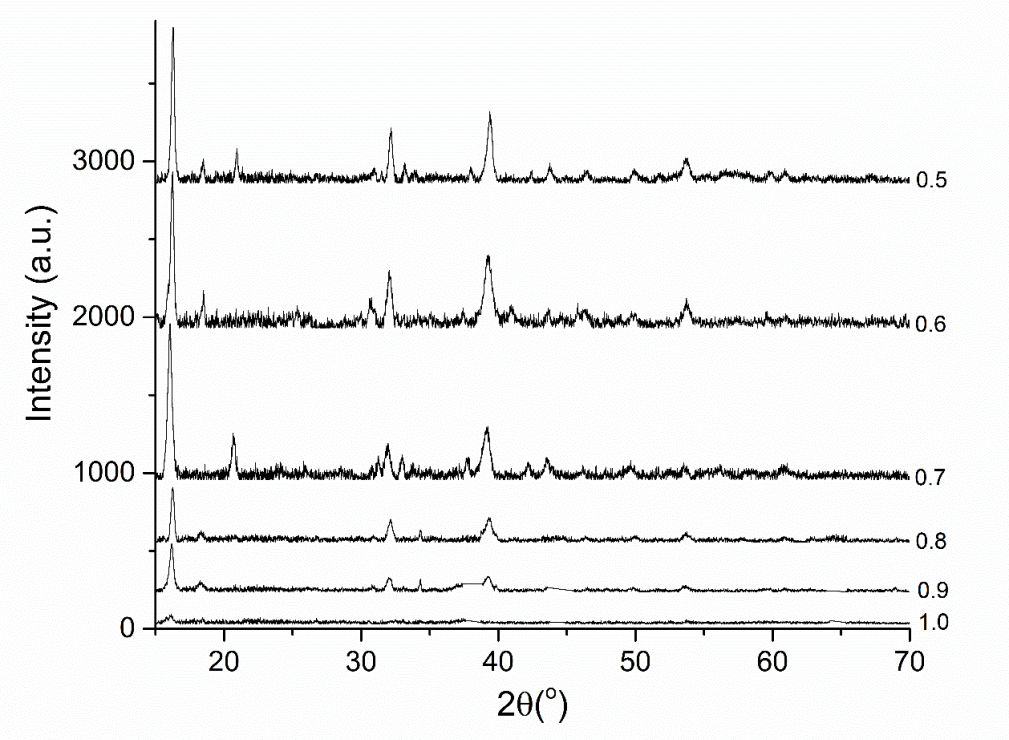

Figure 4.6: XRD diffraction patterns of Co/(CAB-O-SIL M5) 5 wt% of various micelle loadings after plasma treatment of 90 min.

As the metal loading decreases there is an increase in the intensity and narrowing of the reflections, this behaviour would also be consistent with the PS-P2VP as the corresponding phase. As the loading decreases there is more polymer in the system available to form this potentially layered structure (while the metal loading remains constant).

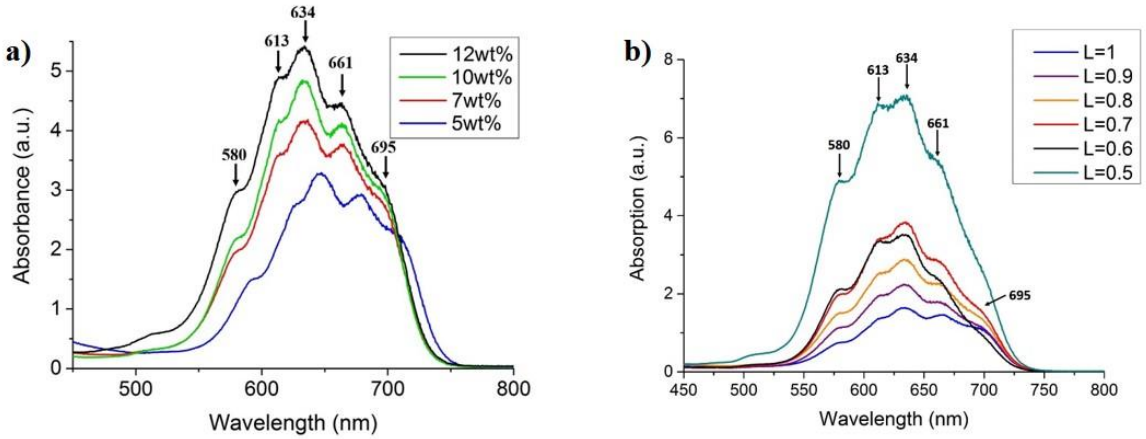

Figure 4.7: UV-Vis spectra of Co/SiO_2 of a) various metal loadings b) various micelle loadings (L).

UV-Vis spectra were also recorded for the samples of both various metal and micelle loadings seen in Figure 4.7a and b respectively. They are discussed together due to their similarity. Both data sets strongly resemble the UV-Vis spectra described earlier in this chapter. The ratios of the peak intensities of the five shoulders of the broad peak between 540 nm and 750 nm do not change significantly as the metal loading increases. While the peak intensities all increase, consistent with an increase in the number of absorbing centres without any sizeable change in the composition of the cobalt content of the samples. The spectra for the 5 wt% samples are shifted to a higher wavelength potentially caused by charge transfer from the ligand to the cobalt.

Variation in the micelle loading (Figure 4.7b), results in a more complex relation in the spectra. Although the amount of cobalt remains constant as micelle loading decreases, and by extension the quantity of the polymer increases the intensity of the peaks increase. Indicating that that the absorbing centres relate to the amount of polymer and that the cobalt absorbing the EM radiation is in the form of a metal complex with aspects of the polymer. Additionally, the ratio of the peak intensity changes with micelle loading. The triplet at 580, 613 and 634 nm assigned to the tetrahedral Co^{2+} transition $\upsilon_3[^4A_2(F)\rightarrow{}^4T_1(P)]$ decreases as micelle loading increases, while the peak at 695 nm assigned to intermetal charge transfer from Co^{2+} to Co^{3+} decreases only slightly. This behaviour may possibly be due to the presence of more Co-ligand-Co interactions at higher micelle loadings, or some variation in the Co-N interactions at lower loadings.

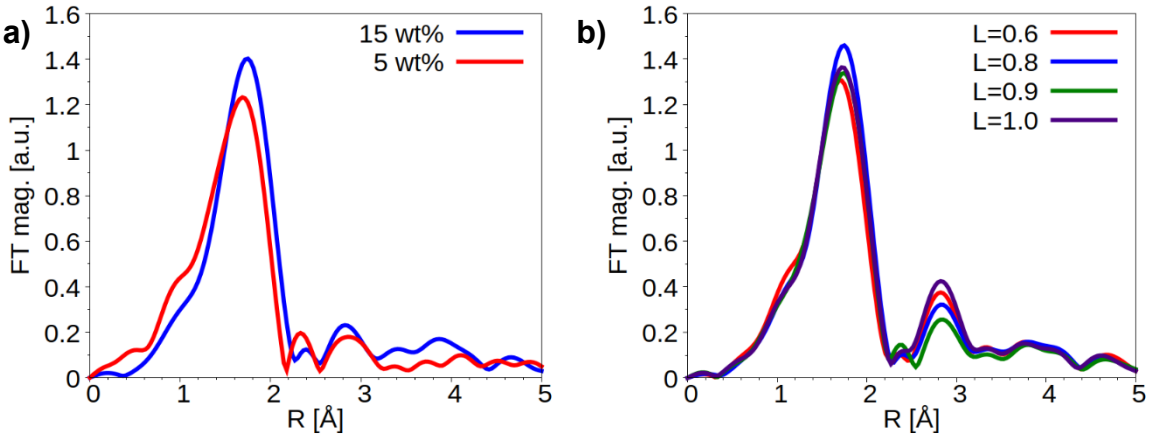

Figure 4.8: Fourier Transforms of EXAFS spectra of Co/(CAB-O-SIL M5) 5 wt% samples of various micelle loadings (0.6, 0.8, 0.9, and 1.0*)*.

Although there is some undefinable variation in the UV-Vis spectra, micelle loading appears to have little effect on the local ordering of the samples as observed using EXAFS (Figure 4.8). Some slight variation is observed, however, there is no obvious trend in the changes with micelle loading.

On the other hand, some variation in the EXAFS is seen between samples of different metal loading. The major feature (a Co-Cl shell), at about 1.8 Å, increases in intensity, which would be consistent with an increase in the local structure order. While R also increases, potentially from an increase in particle size.

4.3.3. Effect of Silica Surface Area

Co/SiO_2 samples were synthesised using SiO_2 supports of various surface areas to determine the effect, if any, of the surface area of the support on particle size and deposition. Nitrogen absorption-desorption measurements were performed on all silica supports from which the surface areas were determined using BET analysis. The values of which are given in Table 4.3 and the corresponding full isotherms are provided in appendix 4.

Table 4.3: Table of silica support specifications used in synthesis.

	Name	**Supplier**	**Purity (%)**	**Particle Size (μm)**	**Surface Area (m^2/g)**
SiO2(a)	Silicon Dioxide	Sigma Aldrich	~99	0.5-10	4.60
SiO2(b)	CAB-O-SIL M5	Acros Organics	99.8	0.2-0.3	120.36
SiO2(c)	Silica, nanopowder	Aldrich Chemistry	99.80	0.012 (primary particle)	108.56
SiO2(d)	Fumed Silica	Sigma Life Sciences	≥ 99.8	0.2-0.3	107.84

The nanoparticles synthesised on the low SA support are clearly visible in TEM images (Figure 4.9). These images show promising sized nanoparticles of 6.20 ± 2.27 nm. However, a large proportion of the nanoparticles have not been deposited on the support, visible on the carbon film of the TEM grid (Figure 4.9b).

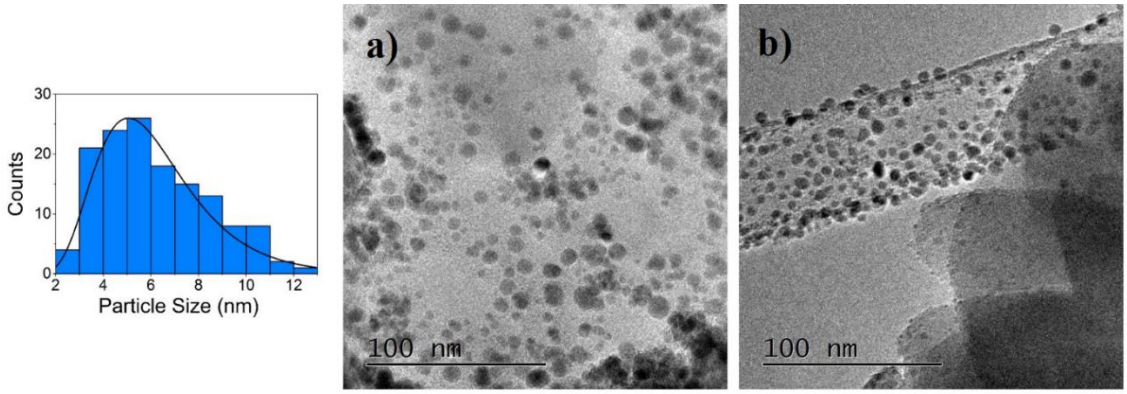

Figure 4.9: TEM images of a plasma treated Co/(low surface area SiO_2). a) on support b) off support and corresponding histogram, particle size 6.20 ± 2.27 nm.

In comparison, TEM images of the high SA silica, CAB-O-SIL M5 and SiO_2 nanopowder, (Figure 4.10) show a negligible quantity of observable nanoparticles off the support. Unfortunately for particle size determination by TEM, the texture (and density) of the high surface area supports obscures any nanoparticles in TEM images and prevents any reliable analysis by that technique.

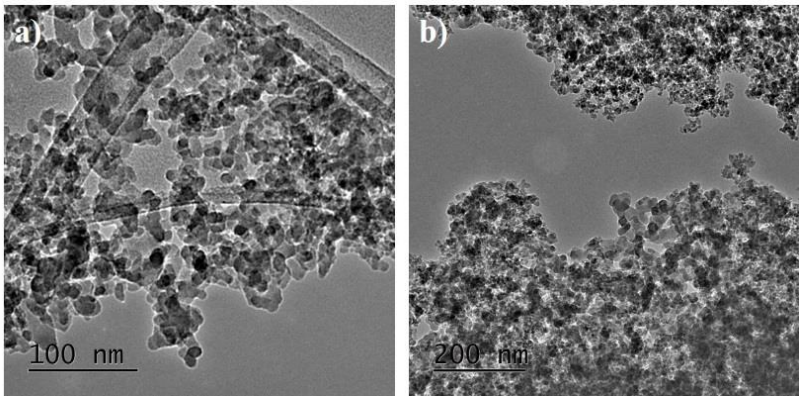

Figure 4.10: TEM images of a) uncalcined Co/(CAB-O-SIL M5)-surface area: 120.36 m_2/g and b) uncalcined Co/(SiO_2 nanopowder) surface area: 108.557 m_2/g.

The difference in nanoparticle deposition between the supports could be caused by the size of the micelles in comparison to the surface area. If more micelles were present in the solution than would fit on the surface of the support, they would be present off the support. However, during drying, toluene evaporates faster from the higher surface area silicas resulting a sample of one colour which appears uniform. Whereas the low surface area supported samples show a gradient of blue, darker at the bottom of the beaker. As the slower

evaporation leads to settling of the remaining solution at the bottom of the beaker producing an inhomogeneous coating. It is probable that the improved saturation of the colour would result in better deposition of the micelles on the support. Either explanation results in a lower-than-expected metal loading on the support surface.

UV-Vis spectra of the uncalcined samples supported on various silica are displayed in Figure 4.11. All the spectra possess the common feature of a broad peak between 540 and 750 nm with five shoulders at 580, 613, 634, 661 and 695 nm corresponding to overlapping bands – most of which were earlier identified as tetrahedral Co^{2+}. The ratio of peak intensities of which vary depending on the silica used suggesting the presence of mixed species. In the previous sub-section, it was shown that the XAS spectra for the Co micelle solutions and solid samples had some differences. The mixed species identified in the UV-Vis may then be due to the same cause, with some differences due to the texture of the support surface.

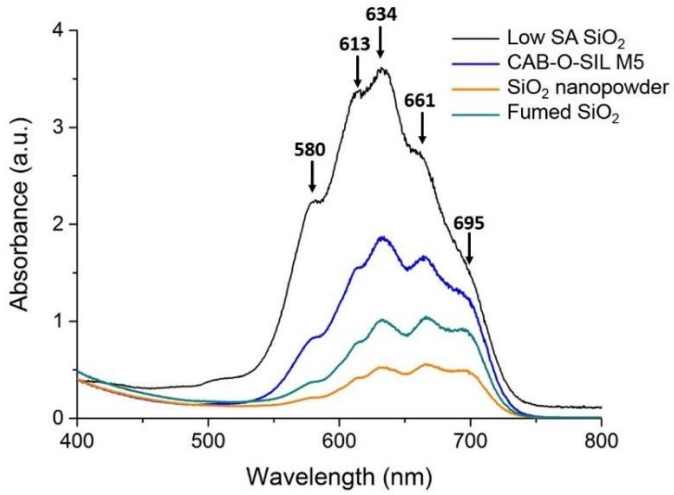

Figure 4.11: UV-Vis spectra of uncalcined Co/SiO_2 using various silica supports.

Some variations in the intensity and peak ratios are observable between the UV-Vis spectra of the samples as the silica support changes from: low SA SiO_2 → CAO-O-SIL M5 → SiO_2 nanopowder → fumed SiO_2. The transitions at 634 nm, 613 nm and 580 nm become more prominent, and the transitions at 661 nm and 695 nm become less pronounced. However, these changes do not appear to correspond to known variations in either the surface area, silica particle

size or Co/SA ratio. Potentially relating to a combination of the two or perhaps even effected by an unknown quality of the various silica supports.

4.3.4. Polymer Removal: Plasma Treatment

The third stage of this IMS method requires the removal of the polymer. Any residual polymer surrounding the nanoparticles will interfere with the functioning of the catalyst[30] and must be removed before FTS. Two methods were used in an attempt to remove the polymer: plasma and heat treatment.

First, plasma treatment was attempted. Samples supported on three different surface area supports were plasma treated for a range of times under 2 h and examined using XAS. Minimal change is observed in the XANES or EXAFS (Figure 4.12) of either of the high surface area supports (Figure 4.12b and c). In Figure 4.12a (EXAFS) there is a significant decrease in the intensity of the feature at 1.8 Å as well as the appearance of a shoulder.

As both samples are from the same original batch, they can be assumed to have closely similar concentrations of cobalt. Therefore, the decrease is likely due to a decrease in Co-species particle size, which is unexpected. However, this is the only sample measured that did not undergo any plasma treatment whatsoever, and this behaviour may be due to the initial stages of plasma treatment rather than some behaviour of the nanoparticles on the low surface area support.

Some variation is also observed in the XANES spectra of samples on different supports (Figure 4.12). The white line intensity increases as the spectra progress from the low surface area support, to the CAB-O-SIL M5, and then to the Silica nanopowder. There is little variation between the XANES spectra of samples on the same support, which suggests that the difference in features is due to some variation between the supports influencing the interaction between the deposited micelles and silica. A similar variation in the white line of XANES spectra was observed between Co-encapsulated micelle solutions and deposited powder samples (Figure 4.4). This was attributed to the difference in Co coordination between the $[CoCl_4]^{2-}$ present in the micelle cores in solution and

the unknown similar structure in the deposited and dried micelles on silica. This change in white line intensity correlates with the decrease in particle size of the support. It may be possible that on supports with larger silica particle size the deposited micelles remain closer in shape to those in solution, resulting in a more similar coordination environment than those on smaller particle size silica. However, from only three samples this is impossible to state conclusively.

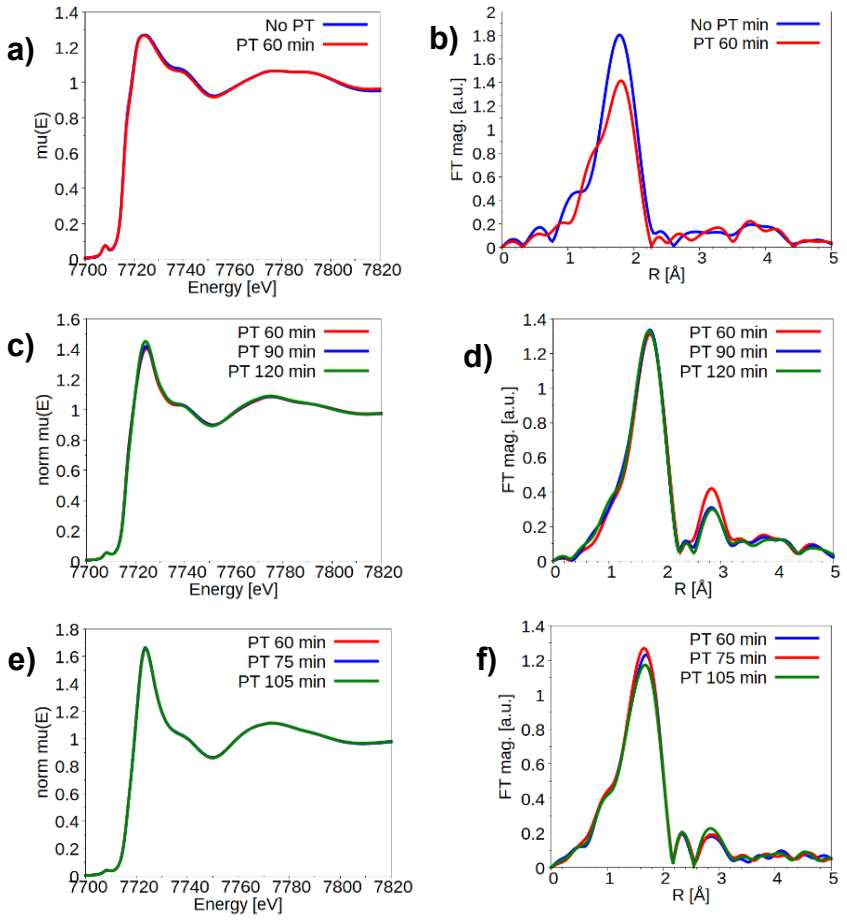

Figure 4.12: Fourier Transforms of the EXAFS and XANES spectra for various length plasma treatments on a) low surface area support b) the CAB-O-SIL M5, and c) Silica nanopowder.

How successful is plasma treatment as a polymer removal treatment? The plasma treatment of samples synthesised using IMS supported on two-dimensional substrates was thought by some to remove the majority of polymer present.[4] TGA measurements of powder silica supported samples indicates that this is not the case here, and that a significant quantity of the polymer remains in the samples even after long plasma treatments.

The relative percentage masses of the initial compounds were calculated using equation 4.1. Then compared with the percentage mass losses measured from the TGA curves. It was assumed that all the water (~45 wt% of the cobalt chloride hexahydrate, $CoCl_2.6H_2O$), was removed from the system during the drying phase as minimal mass loss was observed at, or close to, 100 °C in all the TGA measurements; characteristic of the presence of water. Based on this assumption the relative percentage masses for the initial cobalt compound, polymer, and silica now present in the dried samples in different forms are: 8 % Co, 9 % Cl_2, 46 % PS-P2VP, and 37 % SiO_2.

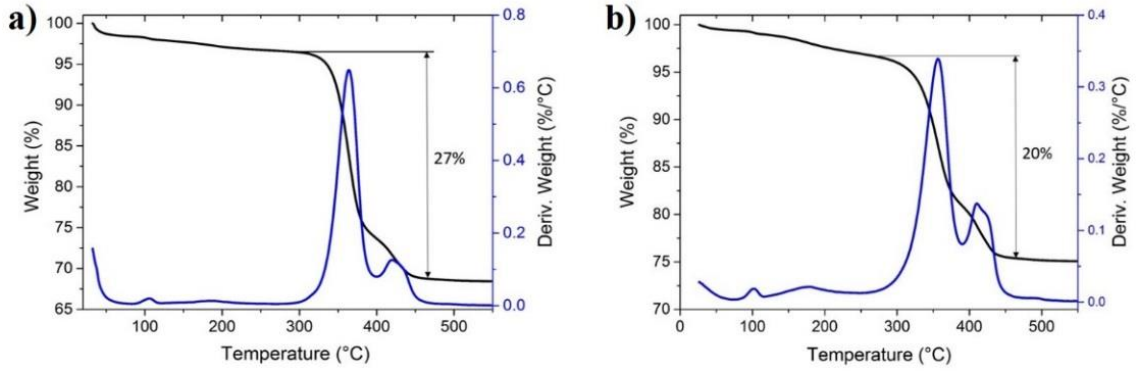

Figure 4.13: TGA curves for a) Co/(SiO_2 nanopowder) not plasma treated b) Co/(SiO_2 nanopowder) after 10 h of plasma treatment.

TGA curves of a Co/(SiO_2 nanopowder) sample which had not been plasma treated and one that had been plasma treated for 10 h are shown in Figure 4.13a and b respectively. Both samples were taken from the same batch to ensure consistent composition. After plasma treatment there is a reduction in the total mass loss of 7 %, mostly from the first stage – 27 % to 20 %. However, this change in mass loss is far lower than the total polymer content (~46 % of the dried sample), therefore the polymer is not fully removed from the sample even after a long plasma treatment of 10 h.

All TGA curves taken of these samples have two stages of mass loss — one at approximately 360 °C and another at 410-420 °C. In earlier work which also analyzed the TGA data discussed here, the two mass losses were assigned to the polymer and cobalt species decomposition. However, it is more challenging to identify the contribution from each component of the system unambiguously as the system has changed meaningfully from the initial components. The cobalt

added to the polymer solution was in the form of cobalt chloride hexahydrate ($CoCl_2.6H_2O$), but in the dried sample was shown to be closer to $[CoCl_4]^{2-}$ in structure. Also, the polymer formed micelles in solution, and there is some evidence of laminar structures forming during the drying phase. The system has changed so much that it is no longer possible to accurately model the thermal behaviour with the TGA curves of the initial compounds. Although they are included in appendix 5 for completeness. However, even without quantification, it remains clear from TGA measurements that a significant quantity of polymer remains after plasma treatments as the mass loss is far lower than the total polymer mass in the sample.

TGA curves were measured for various plasma treatment times up to 10 h. A trend is observed in the mass loss (shown in Figure 4.14). As plasma treatment time increases the mass loss decreases. Therefore, plasma treatment has an effect on the samples, removing some of the mass. However, this relationship plateaus after about 200-300 minutes suggesting a limit has been reached in the effect of plasma treatment on the samples.

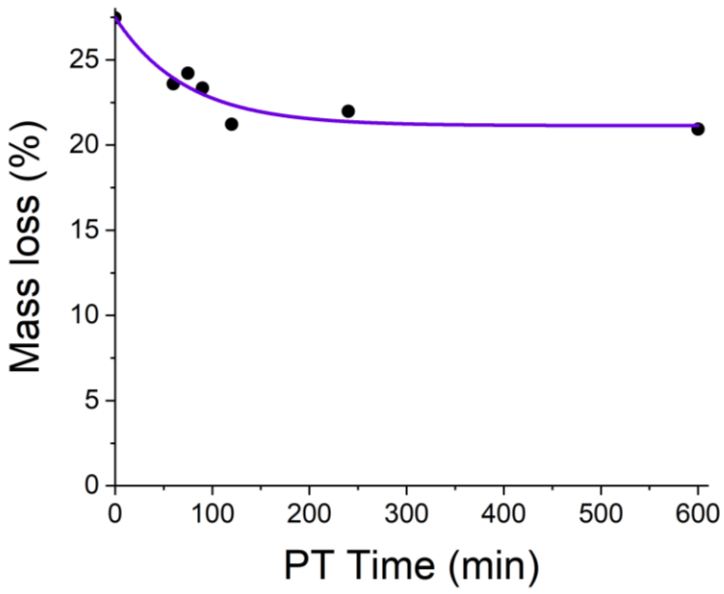

Figure 4.14: Graph of the mass loss observed from TGA measurements of various Co/(SiO_2 nanopowder) 5 wt% Co loading dried samples after various plasma treatment times.

It is interesting to note that the change in mass loss observed with increasing plasma treatment time is mostly from the first mass loss. Appendix 7

separates and plots the behaviour of the first and second mass losses for different plasma treatment times.

The change in mass loss may be due to the decomposition of various compounds. However, of the components of the system, the polymer is the most vulnerable to plasma and UV radiation exposure (both present during plasma treatment) and is the largest component (~46 %). It is reasonable to expect the polymer decomposition to be a meaningful percentage of the change in mass loss.

The mass loss may also include residual chlorine, although it is present in a far smaller weight percentage (9 %), than the polymer. Additionally, it is possible that the silica may also be affected by plasma treatment. However, surface area determination via BHJ of the various silicas alone not plasma treated and after 120 min of plasma treatment were compared (Table 4.4) and shown little variation, suggesting that plasma treatment has little effect on these silicas. The corresponding isotherms are shown in appendix 4.

Table 4.4: Table of surface areas, pore volumes, and pore radii for three silica samples without plasma treatment and after 120 min of plasma treatment.

	Plasma treatment	**Surface area (m^2/g)**	**Pore volume (cc/g)**	**Pore radius (Å)**
Silicon Dioxide	No PT	5	0.02	19
Silicon Dioxide	120 m	5	0.02	19
CAB-O-SIL M5	No PT	120	0.43	15
CAB-O-SIL M5	120 m	121	0.43	16
Silica, nanopowder	No PT	108	0.38	15
Silica, nanopowder	120 m	109	0.40	15

In summary, TGA measurements show that, while some mass loss is observed after plasma treatment, it is significantly less mass than that of the quantity of polymer in the dried sample. Therefore, plasma treatment does not remove a significant quantity of the polymer and is not a viable method of removing it from the dried samples.

The continued presence of large quantities of polymer post plasma treatment would also be consistent with the behaviour of nanoparticles calcined after plasma treatment and while under TEM. Triangular projections are seen in

the TEM image in Figure 4.15a, suggestive of truncated cobalt triangular platelets as in seen in earlier work (appendix 8), where similar samples were calcined at 500 °C without plasma treatment. This effect was attributed to the additional energy present in the system from the exothermic decomposition of the polymer. It is worth noting that the shape of the nanoparticles resemble those seen in PVP capped cobalt nanoparticles,[31] which may suggest that the polymer remains surrounding the nanoparticles effectively capping them even after plasma treatment.

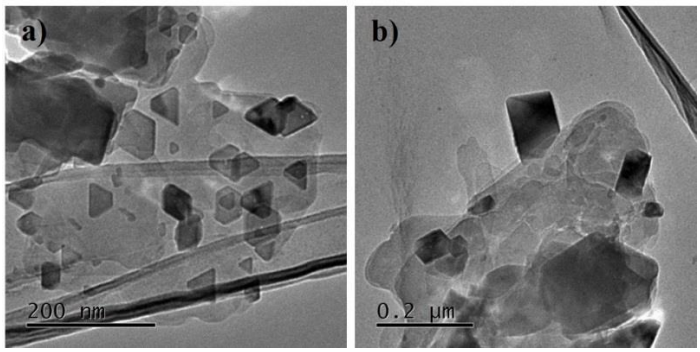

Figure 4.15: TEM images of Co/(low SA SiO_2) 5 wt% plasma treated for 90 min then calcined at 500 °C for 2h.

4.3.5. Polymer Removal: Multiple Heat Treatments

Above, plasma treatment was shown to have limited effect on the calcination of the samples. This is most likely due to the exothermic decomposition of the polymer adding energy to the system resulting in significant sintering of the nano-particles. An alternative method of polymer removal was therefore necessary. However, high temperature calcinations were previously shown to cause considerable sintering resulting in very large particles, in the order of 50 nm, of varying shapes (Figure 4.15 and appendix 8). It was hypothesized that by performing an initial lower temperature treatment before the higher temperature calcination it would be possible to decompose the majority of the polymer first, minimalizing sintering.

A series of Co/SiO_2 samples (5 wt% supported on low SA SiO_2) were synthesised using IMS and were initially calcined in air at 210, 240 and 315 °C.

All were finally subjected to a higher temperature calcination at 550 °C, also performed in air.

The low surface area silica was chosen as the support so it would be possible to capture TEM images (higher SA supports had earlier proved to obscure nanoparticles in TEM images) and determine particle size through that method. After each calcination TEM was performed on the samples to determine particle size, standard deviation in size, and to obtain an idea of particle shape. It was not possible to obtain TEM images before the low temperature calcinations due to the fast rate of beam damage of samples which contained large quantities of polymer.

A visible colour difference was observed between the samples after the initial heat treatments. At 210 °C the sample was a slightly darker blue than that of the untreated samples, at 240 °C it was a black-green colour and after 315 °C black, consistent with Co_3O_4.

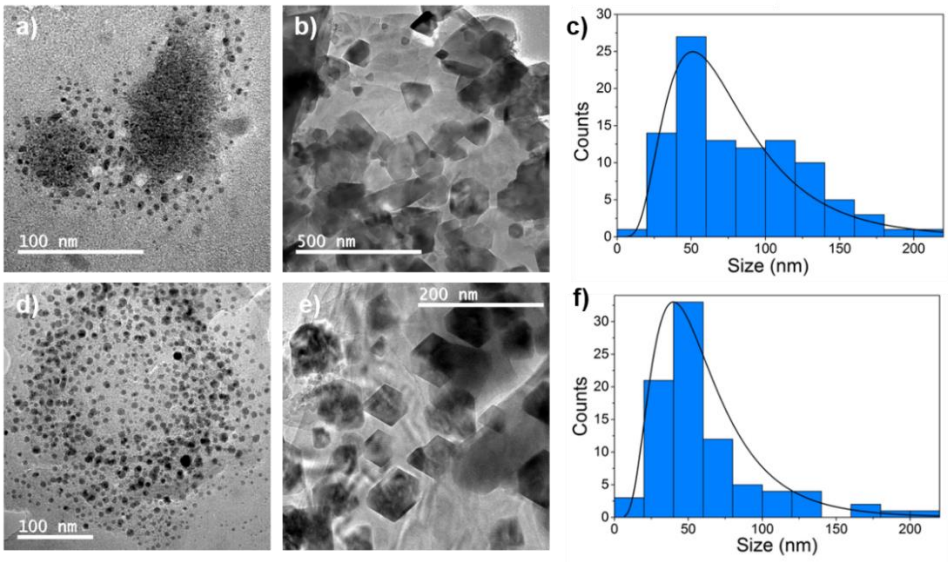

Figure 4.16: TEM images all of Co/(low SA SiO_2) 5 wt% L=1 sample. Sample calcined at 210 °C and then at 550 °C a) Particles not deposited on support b) those deposited on the support and c) particle size distribution of particles on support. And TEM images of sample calcined at 240 °C and then at 550 °C, d) Particles not deposited on support e) those deposited on the support and f) particle size distribution of particles on support.

During TEM, the samples which were only calcined at 210 °C and 240 °C were beam damaged relatively quickly (in a matter of minutes) which suggests the continued presence of the polymer based on previous observations. The

mean particle sizes and corresponding standard deviations at various stages of the calcination procedure for the initial calcination at 210 °C or 240 °C are given in Table 4.5.

The TEM images taken at various stages throughout the synthesis (for both samples, either plasma treatment or those which have been calcined) all include particles which were not deposited on the support. Their presence at all stages of the synthesis suggests that this is a failure to deposit the cobalt encapsulated micelles onto the support during the evaporation of the solvent, which has been shown to be less prominent on high SA supports in chapter 4 section 4.3.3.

Table 4.5: Table of values of average particle size and standard deviation of Co/SiO_2 samples treated by multiple calcinations initially at 210 °C or 240 °C measured from TEM images.

	Co/(Low SA SiO_2) 5 wt% L=1 210 °C				**Co/(Low SA SiO_2) 5 wt% L=1.0 240 °C**			
	1st Cal: 210 °C		**1st Cal: 210 °C 2nd Cal: 550 °C**		**1st Cal: 240 °C**		**1st Cal: 240 °C 2nd Cal: 550 °C**	
	On Support	**Off Support**	**On Support**	**Off Support**	**On Support**	**Off Support**	**On Support**	**Off Support**
Mean Particle Size (nm)	-	27.83	78.67	4.23	-	7.24	61.85	5.49
Std. Dev.	-	12.41	41.19	1.26	-	2.55	37.46	7.53

Clear TEM images of the first low temperature calcinations (210 °C and 240 °C) were impossible to capture due to the polymer beam damage. Once calcined a second time the particles are visible, large, and of irregular shapes. The size of the particles not on the support decrease significantly after the high temperature calcination as they are more exposed to conditions than those on the support.

Further Co/SiO_2 samples were then synthesised using the higher initial heat treatment of 315 °C, again followed by a calcination at 550 °C. Two batches of samples were prepared with different micelle loadings of L=1 and L=0.5, to examine the effect of micelle loading on the nanoparticles during the multiple

calcinations. The mean particle sizes and corresponding standard deviations at various stages of the calcination procedure for the multiple micelle loadings are given in Table 4.6.

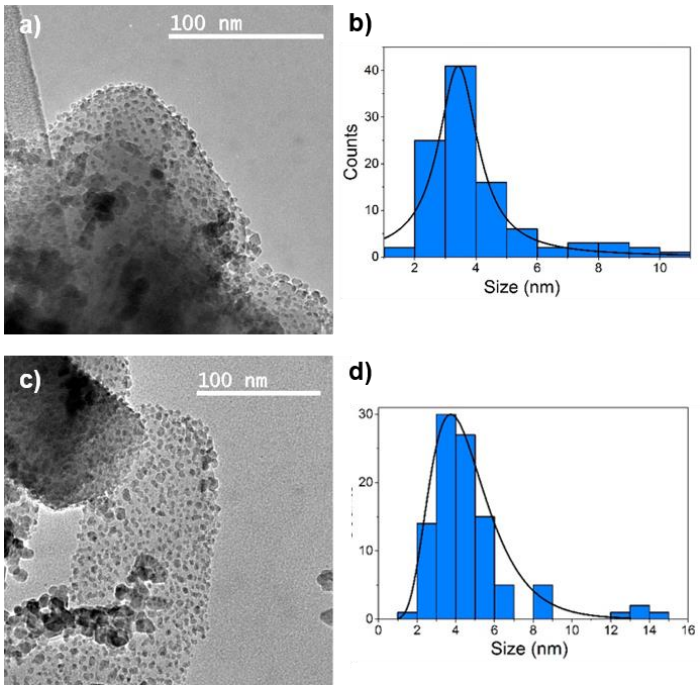

Figure 4.17: Co/(low SA SiO_2) 5 wt% L=0.5 a) TEM image after initial 315 °C calcination and b) corresponding particle size distribution. C) TEM image after 315 °C and 550 °C calcinations and d) corresponding particle size distribution.

Table 4.6: Values for particle size and standard deviation of Co/(Low SA SiO_2) samples of micelle loadings of L=0.5 and 1.0 treated by multiple calcinations initially at 315 °C measured from TEM images.

	Co/(Low SA SiO_2) 5 wt% L=0.5				**Co/(Low SA SiO_2) 5 wt% L=1.0**			
	1st Cal: 315 °C		**1st Cal: 315 °C 2nd Cal: 550 °C**		**1st Cal: 315 °C**		**1st Cal: 315 °C 2nd Cal: 550 °C**	
	On Support	**Off Support**	**On Support**	**Off Support**	**On Support**	**Off Support**	**On Support**	**Off Support**
Mean Particle Size (nm)	3.95	3.99	4.75	3.85	5.03	-	5.92	4.75
Std Dev	1.69	0.95	2.29	2.6	2.25	-	4.18	2.29

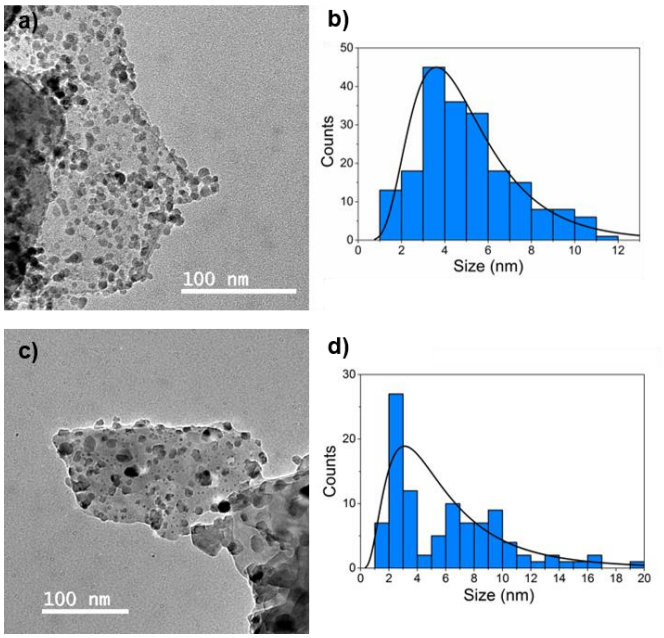

Figure 4.18: Co/(low SA SiO_2) 5 wt% L=1 a) TEM image after initial 300 °C calcination and b) corresponding particle size distribution. C) TEM image after 315 °C and 550 °C calcinations and d) corresponding particle size distribution.

The TEM images of Co/SiO_2 samples calcined at 315 °C only, then after both 315 °C and 550 °C, for micelle loadings of L=0.5 and L=1 are given in Figure 4.17 and Figure 4.18 respectively.

Increases in particle size and size distribution are observed in both samples from the first low temperature calcination to the second higher temperature calcination, and of a similar percentage increase. Those samples of L=0.5 have a lower particle size than those of L=1. This is logical and consistent with the literature.[4] The L=0.5 sample also shows greater particle shape consistency after each subsequent calcination. The behaviour of the off-support particles is similar to that observed in earlier samples (section 4.3.2.). Most particle sizes and standard deviations are substantially lower in those particles which have failed to be deposited onto the support, suggesting interaction with the support has an effect on size.

The smaller particle size distribution in the L=0.5 samples may be related to the Co species in the Co micelle solution. Earlier it was determined that the species present was $[CoCl_4]^{2-}$ or some closely related complex. As the $[CoCl_4]^{2-}$ are counterions to the VP units in the polar core of the micelle, with one lone electron pair available per VP unit, and the charge on the $[CoCl_4]^{2-}$ is 2- then

above a micelle loading of L=0.5 there would be more $[CoCl_4]^{2-}$ than corresponding pyridine units. Any excess $[CoCl_4]^{2-}$ would also be encapsulated, but the excess charge may cause some destabilisation of the micelle, increasing particles size distribution.

Ex situ XAS measurements were performed on three of the multi-calcined samples: 210 °C only, 315 °C only, and 315 °C then 550 °C. A comparison of the XANES spectra for the single calcinations of 210 °C and 315 °C are presented in Figure 4.19. The calcination at 315 °C appears to have decomposed all the $[CoCl_4]^{2-}$ content within the sample – as the XANES has the characteristic features of Co_3O_4 including the edge energy, pre-edge peak and white line intensity. Whereas the 210 °C calcination has not calcined the catalyst, in this case the XANES spectra still closely resembles that of the untreated samples.

In the EXAFS spectra, the 210 °C samples closely resemble the untreated samples (Figure 4.19b). Suggesting the lowest heat treatment temperature had little effect. The spectra of the sample treated at 315 °C, however, is clearly Co_3O_4, and the further calcination at 550 °C seems to result in some sintering as the intensity of the Fourier transform increases. Perhaps a treatment only at 315 °C would be appropriate. However, before running FTS the catalyst would, at the very least, be heated to 550 °C or higher to clean the surface, and so the 315 °C and 550 °C sample is still relevant.

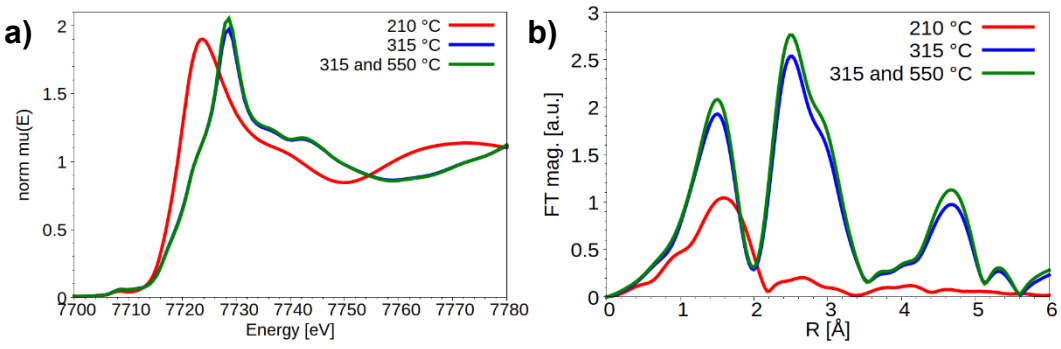

Figure 4.19: A Co/(low SA SiO_2) 5 wt% L=0.5, calcined at 210 °C, 315 °C, 315 °C followed by 550 °C, a) XANES spectra and b) Fourier transforms of the EXAFS spectra.

Temperature dependant XRD measurements were recorded for two samples, one of high metal loading and one of low micelle loading to further investigate the behaviour of the catalysts at various stages of calcination.

The first sample tested was a Co/(low SA SiO_2) of 5 wt% and micelle loading of L=0.5, however the Smartlab diffractometer was not sensitive enough to give clear patterns of these samples (the diffraction patterns from the latter can be seen in appendix 9). Further measurements were taken of a sample of higher metal and micelle loading (Co/(low SA SiO_2) of 12 wt% and micelle loading of L=1.0). Diffraction patterns were recorded at RT, 240°C, 550°C and 800 °C in air with a temperature ramp of 5 °C/min. All measurements above room temperature were recorded after the temperature was held for 2 h in order to allow any phase change to completely occur.

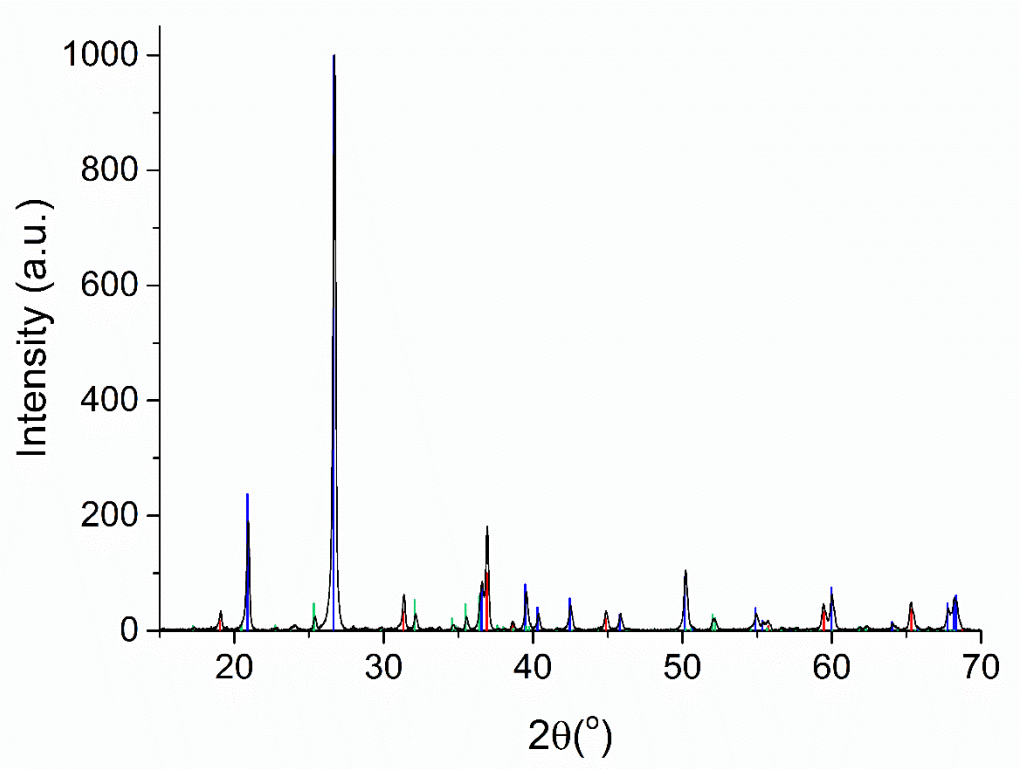

Figure 4.20: Phase ID of: 12wt%, L=1.0 Co/(CAB-O-SIL) samples after temperature dependant XRD measurements. Phases present: Quartz (blue), Co_3O_4 (red), and Co_2SiO_4 (green). Reference patterns from PDF2 database.

The data from the temperature dependant measurements are particularly noisy and a phase ID of the patterns is challenging, although clear changes are observed between the diffraction patterns (Figure 4.21). Therefore, additional

higher quality XRD patterns were recorded of the samples before and after the experiment using the Miniflex diffractometer, which records superior XRD patterns of similar samples (Figure 4.20), more detail is given in appendix 10. Phase identification was performed on these patterns to identify the major components present in the temperature dependant patterns with more accuracy identify the diffraction peaks in the temperature dependant XRD measurements.

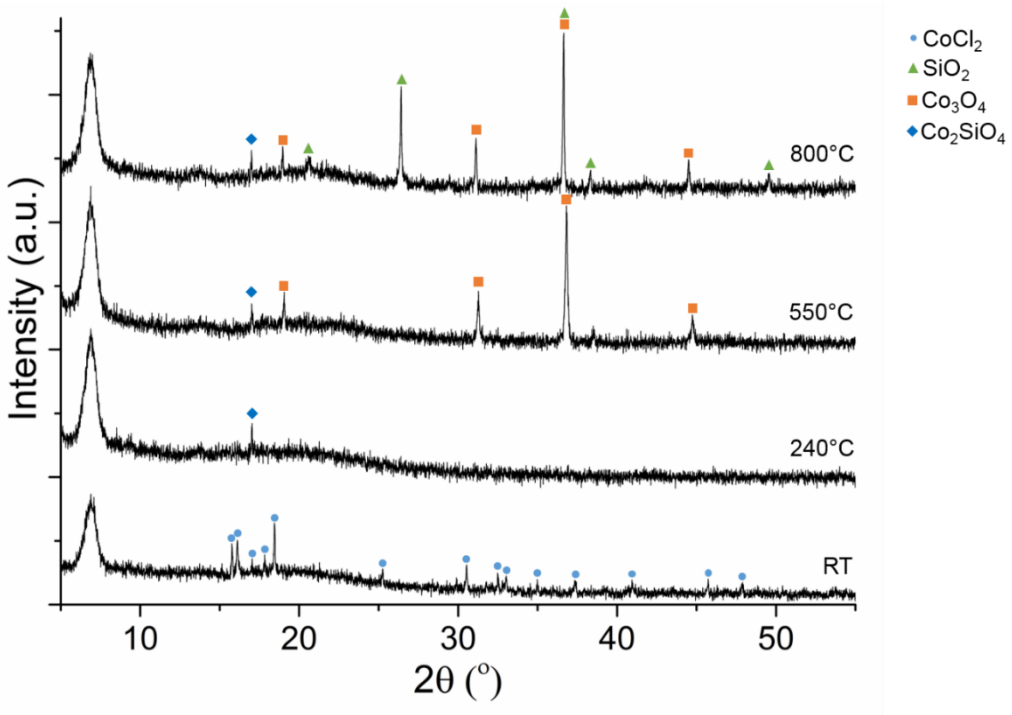

Figure 4.21: Temperature dependant XRD patterns of a 12 wt%, L=1.0 Co/(low SA SiO_2) sample measured at room temperature, 240°C, 550°C and 800°C. Identifying phase changes over the course of the temperature ramps.

Initially, at room temperature, the pattern shows diffraction peaks corresponding to the presence of $CoCl_2.6H_2O$, consistent with earlier observations. After the sample was heated to 240°C and held for 2 h these peaks disappear, accompanied by the appearance of one Co_2SiO_4 peak. After heating at 550 °C Co_3O_4 reflections are additionally observed. Then finally quartz diffraction peaks are observed after heating at 800 °C, as the support begins to crystallise. The amorphous peak at ~7 °2θ is consistent with that of CAB-O-SIL M5.[32] This suggests that the $CoCl_2.6H_2O$ that in the sample decomposes after the first heating step at 240°C and the cobalt forms a crystalline cobalt silicate phase as the cobalt reacts with the support which remains present in the sample

throughout subsequent heating stages. The subsequent heating stages show the formation of Co_3O_4 and crystalline SiO_2.

The presence of some metal support phase is interesting, as the Co/SiO_2 samples analysed in chapter 5 and 6 show no metal support evolution in the high-resolution *operando* XRD. Potentially, the removal of the polymer may result in an interaction between the cobalt and support not seen in other synthesis methods. However, it is only one diffraction reflection so is not conclusive evidence.

4.3.6. Operando X-Ray Absorption Spectroscopy (XAS)

The catalyst chosen for *operando* measurements was the same as discussed in the above section. A 5 wt% Co/SiO_2 catalyst using the low surface area support (SiO_2(a) in Table 4.3), was treated with multiple calcinations (one at 315 °C and as second at 550 °C). As the best particle size control (at the time) was achieved using multiple calcinations and TEM confirmed this on this support.

Catalyst pre-treatment began with surface cleaning of the Co_3O_4 to remove any contaminates from the surface. The XANES spectra at the start and end for this treatment closely resemble one another (Figure 4.22). Both characteristics of oxidic cobalt (Co_3O_4).

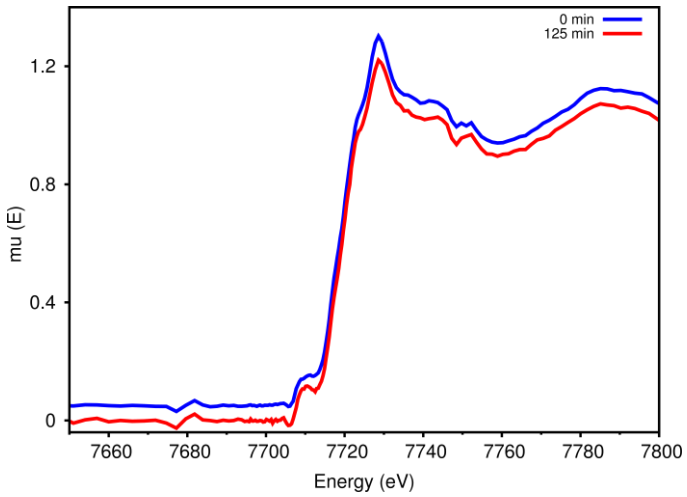

Figure 4.22: XANES spectra of the beginning and end of the catalyst cleaning (offset of 0.05 in mu for start value).

It is worth noting, however, that the data quality is quite poor and that two prominent glitches are visible in the data at 7678.9 eV and 7749.2 eV, becoming very prominent at high temperatures. The spectra in Figure 4.22 are the average of the first and final two spectra in the calcination series. Additionally, the lower surface area supports had less nanoparticle deposition, and so the weight percent may be less than initially assumed. This may explain the difference in data quality. The distinct glitches also suggest that there is a lot of inhomogeneity's in the sample (more than the other samples).

Additionally, the white line in Figure 4.22 is relatively low for a Co_3O_4 sample suggestive of some metallic component. From the phase ID in Figure 4.20 (of a sample on the same support and synthesised in the same manner, but of a cobalt higher weight percentage), shows the presence of some metal support interaction - Co_2SiO_4. However, Co_2SiO_4 also has a strong white line so is probably not the phase observed here.

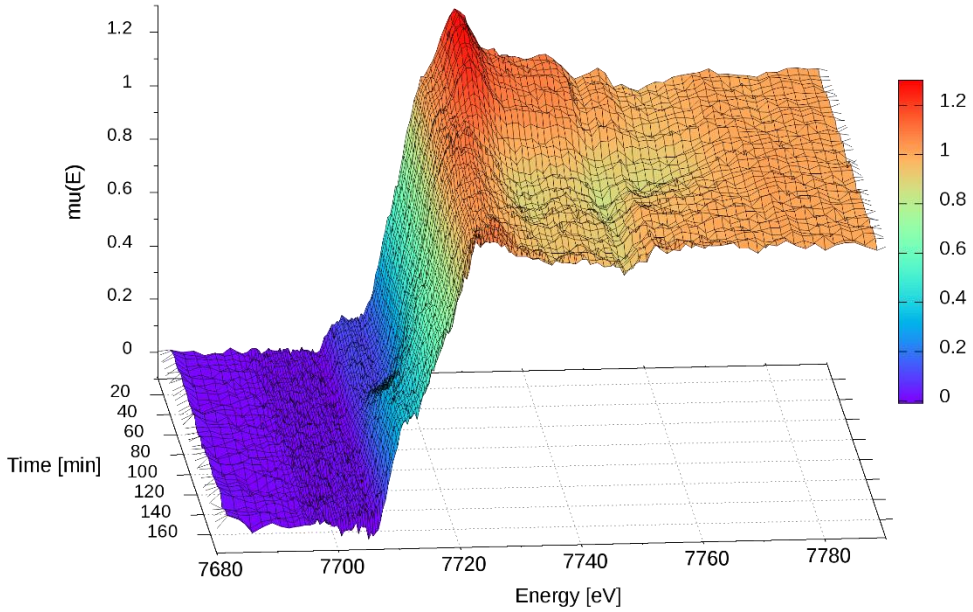

Figure 4.23: 3D continuum of XANES spectra over the course of the reduction of catalyst (of particle size ~6nm supported on low surface area SiO_2). Using a temperature program from 150 °C to 550 °C at a rate of 2 °C/min.

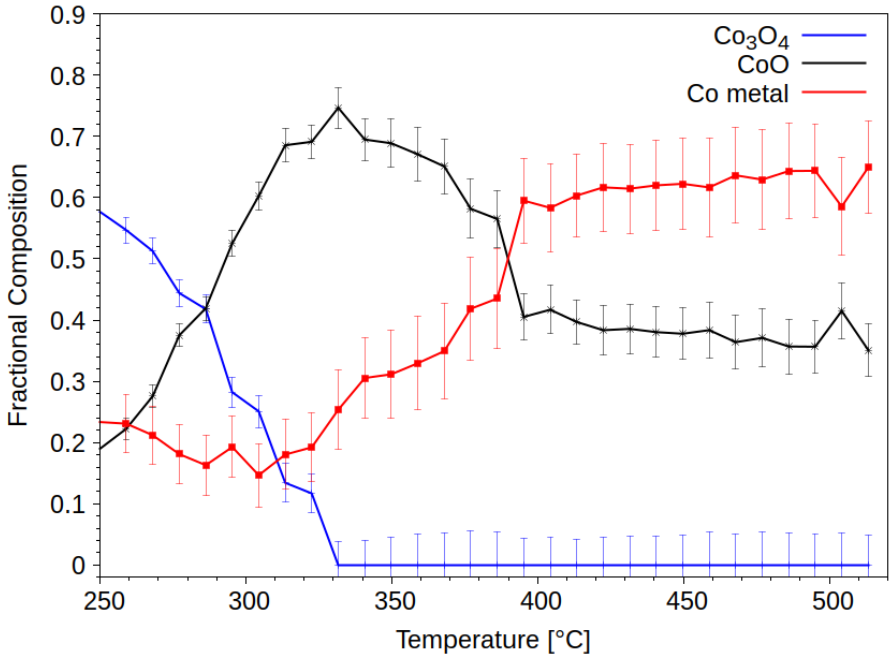

Figure 4.24: LCA of the reduction of the IMS catalyst (particle size ~6nm supported on low surface area SiO_2.)

The XANES spectra over the course of the reduction are mapped in Figure 4.23 and the LCA of the corresponding XANES is shown in Figure 4.24. The reduction follows the standard reduction pathway of Co-based catalysts, Co_3O_4 to CoO to Co^0. As the intense white line of the Co_3O_4 and clear pre-edge peak transform into the absence of a white line and edge shoulder of metallic cobalt. However, there is one odd feature of the LCA. The LCA fitting seems to indicate the presence of Co^0 at the start of the reduction which would be very unlikely under those conditions. The fit could be using the Co^0 reference to compensate for some unknown forth phase which a reference spectrum was not recorded or found. Although, the presence of some Co^0 at the start of the reduction would explain the low intensity white line seen in Figure 4.23, and could be physically possible with the presence of Cl in the system as it is an electron donating species.

The EXAFS spectra (Figure 4.25b) after reduction has both Co-Co shells and a Co-O shell. Although the LCA of the XANES shows a large quantity of CoO remaining (~40 %), the Co-Co shell contribution in the EXAFS appears quite small compared to the oxide.

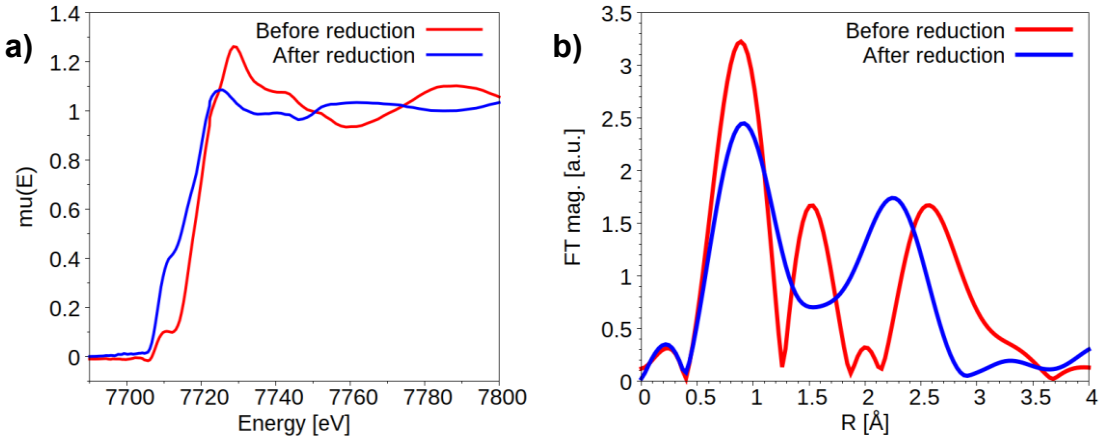

Figure 4.25: a) XANES (smoothed) and b) EXAFS of the Co/SiO_2 catalyst synthesised using IMS before and after reduction.

4.4. Discussion

An IMS method using a block co-polymer surfactant was adjusted to create a Co-based FTS catalyst on a solid support. The aim of this work was to synthesise a model catalyst with tight particle size control.

This technique was limited by the difficulty in removing the polymer – a necessary step before running FTS. Plasma treatment for polymer removal proved to be ineffective as determined by TGA. However, a multiple step heat treatment, first heating to 315 °C then to 550 °C, was successful at removing the polymer and produced a Co/SiO_2 sample with a particle size of 4.75 ± 2.29 nm. This is not an improvement on current methods.

The cobalt phase present in the micelles was identified as $[CoCl_4]^{2-}$ or some related complex based on the XAS. UV-Vis and XAS determined the presence of tetrahedrally coordinated Co but was inconsistent with common tetrahedrally coordinated cobalt-species. A Co-Cl bond with a bond distance constant with $[CoCl_4]^{2-}$ was successfully fit to the EXAFS spectra, and the XANES had similarities with the spectra of similar compounds. It is most likely that the $[CoCl_4]^{2-}$ ions are bonded to the pyridine in the micelle cores, and the differences may arise for those interactions.

Micelle loading had little effect on the EXAFS spectra, however TEM images showed that a tighter particle size control was achieved in samples of lower micelle loading. This variable also effects particle size. This most likely

arises from excess charge in the micelle cores when the ratio of $[CoCl_4]^{2-}$ to VP units in the cores exceed a ratio of 1:2 (L=0.5).

In this work it was shown that higher surface area silica supports have improved particle deposition, with negligible amounts of particles observed off the support by TEM. However, as the larger surface area supports obscured nanoparticles in TEM images, and as this was a key method of determining particles size especially in early work, some low surface area supported catalysts were also synthesised.

Although EXAFS shows that plasma treatment has little effect on the nanoparticles themselves, as mentioned above, the residual polymer presented a major problem. Plasma treatment on the powder supports was ineffective, leaving a large percentage of polymer still in the samples which caused sintering when later calcined (particles of irregular shape ~50 nm). There was also a limit in how much could be removed, with little difference between a plasma treatment of 2 and 10 h.

An initial heat treatment at 315 °C was shown to be adequate to calcine the catalyst while retaining a suitable particle size. A second heat treatment was then needed to clean the surface of the catalyst. The multi-stage heat treatment was an improvement on plasma treatment.

4.5. Conclusion

The aim of the work in this chapter was to tailor an Inverse Micelle Synthesis (IMS) method using block co-polymers as the surfactant, to powdered supports in order to make a model catalyst with tight particle size control. This was not wholly successful. Although a catalyst was synthesised, and the synthesis variables were refined to improve particle size control, the catalyst is not superior to other model catalysts produced in the literature. This was primarily limited by the behaviour or the residual polymer after deposition on the support. The particle size and distribution on deposition is promising, but the polymer must first be removed before FTS. Plasma treatment has proved to be poorer at polymer removal than first thought even on flat substrates and is very ineffective

for powdered supports. A two-stage heat treatment, first to ~315 °C to remove the polymer, then to 550 °C to fully calcine the catalyst and clean the surface was successful in producing Co_3O_4 nanoparticles of 4.75 ± 2.29 nm, but this is still hardly an ideal sample.

In future I would recommend abandoning this method for the application of powdered supports, however it remains a useful synthesis method for 2D catalysts.

4.6. References

1 E. Rytter and A. Holmen, *Catal. Today*, 2016, **275**, 11–19.

2 D. James Martin, D. Decarolis, Y. I. Odarchenko, J. J. Herbert, T. Arnold, J. Rawle, C. Nicklin, H. G. Boyen and A. M. Beale, *Chem. Commun.*, 2017, **53**, 5159–5162.

3 D. Ramimoghadam, S. Bagheri and S. B. Abd Hamid, *Colloids Surfaces B Biointerfaces*, 2015, **133**, 388–411.

4 J. P. Spatz, S. Mo, C. Hartmann, M. Mo, D.- Ulm, T. Herzog, M. Krieger, H. Boyen, P. Ziemann and F. Ju, *Langmuir*, 2000, **16 (2)**, 407–415.

5 B.-H. Sohn, J.-M. Choi, S. Il Yoo, S.-H. Yun, W.-C. Zin, J. C. Jung, M. Kanehara, T. Hirata and T. Teranishi, *J. Am. Chem. Soc.*, 2003, **125**, 6368–6369.

6 G. Kästle, H.-G. Boyen, F. Weigl, P. Ziemann, S. Riethmüller, C. H. Hartmann, J. P. Spatz, M. Möller, M. G. Garnier and P. Oelhafen, *Phase Transitions*, 2003, **76**, 307–313.

7 B. R. Cuenya, S.-H. Baeck, T. F. Jaramillo and E. W. McFarland, *J. Am. Chem. Soc.*, 2003, **125**, 12928–12934.

8 J. P. Spatz, S. Mößmer and M. Möller, *Chem. - A Eur. J.*, 1996, **2**, 1552–1555.

9 G. Kästle, H.-G. Boyen, F. Weigl, G. Lengl, T. Herzog, P. Ziemann, S. Riethmüller, O. Mayer, C. Hartmann, J. P. Spatz, M. Möller, M. Ozawa, F. Banhart, M. G. Garnier and P. Oelhafen, *Adv. Funct. Mater.*, 2003, **13**, 853–861.

10 O. A. Platonova, L. M. Bronstein, S. P. Solodovnikov, I. M. Yanovskaya, E. S. Obolonkova, P. M. Valetsky, E. Wenz and M. Antonietti, *Colloid Polym. Sci.*, 1997, **275**, 426–431.

11 G. Liu, X. Yan, Z. Lu, S. A. Curda and J. Lal, *Chem. Mater.*, 2005, **17**, 4985–4991.

12 A. Dominguez, A. Fernandez, N. Gonzalez, E. Iglesias and L. Montenegro, *J. Chem. Educ.*, 1997, **74**, 1227.

13 Poly(styrene)-b-poly(2-vinyl pyridine), https://www.polymersource.ca/index.php?route=product/category&path=2_2190_16_105_2209_618&subtract=1&categorystart=A-2.1.9.6.1&serachproduct=, (accessed 16 March 2019).

14 D. Decarolis, I. Lezcano-Gonzalez, D. Gianolio and A. M. Beale, *Top. Catal.*, 2018, **61**, 162–174.

15 S. Mossmer, J. P. Spatz, M. Moller, T. Aberle, J. Schmidt and W. Burchard, *Macromol. Rapid Commun.*, 2000, **33**, 4791–4798.

16 D. J. Martin, D. Decarolis, R. Tucoulou, G. Martínez-Criado and A. M. Beale, *Catal. Struct. React.*, 2017, **3**, 63–70.

17 H.-G. Boyen, G. Kästle, K. Zürn, T. Herzog, F. Weigl, P. Ziemann, O. Mayer, C. Jerome, M. Möller, J. P. Spatz, M. G. Garnier and P. Oelhafen, *Adv. Funct. Mater.*, 2003, **13**, 359–364.
18 K. V. Klementev, *Nucl. Instruments Methods Phys. Res. Sect. A Accel. Spectrometers, Detect. Assoc. Equip.*, 2000, **448**, 299–301.
19 B. Ravel and M. Newville, in *Journal of Synchrotron Radiation*, 2005, vol. 12, pp. 537–541.
20 A. Altomare, N. Corriero, C. Cuocci, A. Falcicchio, A. Moliterni and R. Rizzi, *J. Appl. Crystallogr.*, 2015, **48**, 598–603.
21 Quantachrome Instruments, Autosorb(TM): automated gas sorption analyzer, http://www.uni-export.com.pl/files/Qchrome/autosorb_iQ.pdf, (accessed 12 March 2018).
22 Gatan, GMS 3 Software Registration | Gatan, Inc., http://www.gatan.com/datasheets/gms-3-software-registration, (accessed 12 March 2018).
23 ImageJ User Guide - IJ 1.46r, https://imagej.nih.gov/ij/docs/guide/index.html, (accessed 12 March 2018).
24 TA Instruments, TGA Q Series Getting Started Guide, https://engineering.tamu.edu/media/4133232/tga-q500.pdf, (accessed 12 March 2018).
25 M. Llusar, A. Forés, J. A. Badenes, J. Calbo, M. A. Tena and G. Monrós, *J. Eur. Ceram. Soc.*, 2001, **21**, 1121–1130.
26 T. Uemura, M. Ohba and S. Kitagawa, *Inorg. Chem.*, 2004, **43**, 7339–45.
27 T. Yamamoto, *X-Ray Spectrom.*, 2008, **37**, 572–584.
28 N. V. Shmatkova, I. I. Seifullina, V. G. Vlasenko, A. L. Trigub, S. I. Levchenkov and N. V. Khitrich, *Russ. J. Gen. Chem.*, 2017, **87**, 107–116.
29 J. F. W. Mosselmans, P. F. Schofield, J. M. Charnock, C. D. Garner, R. A. D. Pattrick and D. J. Vaughan, *Chem. Geol.*, 1996, **127**, 339–350.
30 D. K. Park, S. J. Lee, J.-H. Lee, M. Y. Choi and S. W. Han, *Chem. Phys. Lett.*, 2010, **484**, 254–257.
31 I. Pastoriza-Santos and L. M. Liz-Marzán, *Adv. Funct. Mater.*, 2009, **19**, 679–688.
32 O. Larlus, S. Mintova, S. T. Wilson, R. R. Willis, H. Abrevaya and T. Bein, *Microporous Mesoporous Mater.*, 2011, **142**, 17–25.
33 S. Mishra, S. Kanungo, *Journal of Thermal Analysis*, 1992, **38**, 2437-2454.

5. Particle size effects on FTS: I) Stable size range

5.1. Introduction

This chapter focuses primarily on *operando* XAS and XRD techniques as applied to a Co-based FTS catalyst – run under identical conditions but performed independently. The three key issues concerning Co^0 FTS catalysts interrogated here are: the reoxidation of smaller Co^0 nanoparticles during FTS, the influence of Co^0 fcc/hcp/intermixed ratio, and the potential formation of metal-support interaction phases during FTS. Two catalysts of two different particle sizes (one in the stable size range and one in the unstable range) were examined in order to determine how these behaviours vary with particle size. By combining XRD and XAS measurements to probe the local and long-range order of the catalyst, a more nuanced analysis of the samples is achieved than by using the individual bulk techniques alone.

The sample examined in this chapter is a Co/MCF-17(silica) catalyst with an average nanoparticle (NP) size of approximately 11 nm, which falls within the stable size range of Co-based FT catalysts supported on silica.[1] The results for the catalyst with a smaller particle size of ~3 nm, which falls within the unstable size range are separated into a different chapter and detailed in chapter 6.

Size effects on Co-based FTS catalysts are well known and are typically attributed to either the lower reducibility of smaller cobalt NPs,[2] or more likely to the size dependent formation of different Co^0 polymorphs (fcc vs hcp) and their differing activities/productivities.[3] Historically, the nanostructural evolution during FTS has been poorly interrogated due to the limitations of standard bulk characterisation techniques – such as XRD and XAS – in the differentiation between fcc and hcp cobalt.

Above the optimum size the particles remain stable, but the activity and selectivity to higher mass hydrocarbons decreases with increasing particle size. The optimum particle size has been shown to be approximately between 6 - 9 nm, with maximum activity at the lower end of the range at approximately 6 nm,[4,5] and maximum selectivity around 8 - 9 nm.[6] This also varies with support type.[7]

Below the optimum size lies an unstable range, below which Co^0 particles become unstable and after which point activity drops off sharply. This was shown to occur in similar catalysts to those discussed here (Co/MCF-17 in the particle size range 3.2-11 nm)[1], as well as in Co/CNF (carbon nano-fibres – a reducable support)[5], and on Al_2O_3 supported catalyst.[8,9]

Two key *operando* studies suggest that the instability of smaller NPs is due to water-induced oxidation of small NPs under FTS conditions – Senecal *et al.*[8] and Tsakoumis *et al.*[9] A more detailed discussion of these studies is found in the literature review (chapter 2). Although these studies differ slightly, they both show clear evidence of reoxidation of smaller Co^0 NPs within the samples. While it would be physically impossible for bulk Co^0 to oxidise under FTS conditions,[12] the Hüttig temperature (the point at which surface atoms become mobile) decreases with NP size, and so Co^0 NPs below approximately 6 nm are theoretically able to undergo surface oxidization at 250 °C (the typical FTS temperature).[13,14]

Although the sensitivities to particle size are well known, their variation over time is not fully understood and there is still a need for research in this area, particularly for *operando* studies using both combined and imaging techniques. Cobalt particles are not entirely stable during FTS, and even display a loss of activity in the shorter term (the first 12 h of FTS), possibly due to the oxidation of smaller NPs (as suggested above), or by carbonization.[15]

5.2. Experimental methods

Samples were prepared using a standard Schlenk technique under an argon atmosphere and provided by S.K. Beaumont (Durham University) and take the form of Co/MCF-17 of average Co particle size of approximately 11 nm. The synthesis is described in chapter 3.

Operando XRD and XAS measurements were collected respectively on ID15 and BM26A at the European Synchrotron Radiation Facility (ESRF). XRD measurements were recorded at 78.5 keV and XAS measurements were recorded at the Co k-edge (7.712 keV) in transmission mode. During *in situ*

experiments catalyst samples were packed into 1 mm diameter borosilicate capillaries, which were mounted in the BM26A sample environment cell.[16] To ensure consistency the same cell was mounted on both beamlines (Figure 5.1).

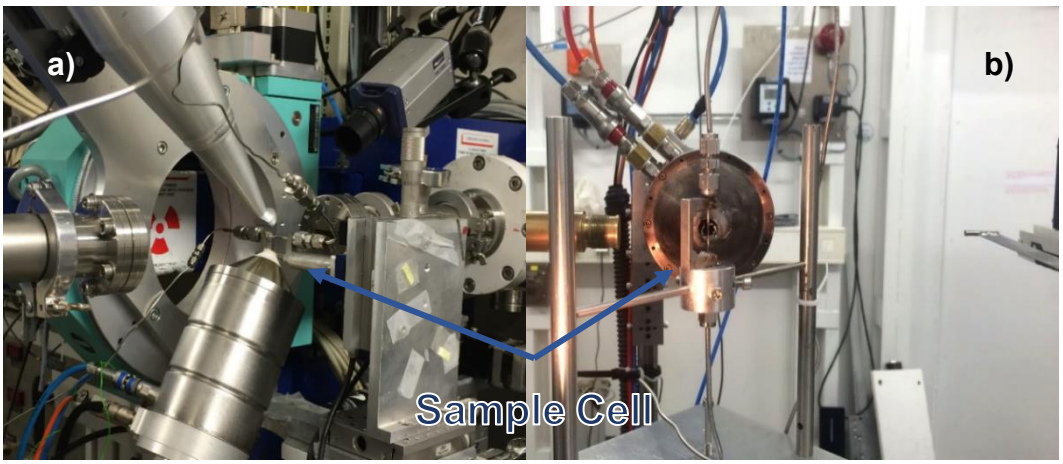

Figure 5.1: Photographs of the set-ups used during a) an XAS experiment on BM26A (DUBBLE) and b) an XRD experiment on ID15A.

The catalyst was calcined in a twostep process, first from room temperature to 350 °C at a ramp rate of 5 °C/min in a flow of He, then from 350 °C to 550 °C at a ramp rate of 10 °C/min in a flow of O_2/He. The catalyst was then reduced in a flow H_2 and heated from 150 °C to 550 °C at a rate of 2 °C/min. FTS was performed at 250 °C at a pressure of 2 bar with a H_2:CO ratio of 2:1.

The pressure for FTS (2 bar) was chosen to limit the formation of waxes and wax build up outside of the heated region, which risk blocking the capillary cell and can limit the time on steam to a couple of hours.[17] Total gas flow was 10 ml/min corresponding to a gas hourly space velocity (GHSV) of 10000 h^{-1}. The temperature was controlled using a heat gun, and simultaneous mass spectrometry (MS) observations were recorded.

Transmission electron microscopy (TEM) images were captured using a Jeol-2100 (200 keV accelerating voltage) at the Research Complex at Harwell. Images were captured using Gatan DigitalMicrograph[18] and the particle sizes in the images were measured using ImageJ. XAS spectra were analysed using Athena and Artemis[19].

XRD patterns were analysed by two separate methods. One using a conventional combination of phase identification and Rietveld refinement, and the second using novel Debye simulations (Longo et al. 2014[20]). 2D image integration and Rietveld refinements were performed using GSASII, phase identification was performed using QualX2[21], and some basic Scherrer analysis was performed using XPowder12. Some pre-processing of the data including intensity correction, trimming the 2θ range to remove the beam stop, and glass background removal were performed using Fortran 90 code and bash script.

Due to the complex nanostructural nature of metallic cobalt (intermixing of hcp and fcc phases as well as the presence of staking faults), the applicability of Rietveld refinement is limited – a full description of these limits is discussed in chapter 3. Therefore, the second method of XRD analysis was also used, the code of which was written in Fortran 77. This consisted of Debye simulations based on the unic model[20] - also described in detail in chapter 3. Four probability factors are used to describe four possible unique combinations of two concatenated blocks of four Co^0 layers. These probability factors can be used to calculate the relative percentages of hcp, fcc, and mixed Co^0 within a given sample, and thus determine nano-structural variation over the reaction time. Additionally, for the first time, primitive Rietveld refinements were added for the oxidic components allowing realistic samples to be simulated and for sequential fitting over the course of a reduction to be attempted.

5.3. Results

5.3.1. Calcination

All calcinations of the as prepared samples were performed as a two-step process comprised of an initial slow calcination in He (RT to 350 °C at 5 °C/min), in order to remove any residual surfactant from synthesis, and a faster calcination in 10 % O_2/He (350 to 550 °C at 10 °C/min), to then fully decompose the cobalt precursor.

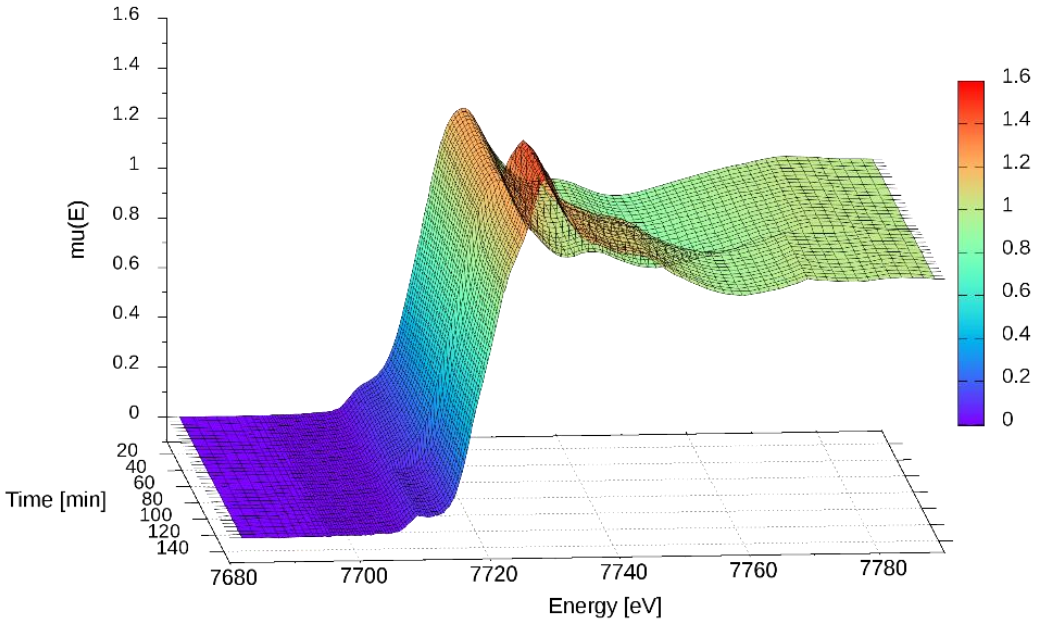

Figure 5.2: The evolution of XANES spectra over the course of calcination. Two step calcination, 0-65 min (RT-350 °C), 65-95 min dwell, then 95-115 min (350-550 °C).

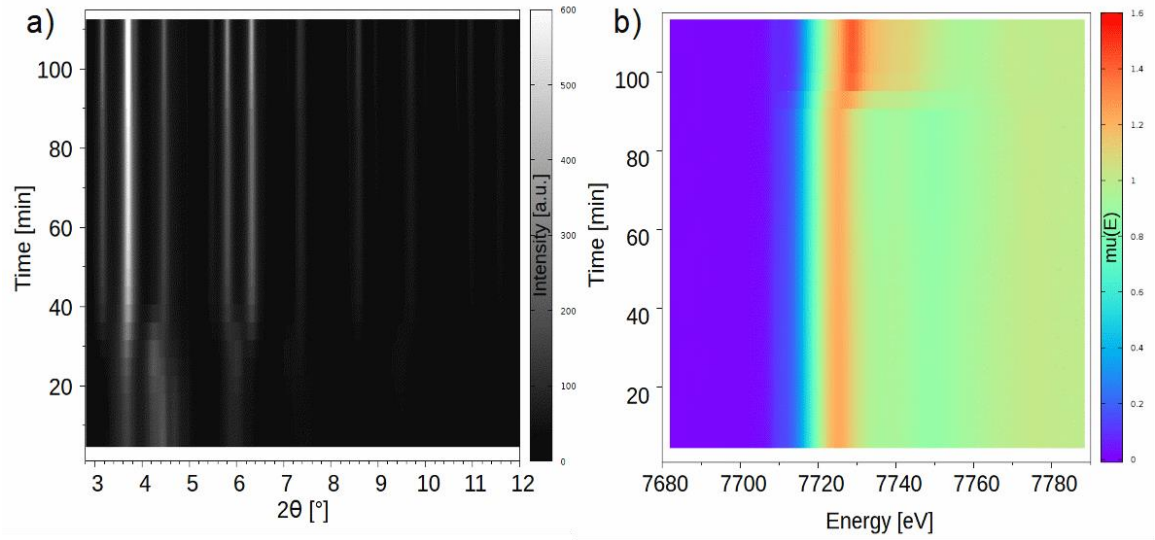

Figure 5.3: Comparison of 2D projections of a) XRD and b) XAS data (equivalent to Figure 5.2) collected over the course of two step calcinations, 0-65 min (RT-350 °C), 65-95 min dwell, then 95-115 min (350-550 °C).

Little variation is observed in the XANES spectra (Figure 5.2) over the first 95 min of calcination, which includes both the first temperature ramp and the 30 min temperature dwell at 350 °C. Instantly, upon the gas change (to an oxidising atmosphere) the rising edge intensity increases (from 1.22 to 1.40), the edge shifts slightly (from 7709.1 to 7710.4 eV), and the pre-edge becomes more

distinct, which is characteristic of the decomposition of cobalt carbonyl ($Co_2(CO)_8$) to Co_3O_4.

However, this is contrary to what is observed in the XRD data, where the decomposition is a gradual process. This difference in behaviour is seen clearly in Figure 5.3, a side-by-side comparison of 2D projections of XRD patterns (Figure 5.3a), and XAS spectra (Figure 5.3b), and their evolution over calcination. While the XAS spectra show a sudden change in composition at the point the gas mixture was switched, the XRD patterns show the gradual decomposition of the precursor into Co_3O_4, starting at approximately 24 min (73 °C in the first temperature ramp).

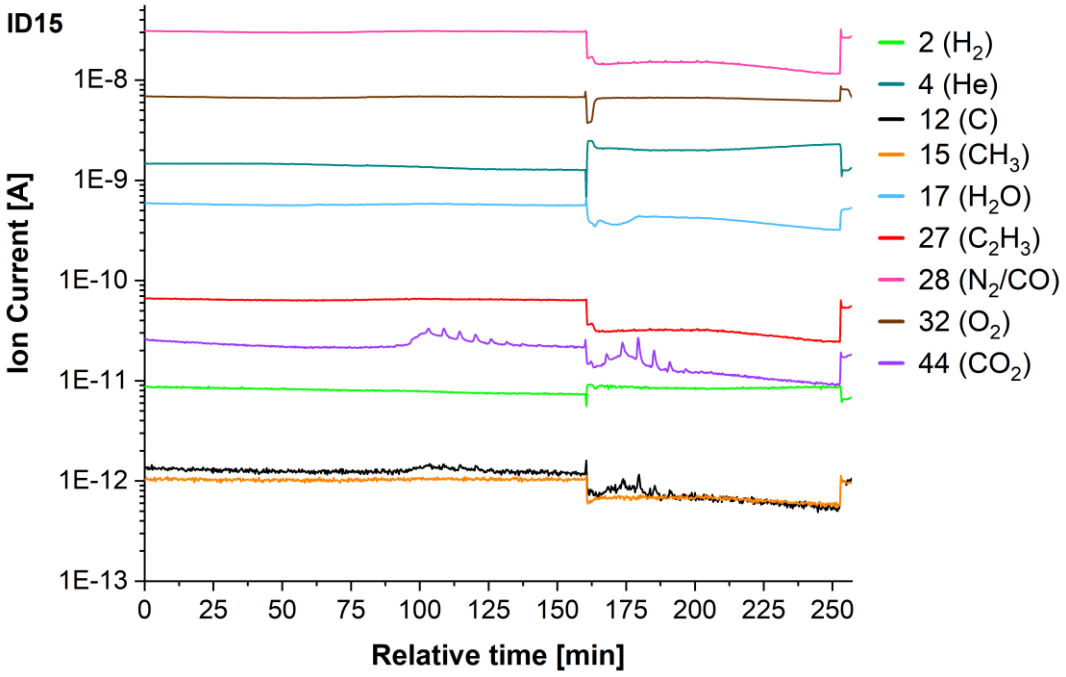

Figure 5.4: Mass spectrometry response recorded during calcination on ID15 during XRD experiments.

The difference may be influenced in part to the size ranges observed by each technique; XRD patterns are strongly dominated by reflections from larger crystallites within a sample. However, a closer inspection of the mass spectrometry (MS) data recorded during the calcination suggests that there was an air leak in the He line during the ID15 beamtime (XRD). In the MS data recorded during the XRD experiments (Figure 5.4) the O_2 response changes little

on the gas change. Whereas, in the MS data recorded during the XAS experiments (Figure 5.5) the O_2 response increases significantly.

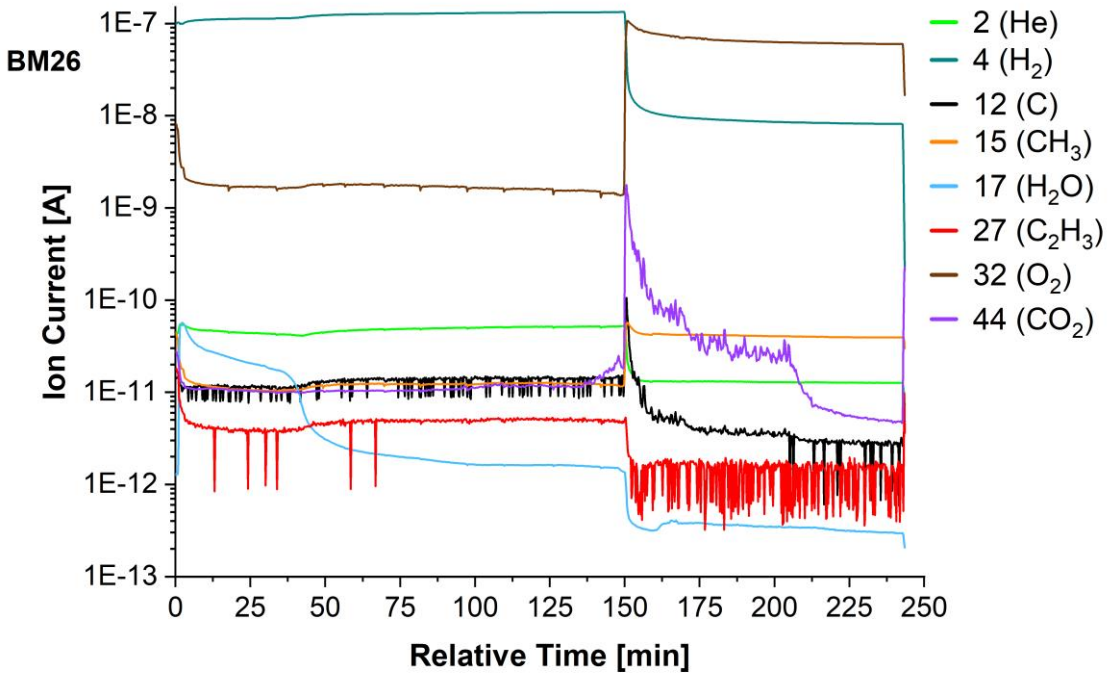

Figure 5.5: Mass spectrometry response recorded during calcination on DUBBLE (BM26A) during XAS experiments.

During the first 45 min of the calcination, the XRD patterns were too amorphous for Rietveld refinement or other conventional XRD analysis. As such, Rietveld refinement was performed on the first possible pattern at 45 min (or 250 °C) and on the last pattern recorded during the calcination. Both CoO and Co_3O_4 are present at both stages of the calcination. The CoO percentage reduces over reduction while the Co_3O_4 percentage increases. The first analysable pattern has an average Co_3O_4 particle size of 4.5 nm, growing to 11.5 nm at the end of calcination (appendix 12). This apparent Co_3O_4 crystallite growth as CoO is oxidised to form Co_3O_4 is consistent with such phase changes in Co-based nanoparticles.

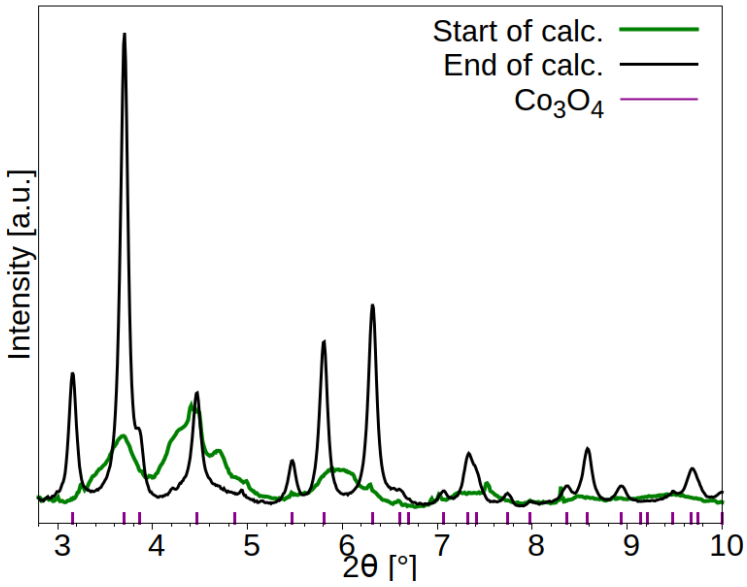

Figure 5.6: Comparison between XRD patterns taken before and after calcination.

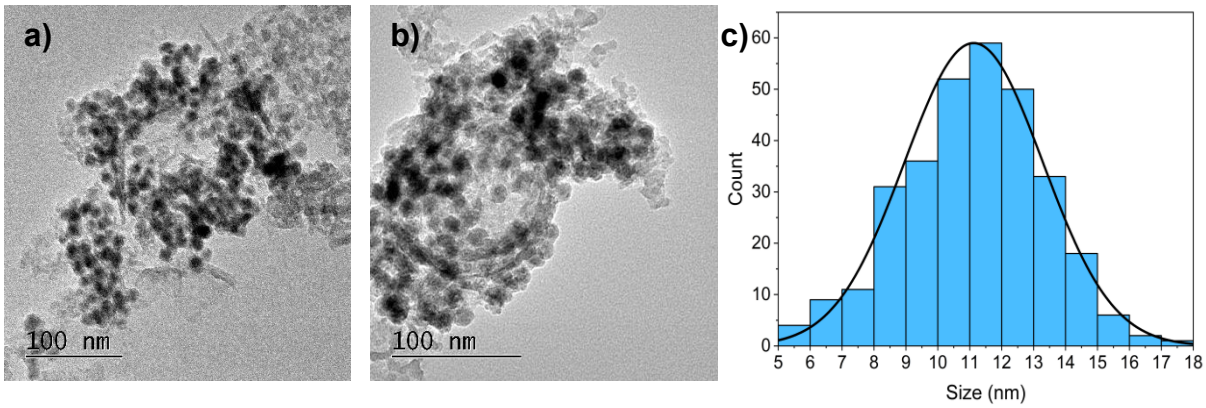

Figure 5.7: a&b) TEM images of Co/MCF-17 catalyst after a calcination in air, heated from RT-350 °C at 5 °C/min, then from 350-550 °C at 10 °C/min. c) A histogram showing particle size distribution as measured from TEM images.

In order to verify the particles size, additional TEM measurements were recorded and are given in Figure 5.7. They show an average particle size of 11 ± 2 nm. This agrees with the XRD data. However, it is worth considering that conventional TEM has a limited resolution and can only see down to ~ 1 nm. Also, that the TEM calcinations were performed in air rather than a O_2/He mix, and therefore these TEM images may only be an approximation.

5.3.2. Reduction

Reductions were carried out in a flow H_2/He(5 %) and heated from 150 to 550 °C at a rate of 2 °C/min.

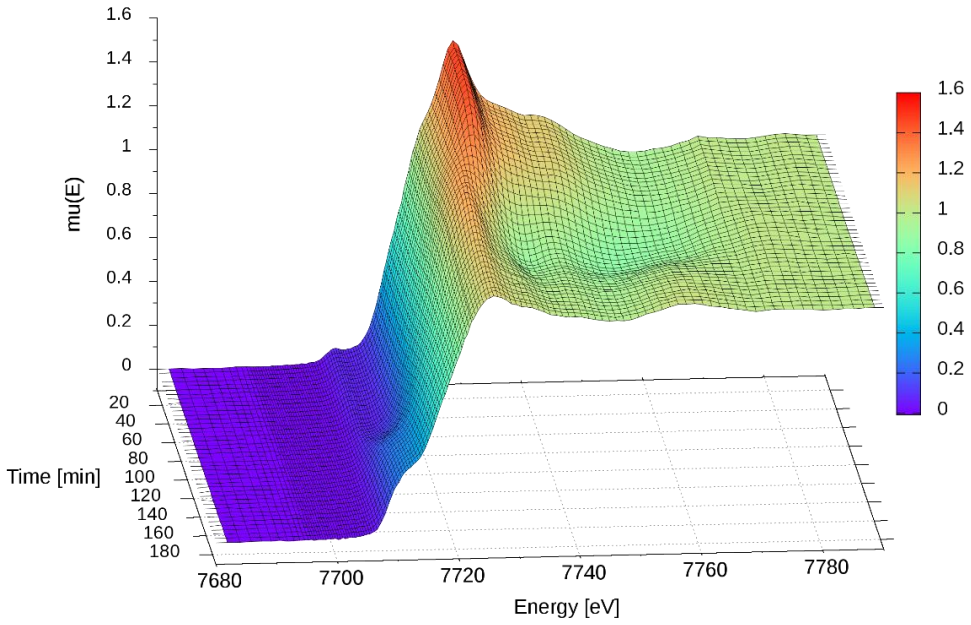

Figure 5.8: Evolution of XANES spectra over the course of reduction – 150 to 550 °C at a ramp rate of 2 °C/min.

Figure 5.8 is a 3D series of XANES spectra showing the evolution over the reduction, consistent with the known reduction pathway of $Co_3O_4 \rightarrow CoO \rightarrow Co^0$. Significant variation in the spectra are first observed at approximately 60 min (270 °C), where the normalised rising edge intensity begins to decrease from 1.42 to 1.21, and the edge shifts to lower energy (from 7719.9 eV to 7717.2 eV), as the sample becomes more metallic. Variation in the pre-edge peak trails behind the other features (starting to change at ~80 min – 290 °C) possibly due to the fact that Co_3O_4 and CoO have similar pre-edge features. The final XANES spectra suggests the continued presence of unreduced oxide as the edge is shifted to higher energies than that of the metal cobalt edge (7708.5 eV compared to 7712 eV).

Linear combination analysis (LCA) of the XANES spectra was performed on the data acquired during the reduction. The LCA is shown in Figure 5.9, which is in agreement with the qualitative assessment of the data. Again, the reduction

follows the typical pathway. Notably, the cobalt in the sample is not fully reduced at the end of the reduction process (only approximately 70 %), with both oxides still observed to be present, most of which is CoO.

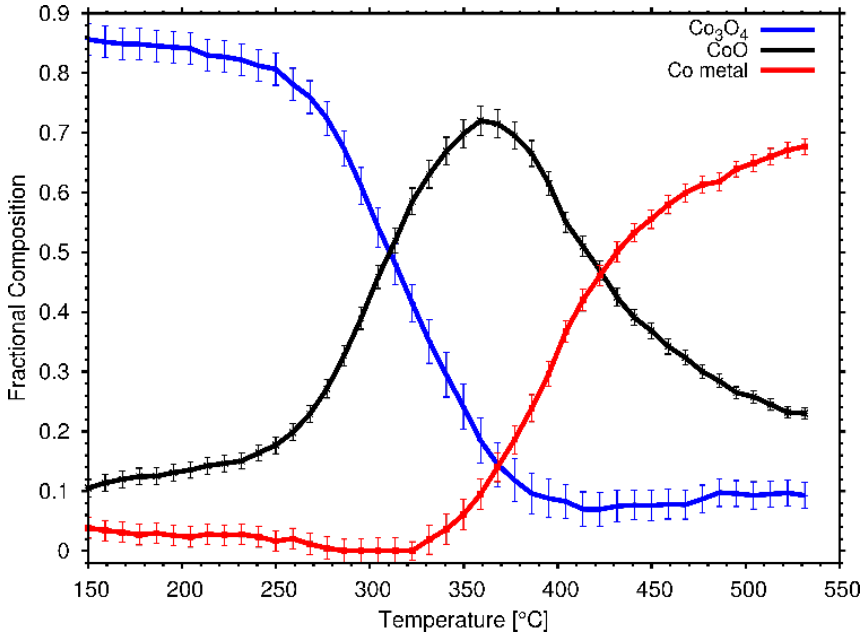

Figure 5.9: Linear combination analysis (LCA) of XANES spectra over the course of reduction in H_2, showing the evolution of the fractional composition of the cobalt content.

The continued presence of oxidic cobalt is also intimated by EXAFS fits of the reduced catalyst that are improved by the addition of a Co-O first shell. Full multiple scattering EXAFS fits are also improved by the addition of the Co-O first shell from CoO (Figure 5.17). Although a Co-O shell from CoO was used in the fit it is not possible to prove conclusively from EXAFS if the low R contribution is from CoO, Co_3O_4, or if it is even oxidic in nature at all. Carbide species with low R contributions are indistinguishable from oxidic components in EXAFS alone. However, as both the XANES and XRD (discussed below) indicate the presence of CoO in the reduced catalyst, it is safe to assume that the low R contribution is a Co-O one.

The corresponding XRD patterns using the same reduction procedure (both gas and temperature procedure) are displayed in Figure 5.10, which shows both the 2D projection of the XRD patterns over the course of reductions, as well as key individual patterns throughout (background subtracted). Once again, the XRD shows the standard reduction pathway of Co-based FTS catalysts and is in

agreement with the XAS spectra. Small reflections from residual Co_3O_4 are also observed in the final XRD patterns.

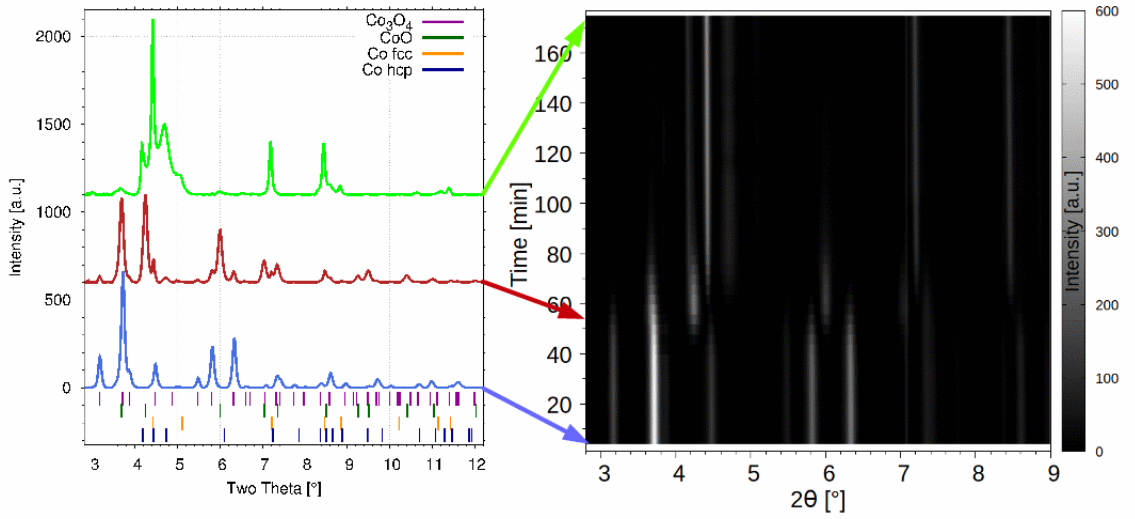

Figure 5.10: A 2D projection of the evolving XRD patterns recorded over the course of reduction and three individual patterns from the start, end and at the point of highest CoO content.

At the start of reduction, Scherrer analysis (corrected for instrumentational broadening) calculates the average particle size to be 11.6 nm, which is consistent with the Rietveld refinement (11.5 nm) and TEM (11.2±2.17 nm) discussed in the calcination section above. At the end of the reduction, although reflections corresponding to oxides are still present, they have a suitably low intensity to render finding the FWHM accurately challenging. In addition, it is challenging to identify by phase ID only if the residual oxide is Co_3O_4 or a mixture of both Co_3O_4 and CoO due to the breadth and small size of the reflection – this is addressed in the Rietveld refinements section later in this chapter.

Unfortunately, all prominent Co^0 reflections in the reduced catalyst are overlapping hcp/fcc reflections and so the extraction of FWHM values is not reliable. Two peaks (fcc[111]/hcp[002] and fcc[311]/hcp[2-12]) were measured for the metallic cobalt to compare values, one gives a higher value than other methods (19.5 nm), and the other a lower value (8.8 nm).

More detailed analysis of the data was then performed using Rietveld refinement and sequential fits were performed over the course of the reduction. Although, it is worth noting that there is a limit to what is achievable in the analysis of metallic cobalt using Rietveld.

Figure 5.11b is the best Rietveld refinement (in terms of statistical agreement factors) of the reduced catalyst and is still a poor fit of the observed data, even after using unphysical preferred orientation (18 spherical harmonic coefficients) – which were held during fitting to reduce the number of fitting parameters. Although flawed, this rough Rietveld refinement can be used to sequentially fit to the reduction of the catalysts. Similar significant preferred orientations have been used during Rietveld refinement of similar Co-based FTS catalysts by J. Paterson *et al*.[28]

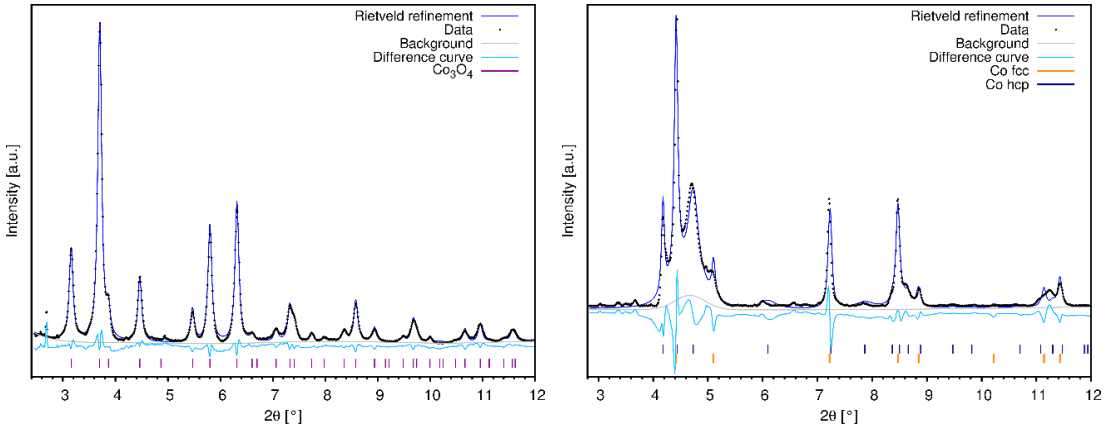

Figure 5.11: Rietveld refinements of XRD patterns recorded at a) the start and b) end of a reduction 150 to 550 °C at a ramp rate of 2 °C.

Sequential fits using Rietveld refinements were performed for the reduction using the refinements above as a starting point. As the metal components (hcp and fcc Co^0) were so unphysical, their individual parameters except for fractional composition were held during the sequential fits.

The fractional composition evolution over the course of reduction determined by sequential refinement are shown in Figure 5.12, both displaying the fcc and hcp components individually (Figure 5.12a), and total metallic Co (Figure 5.12b). The evolution in Figure 5.12b is in agreement with the compositional evolution obtained by LCA of the XANES spectra (Figure 5.9) – the typical $Co_3O_4 \rightarrow CoO \rightarrow Co^0$ reduction pathway. Although there are two key differences. First the reduction starts and ends at lower temperatures (maximum CoO composition is seen at 270 °C in the XRD patterns but at 360 °C in the XANES spectra). This is most likely due to the ease of reducibility of the larger

particles observed by XRD. Other studies have shown an stronger interaction between the nanoparticles and support in smaller nanoparticles,[8] which may also be a contributing factor.

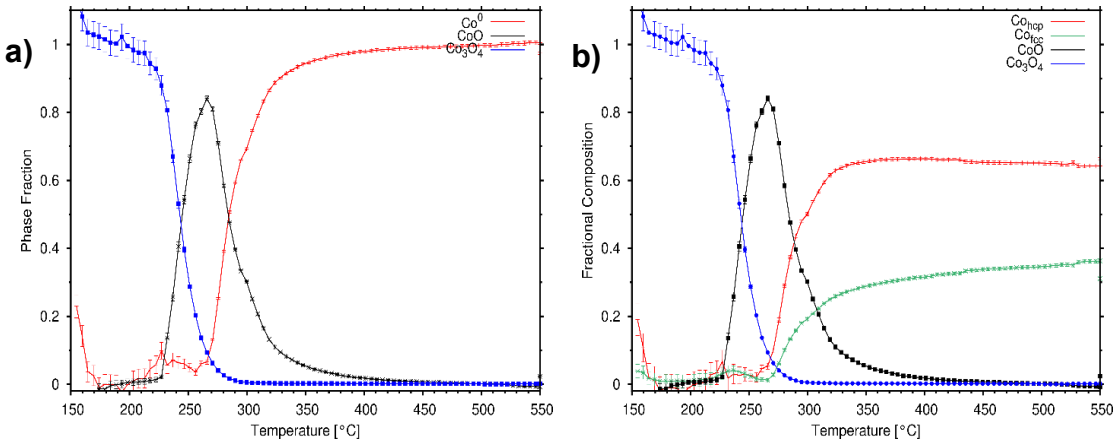

Figure 5.12: Rietveld refinement sequential fits of XRD patterns over the course of a reduction, displaying a) the total metal Co^0, and b) fcc and hcp Co^0 individually.

However, the evolution of the fractional composition shown in Figure 5.12a closely resembles previous time-resolved data extracted from Rietveld refinements.[22] This may be due to the similarities of the samples, or perhaps a consequence of the compromises needed to fit the data. To confirm this, as a comparison, sequential fitting using the unic model was also performed and can be seen in Figure 5.13.

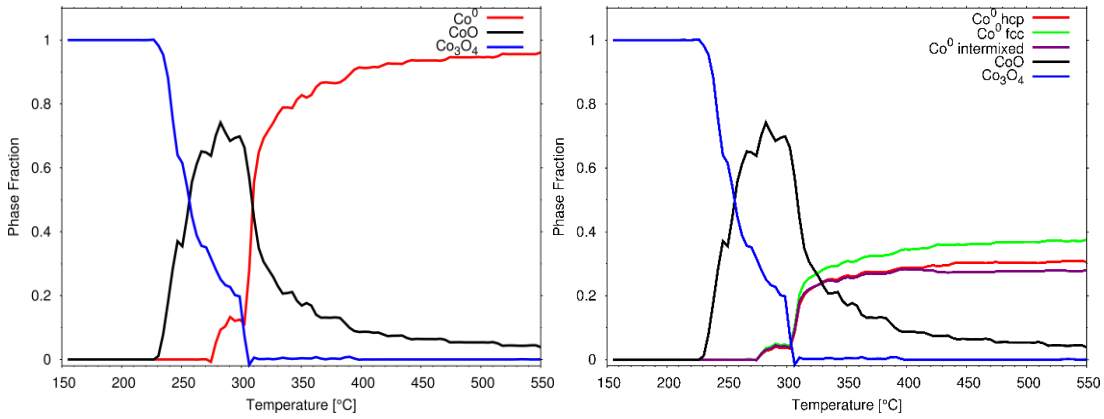

Figure 5.13: Sequential fitting (Debye simulation) over the course of a reduction. Displaying in a) the oxide and total metallic cobalt contributions, and in b) the oxide and individual fcc, hcp and intermixed Co^0 contributions. Analysis was performed using the same XRD data as the Rietveld refinement in Figure 5.11.

The fitting above was an early test of sequential fitting using Debye simulations of this kind. As such, there is still significant room for improvement in the fitting procedure. The evolution of the fractional percentages in Figure 5.13 is jagged at many points throughout the reduction. The individual simulations are computationally expensive and therefore take a long time to fully fit. So, to improve such sequential fitting for any future use it would be necessary to either allot significantly more time to fitting, or to rewrite the code to be able to run on multiple cores simultaneously (using MPI – message passing interface). However, this is beyond the scope of this project.

Errors are excluded from Figure 5.13. Minuit generates estimated errors that are not accurate in this case where the true minimum was not reached. The true errors could have been calculated; however, this would have required running fits for every parameter in every pattern and was deemed to computationally expensive for preliminary tests of sequential fits.[29]

Table 5.1: Comparison of the extent of reduction as determined by LCA of the XANES spectra, Rietveld refinement of the XRD patterns and Debye simulations of the XRD patterns.

	Percentage composition (%)		
		XRD	
	XANES	**Rietveld refinement**	**Debye simulations (unic)**
Co_3O_4	9	0	0
CoO	22	0	5
Total Co^0	69	100	95
Co_{hcp}	-	64	34
Co_{fcc}	-	36	21
Co mixed	-	-	40

Although there are issues with the Debye simulations over the reduction, the trend seems chemically reasonable and stable - if not highly accurate for individual simulations.

Table 5.1 provides a comparison between the percentage composition as determined by XAS (LCA of the XANES), and XRD (both from Rietveld

refinement and Debye simulations). XANES is sensitive to all the cobalt present, even small particles, and so gives a more accurate determination of the oxide composition than the XRD analyses. However, XAS cannot differentiate between the Co^0 polymorphs here. In a simpler metal only system XANES simulations could be applied to give the approximate percentage of the polymorphs, but the oxide components of a more realistic catalyst prevent this analysis.

The Rietveld refinements are a poor chemical fit with unrealistic preferred orientations used to compensate for the effect of stacking faults and are not able to detect mixed fcc/hcp phases. However, the analysis and software are well known and robust.

In the sequential Debye simulations of the reduction, the ratios of hcp, fcc, and intermixed Co^0 are an improvement on the Rietveld refinements, and are consistent with those of the full, complete unic model fitting given in the section below. Also, a noticeable initial appearance of metallic Co^0 (~5 % of total cobalt composition) between 275-300 °C. This could be the fast reduction of some large cobalt oxide particles within the sample, which would reduce at a lower temperature. A possible corresponding feature can be seen in the Rietveld sequential fits (Figure 5.8s) at the lower temperature of 220-260 °C, although the errors in factional composition are very large in that region and the feature may not be real. However, the Debye simulations were far more computationally expensive than the Rietveld sequential fitting, taking days compared to minutes. Although there is much scope for improving the computational expense.

5.3.3. Fischer-Tropsch Synthesis

The Co/MCF-17 catalyst is very stable. Over the initial 12 h of FTS, only very subtle changes are observed in both the XRD and XAS data. In this section conventional XRD analysis is performed, followed by XAS analysis, and then the XRD data is revisited using Debye simulations based on the unic model, building on the conventional analysis, to provide new insight with the novel Debye simulations.

Figure 5.14 provides three magnified regions of the XRD patterns showing the most prominent reflections in the XRD pattern of the reduced catalyst. The fcc(111)/hcp(002), fcc(220)/hcp(2-10), and fcc(311)/hcp(2-12) overlapped reflections, which are positioned at approximately 4.42, 7.21 and 8.47 °2θ behave similarly. The intensity of these reflections increases and their position shifts to lower 2θ °.

The slight variations seen in Figure 5.14 are quantified in Table 5.2, which provides the position of the maximum and the width of the peaks corresponding to the overlapping Co^0 reflections. This behaviour could be due to sintering of the NPs, however, a slight broadening of the reflections is also observed (Figure 5.14 and Table 5.2), which is inconsistent with sintering where the reflections would be expected to narrow as the crystallites increase in size.

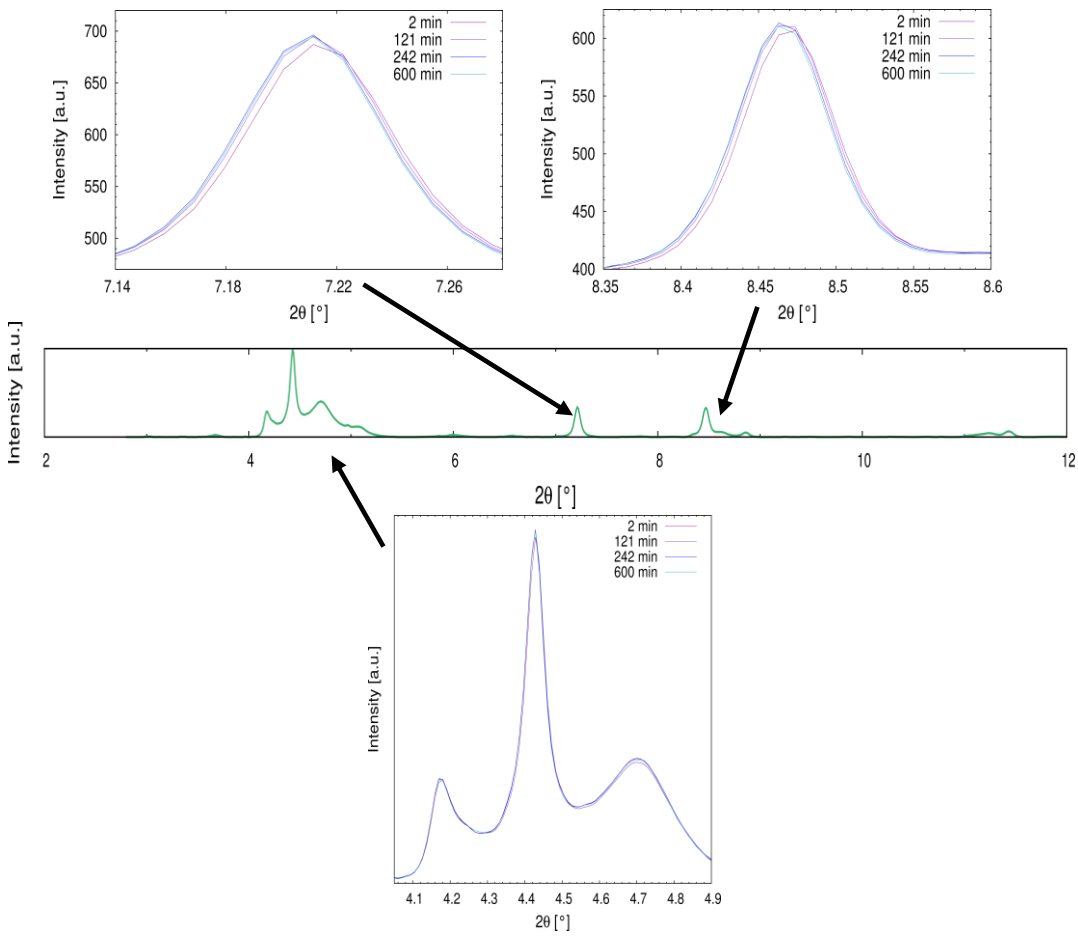

Figure 5.14: XRD pattern of reduced catalyst, including magnified regions containing the major features in the Co^0 pattern. Each magnified box shows the evolution of that region of the XRD pattern of at intervals throughout FTS.

An alternative cause of the evolution of the Co^0 reflections over the 12 h of FTS may be a change in the fcc/hcp/intermixed Co^0 ratio over the course of the reaction.[23] The largest overall variation in the diffraction patterns, as seen in Figure 5.14, (as well as in the EXAFS data) occurs within the first 2 h of FTS. This corresponds to changes in the mass spectrometry response (Figure 5.15) of some of the hydrocarbons over the first 2-3 h of the reaction – suggestive of some form of structural change in the initial stages of the reaction.

Table 5.2: Table detailing the variation in the major Co^0 reflections during FTS (at 2, 194, and 600 min), including information on the reflection position.

	Time (min)	**2θ (°)**	**d (Å)**
hcp [111] fcc [002]	2	4.515	2.004
	121	4.514	2.005
	600	4.512	2.006
hcp [220] fcc [2-10]	2	7.355	1.230
	121	7.353	1.231
	600	7.352	1.231
hcp [311] fcc [2-12]	2	8.640	1.048
	121	8.630	1.049
	600	8.625	1.050

Both methane (m/e=15), and ethene (m/e=26) exhibit a gradual decline throughout the 12 h of FTS, with the most significant decrease seen in the first 3 h. The butane (m/e=55) response, on the other hand, decreases sharply in the first 20 min, and continues to decrease over the first 5 h of FTS. During this time, the He response remains stable (appendix 13), while the H_2 response shows a slight increase as less H_2 is used during FTS (Figure 5.15). Other mass responses remain stable (appendix 13). This would mean that the variation in the hydrocarbon responses is real, as opposed to settling of the mass spectrometer signal.

Slightly different behaviour in the mass spectrometry responses are observed between the XAS and HR-XRD experiments. This is most likely due to differences in the spectrometers used in the experiments, as well as differences

in the sensitivities of the individual channels. Full mass spectrometry responses are given in (appendix 13).

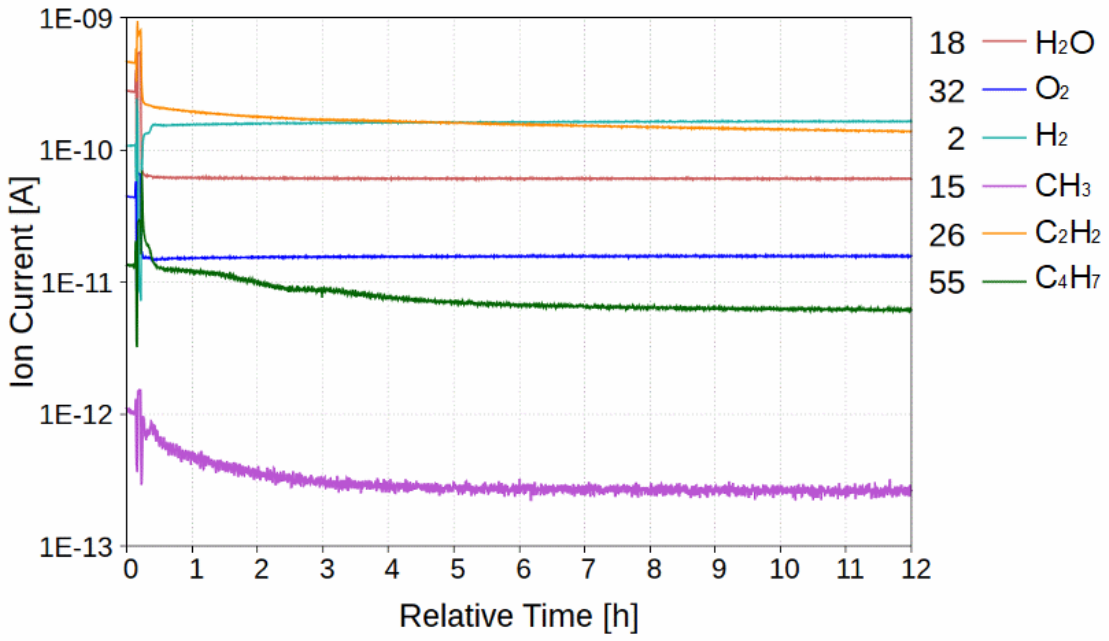

Figure 5.15: Mass spectrometry response over 12 h of FTS during HR-XRD measurements on ID15.

As with the XRD data, the EXAFS data varies only subtly over the course of 12 h of FTS, with the majority of variation seen in the first 2 h. Potential variation of the fcc and hcp content is also suggested by the EXAFS, as there is some difference in the 2nd and 3rd shells which is where the main differences between fcc and hcp Co^0 are observed, hinting at some variation in the Co^0 nanostructure. However, the nanoparticles are so large that any increase in size would have a minimal effect on the Fourier Transform (FT). An increase in the first shell is observed which may suggest an increase in particle size, but simple sintering would lead to a change in the intensity of all FT peaks, not just the first shell.

Full multiple scattering fits of these EXAFS data were attempted, however there were strong correlations between the N and σ^2 values due to the multiple component nature of the system and possibly due to the geometry of the cylindrical capillary cell used.

Simpler 1st shell fitting was performed, which included both the Co-Co 1st shell of metallic cobalt and the 1st Co-O shell of CoO. CoO was chosen over Co_3O_4 as the LCA during reduction suggests CoO as the more abundant oxide species, although both paths are similar. The presence of the oxide 1st shell improves both the statistics of the fit and the physical reasonableness of N, although spectral leakage from higher shells cause some issues with the fitting of ΔR. This spectral leakage also changes slightly throughout FTS due to the changes in the second and third shells not addressed in the first shell model.

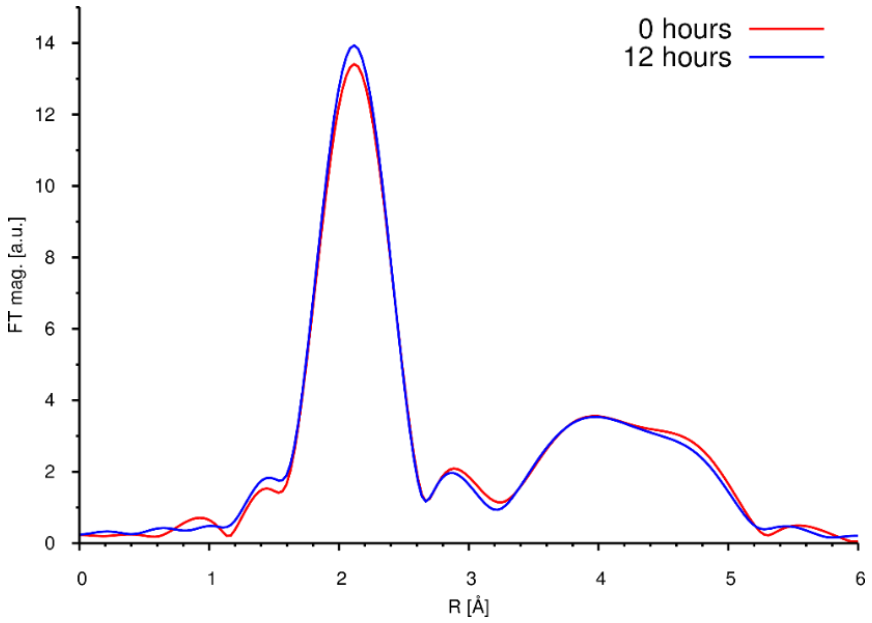

Figure 5.16: Fourier transform of EXAFS data at the start and end of 12 h of FTS.

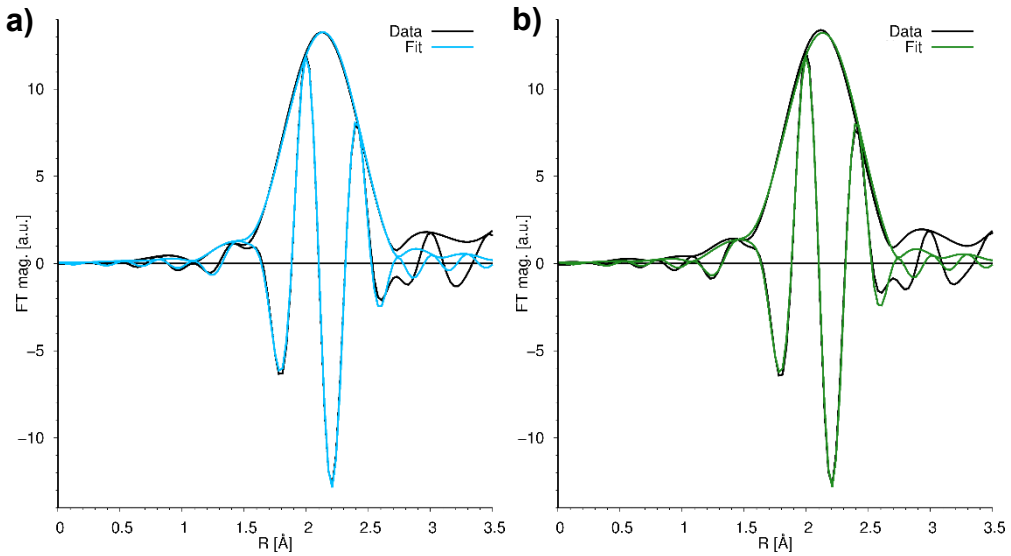

Figure 5.17: First shell EXAFS fits at a) 0 h and b) 12 h of FTS. Showing the observed data against the corresponding fits.

The average NP sizes at the beginning and end of FTS were estimated based on the work of Beale *et al.* (2010).[24] The estimated average particle size (assuming a spherical particle) from the first shell fits increases from 5.8 nm to 6.3 nm during FTS. Both the values and behaviour are different to XRD and the values are also inconsistent with the TEM measurements.

Table 5.3: Table of parameters from first shell fitting of EXAFS spectra over the course of FTS.

	Co-Co (Co^0)					Co-O (CoO)				R factor (k2 weight)
Time (min)	**N**	**σ^2**	**e0**	**R**		**N**	**σ^2**	**e0**	**R**	
0	8.09	0.010	1.083	2.508		1.35	0.008	1.083	2.046	0.016
58	8.15	0.009	1.083	2.508		1.30	0.008	1.083	2.045	0.020
131	8.16	0.010	1.083	2.508		1.40	0.008	1.083	2.044	0.019
193	7.98	0.009	1.083	2.510		1.21	0.008	1.083	2.039	0.020
255	8.12	0.010	1.083	2.509		1.31	0.008	1.083	2.035	0.015
317	8.12	0.009	1.083	2.509		1.23	0.008	1.083	2.046	0.015
380	8.06	0.009	1.083	2.510		1.22	0.008	1.083	2.041	0.019
442	8.14	0.010	1.083	2.508		1.24	0.008	1.083	2.037	0.017
504	8.37	0.010	1.083	2.509		1.41	0.008	1.083	2.043	0.017
566	8.46	0.010	1.083	2.509		1.39	0.008	1.083	2.045	0.019
629	8.38	0.010	1.083	2.509		1.38	0.008	1.083	2.041	0.015

The parameters from the EXAFS first shell fits are given in Table 5.3. The FEFF card used to calculate the scattering paths was created using Co^0 hcp and CoO .cif files in ATOMS. The Δr values are inconsistently smaller and larger than those of R_{eff} (the effective scattering distance in bulk) probably due to the averaging of the distances in the hcp and fcc Co^0. Based on the complex nature of Co^0 nanostructure and the results given using Debye simulations of the XRD data above, that both fcc and hcp are present in substantial quantities within the sample.

The coordination number evolution over FTS taken from Table 5.3 is shown in Figure 5.18. This graph is included to show the trend in increasing N in spite of the large error, typical of values of N calculated using EXAFS fitting.

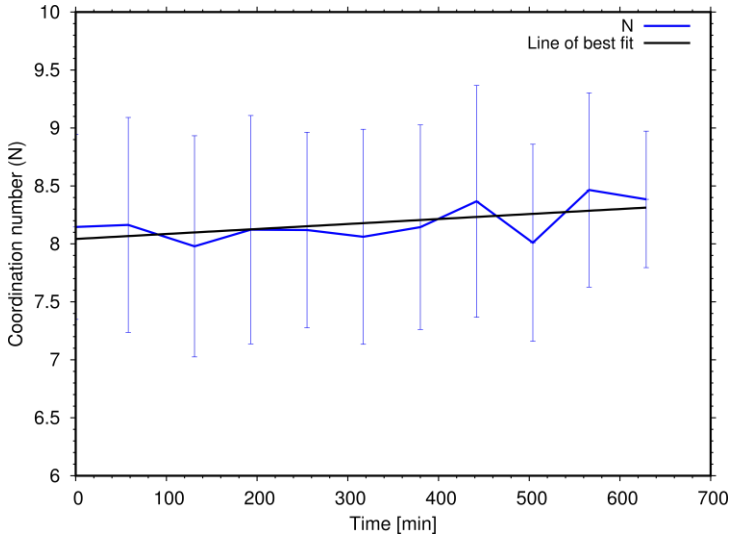

Figure 5.18: Graph of coordination number (N) as determined by 1st shell fitting of the EXAFS data at points during FTS. Highlighting the large error in N compared to the trend in the data.

Bearing in mind the inherent limitations of EXAFS analysis on such a multicomponent system it is also worth examining the variation in the XANES over FTS. The variation is minimal when examined purely by eye, however the trends of the cobalt components as determined by LCA (Figure 5.19) show a slight increase in Co^0 (0.63 to 0.67), a slight decrease in CoO (0.26 to 0.22), and a negligible change in the Co_3O_4 fractional composition.

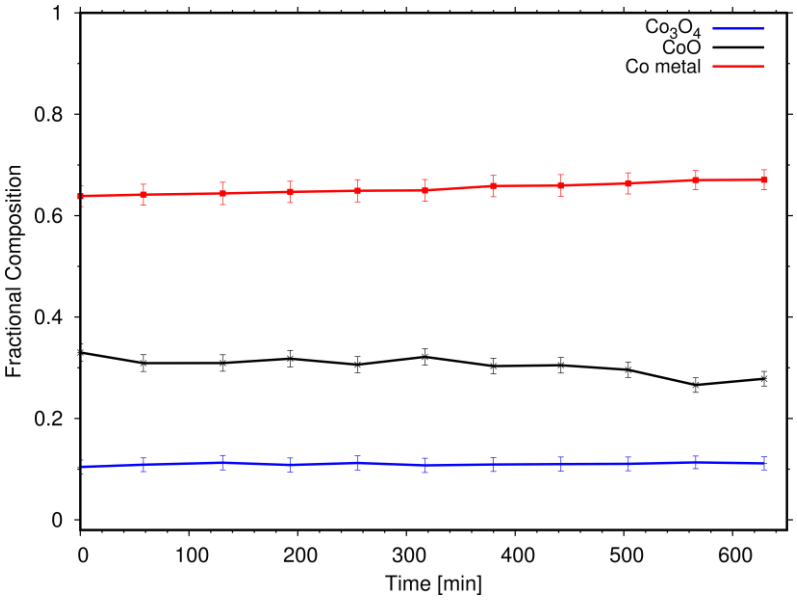

Figure 5.19: Fractional composition variation of cobalt-based components over the course of FTS as determined by LCA of the XANES data.

Although the errors are large in comparison to the variation, the trends are clear across the 12 h of FTS and suggests the continuing reduction of the residual CoO into Co^0 in the reducing environment of FTS conditions. This is consistent with the very slight increase in the coordination number (N) of the first Co-Co shell in the EXAFS fitting above – suggesting that the increase in N is due to sintering. This is not conclusively observed in the XRD, which could mean that both the CoO and metallic cobalt percentage variation could be in smaller nanoparticles in the system, unobservable by XRD.

Rietveld refinement fails as an analysis technique in systems similar to these cobalt metal systems due to their complex nanostructure (Figure 5.11) and offer no help in describing the variation seen over FTS. Not only are unphysical parameters required to force the fit, but the fit is still too poor to follow the subtle variations observed. Whereas, it is possible to achieve far superior, and more chemically appropriate fits for this data via Debye simulations using the unic model.

Debye simulations of the diffraction patterns at 0 h and 12 h of FTS are given in Figure 5.20. It should be noted that these simulations also fit the background using a polynomial spline, and the data shown are with that theoretical background subtracted – the full fitted data plus individual components are in (appendix 14).

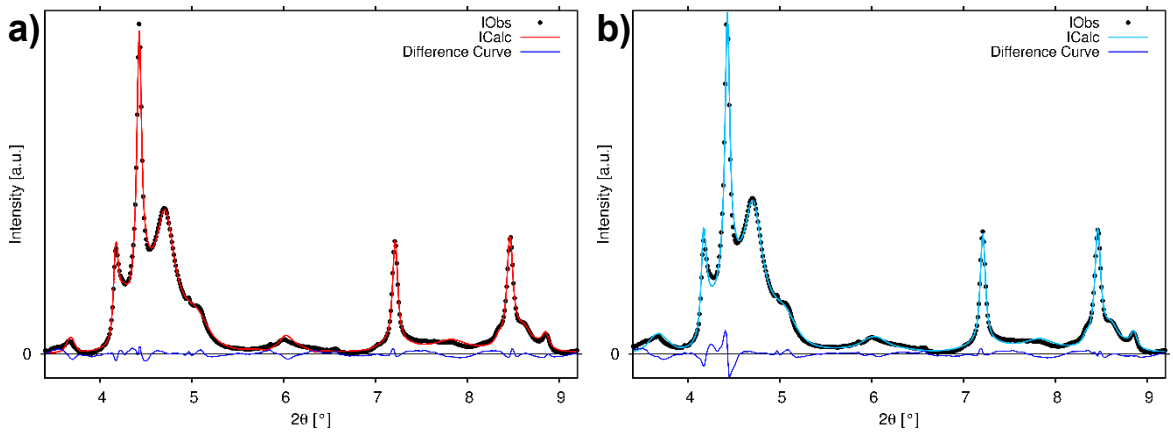

Figure 5.20: Debye simulations based on the unic model fitted to experimental data of a) the initial, and b) the final XRD pattern during 12 h of FTS. Where IObs, and ICalc are the observed and calculated intensities respectively, and the difference curve is the difference between the two.

The initial fit had an R-factor of 0.0084, a χ^2 of 0.688 and a R-factor for background fitting of 0.117. The final fit had an R-factor of 0.0137, a χ^2 of 0.135, and a background R-factor of 0.116. The Debye simulations are both a better fit statistically and in terms of chemical reasonableness than that of the Rietveld refinements.

Table 5.4: Percentages of purely fcc, hcp, and intermixed blocks within the scattering domains of Co^0. Initial and final values before and after 12 h of FTS, as well as the variation.

	Fractional Percentage (%)		
	Time=0 h	**Time=12 h**	**Variation**
f_{cc}	20.28±0.01	21.53±0.01	1.24
$f_{ch}+f_{hc}$	38.68±0.01	42.45±0.01	3.77
f_{hh}	41.02±0.01	35.10±0.01	-5.04

The probability factors of the possible concatenations change from the initial to final pattern fit by α: 0.713 to 0.713, β: 0.301 to 0.291, γ: 0.235 to 0.235, and δ: 0.501 to 0.602. From the probability factors, the ratio of fcc, hcp and mixed blocks are calculated using equations 3.12 – 3.15. The values of which are shown as percentages in Table 5.4.

The full MINUIT parameter files for both diffraction patterns, including all inputted and fitted variables for the simulations, are given in appendix 15. The relative percentages of the fcc, hcp, and mixed Co^0 components change meaningfully over the course of 12 h of FTS. An increase is observed in both the intermixed and fcc components (3.77 % and 1.24 % respectively), at the expense of the hcp component (-5.03 %).

Table 5.5: Percentage composition of the sample before and after 12h of FTS as determined by Debye simulations.

	Percentage composition (%)	
	0h	**12h**
Co^0	99.9±1.0	99.8±1.0
CoO	0.2±1.0	0.2±1.0

In the same simulations, the scattering domain size increases from 13.4±0.01 nm to 14.1±0.01 nm, while the change in standard deviation is minimal 18.0±0.001 nm to 17.7±0.001 nm (uncorrected for instrumentational broadening). The Debye simulations (Table 5.5) suggest that there is a negligible quantity of Co_3O_4 in the samples both before and after 12 h of FTS, and a minimal change in the Co^0 and CoO. This contradicts the XAS analysis where a continued, but slight, reduction is observed. Smaller nanoparticles have been shown to bind to the support strongly and be difficult to reduce.[8] The XRD and XAS observations together would be consistent with the continued reduction of those smaller nanoparticles.

5.4. Discussion

The work included in this chapter is closely related to that carried out in the following chapter: 6. As such some discussion of the results from both chapters concerning the difference in behaviour between nanoparticle sizes is included in the discussion section of the companion chapter.

The work here aimed to interrogate three key issues concerning Co^0 FTS catalysts: i) the reoxidation of smaller Co^0 nanoparticles during FTS, ii) the influence of Co^0 fcc/hcp/intermixed ratio, and iii) the potential formation of support interaction phases during FTS. The reoxidation issue is discussed in the unstable size range chapter which follows as it is more relevant there.

Additionally, the 2 bar FTS pressure used in the experiments, while still far off industrial pressures of 20 bar, is an improvement on the vast majority of operando X-ray studies reported in the literature.

Both the calcination and reduction proceeded as expected, with some differences observed between the XRD and XAS data due to the heavier weighting of large crystallites/scattering domains in the XRD and the ability of XAS to probe all cobalt-content, even that which may be atomically dispersed. For example, the reduction appears to occur earlier in the XRD data, and the calcination appears to be almost instantaneous in the XAS spectra. During FTS small variations were observed in both the XRD and XAS data – consistent with

a stable, relevant catalyst. These variations were most pronounced during the first 2 h of FTS which corresponded to changes in mass spectrometry response, with the decrease of some key hydrocarbons and a corresponding increase in H_2 response.

Debye simulations using the unic model – capable of determining the ratio of fcc, hcp and intermixed Co^0 from high resolution XRD patterns – were used to determine if there was any change in the metallic nanostructure during FTS. This proved to be a far better statistical fit to the XRD data than Rietveld refinement, that also provided a significant improvement in chemical reasonableness of the fit. These simulations indicate an increase in fcc and intermixed Co^0 during 12 h of FTS of 1.24 % and 3.77 % respectively, while suggesting a decrease in the hcp Co^0 content of 5.03 %. Hcp Co^0 is believed to be the more active Co^0 polymorph as determined by computational studies[25], although as it is difficult to determine the hcp/fcc Co^0 ratio or synthesize samples of purely one polymorph or the other, this is still debated. As such the decrease observed may explain the decrease in mass spectrometry response of some hydrocarbons, the potential source of a loss of activity/productivity during FTS.

While there is a change in Co^0 nanostructure, a change in nanoparticle size is also seen in the Debye simulations using the XRD data and possibly inferred by first shell fitting of the EXAFS spectra. The Debye simulations shown a scattering domain increase from 13.4 nm to 14.1 nm – which may be a cause of deactivation. The coordination number (N) of the first Co-Co shell derived by first shell fitting of the EXAFS data increased during FTS. Although the increase is within the large error of values of N found through this method, the increasing trend in N is observed over FTS. This increase could be due to either an increase in Co^0 particle size, or an increase in the Co^0 content from continued reduction. LCA of the corresponding XANES spectra show a slight increase in Co^0 and decrease in CoO so it is more likely that the increase in N is due to increasing particle size.

The two techniques are not in agreement as to the fractional composition of the cobalt-based compounds in the samples, or their variation over FTS. As mentioned in the above paragraph, LCA of the XANES spectra is consistent with

the continued reduction of Co^0. Whereas, in the XRD Debye simulations, there is very little CoO detected (~0.2 %) and no Co_3O_4, however the CoO shows a negligible increase from 0.16 % to 0.23 %. It is reasonable for the techniques to detect different fractional compositions as the XAS is more sensitive to smaller nanoparticles or clusters which are more likely to be unreduced oxides. The behaviour seen in the XRD patterns is similar to that observed in the PDF-CT study Senecal *et al.*[8], where Co^0 particles under 7 nm oxidised to CoO in the initial stages of FTS. The discussion on particle size sensitive oxidation is continued in the following chapter, although it is interesting that some effect is also seen in this sample.

5.5. Conclusion

The aim of this work was to use combined synchrotron-based *operando* X-ray techniques to interrogate three key issues still not fully resolved in the study of Fischer-Tropsch catalysts. These were the influence of the metallic nanostructure (fcc/hcp/intermixed Co^0) on FTS, the reoxidation of smaller metallic cobalt nanoparticles during the initial stages of FTS, and the potential presence of metal oxide support interactions.

This work is new in two respects. Firstly, in terms of the system studied. Much of the work on Co-based FTS catalysts focus' on Co/Al_2O_3 or Co/TiO_2 systems. Whereas, this work has been based on the less well interrogated Co/MCF-17 (silica). Secondly, this work is new in terms of the analysis methods used. Debye simulations of XRD patterns using the unic model were applied to a realistic catalyst for the first time. Debye simulations model metallic cobalt based systems with a higher degree of chemical reasonableness than Rietveld refinement, which cannot account for stacking faults commonly present in Co^0. [20]

The most significant result from this first part of the twin chapter work is the determination of fcc, hcp and intermixed Co^0. This shows a decrease in the more active hcp polymorph of ~5 % at the expense of both fcc and intermixed Co^0 phases, which correlates with a decrease in hydrocarbon mass spectrometry responses during FTS. This is suggestive of a relationship between activity of the catalyst and its nanostructure, not frequently discussed in the literature.

Not only is this method a vast improvement over Rietveld refinement for these stacking fault rich systems, but the tailor-made software is an improvement over other Debye modelling methods which involve redefining the base model for every sample in a way that leaves room for unphysical models such as those needed for Rietveld refinements.

An alternative method of determining hcp vs fcc Co^0 ratio in these catalysts uses NMR.[26] Although useful, NMR is limited in comparison to the unic-based Debye simulations of XRD patterns as it determines less information on the sample (the percentage composition of hcp and fcc only – limiting knowledge of the effect of staking faults and intermixed phases), and is less accurate (±3 %).

This is the first time this unic model method has been applied to *operando* catalyst studies, and therefore there are some improvements to be made. The sequential fitting using Debye simulations would require the alteration of the code to run on multiple cores simultaneously to be time efficient – this would also improve the functioning of the normal simulations. Additionally, A. Martorana and co-workers[20,27] are amending the code to be performed on PDF data alongside PDF analysis which could bring more clarity to the issue of the oxidation of smaller Co^0 nanoparticles, seen here and in other studies.

5.6. References

1 G. Melaet, W. T. Ralston, C.-S. Li, S. Alayoglu, K. An, N. Musselwhite, B. Kalkan and G. A. Somorjai, *J. Am. Chem. Soc.*, 2014, **136**, 2260–2263.

2 A. Y. Khodakov, A. Griboval-Constant, R. Bechara and V. L. Zholobenko, *J. Catal.*, 2002, **206**, 230–241.

3 Y. Qi, J. Yang, D. Chen and A. Holmen, *Catal. Letters*, 2014, **145**, 145–161.

4 J. P. den Breejen, P. B. Radstake, G. L. Bezemer, J. H. Bitter, V. Frøseth, A. Holmen and K. P. de Jong, *J. Am. Chem. Soc.*, 2009, **131**, 7197–203.

5 G. L. Bezemer, J. H. Bitter, H. P. C. E. Kuipers, H. Oosterbeek, J. E. Holewijn, X. Xu, F. Kapteijn, A. J. van Dillen and K. P. de Jong, *J. Am. Chem. Soc.*, 2006, **128**, 3956–3964.

6 E. Rytter, N. E. Tsakoumis and A. Holmen, *Catal. Today*, 2016, **261**, 3–16.

7 G. Jacobs, T. K. Das, Y. Zhang, J. Li, G. Racoillet and B. H. Davis, *Appl. Catal. A Gen.*, 2002, **233**, 263–281.

8 P. Senecal, S. D. M. Jacques, M. Di Michiel, S. A. J. Kimber, A. Vamvakeros, Y. Odarchenko, I. Lezcano-Gonzalez, J. Paterson, E. Ferguson and A. M. Beale, *ACS Catal.*, 2017, **7**, 2284–2293.

9 N. E. Tsakoumis, J. C. Walmsley, M. Rønning, W. Van Beek, E. Rytter and A. Holmen, *J. Am. Chem. Soc.*, 2017, **139**, 3706–3715.

10 C. H. Mejía, T. W. van Deelen, and K. P. de Jong, *Nature Comms.,* 2018, **9**, 2041-1723.
11 J. J. Herbert, P. Senecal, D. J. Martin, W. Bras, S. K. Beaumont and A. M. Beale, *Catal. Sci. Technol.*, 2016, **6**, 5773–5791.
12 E. van Steen, M. Claeys, M. E. Dry, J. van de Loosdrecht, E. L. Viljoen and J. L. Visagie, *J. Phys. Chem. B*, 2005, **109**, 3575–3577.
13 M. Wolf, H. Kotzé, N. Fischer and M. Claeys, *Faraday Discuss.*, 2017, **197**, 243–268.
14 M. Claeys, M. E. Dry, E. Van Steen, P. J. Van Berge, S. Booyens, R. Crous, P. Van Helden, J. Labuschagne, D. J. Moodley and A. M. Saib, *ACS Catal.*, 2015, **5**, 841–852.
15 J. C. Mohandas, M. K. Gnanamani, G. Jacobs, W. Ma, Y. Ji, S. Khalid and B. H. Davis, *ACS Catal.*, 2011, **1**, 1581–1588.
16 S. Nikitenko, A. M. Beale, A. M. J. van der Eerden, S. D. M. Jacques, O. Leynaud, M. G. O'Brien, D. Detollenaere, R. Kaptein, B. M. Weckhuysen and W. Bras, *J. Synchrotron Radiat.*, 2008, **15**, 632–640.
17 K. Høydalsvik, J. B. Fløystad, A. Voronov, G. J. B. Voss, M. Esmaeili, J. Kehres, H. Granlund, U. Vainio, J. W. Andreasen, M. Rønning and D. W. Breiby, *J. Phys. Chem. C*, 2014, **118**, 2399–2407.
18 Gatan, GMS 3 Software Registration | Gatan, Inc., http://www.gatan.com/datasheets/gms-3-software-registration, (accessed 12 March 2018).
19 B. Ravel and M. Newville, in *Journal of Synchrotron Radiation*, 2005, vol. 12, pp. 537–541.
20 A. Longo, L. Sciortino, F. Giannici and A. Martorana, *J. Appl. Crystallogr.*, 2014, **47**, 1562–1568.
21 A. Altomare, N. Corriero, C. Cuocci, A. Falcicchio, A. Moliterni and R. Rizzi, *J. Appl. Crystallogr.*, 2015, **48**, 598–603.
22 K. H. Cats and B. M. Weckhuysen, *ChemCatChem*, 2016, **8**, 1531–1542.
23 Stephen W. T. Price, D. J. Martin, A. D. Parsons, W. A. Sławiński, A. Vamvakeros, S. J. Keylock, A. M. Beale and J. F. W. Mosselmans, *Sci. Adv.*, 2017, **3**, e1602838.
24 A. M. Beale and B. M. Weckhuysen, *Phys. Chem. Chem. Phys.*, 2010, **12**, 5562–5574.
25 M. Sadeqzadeh, H. Karaca, O. V. Safonova, P. Fongarland, S. Chambrey, P. Roussel, a. Griboval-Constant, M. Lacroix, D. Curulla-Ferré, F. Luck and a. Y. Khodakov, *Catal. Today*, 2011, **164**, 62–67.
26 V. V. Matveev, D. A. Baranov, G. Y. Yurkov, N. G. Akatiev, I. P. Dotsenko and S. P. Gubin, *Chem. Phys. Lett.*, 2006, **422**, 402–405.
27 A. Longo and A. Martorana, *J. Appl. Crystallogr.*, 2008, **41**, 446–455.
28 J. Paterson, M. Peacock, E. Ferguson, M. Ojeda, and J. Clarkson, *Applied Catalysis A: Genera*l, 2017, **546**, 103-110.
29 F. James, *Unpublished*, 1994, 50.

6. Particle size effects on FTS: II) Unstable size range

6.1. Introduction

This chapter is the second part of a pair. Together they form an in-depth study of two Co/MCF-17(silica) catalysts of varying sizes. Both catalysts were synthesised in the same manner. One with a particle size of approximately 11 nm which falls in the stable size range for silica supported catalysts (addressed in the previous chapter), and the other of approximately 3 nm falling within the unstable size range discussed here. Much of the content of the introductions to both chapters overlap due to their shared focus and so will not be repeated in detail here. Additionally, as this is a companion chapter to the previous one, the discussion and conclusion sections here also include discussion and comparison between the behaviours of both the smaller and larger sized nanoparticle catalysts.

The aim of these two companion chapters is to use *operando* X-Ray absorption spectroscopy (XAS) and X-Ray diffraction (XRD) to determine the significance of the reoxidation of small Co^0 nanoparticles during the initial stages of Fischer-Tropsch Synthesis (FTS), the metallic Co nanostructure (fcc/hcp/intermixed ratio), and the supposed formation of support interaction phases during FTS. As the particle size examined here is firmly in the unstable range, the focus of this chapter will be on the oxidation of small metal nanoparticles during FTS.

Cobalt particle size affects both the activity and selectivity of FTS catalysts. Particles of approximately 6 nm have been shown to have maximum activity,[1,2] while maximum selectivity has been shown to range between 8-9 nm.[3] At some point below the optimum size Co^0 nanoparticles become unstable and prone to oxidation under FTS conditions.[4] While some studies have shown that only small Co^0 crystallites form oxides (~4.5 nm)[5,6], larger unstable particles have also been observed at 6.5 nm.[7]

The Co^0 particles in this work are approximately 3 nm. They fall within the lower, unstable size range. By studying this size of catalyst and comparing the

data with the earlier 11 nm chapter, both the size dependent reoxidation and potential metal support interaction should be examined. As the nanoparticles examined in this chapter are so small, a greater weighting is placed on the XAS analysis than the XRD. This is because XAS is sensitive to particles of less than 3 nm.[14]

6.2. Experimental methods

Samples were prepared using a standard Schlenk technique under an argon atmosphere, provided by S.K. Beaumont (Durham University), and which take the form of Co/MCF-17 with an average Co particle size of approximately 3 nm.

Operando XRD and XAS measurements were collected respectively on ID15 and BM26A at the European Synchrotron Radiation Facility (ESRF), Grenoble, France. XRD measurements were recorded at 78.5 keV and XAS measurements were recorded at the Co k-edge (7.712 keV) in transmission mode. During *in situ* experiments catalyst samples were packed into 1 mm diameter borosilicate capillaries, which were mounted in the BM26A sample environment cell.[8] To ensure consistency the same cell was mounted on both beamlines.

The catalyst was calcined in a two-step process. First heated from room temperature to 350 °C at a ramp rate of 5 °C/min in a flow of He, then from 350 °C to 550 °C at a ramp rate of 10 °C/min in a flow of O_2/He. The catalyst was then reduced in a flow H_2 and heated from 250 °C to 650 °C at a rate of 2 °C/min. The reduction starts and ends at a higher temperature than that of the previous chapter, as a higher temperature was needed to reduce the smaller nanoparticles.

FTS was performed at 250 °C at a pressure of 2 bar with a H_2:CO ratio of 2:1. Due to the instability of the catalyst, during the beamtime on BM26A, the catalyst oxidised under FTS conditions. Therefore, the gas and temperature procedure deviated from this standard, and additional reductions were performed, which will be elaborated on later in this work.

As in the last chapter, the pressure for FTS was chosen as 2 bar, to limit the formation of waxes and wax build up outside of the heated region.[9] Total gas flow was 10 ml/min corresponding to a gas hourly space velocity (GHSV) of 10000 h^{-1}. The temperature was controlled using a heat gun, and simultaneous mass spectrometry (MS) observations were recorded.

Transmission electron microscopy (TEM) images were captured using a Jeol-2100 (200 keV accelerating voltage) at the Research Complex at Harwell. Images were captured using Gatan DigitalMicrograph[10] and the particle sizes in the images were measured using ImageJ. XAS spectra were analysed using Athena and Artemis[11].

2D image integration and Rietveld refinements of the XRD data were performed using GSASII, phase identification was performed using QualX2[13], and some basic Scherrer analysis was performed using XPowder12. Some pre-processing of the data including intensity correction, trimming the 2θ range to remove the beam stop, and glass background removal were performed using Fortran 90 code and bash script.

Due to the limits of conventional XRD analysis for the study of small nanoparticles and those with complex nanostructure such as metallic cobalt, Debye simulations using a unic model were applied to this data. In this model, four probability factors are used to describe four possible unique combinations of two concatenated blocks of four Co^0 layers. These probability factors can be used to calculate the relative percentages of hcp, fcc, and mixed Co^0 within a given sample, and thus determine nano-structural variation over the reaction time.

6.3. Results

6.3.1. Calcination

The calcination procedure used here is identical to that used in the previous chapter. Calcinations were performed as a two-step process comprised of an initial slow calcination in He (RT to 350 °C at 5 °C/min), in order to remove any residual surfactant from synthesis, and a faster calcination in O_2/He (350 °C to 550 °C at 10 °C/min).

The XANES evolution over this calcination is presented in Figure 6.1. Much like the larger nanoparticles in chapter 5, the largest change in the spectra is noted on the switch in gas composition at 65 mins. Approximately at the change of gas. The difference in the evolution of the catalyst during this stage may be due to the air leak in the He line during the XRD experiments.

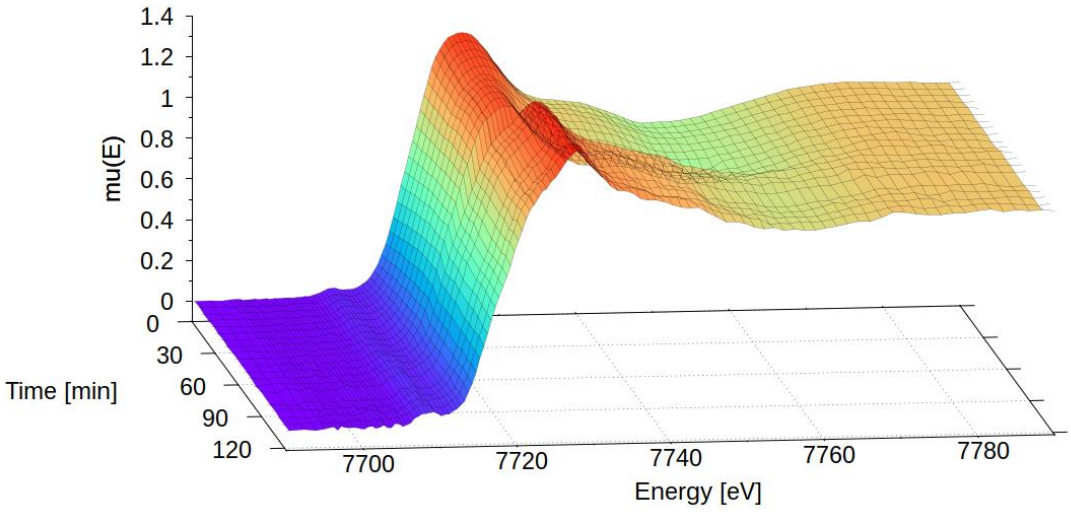

Figure 6.1: 3D evolution of XANES spectra over calcination (RT to 350 °C at 5 °C/min, and 350 °C to 550 °C at 10 °C/min).

The initial spectra more closely resemble oxidic spectral components than those of the larger nanoparticles, with a distinct pre-edge peak clearly separate from the rising edge. Principle component analysis (PCA) was performed on the XANES spectra taken during calcination. The initial spectra during calcination are best fitted to the original data using three components, whereas the final data set is composed of two components. However, target transforms of the Co_3O_4 and CoO reference spectra were not successful for any of the spectra over calcination, possibly due to the effect of the small NP size (particularly during calcination), on XANES rather than their absence in the data ensemble. The final two components must be the oxides (Co_3O_4 and CoO), and perhaps in the initial spectra there is both the oxides and the residual cobalt precursor. The failure of target transform of the PCA of the XANES data is only an issue with the calcination data.

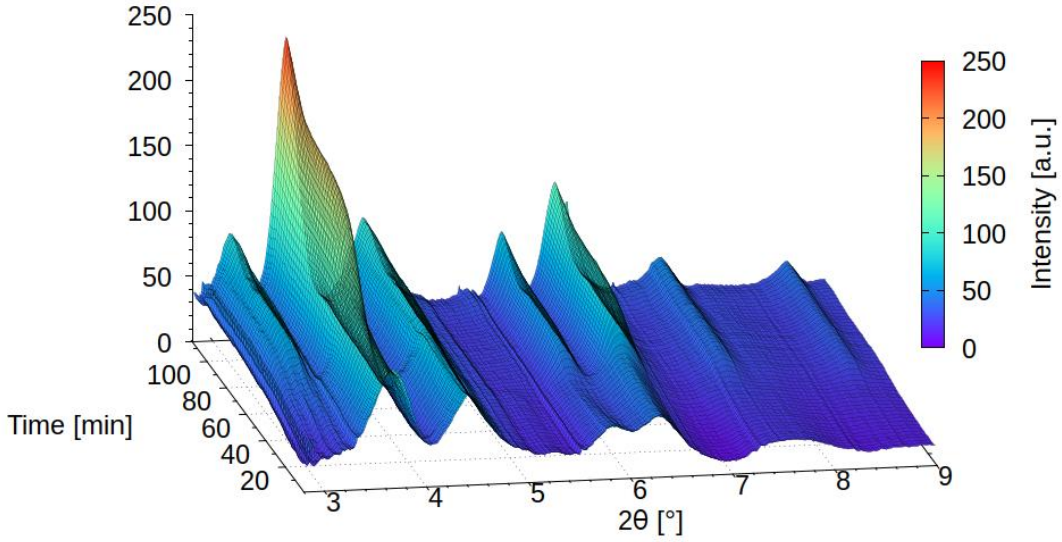

Figure 6.2: The evolution of XRD patterns over the course of calcination (RT to 350 °C at 5 °C/min, and 350 °C to 550 °C at 10 °C/min).

XRD patterns during the calcination (Figure 6.2), also would suggest the presence of Co_3O_4 initially, as some broad Co_3O_4 reflections corresponding to the most intense reflections are present in the first patterns. While the XRD shows the presence of Co_3O_4 at the start of calcination, PCA of the initial XAS spectra also shows three fractional components – most likely including the precursor. Therefore, a full calcination was necessary, and even if the catalyst had already been calcined, the same procedure would have needed to be applied to clean the surface.

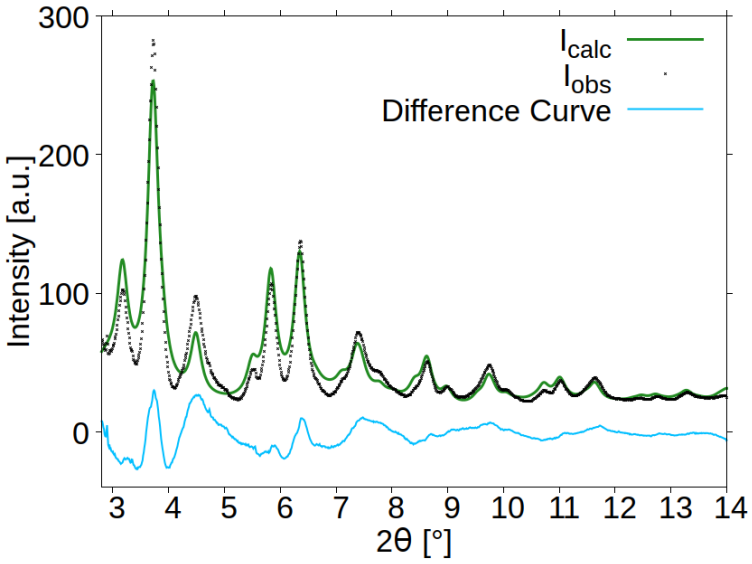

Figure 6.3: Rietveld refinement of 3nm Co/MCF-17 catalyst after calcination, showing Co_3O_4 reflections.

Because of the small crystallite size Rietveld refinement was challenging, and the fit is not good - Figure 6.3. The Co_3O_4 crystallite size was determined to be 4 nm by Rietveld refinement, and 3.3±0.8 nm by Scherrer analysis (corrected for instrumental broadening).

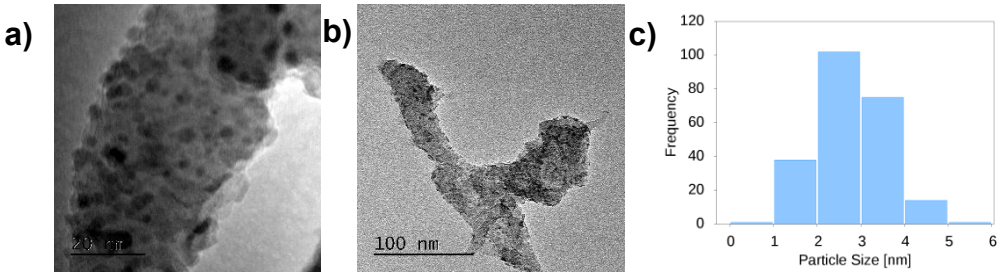

Figure 6.4: a&b) TEM images of Co/MCF-17 catalyst after a calcination in air, heated from RT-350 °C at 5 °C/min, then from 350 - 550 °C at 10 °C/min. c) A histogram showing particle size distribution as measured from TEM images.

To verify the particles size, additional TEM measurements were recorded and are given in Figure 6.4. They show an average particle size of 3.1±0.7 nm up from a size of 2.8±0.8 nm before calcination. The standard deviation remains similar, reducing slightly. These measurements agree with the crystallite size as determined by Scherrer analysis. However, calcinations performed for TEM imaging were performed in air rather than a O_2/He mix, and therefore these TEM images may not be representative of the true calcination.

6.3.2. Reduction

As the nanoparticles were smaller in this section of the study, a higher reduction temperature was required to reduce the catalyst. The same ramp rate of 2 °C were used, but based on our knowledge of the system, and in order to save time, the starting temperature was increase to 250 °C compared to that of 150 °C in chapter 5. Therefore, reductions were carried out in a flow H_2/He(5 %), and heated from 250 to 650 °C at a rate of 2 °C/min.

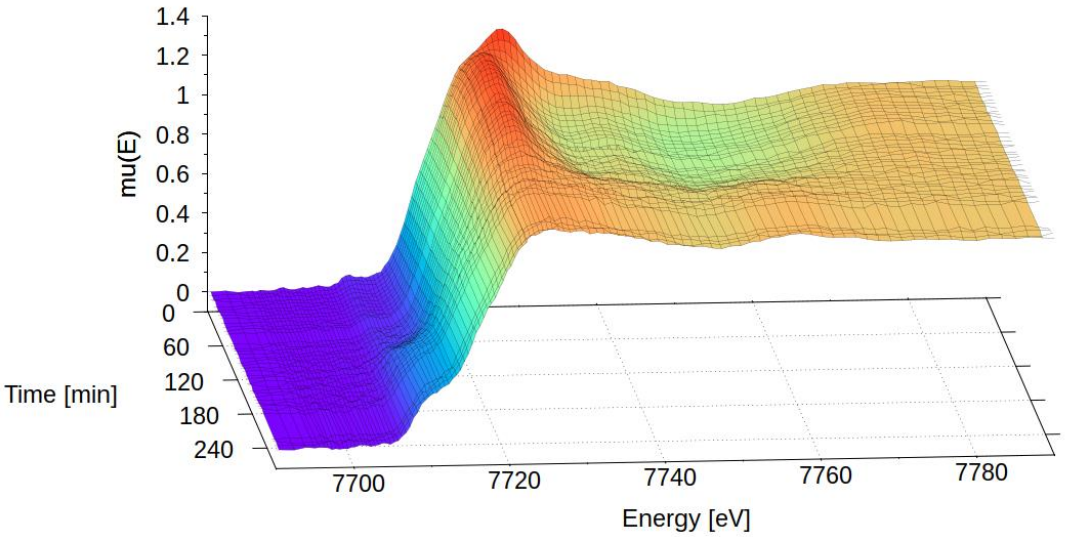

Figure 6.5: Evolution of XANES over the course of the reduction (250 to 650 °C at 2 °C/min in H_2/He(5%))

Figure 6.5 is a 3D presentation of the XANES spectra over the reduction – moving from the back to the front of the image with time. The Co_3O_4 content appears to start to reduce to CoO within the first 20-30 min, which is comparable to that of the larger nanoparticles size Co/MCF-17 catalyst. Then to be dominated by Co^0 gradually over the remaining time of the reduction.

Linear combination analysis (LCA) was performed on the XANES data over the course of the reduction. The fitting was significantly less accurate than that of the larger particles, most probably due to the known change in XANES spectra due to nanoparticle size. Although there is a size effect on the XANES and the errors are larger in comparison, PCA of the same XANES spectra resulted in successful target transforms on the key cobalt-based phases: Co_3O_4, CoO, and Co^0. This means that the references are still components of the spectra

even if as slight change in the XANES spectra are observed due to the small nanoparticle size.

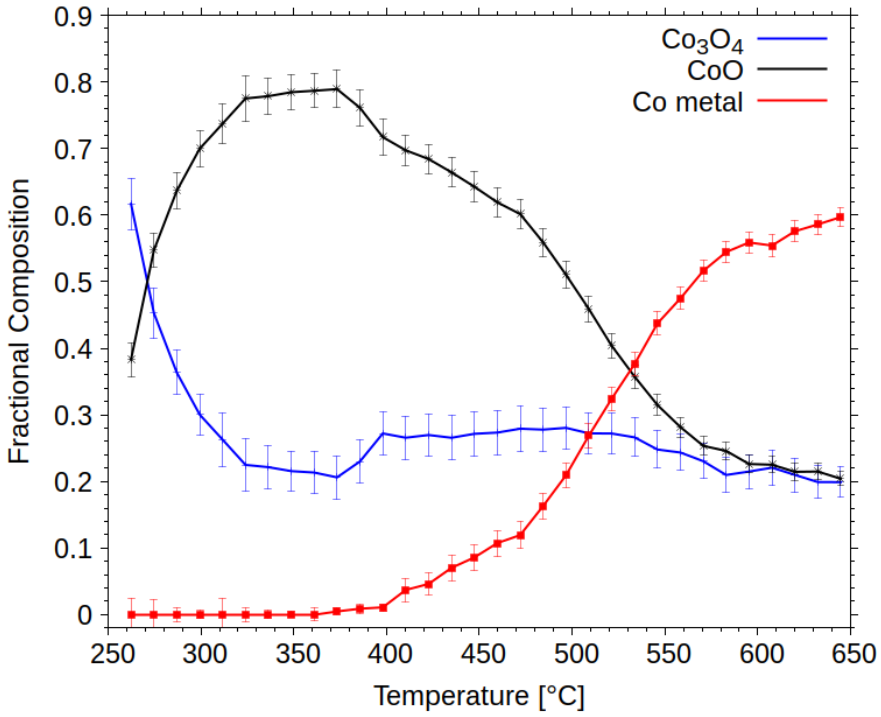

Figure 6.6: LCA of XANES spectra during the reduction (250 to 650 °C at 2 °C/min in H_2/He(5 %)).

The initial oxide ratio (CoO/Co_3O_4), as fitted by LCA, in this sample is different to that of the ~11 nm catalyst (chapter 5) at the same temperature. In the larger nanoparticle sample the initial composition according to LCA of the XANES is 80 % Co_3O_4, and 20 % CoO. Whereas, here, the ~3 nm catalyst there is a far higher percentage of CoO, with approximately 60 % Co_3O_4, and 40 % CoO. The metallic cobalt percentage after reduction is lower than in the larger nanoparticle sample (~60 % compared to 69 %). The maximum CoO fractional composition falls at approximately 350 °C, just below that of the larger nanoparticles (~370 °C).

Much like the XANES spectra, the XRD patterns (Figure 6.7) show the reduction of Co_3O_4 to CoO earlier in the run due to the higher starting temperature than that of the other sample with a larger particle size. This is evident by the disappearance of the Co_3O_4 reflection at 3.16 °2θ, the shift for the peak at approx. 3.7 °2θ to lower 2θ, and the disappearance of the three Co_3O_4 reflections in the

range 5.5-6.5 °2θ to be replaced by the CoO reflection at 6.00 °2θ. Over the remainder of the reduction the CoO gradually reduces to Co^0, although CoO reflections are still prominent suggesting that a large quantity remains unreduced.

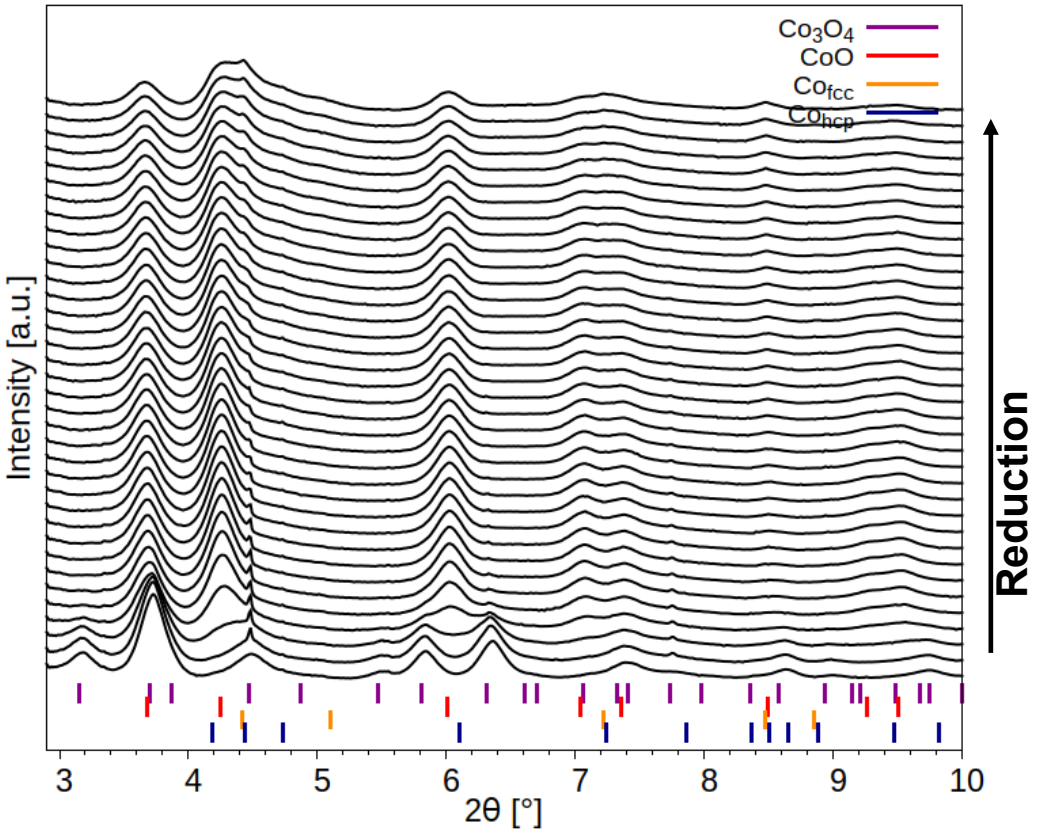

Figure 6.7: The evolution of XRD patterns over the course of the reduction (210 minutes), 250 to 650 °C at 2 °C/min in H_2/He (5 %). Moving from the bottom of the graph to the top during the reduction.

What appears to be an additional phase is present in the data (Figure 6.7), from the second pattern onwards, but which reduces in intensity over the course of the reduction. The reflections are at 4.483, 4.730, 7.751, and 10.038 ° 2θ. It was not possible to match these reflections to any distinct phase that may have been present in the sample, except for some Co_3O_4 reflections. The most intense reflection at 4.483 ° 2θ appears rather significantly less broad than the rest of the peaks. This could be one large particle of Co_3O_4 being clipped by the X-ray beam, with only some reflections not present due to the orientation of the crystal.

6.3.3. Catalyst instability under Fischer-Tropsch conditions

The 3 nm Co/MCF-17 catalyst proved to be unstable under FTS conditions – as was predicted by its particle size. This is apparent in the XAS data, however the behaviour of the XRD and XAS data differ during FTS. High resolution XRD patterns show a slight variation over the course of FTS, while XAS show a gradual oxidation of the catalyst during the first hour under FTS conditions. This is most likely because the XAS is more sensitive to the smaller and the most unstable Co^0 nanoparticles.

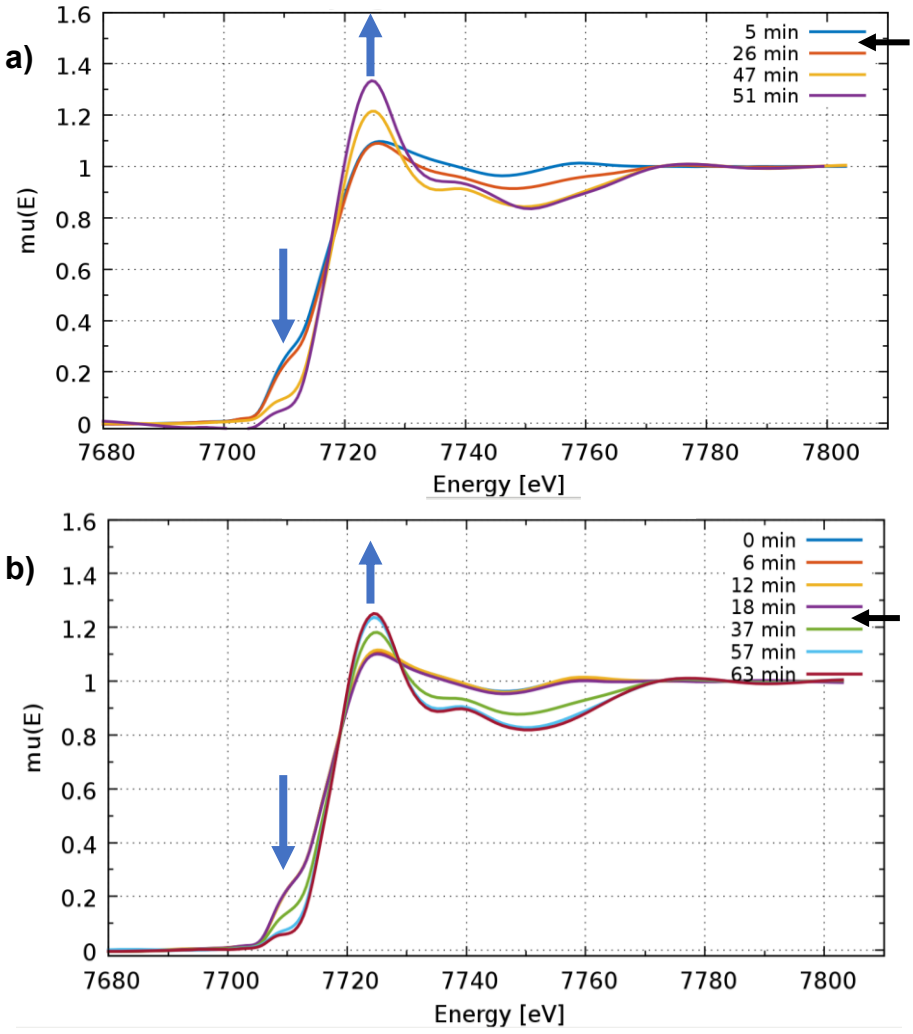

Figure 6.8: XANES spectra during approximately the 1st hour under FTS conditions showing the oxidation of the unstable 3 nm Co/MCF-17catalyst. A) FTS run 1 and b) FTS run 2. The black arrows represent the approx. start time that the gas change reaches the cell. Blue arrows indicate evolution over time.

As the catalyst oxidised under FTS conditions, the catalyst was then reduced again after (re)oxidation. The oxidation of the Co^0 during FTS is seen directly in the XANES spectra (Figure 6.8).

Two oxidations are shown in Figure 6.8, the first performed after the standard reduction at 2 °/min, and the second using the same sample after the oxidation shown in Figure 6.8a and a faster reduction at 5 °/min.

After the first oxidation and re-reduction the same behaviour is observed, whereby the metallic cobalt oxidises under FTS conditions. LCA of the XANES spectra for both FTS runs (Figure 6.9) show this process happens at a similar rate for both experiments.

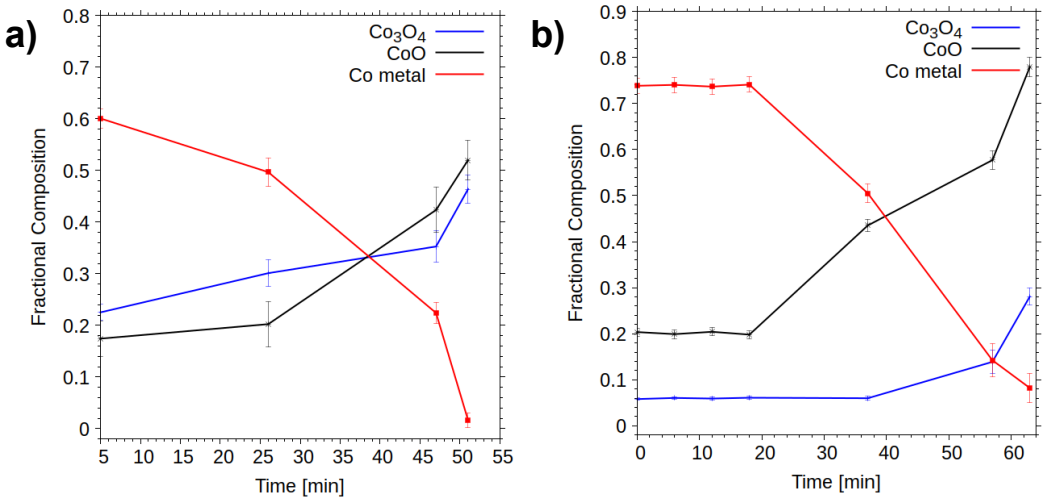

Figure 6.9: Linear combination analysis of the XANES spectra during a) FTS run 1 and b) FTS run 2.

Unfortunately, the first run under FTS conditions did not reach a stable state as it was assumed there was an issue with the gas system. This was not possible to rule out during the experiment as the mass spectrometer was malfunctioning. The second run did appear to just reach a near stable state as seen in the XANES (Figure 6.8b).

Since the particles underwent an oxidation under FTS conditions and a further reduction, similar to a reduction-oxidation-reduction experiment.[16] It was assumed that the particles would have increased in size from the first FTS run to the second. However, a comparison of the EXAFS spectra of the calcination and

oxidation, and after both reductions, suggests that the particles may have actually reduced in size. If this was only an issue after reductions it could be due to a poorer reduction in the second FTS run, but it is also seen in the oxidized sample.

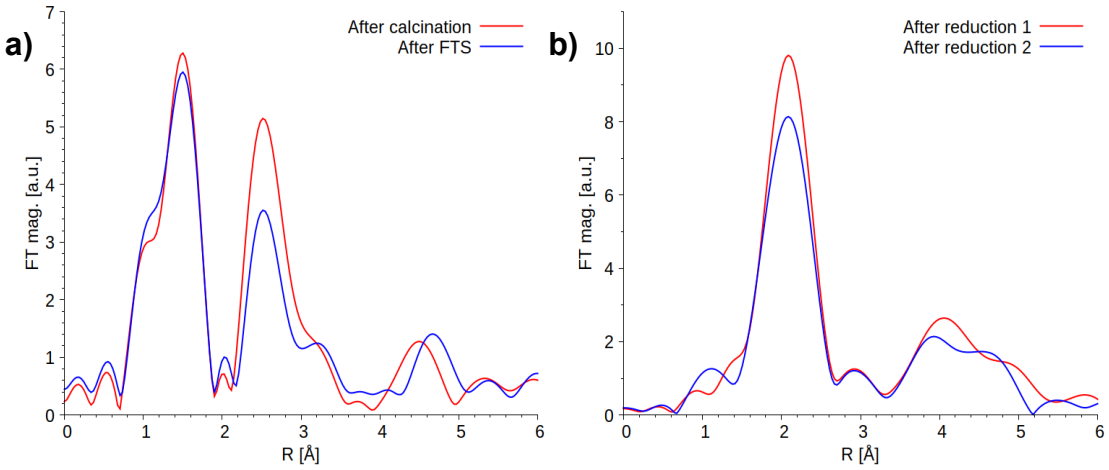

Figure 6.10: Comparison of the EXAFS spectra a) before the calcination and the first FTS run and, b) after the first and second reduction.

First shell fitting was carried out on the EXAFS spectra (Figure 6.11), and the average NP sizes at the beginning of reduction 1 and 2 (before the FTS runs that resulted in reoxidation), were estimated based on the work Beale *et al.* (2010).[14] The estimated average particle size (assuming a spherical particle) from the first shell fits increases from 5.85 nm to 6.3 nm during FTS. Both the values and behaviour are different to XRD. The values for the fit given in Table 1.

However, any decrease in the Fourier transform magnitude of the EXAFS may instead be due to a lower concentration of the corresponding Co species. To verify this LCA was carried out on the spectra to find the fractional composition according to the XANES spectra. In the oxide samples (after the calcination and first oxidation under FTS conditions), the Co_3O_4 decreases slightly from 0.69 to 0.64, and the CoO increases from 0.32 to 0.36. In the catalyst after both reductions the factional composition of CoO remains relatively stable (0.23 to 0.24), while the Co^0 decreases from 0.69 to 0.54, and Co_3O_4 increases from 0.08 to 0.23. This does not account for the unexpected behaviour of the oxides.

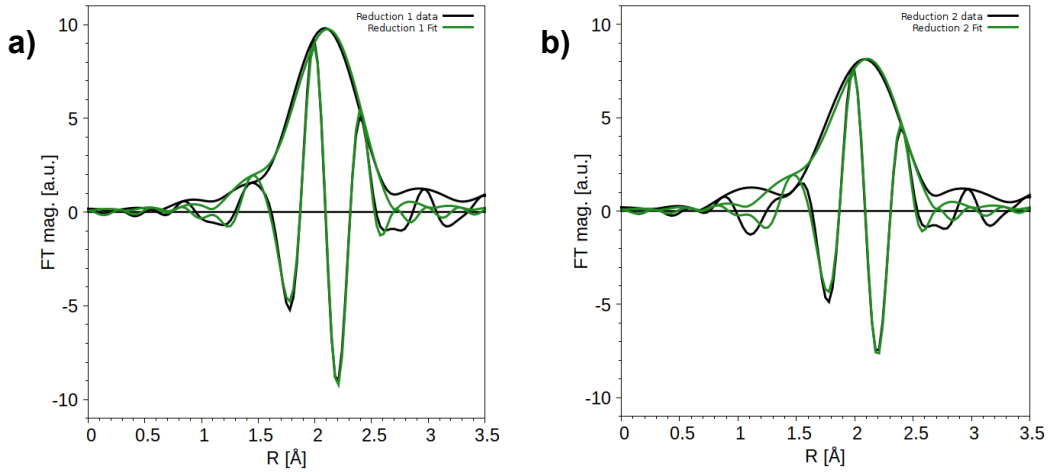

Figure 6.11: First shell EXAFS fits on the reduced catalysts before a) the first unstable FTS run and, b) the second unstable FTS run; showing the observed data against the corresponding fits.

Table 1: Table of parameters from first shell fitting of EXAFS spectra after reduction 1 and 2.

	Co-Co (Co^0)				Co-O (CoO)				R-factor (k2 weight)
Time (min)	**N**	**σ^2**	**e0**	**R**	**N**	**σ^2**	**e0**	**R**	
Red 1	4.99	0.0105	-0.874	2.492	0.99	0.009	-0.874	1.977	0.00439
Red 2	4.01	0.0103	-0.874	2.488	1.18	0.009	-0.874	1.985	0.01481

The time between gas change and mass spectrometry response on the BM26A gas rig was ~3:30/4:00 min at atmospheric pressure and ~15:00 min at 2 bar during other experiments. This corresponds to the approximate start of the oxidation observed in the XANES (Figure 6.8 and Figure 6.9), suggesting the oxidation starts to occur as soon as the catalyst is in contact with the syngas. If the oxidation was due to some leak in the system that might have allowed oxygen to enter the cell, the oxidation would have been very quick. However, the gradual reduction points to size effects as the cause.

Unfortunately, the mass spectrometer on BM26A was malfunctioning during this experiment. A short second run of this experiment was performed in house, but the mass spectrometer broke again. Therefore, a comparison of the spectrometry data from the ID15 and BM26A experiments is not possible. However, mass spectrometry data was recorded during the ID15 beamtime.

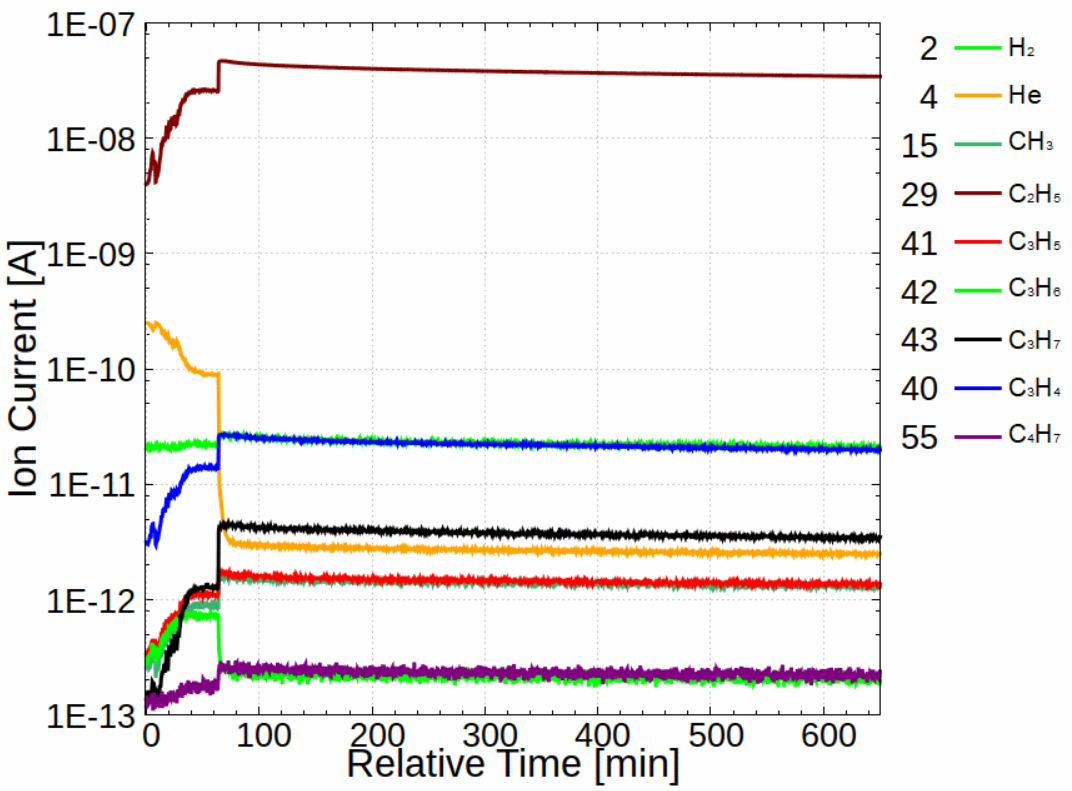

Figure 6.12: Mass spectrometry response over 12 h of FTS during HR-XRD measurements on ID15.

In the mass spectrometry recordings, all the hydrocarbons displayed in Figure 6.12 decrease gradually over the course of FTS, except for m_z=42. This is similar to chapter 5 but with weaker responses possibly due to difference between the catalyst or the difference between the mass spectrometers used. However, the H_2 response also decreases over the course of FTS suggesting the cause is the setting of the instrument. The He drops as there is more He in the H_2/He mixture than in the FTS gas mixture.

During FTS very little change is observed in the XRD, in either the metal and oxide phases (Figure 6.13). Scherrer analysis of the patterns give an approximate metal crystallite size of 4 nm, and an approximate CoO size of 3 nm. CoO was the only oxide phase present in the XRD patterns after the early stages of reduction (Figure 6.7).

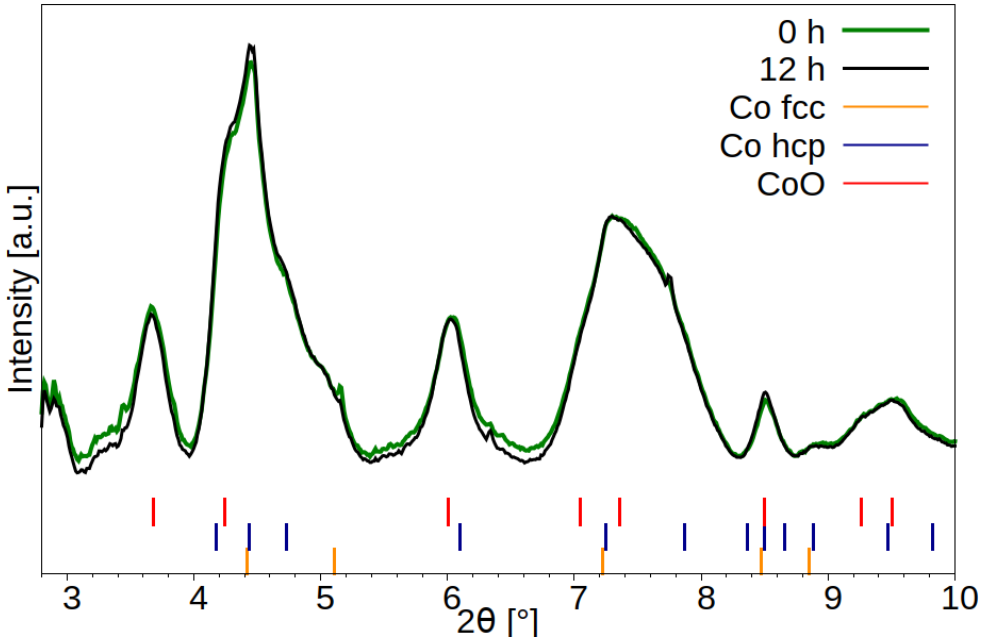

Figure 6.13: XRD patterns of 3 nm Co/MFC-17 catalyst at the start and end of 12 h of FTS.

6.4. Discussion

The aim of this chapter was to study the behaviour of a 3 nm Co/MCF-17 catalyst, that falls within the unstable size range of FTS catalysts, and to compare this to work in the previous chapter on a larger particle sized catalyst that is stable under FTS conditions. To determine the significance of the oxidation of small Co^0 nanoparticles, which is the cause of the instability, and the supposed formation of metal support interaction phases before or during FTS.

During pre-treatment, the 3 nm catalyst required a higher reduction temperature compared to the larger size catalyst, as expected, however still remained less reduced in comparison. LCA of the XANES shows 69 % and 60 % Co^0 in the 11 and 3 nm samples respectively, both have approximately 20 % CoO, while more Co_3O_4 remains in the 3 nm sample at 20 % and ~10 % in the 11 m sample. After reduction the only oxide identifiable in the XRD patterns is CoO, and so the reasonable quantities of Co_3O_4 must be smaller than at least some of the CoO content.

Upon exposure to FTS conditions the two sized catalysts behave very differently. The 11 nm catalyst is incredibly stable, with very little change observed in either the XRD or the XAS. The variations were attributed to a change

in Co^0 particle size most likely due to the continued reduction of the catalyst and in a variation in the ratio between Co^0 polymorphsd. Whereas the 3 nm catalyst starts to oxidize on exposure to FTS conditions, fully reducing in approximately 1 h as determined by XAS. XRD during this period shows little variation as the technique observes the larger particles within the size range present, which remain stable. The behaviour observed by XRD means that even a Co/MCF-17 catalyst with an approximate size of 3.25±0.83 nm as determined by XRD (Scherrer analysis) or by TEM of 3.14±0.69 nm, contains large enough particles for some to remain stable.

Bearing in mind the behaviour of the XRD and in retrospect, this experiment may have been improved by being performed as a PDF experiment. To have done this would have sacrificed spatial resolution important for the larger NP sample, however it would have provided significantly more information on the smaller NP sample and so would have been worthwhile.

No clear evidence for the influence of metal support interaction on Co stability was observed in the Co/MCF-17 samples of either size, let alone an increase over the course of FTS as was observed in other studies (Tsakoumis *et al.*[15]). Any metal support interaction would be more obvious in a sample of smaller particle size as the relative fractional composition would be higher.

6.5. Conclusion

In combination with the previous chapter, the aim of this work was to use combined synchrotron-based *operando* X-ray techniques to interrogate three key issues still not fully resolved in the study of Fischer-Tropsch catalysts. These were the influence of the metallic nanostructure (fcc/hcp/intermixed Co^0) on FTS, the reoxidation of smaller metallic cobalt nanoparticles during the initial stages of FTS, and the potential presence of metal oxide support interactions.

As with the earlier larger sized nanoparticle chapter, the novelty of this work lies in the system studies (Co/MCF-17 (silica)), and the pressure at which the FTS experiment was conducted. The pressure used was 2 bar, an improvement on many studies which are typically run at atmospheric pressure.

This chapter focused on the two aims regarding reoxidation of small Co^0 nanoparticles and metal oxide support interactions. The 3 nm Co/MCF-17 catalyst was unstable under FTS conditions as predicted by its size and in line with other work in the literature.[5,6,7] The small nanoparticles appear to have oxidised over the first hour of exposure to FTS condition as observed by XAS. However, little change was observed over the same time period by the XRD patterns, only some change in the diffuse scattering. The very small quantity of larger nanoparticles in the system observed by XRD were in the stable size range.

Additionally, no metal support phases were detected in this sample (or the larger Co/MCF-17 sample in the previous chapter). Neither was any metal support phase formation observed during FTS as has been reported in XAS studies of Co/Al_2O_3 systems.[15] Such phases would be clearly observable in the XAS spectra, unlike Co/Al_2O_3 catalysts where $Co_xAl_yO_z$ phases resemble Co_3O_4. Metal support interaction would also be more obvious in a sample of smaller particle size as the relative fractional composition would higher. The absence of evidence of metal support interaction in the 3 nm catalyst would indicate that this is not an issue for these catalysts. Although there are some differences in behaviour between silica and alumina supported cobalt-based catalysts there are many similarities. The absence of metal support interaction in this catalyst combined the problems differentiating between $CoAl_2O_4$ and Co_3O_4 when present in the small quantities seen in these catalysts, adds weight to the suggestion that metal oxide supports may not be an issue with these catalysts after all.

6.6. References

1 J. P. den Breejen, P. B. Radstake, G. L. Bezemer, J. H. Bitter, V. Frøseth, A. Holmen and K. P. de Jong, *J. Am. Chem. Soc.*, 2009, **131**, 7197–7203.

2 G. L. Bezemer, J. H. Bitter, H. Kuipers, H. Oosterbeek, J. E. Holewijn, X. Xu, F. Kapteijn, A. J. van Dillen, K. P. de Jong, A. J. Van Diilen and K. P. de Jong, *J. Am. Chem. Soc.*, 2006, **128**, 3956–3964.

3 E. Rytter, N. E. Tsakoumis and A. Holmen, *Catal. Today*, 2016, **261**, 3–16.

4 M. Claeys, M. E. Dry, E. Van Steen, P. J. Van Berge, S. Booyens, R. Crous, P. Van Helden, J. Labuschagne, D. J. Moodley and A. M. Saib, *ACS Catal.*, 2015, **5**, 841–852.

5 E. van Steen, M. Claeys, M. E. Dry, J. van de Loosdrecht, E. L. Viljoen and J. L. Visagie, *J. Phys. Chem. B*, 2005, **109**, 3575–3577.

6 P. J. van Berge, J. van de Loosdrecht, S. Barradas and A. M. van der Kraan, *Catal. Today*, 2000, **58**, 321–334.
7 P. Senecal, S. D. M. Jacques, M. Di Michiel, S. A. J. Kimber, A. Vamvakeros, Y. Odarchenko, I. Lezcano-Gonzalez, J. Paterson, E. Ferguson and A. M. Beale, *ACS Catal.*, 2017, **7**, 2284–2293.
8 S. Nikitenko, A. M. Beale, A. M. J. van der Eerden, S. D. M. Jacques, O. Leynaud, M. G. O'Brien, D. Detollenaere, R. Kaptein, B. M. Weckhuysen and W. Bras, *J. Synchrotron Radiat.*, 2008, **15**, 632–640.
9 K. Høydalsvik, J. B. Fløystad, A. Voronov, G. J. B. Voss, M. Esmaeili, J. Kehres, H. Granlund, U. Vainio, J. W. Andreasen, M. Rønning and D. W. Breiby, *J. Phys. Chem. C*, 2014, **118**, 2399–2407.
10 Gatan, GMS 3 Software Registration | Gatan, Inc., http://www.gatan.com/datasheets/gms-3-software-registration, (accessed 12 March 2018).
11 B. Ravel and M. Newville, in *Journal of Synchrotron Radiation*, 2005, vol. 12, pp. 537–541.
12 A. Longo, L. Sciortino, F. Giannici and A. Martorana, *J. Appl. Crystallogr.*, 2014, **47**, 1562–1568.
13 A. Altomare, N. Corriero, C. Cuocci, A. Falcicchio, A. Moliterni and R. Rizzi, *J. Appl. Crystallogr.*, 2015, **48**, 598–603.
14 A. M. Beale and B. M. Weckhuysen, *Phys. Chem. Chem. Phys.*, 2010, **12**, 5562 –5574.
15 N. E. Tsakoumis, J. C. Walmsley, M. Rønning, W. Van Beek, E. Rytter and A. Holmen, *J. Am. Chem. Soc.*, 2017, **139**, 3706–3715.
16 C. H. Mejía, T. W. van Deelen, and K. P. de Jong, *Nature Comms.,* 2018, **9**, 2041-1723.

7. Summary and conclusions

This work focused on particle size effects in Co-based Fischer Tropsch Synthesis (FTS) catalysts. In the first experimental chapter (chapter 4) an attempt was made to tailor an inverse micelle synthesis (IMS) frequently used to synthesize gold nanoparticles on 2D supports to powdered silica supported Co-based catalysts. Then in the next pair of experimental chapters (chapters 5 and 6) a Co/MCF-17 catalyst of two different sizes; one of a stable size (11 nm), and one vulnerable to reoxidation (3 nm) were studied using synchrotron-based *operando* X-ray techniques.

IMS using block copolymers was not successful at synthesizing model catalyst with better particle size control than other cheaper and more standard methods. On a powder support it becomes more challenging to remove the residual polymer micelles than on 2D supports, which affects the particle size distribution. However, there is no significant information in the rare published work of similar synthesis for cobalt-based systems[4,5] of the chemistry of the micelle cores. This work determined that the cobalt in the cores takes the form of $CoCl_4$ ions which interact with the pyridine units, and so adds to the knowledge of the system. In future this synthesis method needs further work to determine if it is viable as a method to produce catalysts on powder supports, although it is still viable for 2D catalysts for study using surface science techniques.

In the pair of *operando* characterization chapters, the aim was to interrogate three key issues that relate to FTS. They were the influence and evolution of the metallic nanostructure (fcc/hcp/intermixed Co^0) on FTS, the reoxidation of smaller metallic cobalt nanoparticles during the initial stages of FTS, and the potential presence of metal oxide support interactions.

The 11 nm Co/MCF-17 catalyst was shown to be very stable changing very little over 12 h of FTS as observed by both XRD and XAS. Both XAS and the Debye simulations[1] do suggest a slight increase in particle size. XANES shows a simultaneous reduction of the CoO signal although XRD reveals minimal change in the CoO reflection during FTS. The Debye simulations also suggest a change in the ratio of Co^0 polymorphs. An increase was observed in the both the

intermixed and fcc components (3.77 % and 1.24 % respectively), at the expense of the hcp component (-5.03 %).

The application of Debye simulations using the unic model to realistic systems is very interesting but needs to be expanded to make more solid conclusions on the effect of the Co^0 nanostructure on FTS. Further work could include combining lab-based catalytic studies and *in situ/operando* XRD/PDF experiments on samples of varying fcc/hcp ratios and some comparison between the fcc/hcp ratio determined by Debye simulations and NMR.[2]

The 3 nm Co/MCF-17 catalyst was unstable under FTS conditions as expected, gradually oxidizing during the first hour after exposure to syngas. The oxidation was observed clearly in the XAS spectra; however, little change was observed in the XRD patterns. The very small quantity of larger nanoparticles in the system observed by XRD were in the stable size range. As with many combined studies, the difference between the size of particles/crystallites best observed by XAS and XRD respectively led to different observations – most acute in the reduced 3 nm sample but also clear in the calcination of the 11 nm samples. This issue could have been reduced by performing PDF and examining the diffuse scattering as well as the diffraction, although this would have compromised the resolution of the reflections.

Metal oxide support interactions were not detected in either the 3 nm or 11 nm sample at any point through pre-treatment and FTS, in contrast to what has been reported in other XANES studies.[3] The absence of support interactions in the small nanoparticle catalyst is the most meaningful as any support interaction would comprise a larger percentage of the total composition and be more obvious especially in the XAS spectra.

7.1. References

1 A. Longo, L. Sciortino, F. Giannici and A. Martorana, *J. Appl. Crystallogr.*, 2014, **47**, 1562–1568.

2 V. V. Matveev, D. A. Baranov, G. Y. Yurkov, N. G. Akatiev, I. P. Dotsenko and S. P. Gubin, *Chem. Phys. Lett.*, 2006, **422**, 402–405.

3 N. E. Tsakoumis, J. C. Walmsley, M. Rønning, W. Van Beek, E. Rytter and A. Holmen, *J. Am. Chem. Soc.*, 2017, **139**, 3706–3715.

4 H.-G. Boyen, G. Kästle, K. Zürn, T. Herzog, F. Weigl, P. Ziemann, O. Mayer, C. Jerome, M. Möller, J. P. Spatz, M. G. Garnier and P. Oelhafen, *Adv. Funct. Mater.*, 2003, **13**, 359–364.
5 G. Liu, X. Yan, Z. Lu, S. A. Curda and J. Lal, *Chem. Mater.*, 2005, **17**, 4985–4991.

8. Appendices

8.1. Appendix 1

West Texas Intermediate (WTI or NYMEX) crude oil prices per barrel (retrieved from https://www.macrotrends.net/1369/crude-oil-price-history-chart). Grey sections indicate recessions.

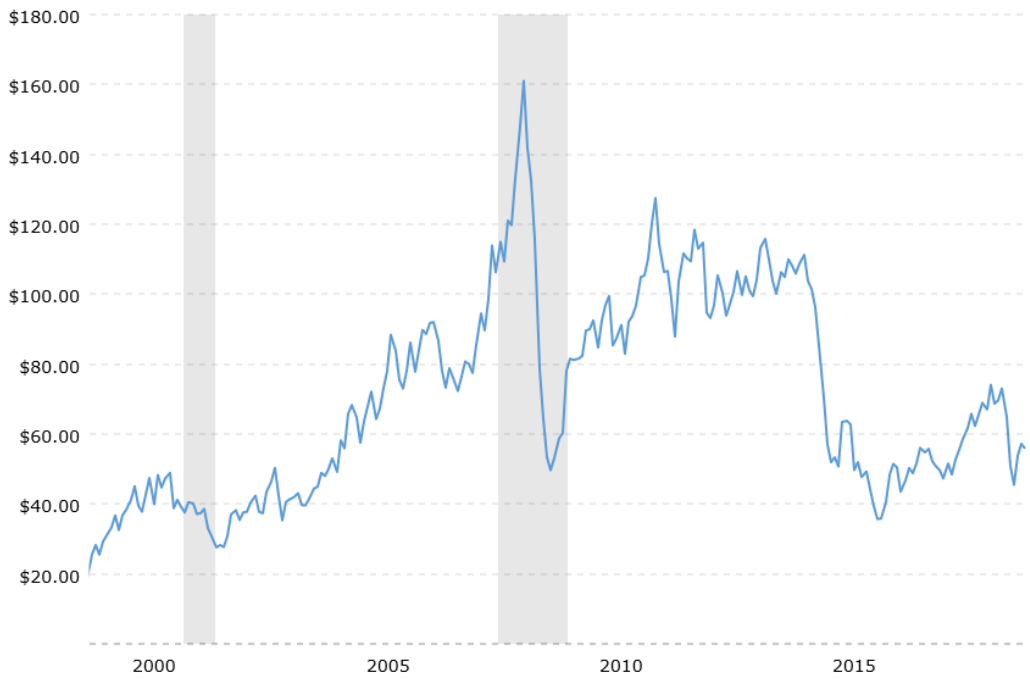

Figure A1: Graph showing WTI crude oil price/barrel over the previous 20 years.

8.2. Appendix 2

Example Minuit data card:

Probability factors

Horizontal and vertical strain

Scattering domain size and std dev

```
 SET TITLE
'[TITLE]'
PARAMETERS
  1'alfa  cc_c     '      [value]  [step]   [Low restraint]   [High restraint]
  2'beta  hc_c     '      [value]  [step]   [Low restraint]   [High restraint]
  3'gamma hh_c     '      [value]  [step]   [Low restraint]   [High restraint]
  4'delta ch_c     '      [value]  [step]   [Low restraint]   [High restraint]
  5'str1  hor      '      [value]  [step]   [Low restraint]   [High restraint]
  6'str2  vert     '      [value]  [step]   [Low restraint]   [High restraint]
  7'a0             '      [value]  [step]   [Low restraint]   [High restraint]
  8'c0             '      [value]  [step]   [Low restraint]   [High restraint]
  9'rav            '      [value]  [step]   [Low restraint]   [High restraint]
 10'std            '      [value]  [step]   [Low restraint]   [High restraint]
 11'off            '      [value]  [step]   [Low restraint]   [High restraint]
 12'bi             '      [value]  [step]   [Low restraint]   [High restraint]
 13'scale          '      [value]  [step]   [Low restraint]   [High restraint]
 14'b0             '      [value]  [step]   [Low restraint]   [High restraint]
 15'b1             '      [value]  [step]   [Low restraint]   [High restraint]

0.1579   [wavelength]
cws      [cluster with background fitting (spline or Chebyshev)]
BG.txt   [background pattern]
spline.dat          [spline nodes]
simplex  [Fitting algorithm]
save
exit
```

Additional oxide parameters:

```
66'cell    '      0.80838E+01   0.00001D-04   0.00D+00        9.000000
67'cell    '      0.80838E+01   0.00001D-04   0.00D+00        9.000000
68'cell    '      0.80838E+01   0.00001D-04   0.00D+00        9.000000
69'biox    '      0.30792E+00   0.00001D-04   0.00D+00        0.10D+04
70'u       '      0.58417E+02   0.00001D-04
71'v       '      -0.55113E+01  0.00001D-04
72'w       '      0.23102E+00   0.00001D-04
73'x       '      0.30608E+01   0.00001D-04   0.00D+00
74'y       '      0.00000E+00   0.00000D-04   0.00D+00
75'scale   '      0.00000E-08   0.00001D-08    0.00D+00
76'ocp     '      0.10000E+01   0.00000D-04
77'ocp     '      0.10000E+01   0.00000D-04
78'ocp     '      0.10000E+01   0.00000D-04
```

79'cell	'	0.42509E+01	0.000001D-04	0.00D+00	9.000000
80'cell	'	0.42662E+01	0.000001D-04	0.00D+00	9.000000
81'cell	'	0.42662E+01	0.000001D-04	0.00D+00	9.000000
82'biox	'	0.61732E+01	0.00001D-04	0.00D+00	0.10D+04
83'u	'	0.84197E+02	0.00001D+01		
84'v	'	-0.58410E+01	0.00001D-05		
85'w	'	0.22470E+00	0.00001D-05		
86'x	'	0.29348E+01	0.00001D-00	0.00D+00	
87'y	'	0.00000E+00	0.00000D-00	0.00D+00	
88'scale	'	0.69630E-06	0.00100E-06	0.00000D-06	
89'ocp	'	0.10000E+01	0.00000D-04	0.00D+00	
90'ocp	'	0.10000E+01	0.00000D-04	0.00D+00	

8.3. Appendix 3

Co/SiO_2 (IMS) sample – XRD patterns taken by the MiniFlex diffractometer before background and sample holder reflection removal.

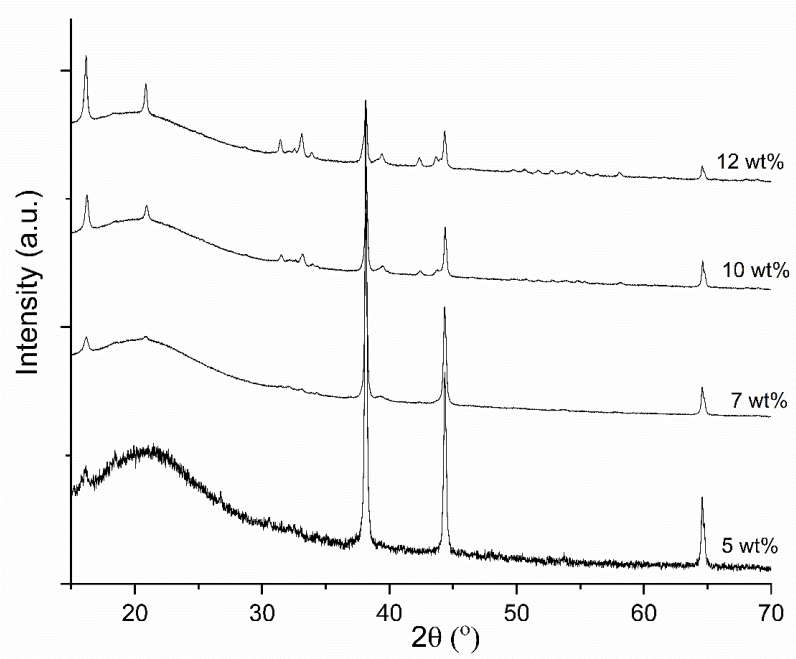

Figure A2: XRD patterns taken by the MiniFlex diffractometer before background and sample holder reflection removal.

8.4. Appendix 4

Isotherms of the various silicas used to synthesis catalyst using inverse micelle synthesis in 4. Inverse Micellular Synthesis of Co-based FT Catalysts. SiO2(a) is low surface area SiO2, SiO2(b) is CAB-O-SIL M5, SiO2(c) is nanopowder, and SiO2(d) is fumed SiO_2.

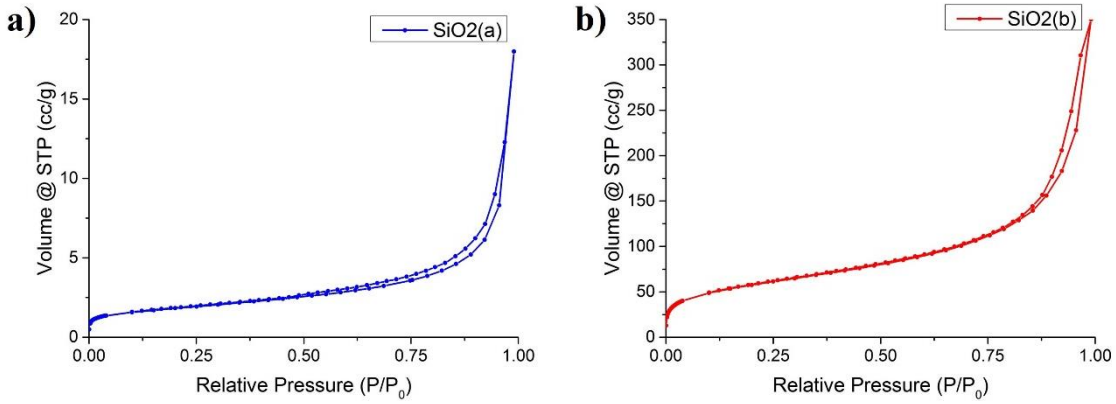

Figure A3: Isotherms of: a) Low SA SiO_2 – no plasma treatment b) CAB-O-SIL M5 – no plasma treatment.

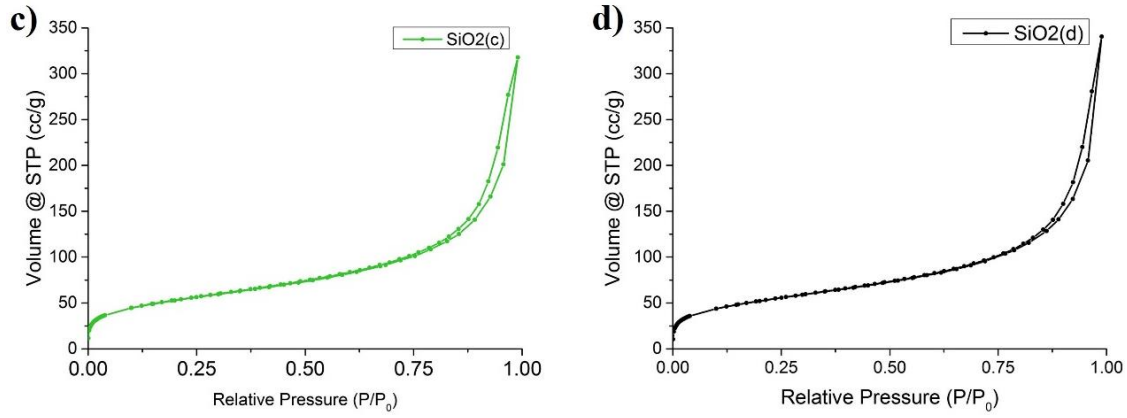

Figure A4: Isotherms of: c) SiO_2 nanopowder – no plasma treatment, d) fumed SiO_2 – no plasma treatment.

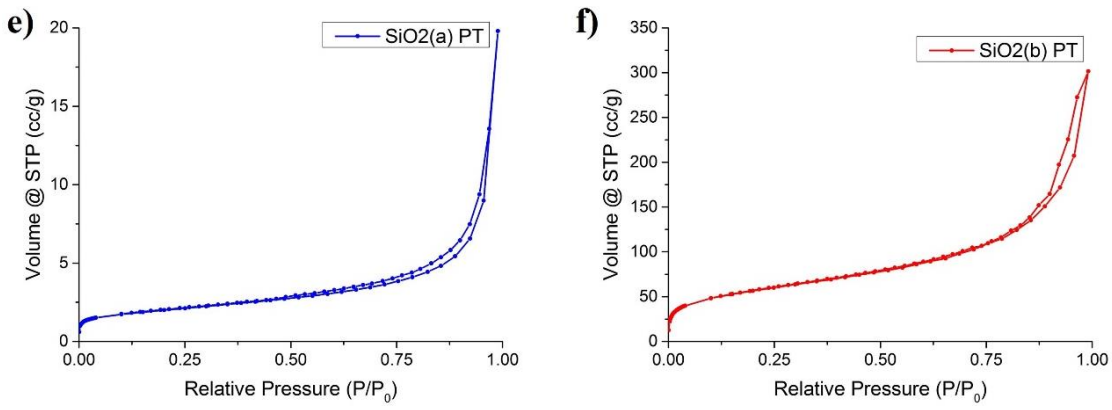

Figure A5: Isotherms of: e) Low SA SiO_2 – 90 min plasma treatment f) CAB-O-SIL M5 – 90 min plasma treatment.

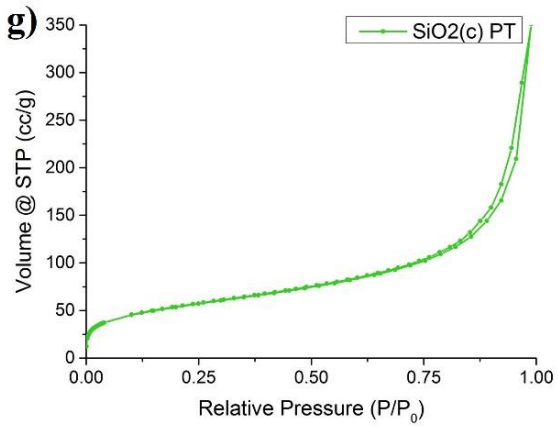

Figure A6: Isotherm of: g) SiO_2 nanopowder – 90 min plasma treatment.

8.5. Appendix 5

Thermogravimetric analysis (TGA) of polymer alone.

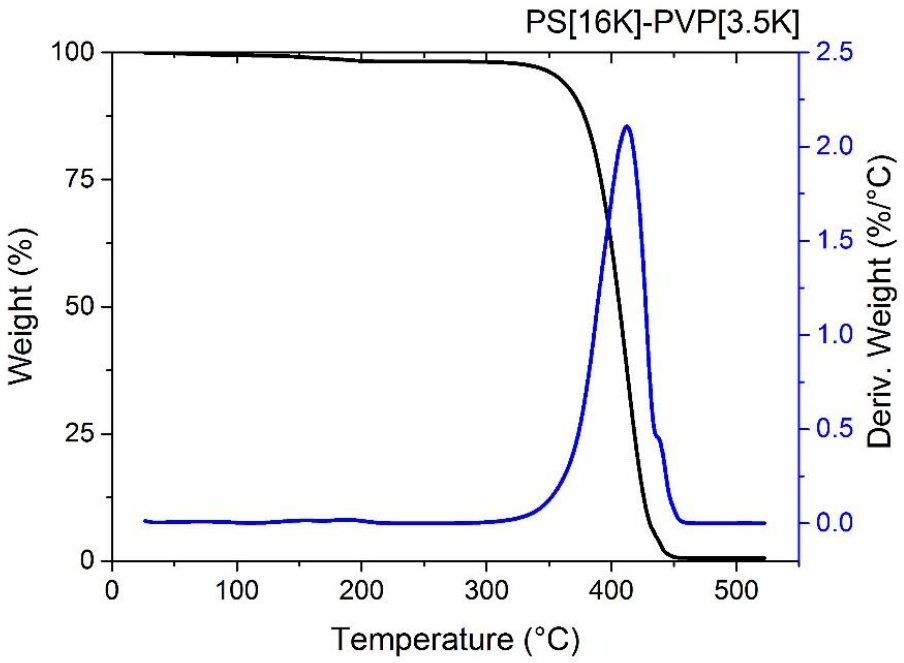

Figure A7: TGA curve of polymer - PS-PVP[16K-3.5K], recorded in air.

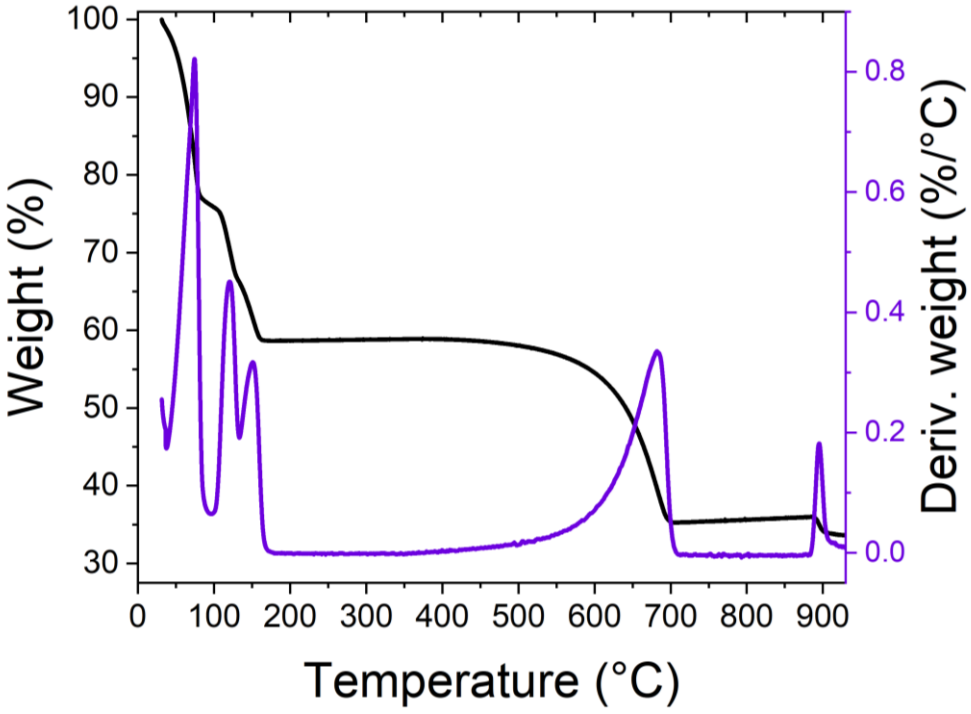

Figure A8: TGA curve of $CoCl_2.6H_2O$ recorded in air.

8.6. Appendix 6

Thermogravimetric analysis (TGA) curves of various sample synthesised by IMS; plasma treated for various lengths of time.

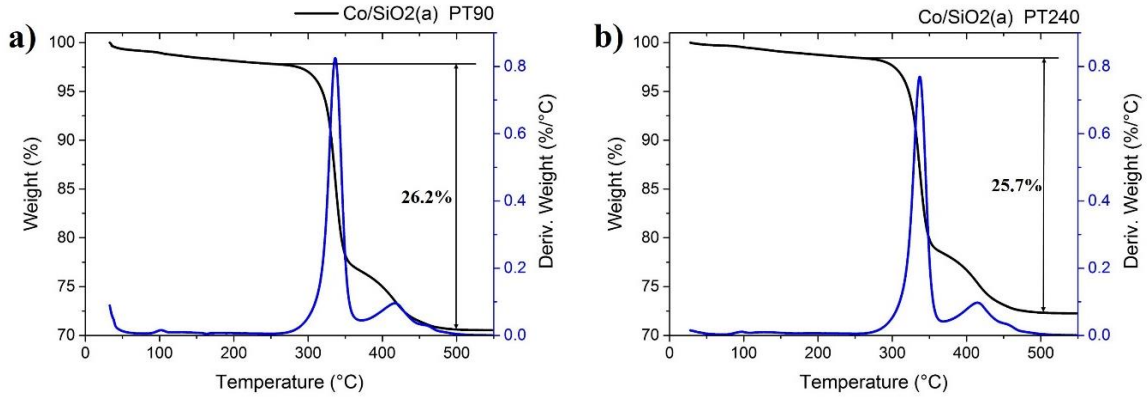

Figure A9: TGA curves for Co/(Low SA SiO_2) after plasma treatment of: a) 90 min and b) 240 min.

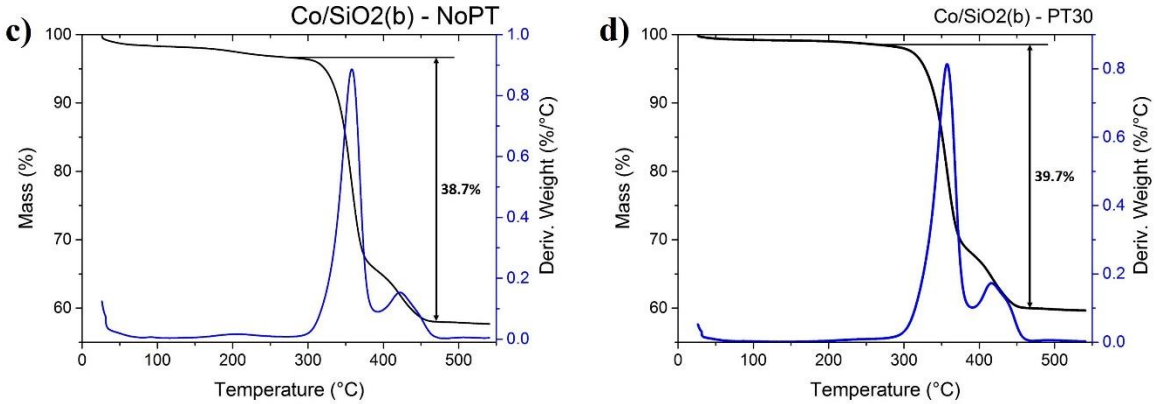

Figure A10: TGA curves for Co/(CAB-O-SIL M5) c) no plasma treatment and d) 30 min plasma treatment.

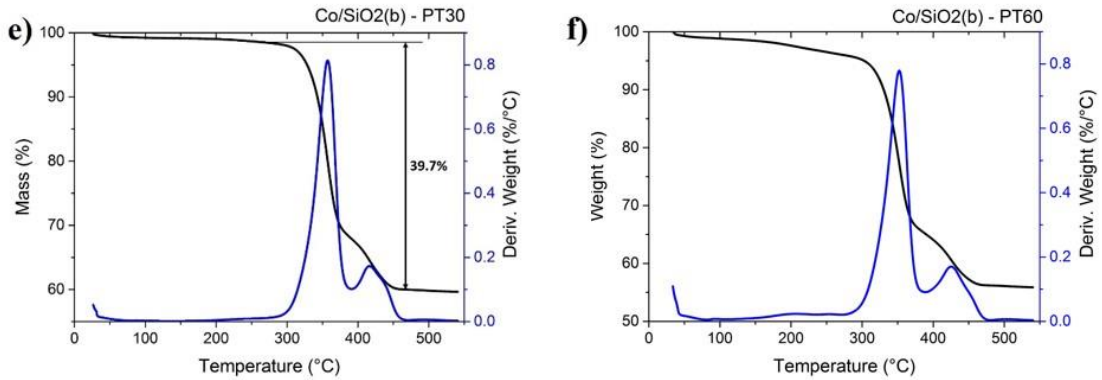

Figure A11: TGA curves for Co/(CAB-O-SIL M5) after plasma treatment of: e) 30 min and f) 60 min.

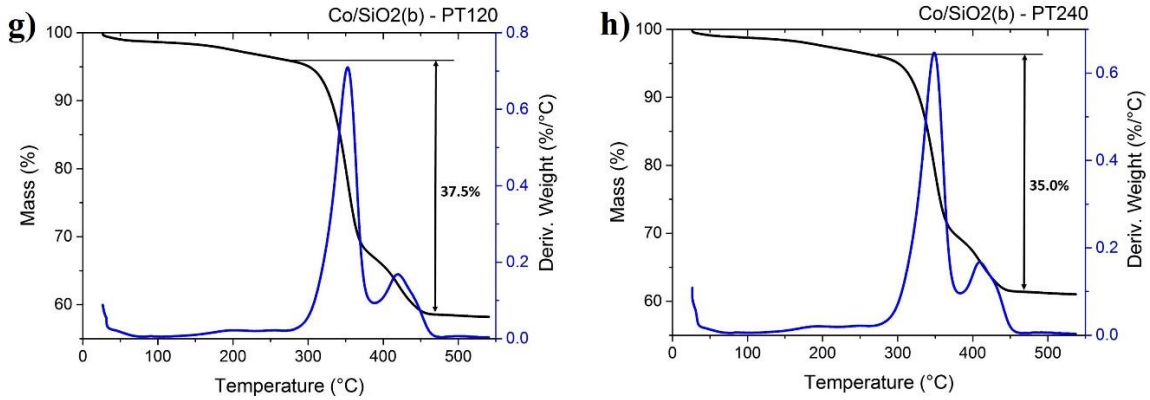

Figure A12: TGA curves for Co/(CAB-O-SIL M5) after plasma treatment of: g) 120 min and f) 240 min.

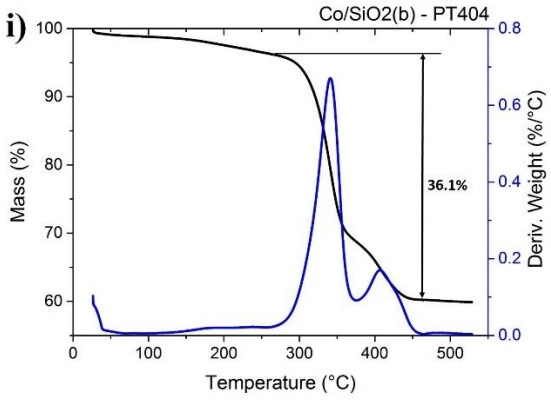

Figure A13: TGA curves for Co/(CAB-O-SIL M5) after plasma treatment of: i) 120 min.

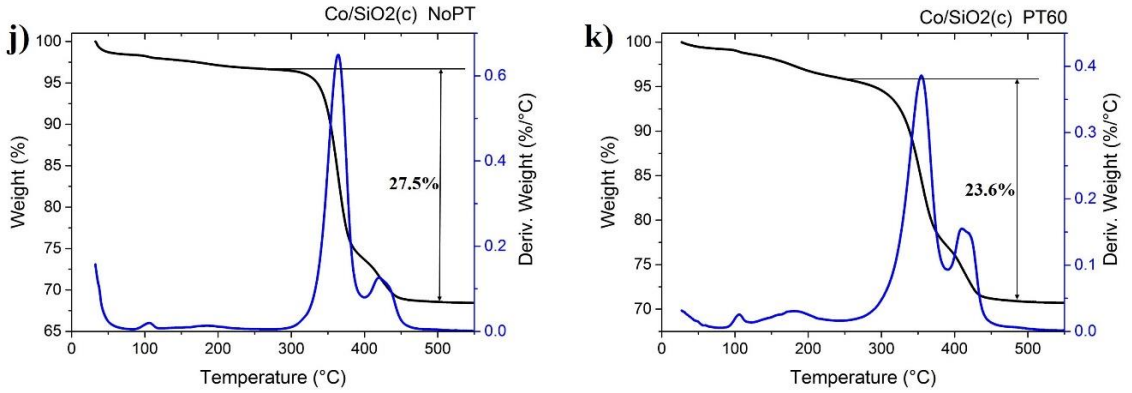

Figure A14: TGA curves for Co/(SiO_2 nanopowder) after j) no plasma treatment k) a plasma treatment of 120 min.

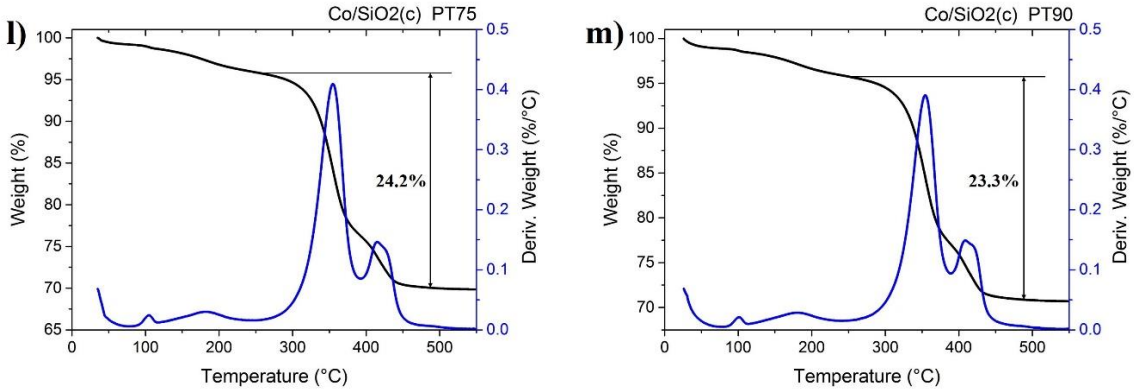

Figure A15: TGA curves for Co/(SiO_2 nanopowder) after plasma treatments of: l) 75 min and m) 90 min.

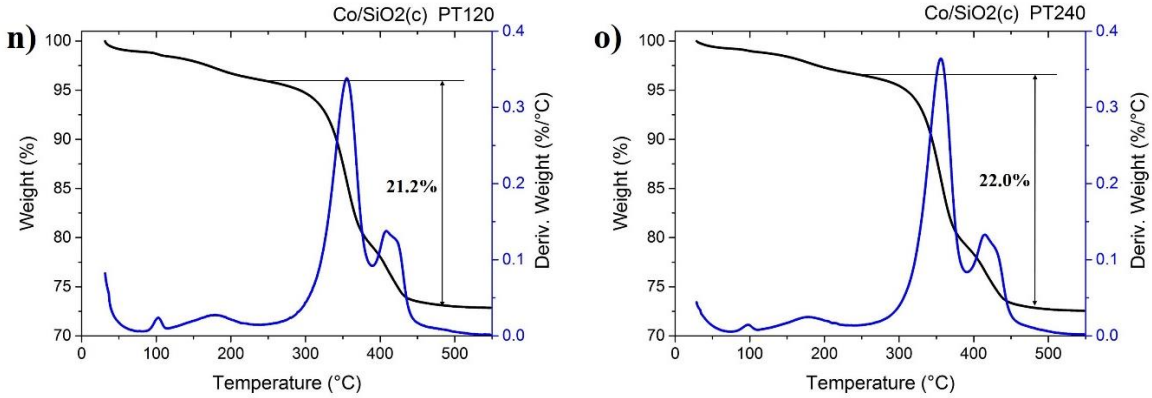

Figure A16: TGA curves for Co/(SiO_2 nanopowder) after plasma treatment of: n) 120 min and o) 240 min.

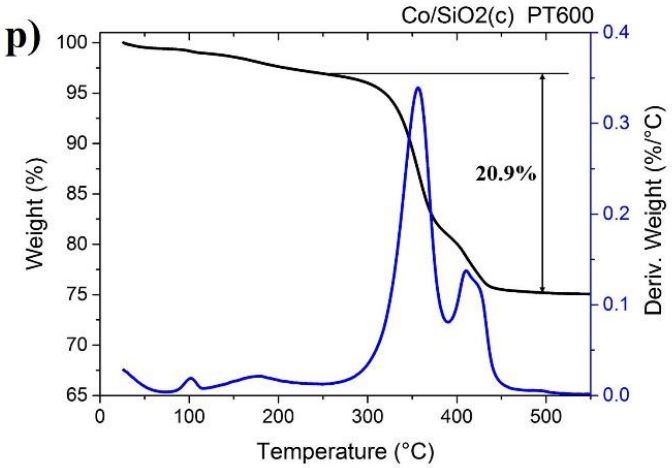

Figure A17: TGA curves for Co/(SiO_2 nanopowder) after plasma treatment of: p) 600 min.

8.7. Appendix 7

Graphs which separate and plots the behaviour of the first and second mass losses as recorded from TGA curves of Co/(SiO_2 nanopowder) samples for various plasma treatment times.

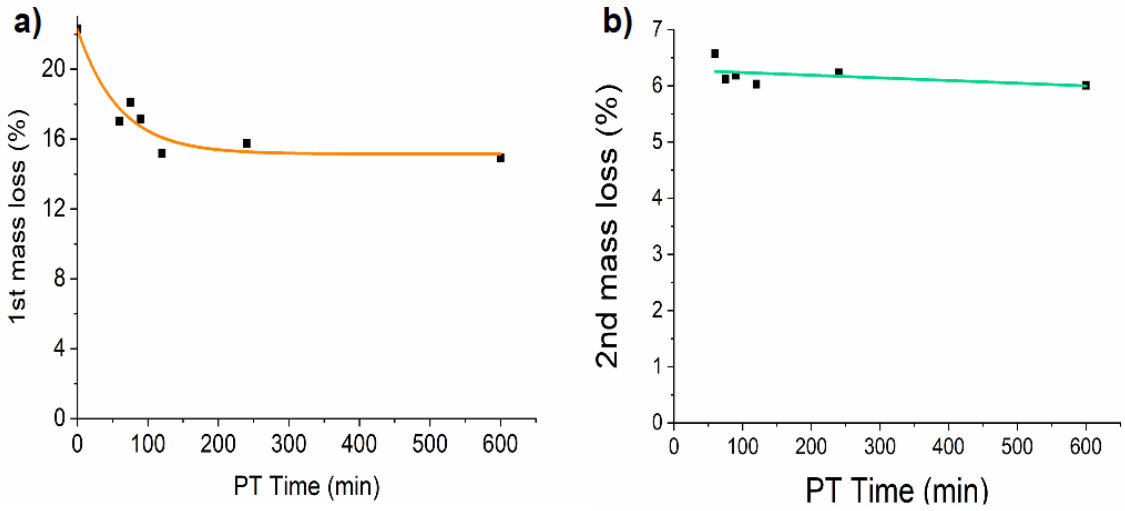

Figure A18: Graphs of mass losses taken from 1st and 2nd mass loss stages of TGA curves of the dried and plasma treated Co/(SiO_2 nanopowder) samples.

8.8. Appendix 8

TEM images from earlier work, Co/Quartz not plasma treated and calcined for 18 and 20 h, showing large irregular Co_3O_4 nanoparticles.

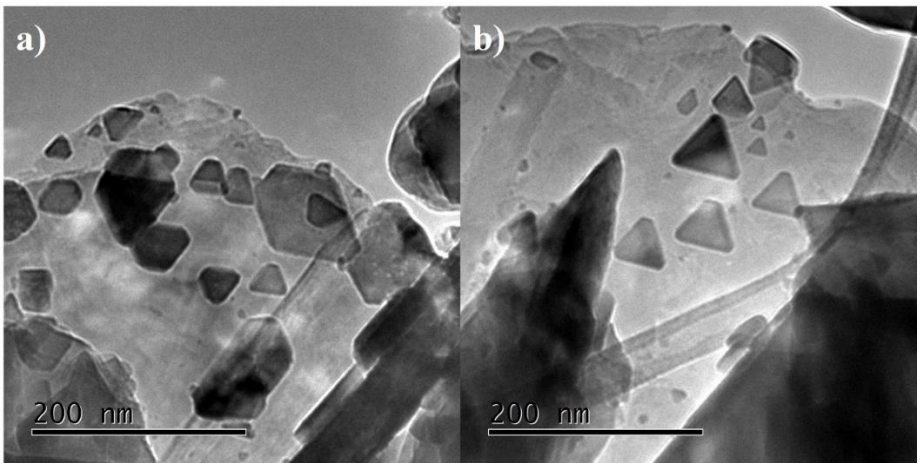

Figure A19: TEM images of Co/Quartz samples calcined at 500°C, with a temperature ramp rate of 3°C/min for 18 h and 20 h respectively.

8.9. Appendix 9

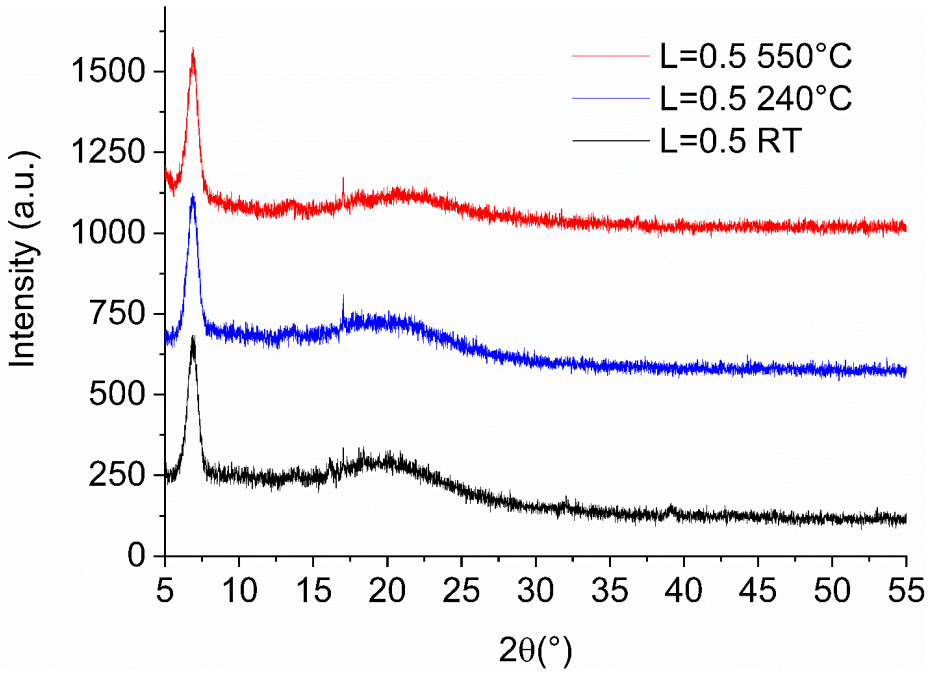

Figure A20: Temperature dependant XRD patterns for Co/(CAB O SIL) 5 wt% with a micelle loading of L=0.5.

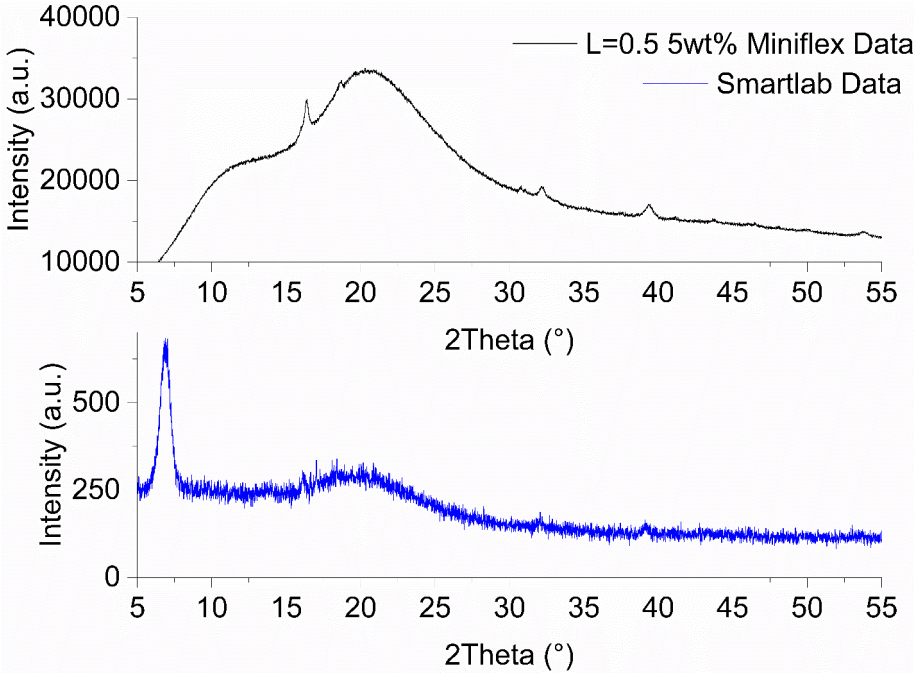

Figure A21: Comparison between MiniFlex and Smartlab measurements of L=0.5, 5 wt% Co/Low SA SiO_2.

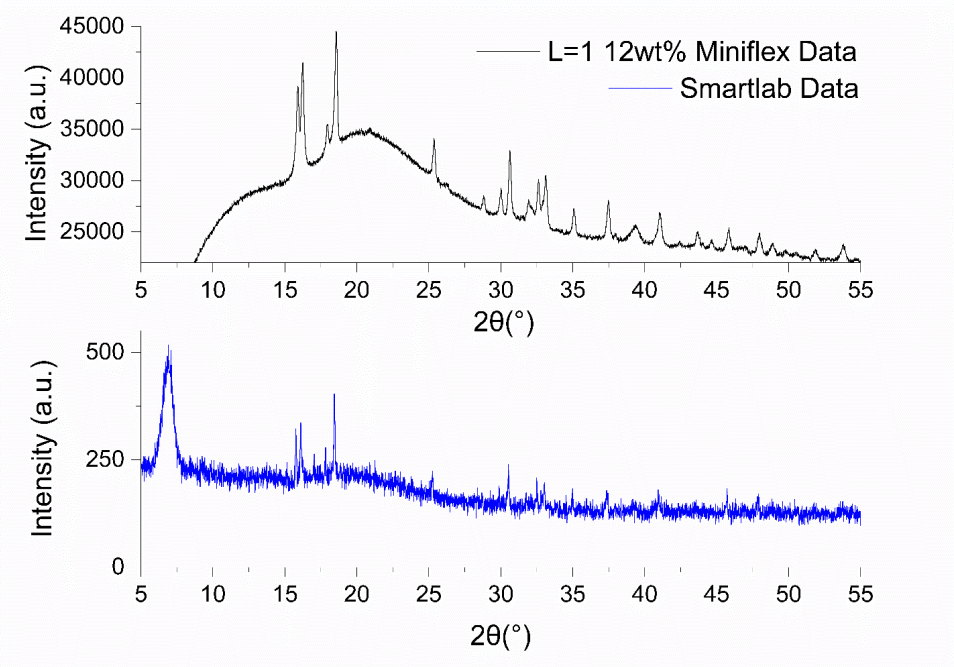

Figure A22: Comparison between MiniFlex and Smartlab measurements of L=1.0, 12 wt% Co/Low SA SiO_2.

8.10. Appendix 10

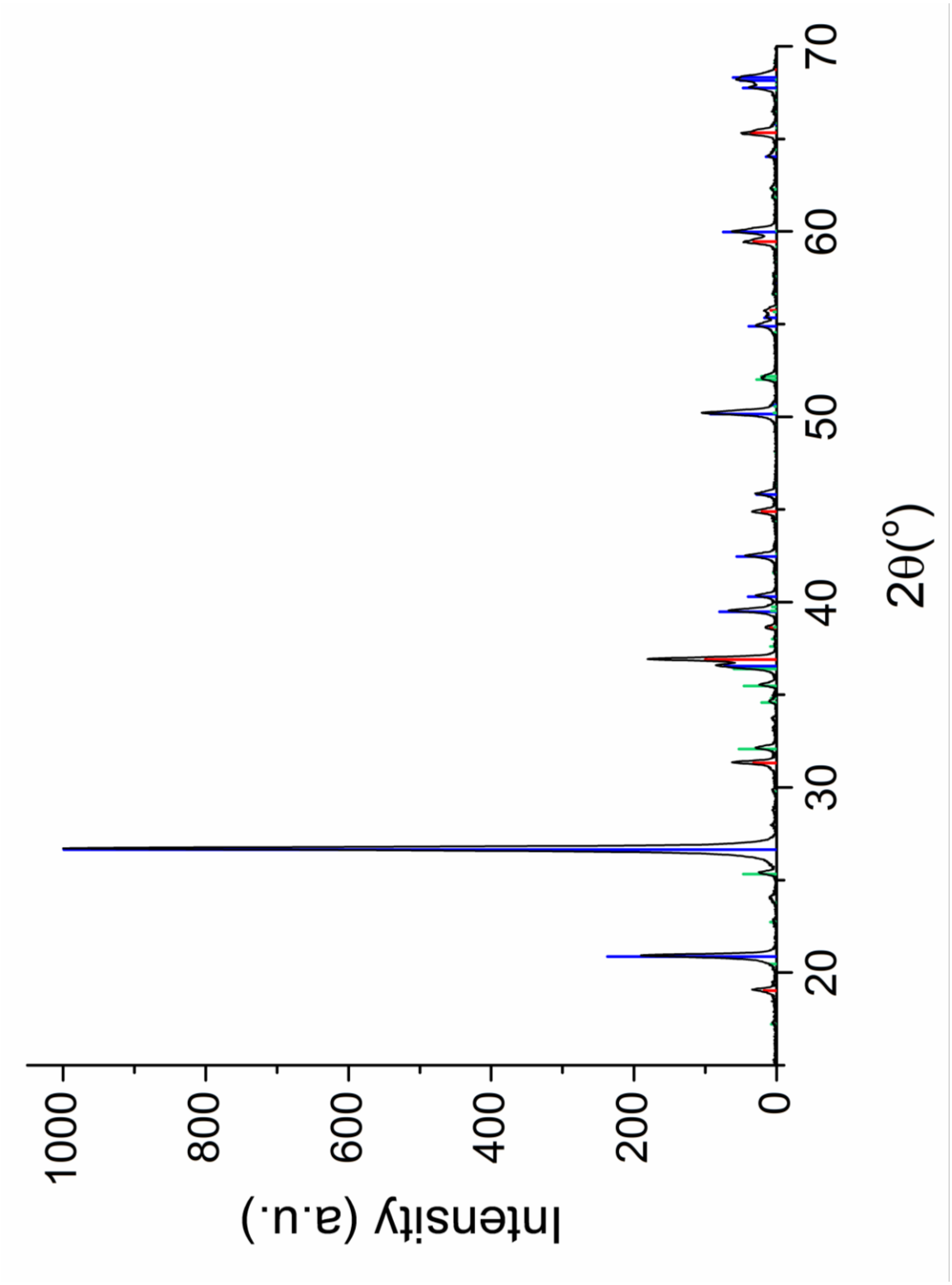

Figure A23: Enlarged copy of Figure 4:20. Phase ID of: 12wt%, L=1.0 Co/(CAB-O-SIL) samples after temperature dependant XRD measurements. Phases present: Quartz (blue), Co_3O_4 (red), and Co_2SiO_4 (green).

8.11. Appendix 11

The geometry of the MiniFlex diffractometer limits the measurable 2θ range, as the angle of the flat sample holder is varied to control 2θ resulting in the spillage of powder samples below ~10-15° 2θ and above ~80° 2θ. In order to compare diffraction data from the MiniFlex and the Smartlab some larger 2θ range measurements were obtained on the MiniFlex by applying the powder on the usual sample holder coated in vacuum grease. This had the effect of reducing intensity and introducing a phase shift of 0.6° 2θ, (Figure A24) shows a comparison between diffraction patterns taken of the same Co/SiO_2 sample with and without vacuum grease.

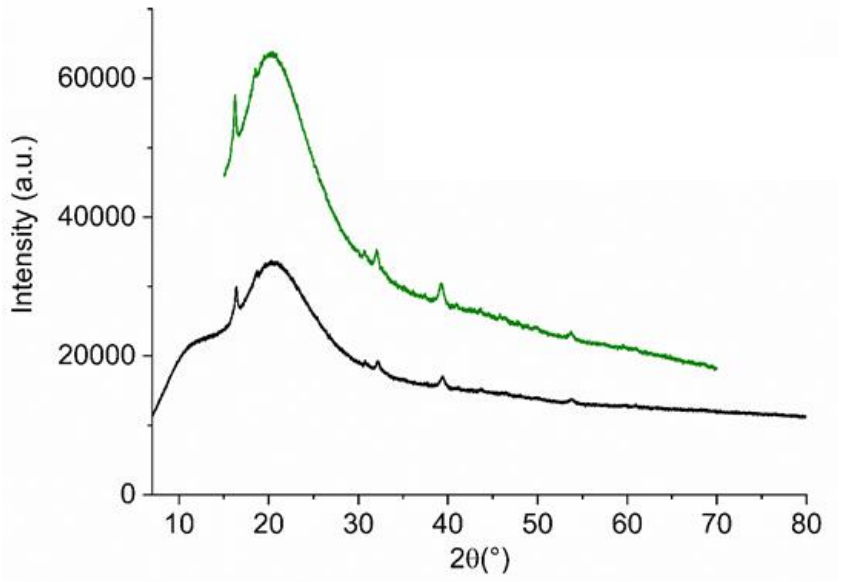

Figure A24: XRD patterns without background subtraction for Co/(CAB O SIL) 12 wt%, as recorded by the MiniFlex diffractometer, with and without grease to hold sample in place.

8.12. Appendix 12

XRD patterns recorded during the calcination of the 11 nm Co/MCF-17 catalyst. An early XRD pattern recorded at approximately 40 minutes into the calcination when the sample became to become crystalline, and at the end of the reduction

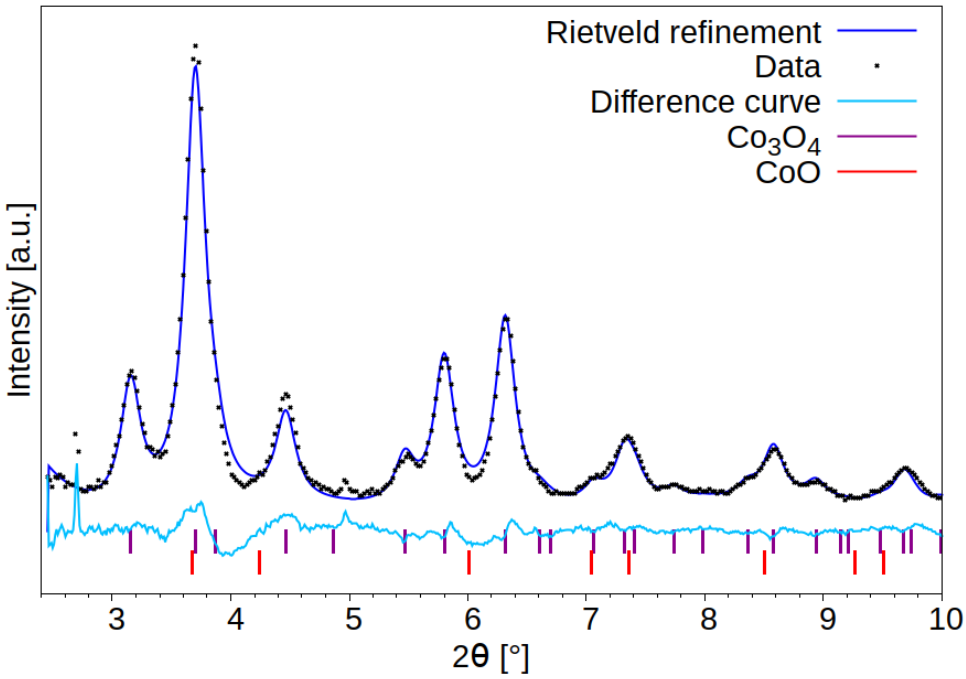

Figure A25: An early XRD pattern recorded at approximately 40 minutes into the calcination of the 11 nm Co/MCF-17 catalyst.

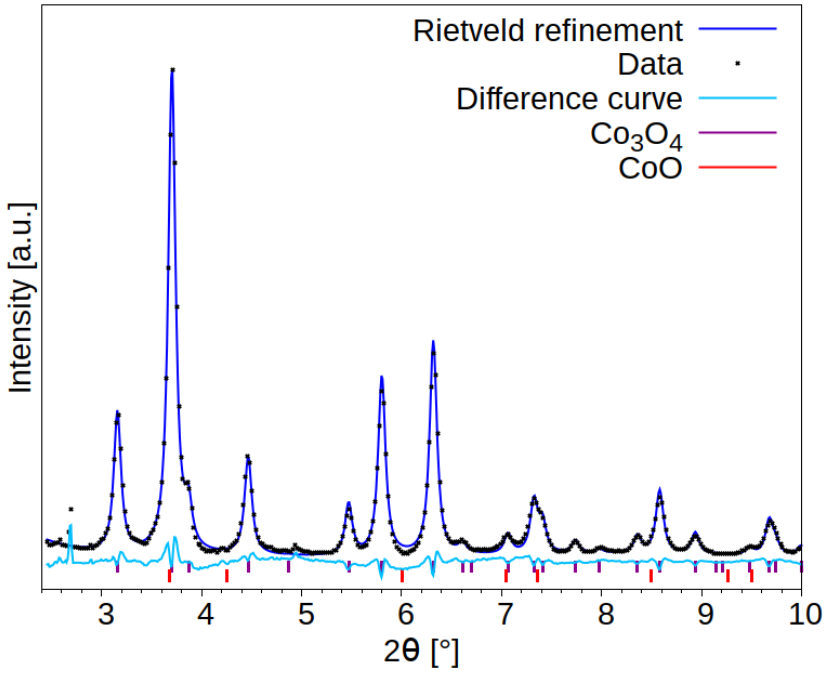

Figure A26: XRD pattern recorded after the calcination of the 11 nm Co/MCF-17 catalyst.

8.13. Appendix 13

Mass spectrometry responses recorded during FTS measurements at BM26A and ID15.

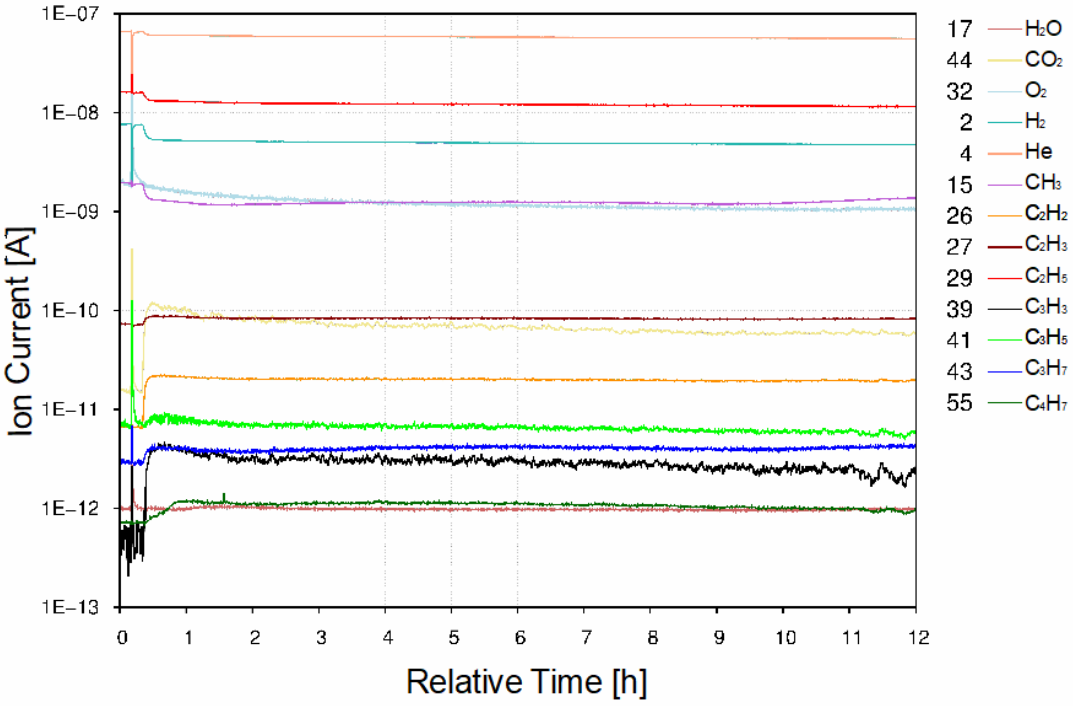

Figure A27:Full mass spectrometry response of the 11 nm Co/MCF-17 catalyst during FTS only (DUBBLE).

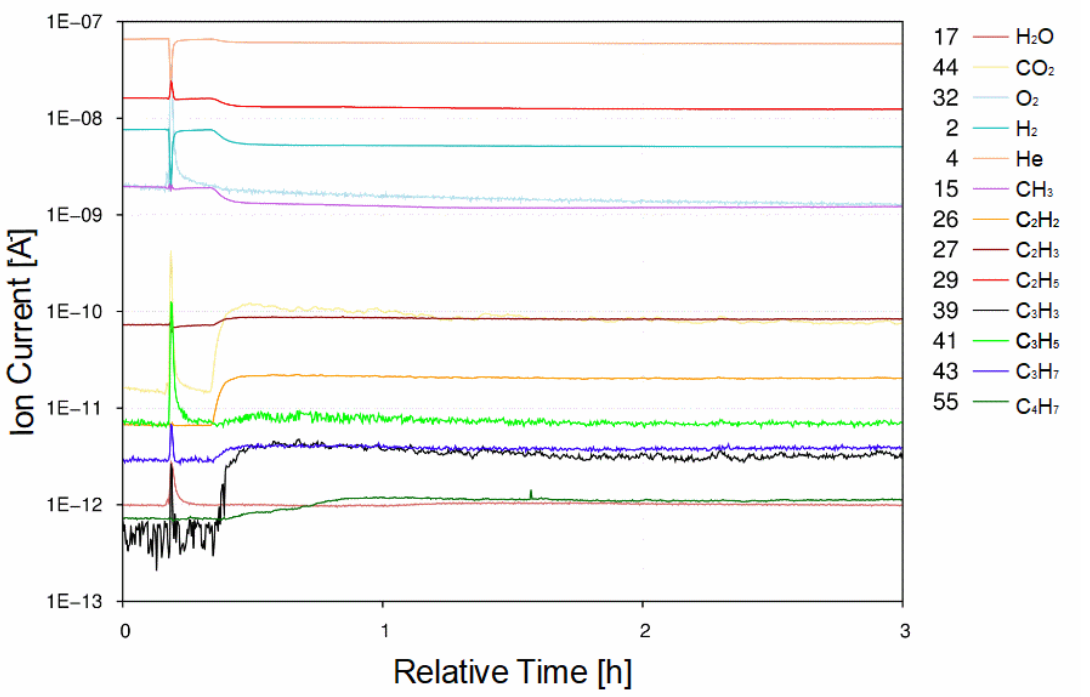

Figure A28: Mass spectrometry response of the 11 nm Co/MCF-17 catalyst during FTS only (DUBBLE). Only showing first 3 h for improved visualisation of the initial variation.

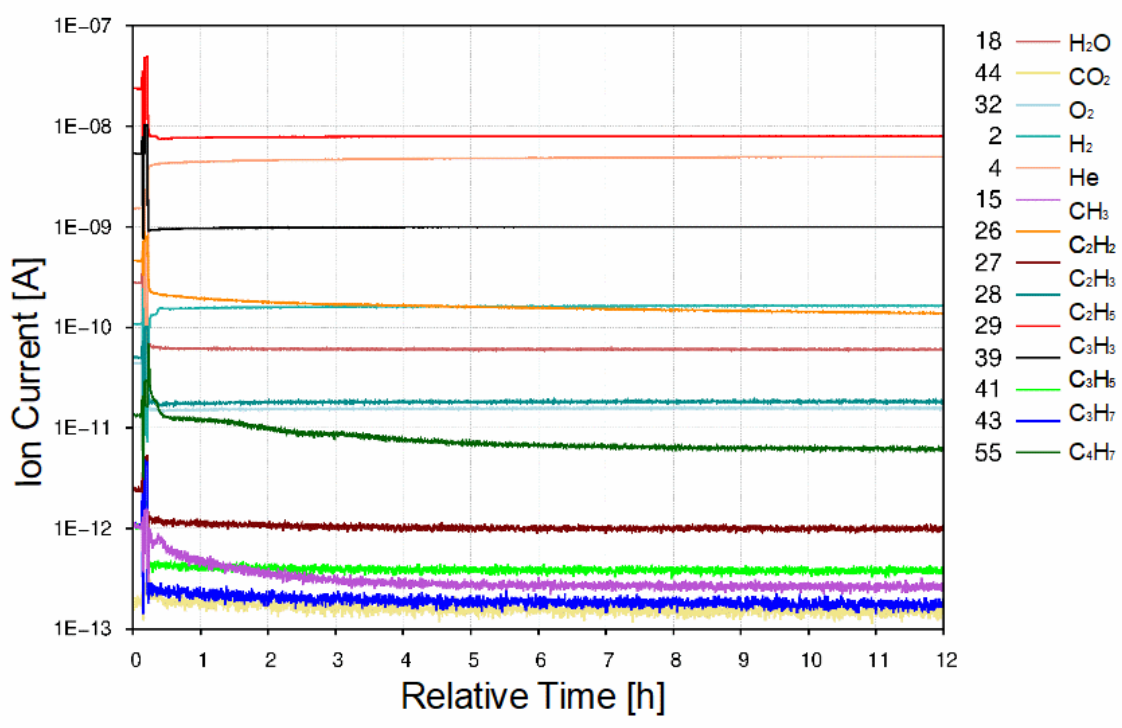

Figure A29: Mass spectrometry response of 11 nm Co/MCF-17 catalyst during FTS (ID15 MS).

8.14. Appendix 14

Debye simulations of the initial and final fit of XRD patterns of the 11 nm Co/MCF-17 catalyst, including background.

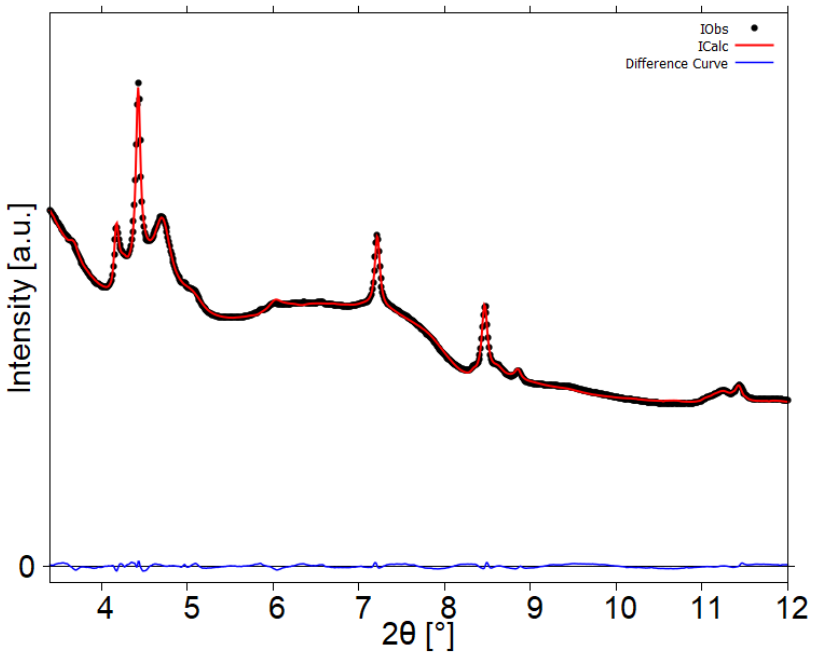

Figure A30: Debye simulations of XRD at 0 h of FTS with background – 11 nm Co/MCF-17.

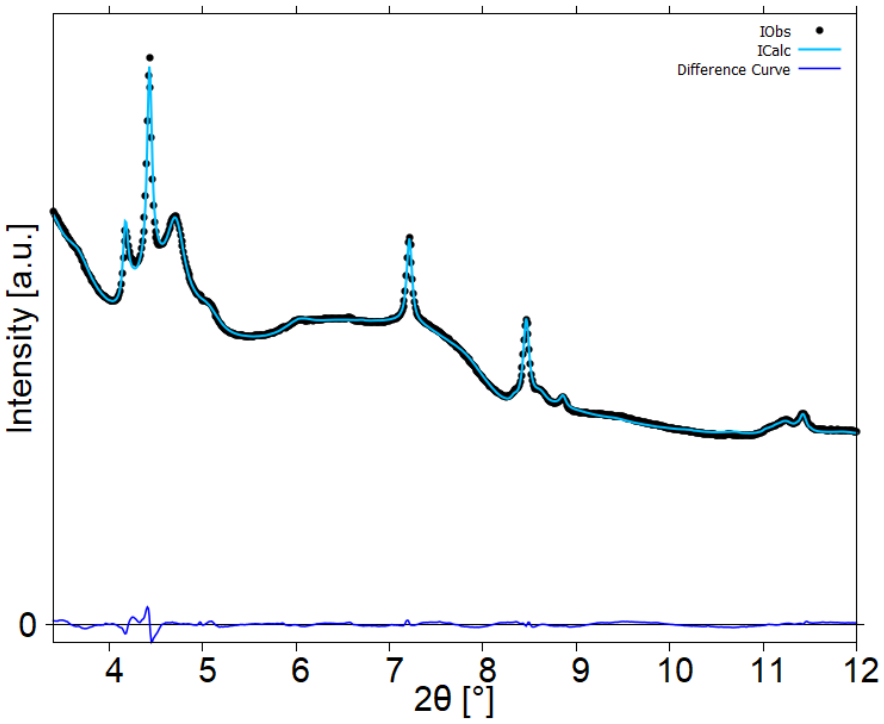

Figure A31: Debye simulations of XRD at 12 h of FTS with background – 11 nm Co/MCF-17.

8.15. Appendix 15

Minuit output file for Debye simulation of XRD pattern recorded at the start of Fischer Tropsch Synthesis.

SET TITLE
'Start re_run, scaled'
PARAMETERS

1	'alfa cc_c '	0.71307E+00	0.10000E-04
2	'beta hc_c '	0.30096E+00	0.10000E-04
3	'gamma hh_c '	0.23517E+00	0.10000E-04
4	'delta ch_c '	0.50109E+00	0.10000E-04
5	'str1 hor '	0.56468E-03	0.00000E+00
6	'str2 vert '	0.24372E+01	0.00000E+00
7	'a0 '	0.25122E+01	0.10000E-04
8	'c0 '	0.20475E+01	0.10000E-04
9	'rav '	0.13373E+02	0.10000E-02
10	'std '	0.18003E+02	0.10000E-04
11	'off '	0.85901E-02	0.10000E-02
12	'bi '	0.73341E+00	0.10000E-04
13	'scale '	0.43204E-03	0.10000E-07
14	'b0 '	0.49493E+00	0.10000E-04
15	'b1 '	0.17481E+01	0.10000E-03
66	'cell '	0.80838E+01	0.00000E-08
67	'cell '	0.80838E+01	0.00000E-08
68	'cell '	0.80838E+01	0.00000E-08
69	'biox '	0.30793E+00	0.00000E-08
70	'u '	0.58417E+02	0.00000E-08
71	'v '	-0.55113E+01	0.10000E-08
72	'w '	0.23102E+00	0.10000E-08
73	'x '	0.30608E+01	0.00000E-08
74	'y '	0.00000E+00	0.00000E+00
75	'scale '	0.13515E-12	0.10000E-12
76	'ocp '	0.10000E+01	0.00000E+00
77	'ocp '	0.10000E+01	0.00000E+00
78	'ocp '	0.10000E+01	0.00000E+00
79	'cell '	0.42509E+01	0.10000E-09
80	'cell '	0.42662E+01	0.00000E-09
81	'cell '	0.42662E+01	0.00000E-09
82	'biox '	0.61752E+01	0.00000E-08
83	'u '	0.84222E+02	0.10000E-03
84	'v '	-0.58409E+01	0.10000E-09
85	'w '	0.22470E+00	0.10000E-09
86	'x '	0.29358E+01	0.00000E-04
87	'y '	0.00000E+00	0.00000E+00
88	'scale '	0.69644E-06	0.10000E-08
89	'ocp '	0.10000E+01	0.00000E+00
90	'ocp '	0.10000E+01	0.00000E+00

Minuit output file for Debye simulation of XRD pattern recorded after 12 h of Fischer Tropsch Synthesis.

SET TITLE
'End re_run, scaled'
PARAMETERS

1'alfa cc_c	'	0.71274E+00	0.10000E-04
2'beta hc_c	'	0.29136E+00	0.10000E-04
3'gamma hh_c	'	0.23498E+00	0.10000E-04
4'delta ch_c	'	0.60154E+00	0.10000E-04
5'str1 hor	'	0.77647E-03	0.10000E-04
6'str2 vert	'	0.24404E+01	0.10000E-04
7'a0	'	0.25139E+01	0.10000E-04
8'c0	'	0.20489E+01	0.10000E-04
9'rav	'	0.14091E+02	0.10000E-02
10'std	'	0.17655E+02	0.10000E-04
11'off	'	0.89359E-02	0.10000E-06
12'bi	'	0.73213E+00	0.10000E-04
13'scale	'	0.43668E-03	0.10000E-07
14'b0	'	0.52413E+00	0.10000E-04
15'b1	'	0.17563E+01	0.10000E-03
66'cell	'	0.80839E+01	0.00000E-08
67'cell	'	0.80838E+01	0.00000E-08
68'cell	'	0.80838E+01	0.00000E-08
69'biox	'	0.33594E+00	0.00000E-08
70'u	'	0.98522E+02	0.10000E-07
71'v	'	0.15894E+00	0.10000E-07
72'w	'	0.81460E+00	0.10000E-07
73'x	'	0.82045E+01	0.00000E-07
74'y	'	0.00000E+00	0.00000E+00
75'scale	'	0.18182E-11	0.10000E-11
76'ocp	'	0.10000E+01	0.00000E+00
77'ocp	'	0.10000E+01	0.00000E+00
78'ocp	'	0.10000E+01	0.00000E+00
79'cell	'	0.42662E+01	0.00000E-08
80'cell	'	0.42662E+01	0.00000E-08
81'cell	'	0.42662E+01	0.00000E-08
82'biox	'	0.68782E+01	0.00000E-08
83'u	'	0.87262E+02	0.10000E-02
84'v	'	-0.53833E+01	0.10000E-08
85'w	'	0.51028E+00	0.10000E-08
86'x	'	0.27021E+01	0.00000E-03
87'y	'	0.00000E+00	0.00000E+00
88'scale	'	0.10182E-05	0.10000E-08
89'ocp	'	0.10000E+01	0.00000E+00
90'ocp	'	0.10000E+01	0.00000E+00